



# One-dimensional Bose Gases on an Atom Chip: Correlations in Momentum Space and Theoretical Investigation of Loss-induced Cooling.

Aisling Johnson

## ► To cite this version:

Aisling Johnson. One-dimensional Bose Gases on an Atom Chip: Correlations in Momentum Space and Theoretical Investigation of Loss-induced Cooling.. Optics [physics.optics]. Université Paris Saclay (COmUE), 2016. English. NNT: 2016SACLO013 . tel-01432392

**HAL Id: tel-01432392**

<https://pastel.hal.science/tel-01432392>

Submitted on 11 Jan 2017

**HAL** is a multi-disciplinary open access archive for the deposit and dissemination of scientific research documents, whether they are published or not. The documents may come from teaching and research institutions in France or abroad, or from public or private research centers.

L'archive ouverte pluridisciplinaire **HAL**, est destinée au dépôt et à la diffusion de documents scientifiques de niveau recherche, publiés ou non, émanant des établissements d'enseignement et de recherche français ou étrangers, des laboratoires publics ou privés.

NNT : 2016SACLO013

**THESE DE DOCTORAT**  
**DE L'UNIVERSITE PARIS-SACLAY**  
préparée à  
**L'INSTITUT D'OPTIQUE GRADUATE SCHOOL**

**ÉCOLE DOCTORALE N°572**  
Ondes et Matière (EDOM)

Spécialité de doctorat : Physique

par

**Aisling Johnson**

**One-dimensional Bose Gases on an Atom Chip:  
Correlations in Momentum Space and Theoretical  
Investigation of Loss-induced Cooling.**

Thèse présentée et soutenue à l'Institut d'Optique, le 9 Décembre 2016.

Composition du jury :

M. Antoine Browaeys	Président	Institut d'Optique
M. Klaasjan van Druten	Rapporteur	Université d'Amsterdam
Mme Hélène Perrin	Rapportrice	Université Paris 13
M. Daniel Comparat	Examinateur	Université Paris Saclay
M. Jakob Reichel	Examinateur	Université Paris 6
Mme Anna Minguzzi	Examinatrice	Université Grenoble Alpes
Mme Isabelle Bouchoule	Directrice de thèse	Institut d'Optique



---

## Remerciements

---

Une thèse, c'est à la fois court et long. Court, parce que développer un projet scientifique solide en trois ans sur un montage expérimental complexe est un vrai défi. Long, parce qu'en trois ans, on change, on mûrit et surtout on fait des rencontres. J'ai de nombreuses personnes à remercier pour cette aventure qui touche à sa fin.

Tout d'abord, merci à Chris Westbrook de m'avoir permis de rejoindre le groupe Optique Atomique. Je remercie chaleureusement les rapporteurs qui ont relu mon manuscrit, et les autres membres du jury pour leur participation et leur intérêt porté à ce travail de thèse. Ensuite, merci Isabelle, pour m'avoir fait confiance et m'avoir fait profiter de ton talent de physicienne. Puis Max, qui nous a rejoint il y a maintenant une année, pour avoir apporté une nouvelle dynamique à notre petite équipe. I'm also grateful to Bess (I know you speak French now but somehow English seems more appropriate): you taught me a lot during my first steps on the setup, so thank you! Je voudrais aussi remercier tous les stagiaires qui ont passé du temps avec nous : Laetitia, Grégoire et Raphaël. Bonne chance à vous tous pour la suite. Nous avons la chance d'avoir collaboré avec plusieurs théoriciens : Giuseppe Carleo, Tommaso Roscilde et Stuart Szigeti. J'ai beaucoup apprécié ces collaborations et les discussions scientifiques. Thibault et Tarik, je ne vous ai que brièvement connus lors de mon stage mais j'ai apprécié de vous rencontrer. La manip doit aussi beaucoup à nos électroniciens André et Fred, et à nos mécaniciens André et Patrick.

Ces années n'auraient pas été aussi riches sans tout le reste du groupe Optique Atomique : j'ai bien profité de l'excellent environnement scientifique apporté par les autres membres permanents : Alain, Vincent, Thomas, Denis, Laurent, Marc et Chris. La vie de laboratoire repose aussi sur l'interaction que j'ai eue avec les thésards, stagiaires et post-docs : Lauriane, Jérémie, Almaz, Kilian, Raphaël, Lynn, Ralf, Guillaume (Salomon), Guilhem, Rockson, Steven, Tobias, Yami, Kévin, Marie (Piraud), Marie (Bonneau), Josselin, Vincent, Pierre, Amaudric, Anaïs, Mukhtar, Guillaume, Hugo, Cécile (Carcy), Quentin, Lorenzo, Julien, Cécile (Crosnier), Marco, Maxime (et là j'espère que je n'ai oublié personnel!). Je retiendrai les longues pauses café (avec une pensée pour Hélène qui nous a préparé ce café tous les jours), les soirées tartiflettes, d'écouter du métal, les bières bues ensemble, les séances d'escalade, les matchs de basket de très haut niveau, et j'en oublie sans doute. Mention spéciale pour ceux qui m'ont filé un coup de main pour pomper l'eau lorsqu'on a vidé le circuit de refroidissement, et pour le nettoyage du sous-sol : je n'oublie pas Florence Nogrette et Sergio Martinez pour m'avoir prêté main forte ce jour-là, et le service technique pour sa disponibilité. J'ai aussi beaucoup apprécié interagir avec les autres groupes de recherche du laboratoire, notamment Optique Quantique.

L'enseignement a été une part importante de cette thèse : je garderai de bons souvenirs des TP et TD, ainsi que des élèves. Merci aux enseignants avec qui j'ai travaillé pour la très bonne ambiance de l'équipe pédagogique : Julien Villemejane, Fabienne Bernard, Lionel Jacubowiez, Henri Bénisty, Julien Moreau, Sylvie Lebrun, Nathalie Barbier, Franck Delmotte.

Je remercie le bureau des Arts de Sup Optique de m'avoir permis de squatter la salle de musique, et les musiciens avec qui partagé de bons moments en particulier lors des fêtes de début d'année et du dernier barbecue.

Pour la logistique et l'administration, merci à Martine Basset pour ses bonbons, Eric Charron et Patrick Georges pour leur disponibilité et leur écoute, et l'adminstration de l'Institut d'Optique et de l'Université Paris Sud en général. Je ne peux pas m'empêcher d'avoir une pensée pour les bus d'Albatrans et le RER B qui n'ont pas toujours brillé par leur ponctualité et leur efficacité.

Je souhaite enfin remercier les personnes qui n'ont pas participé directement à la thèse, mais qui m'ont accompagnée pendant ces années passées en région parisienne : le 3-RUE-JEANNE !!!, que cette colocation reste mythique, mes colocataires actuels au Parc d'Ardenay, mes partenaires de musique, de grimpe et de footing (un esprit sain dans un corps sain !), le Track'n'Art de l'ENS Cachan, et les potes d'ici et ailleurs. Dédicace au Ciné-Pal, au Divan du Monde et au Sunset pour les nombreux concerts, aux nombreux groupes de musique qui m'ont accompagnés pendant les heures passées en salle de manip, le sauna de Vitry-sur-Seine, RoboRally pour les fou-rires, et bien d'autres. Et oui, j'ai fini par retrouver mes atomes, pour ceux qui se poseraient encore la question ;-)

Et enfin, un grand merci à ma famille ; tout particulièrement mes parents et ma sœur, et ceux qui ont pu faire le déplacement pour la soutenance. Go raibh maith agaibh go léir: bhí spéis agaibh i gconaí i mo chuid oibre, fiú gan í a thuisceint. Tá mé buíoch faoin tacaíocht. J'apprécie le soutien et l'intérêt que vous avez toujours porté à ma thèse, malgré le sujet un peu obscur. Et Mathieu, c'est sans doute toi qui as suivi de plus près mes aventures, alors merci pour ton écoute et ta patience.

---

## Contents

---

<b>Introduction</b>	<b>1</b>
<b>1 Theoretical overview: one-dimensional Bose gases</b>	<b>5</b>
1.1 One-dimensionality and interactions in a tight confinement . . . . .	5
1.2 Exact description and phase diagram . . . . .	6
1.2.1 Lieb-Liniger model . . . . .	7
1.2.2 Yang-Yang thermodynamics . . . . .	8
1.2.3 Absence of condensation but a variety of phases . . . . .	9
1.2.4 Numerically exact methods . . . . .	11
1.3 Tools for the weakly-interacting gas . . . . .	13
1.3.1 Quick detour: the non-interacting gas . . . . .	13
1.3.2 Gross-Pitaevskii equation . . . . .	14
1.3.3 Bogoliubov transformation . . . . .	16
1.3.4 Classical field description . . . . .	17
1.4 Equilibrium correlation functions over the crossover . . . . .	19
1.4.1 Definitions . . . . .	19
First-order correlation function . . . . .	19
Second-order correlation function . . . . .	20
1.4.2 Ideal Bose Gas . . . . .	20
1.4.3 Quasi-condensate . . . . .	21
Density fluctuations . . . . .	21
$g^{(1)}$ function . . . . .	23
<b>2 Upgrade of the experimental apparatus</b>	<b>25</b>
2.1 Overview of the experimental setup . . . . .	25
2.2 The laser system . . . . .	26
2.2.1 Implementation of a new setup: Master 1, Master 2, Repumper . . . . .	26
Master 1 and repumper servoloop . . . . .	26
Master 1 and Master 2 servoloop . . . . .	27
Schematic of the complete setup . . . . .	28
2.2.2 More power and optical fibres . . . . .	29
Tapered Amplifier . . . . .	29
Fibre cluster and MOT light . . . . .	30
2.3 The heart of the experiment: the atom chip . . . . .	31
2.3.1 Chip layout and trap configurations . . . . .	31
Principle of magnetic trapping . . . . .	31
Loading traps: U, Z configurations . . . . .	32
Final trap: modulated guide . . . . .	33

	Choice of the modulation frequency . . . . .	35
	New chip layout . . . . .	35
2.3.2	From the cleanroom to the vacuum chamber . . . . .	35
	A word on the fabrication . . . . .	35
	Mounting the chip on the experiment . . . . .	37
2.4	The imaging system . . . . .	40
2.4.1	A new high-resolution objective . . . . .	40
	Technical specifications . . . . .	40
2.4.2	Required changes to the setup . . . . .	41
	Vacuum system . . . . .	41
	Optical system . . . . .	42
<b>3</b>	<b>Producing, probing and understanding the one-dimensional Bose gas</b>	<b>45</b>
3.1	Producing: the experimental cycle . . . . .	45
3.1.1	The sequencer: computer-experiment interface . . . . .	45
3.1.2	Towards loading the final trap . . . . .	46
	External and on chip MOT . . . . .	46
	Optical Molasses and pumping . . . . .	46
	Z trap and ACDC trap . . . . .	47
3.1.3	The final trap . . . . .	48
	Loading method . . . . .	48
	Characteristics: trapping frequencies . . . . .	49
3.2	Probing: absorption imaging . . . . .	50
3.2.1	Principle . . . . .	51
3.2.2	Improving the SNR . . . . .	52
3.2.3	Testing the objective with the atoms . . . . .	53
	Determining the resolution from pixel correlations . . . . .	54
	Atom number calibration . . . . .	55
3.3	Understanding: analysis methods . . . . .	55
3.3.1	Real space diagnoses . . . . .	56
	Modified equation of states in the 1D-3D crossover . . . . .	56
	Local Density Approximation . . . . .	56
	Longitudinal density profile . . . . .	57
	Atom number fluctuations . . . . .	58
3.3.2	Momentum space measurements . . . . .	59
	Magnetic focussing - principle . . . . .	60
	Momentum distribution measurements . . . . .	61
	Imaging in non-infinite conjugation . . . . .	62
<b>4</b>	<b>Momentum-space correlations of a one-dimensional Bose Gas</b>	<b>65</b>
4.1	Predictions . . . . .	66
4.1.1	Predictions for the homogeneous gas . . . . .	66
	General form of $\mathcal{G}(k, k')$ . . . . .	66
	Quasi-condensate regime: Luttinger liquid approach . . . . .	67
	True condensate vs quasi-condensate behaviour . . . . .	68
	Quantum Monte Carlo on the crossover . . . . .	70
4.1.2	Effects of an external trapping potential and finite resolution . . . . .	71
	Trapped gas in the local density approximation . . . . .	71

	Convolution with the imaging response function	72
4.2	Experimental results	72
4.2.1	Experimental protocol and data analysis	72
4.2.2	Presentation of the three data sets	73
4.2.3	Measured correlation maps for each set of data	74
	Correlations for data A - IBG	74
	Quasi-condensate: Data C	76
	On the crossover: Data B	77
	A single intensive quantity to summarise the data	78
4.3	Discussions	80
4.3.1	Effect of normalising atom number	80
	Homogeneous gas	81
	Inhomogeneous cloud	81
4.3.2	Contrast with true long-range order	82
5	<b>Non thermal states resulting from atom losses</b>	85
5.1	Context: cooling via uniform atom loss	85
5.1.1	The cooling paradox of 1D gases	85
5.1.2	Origins of the dissipative cooling mechanism	86
	Observations	86
	Model	86
5.2	Emergence of non-thermal states: a classical field study	88
5.2.1	Toy model: linearised approach in homogeneous systems	88
5.2.2	Non-linear Schrödinger equation with losses	90
5.2.3	Trapped systems	91
	Experimental observation	91
	Simulation	94
5.3	Relation with integrability	97
5.3.1	Thermodynamic arguments	97
5.3.2	Breaking the integrability: coupled NLSE	98
5.4	Beyond classical field: effect of atom quantisation	100
5.4.1	Modelling the quantised losses	100
	Stochastic Gross-Pitaevskii equation	100
	Evolution of the Bogoliubov modes	101
5.4.2	Simulation	102
6	<b>Perspective: a one-dimensional lattice for a magnetically trapped one-dimensional Bose gas</b>	105
6.1	Physical background: Mott transition and specificities of 1D	105
6.1.1	Generalities on the Mott transition	105
6.1.2	Mott physics in dimension one	107
	Two models: sine-Gordon vs Bose-Hubbard	107
	Bose-Hubbard model and generic Mott transition	108
	Commensurate/incommensurate and Pinning transitions	108
6.1.3	Effects of finite temperature and trapping potential	109
	Trapped systems	109
	Finite temperature	110
6.2	Experimental setting up of the lattice	112

6.2.1	Lattice setup . . . . .	112
6.2.2	Digital micromirror device . . . . .	112
6.3	Experimental constraints . . . . .	114
6.3.1	Optical power to reach the Mott transition . . . . .	114
6.3.2	Geometrical constraints on the beam . . . . .	116
6.4	Prospective studies . . . . .	118
6.4.1	Context . . . . .	118
6.4.2	Equilibrium physics . . . . .	118
6.4.3	Out-of-equilibrium dynamics . . . . .	120
<b>Conclusions</b>		<b>123</b>
<b>A More detailed calculations for the momentum correlations</b>		<b>125</b>
A.1	Correlations in the local density approximation . . . . .	125
A.2	The intensive quantity C and its relevant limits . . . . .	126
<b>B Split-time method</b>		<b>129</b>
<b>C Numerical methods for the trapped gas</b>		<b>131</b>
<b>D Recovering the stochastic GPE in the truncated Wigner approach</b>		<b>133</b>
<b>E Résumé en français</b>		<b>137</b>

---

## Introduction

---

Dimensionality plays an interesting role in physical systems. Low-dimensional systems ( $D < 3$ ), by their constrained nature, behave differently than their high-dimensional analogues. Take for instance a  $D$ -dimensional random walk: the probability of return to the origin is one for a number of spatial dimensions smaller than three, a mathematical result due to Pólya (1921). The initial interest in 1D problems first came from theoretical motivations: they often constitute simple toy-models, where analytical solutions are easier to find (with analytical approaches often failing for  $D > 1$ ). The Ising model in 1D [77, 99] can be solved in a rather straightforward manner, while the two-dimensional solution later found by Onsager [114] is much more involved, and is a very specific example of an analytically solvable problem for  $D > 1$ . More general than the Ising model, the Heisenberg model for spins is also solvable exactly in 1D. This was done by Bethe in the 1930s, thus creating a landmark by applying an Ansatz which now bears his name [10].

Bethe's breakthrough is a prime example of finding exact solutions to a very specific class of so-called integrable problems. In classical physics, the numbers of conserved quantities in such systems is equal to their number of degrees of freedom so that they only explore a small region of phase space: in other terms they are not ergodic. Integrability may also occur in quantum systems, although the question of how to characterise quantum integrable systems is still a subject of active research [122]. Classical or quantum, many examples of integrable systems are one-dimensional: the Luttinger liquid [103, 138] which describes bosonic or fermionic fields in the low-energy limit, non-linear partial differential equations such as the sine-Gordon model in 1D or the non-linear Schrödinger equation in 1D, and finally the Lieb-Liniger model [100, 101] (modelling bosons with contact interactions in 1D) are famous examples which we will meet later in this thesis. Alongside this wide class of exactly-solvable problems, a number of theoretical methods were developed for this reduced dimension [27].

Integrability is not just a mathematical feature: such systems are not expected to relax towards an equilibrium state described by a Gibbs ensemble, as opposed to ergodic systems. For systems close to integrability (as in experiments), different time scales are expected to emerge with the possibility of "prethermalisation" [9], namely the existence of an out-of-equilibrium stationary state. The specific behaviour of integrable or close-to-integrable models makes them an ideal playground to study the open question of relaxation of isolated quantum systems in general.

Despite the apparent simplicity of 1D models which allow to find analytical solutions,

they exhibit rich physics with no equivalence in higher dimensions. As well as consequences on the dynamics of such systems, their constrained nature also lead to distinct equilibrium behaviours. If the interactions are added to the equation, the movement of a single particle is forced onto its neighbours, creating long-wavelength collective excitations. For quantum systems, low-energy fluctuations exist even for vanishing temperatures, and their enhanced effect in 1D prevents the emergence of long-range order and rules out the possibility of Bose-Einstein condensation. But the presence of repulsive interactions leads to the existence of different phases, such as the phase-fluctuating condensate for weak interactions or the Tonks gas for strong interactions: in this strongly-correlated limit where the single-particle wavefunctions have no possibility of overlapping the non-penetrating bosons behave as fermions. The fermionised Tonks gas also illustrates that strong correlations are naturally present in 1D: to reach such correlated states in 3D, additional ingredients are necessary, for instance a periodic potential for the Mott insulating phase.

At first, most interest in these systems was purely theoretical, leading to numerous models and methods of which a few are enumerated above<sup>1</sup>. Progress in nanotechnology and fabrication methods later lead to the actual realisation of one-dimensional systems in condensed matter like conducting polymers [71], carbon nanotubes [14] (where the electrons obey the Luttinger liquid model), semi-conductor nanowires [151] (with the demonstration of quantized conductance) or arrays of Josephson junctions [146] (one of the first realisations of a one-dimensional bosonic phase). Topological edge states involved in the fractional Hall effect also showed Luttinger-liquid like behaviour [28]. A relationship between one-dimensionality and unconventional superconductivity has been speculated<sup>2</sup>. One-dimensional systems are not only present in condensed matter. An optical fibre is naturally one-dimensional, and the propagation of high-intensity light taking into account non-linearities obey non-linear partial differential equations such as the sine-Gordon or non-linear Schrödinger equations, with their non-linear characteristic acting as an analogue to interactions between massive particles. Experiments have demonstrated for instance solitons in such fibre optics: these studies are motivated by telecommunication applications and the generation of highly-localised (in time) intense light pulses [89]. So far, quantum features have not been explored with optical systems.

Of all experimental realisations of one-dimensional systems, the theorist's favourites are certainly ultra-cold atomic gases. In a rich community of analog quantum simulators, these synthetic quantum gases offer a clean and highly controllable environment to study all types of physical problems, including those in one dimension. Mainly two methods are available to realise ultracold one-dimensional gases systems experimentally. Their one-dimensional character requires a very strong transverse confinement, achieved with two-dimensional optical lattices [47, 90, 117, 136], or magnetic trapping with micro-wires close to a surface [43, 72, 144]. Examples of models realised by these experiments are the Bose-Hubbard and Lieb-Liniger models, both with bosonic species. Until recently, these experiments focussed on equilibrium properties of such gases, unveiling the theoretically-known phenomena mentioned above, such as the

---

<sup>1</sup>Reference [27] is a review of numerous theoretical methods available for one-dimensional Bosons

<sup>2</sup>See for instance [32, 140], among the publications of the field.

observation of a Tonks gas [117], the study of the Mott transition in 1D [136], or the characterisation of quasi-condensation in the weakly-interacting limit of Lieb-Liniger gases [6,43,79]. The natural phase fluctuations present in the system also constitutes an advantage for interferometry applications [133]. Finally, the integrability of the Lieb-Liniger model realises an ideal testbed for the study of out-of-equilibrium dynamics in isolated quantum systems, with the existence of long-lived out-of-equilibrium states [50,92], the observation of prethermalisation [64], the propagation of correlations following a quench [30,97] and the observation of a generalised Gibbs ensemble [96]. A continuous dialogue between theory and experiment lead to great progress in the field in the past twenty years.

Our experimental setup uses an atom chip to highly confine bosonic  $^{87}\text{Rb}$  atoms in very elongated traps, such that the transverse degrees of freedom are frozen. Until recently, the experiment mostly focussed on equilibrium characterisation of the phase diagram of a one-dimensional Bose gas with repulsive interactions [5,6,43,51,79,80]. However our setup is also well suited for the investigation of out-of-equilibrium physics: we can control longitudinal and transverse confinements separately which allows us to implement different excitations schemes such as transverse modulation [82] or longitudinal quenches [50]. The study of the breathing mode [50] lead the way to these new physical problems we wish to tackle, and my PhD thesis marks a transition to a new atom chip setup, improved towards these new studies. My manuscript is organised in the following manner:

- In Chapter one, I wish to give a brief theoretical background on one-dimensional Bose gases, as a starting point to the physics discussed in the rest of the manuscript. The equilibrium properties of the system of interest are presented, as well as some theoretical tools used for my doctoral work.
- In Chapter two, I detail the upgrades brought to the experimental setup for its improvement. Many modifications were implemented, justified by two main improvements: the overall stability of the setup on the one hand and the improvement of the imaging system on the other hand.
- In Chapter three, the experimental cycle to produce our ultracold samples is introduced. I then explicit the methods used to probe the produced samples: high-resolution absorption imaging. Finally, I enumerate the diagnosis tools developed over the years on the setup, in real space as well as in momentum space.
- Chapter four describes in detail the results on momentum-space correlations of a one-dimensional Bose gas, at equilibrium: these experiments were performed with the previous setup, in the first year of the PhD studies. I present the experimental results and their agreement with analytical as well as quantum Monte-Carlo calculations.
- The fifth Chapter is dedicated to the study of a dissipative cooling mechanism in the 1D Bose gas, and the emergence of a non-thermal state from atom loss. Classical field simulations in both the homogeneous and trapped systems are presented, and compared to experimental results where the detection of such a

state is demonstrated. Emergence of such a non-thermal state is due to the integrable character of the classical field problem at play, which we prove numerically by considering a system of coupled quasi-condensates of different mass, non-integrable unlike the single quasi-condensate. Finally, we derive the stochastic Gross-Pitaevskii equation considered in [65] with an alternative method, and recover results in agreement with their findings.

- The final Chapter presents a final upgrade to the experimental setup, not completely constructed yet: the building of a longitudinal optical lattice on top of the magnetic confined provided by the chip. I first review existing results on physics in dimension one with a periodic potential. The setup, almost complete, is then presented, followed by an overview of the questions we wish to consider in a near future.

# CHAPTER 1

---

## Theoretical overview: one-dimensional Bose gases

---

This Chapter aims at giving a brief overview of the properties of the repulsive weakly-interacting Bose gas in one dimension, and its theoretical description(s). First, the criterion for one-dimensionality will be raised and put in perspective with scattering in a highly-confining transverse potential, before turning to the seminal models of the one-dimensional Bose Gas and its complete phase diagram. There are numerous models and methods (implemented analytically and numerically) available. Some are exact, but we also value more accessible although approximative approaches which already give insight into many physical features. For some physical quantities we are unable to carry out the complete exact calculation and we thus turn to these approximations.

### 1.1 One-dimensionality and interactions in a tight confinement

Consider a one-dimensional Bose gas in a box of length  $L$  with periodic boundary conditions. Motion is frozen in transverse directions, such that the three-dimensional wavefunction can be factorised as<sup>1</sup>

$$\Psi(\mathbf{r}_1, \dots, \mathbf{r}_N) = \Psi(z_1, \dots, z_N) \prod_{n=1}^N \phi_0(x_i, y_i), \quad (1.1)$$

where  $\phi_0$  is the single particle wavefunction in the lowest transverse quantum state. Inhibition of transverse motion is ensured by a tight transverse confining potential, such that all energy scales in the system must be smaller than the transverse energy gap. For a harmonic transverse confinement (corresponding to the experimental implementation of these systems), the condition translates to

$$k_B T, \mu \ll \hbar \omega_\perp. \quad (1.2)$$

Dynamics are thus restricted to the longitudinal direction and from now on one can consider  $\Psi(z_1, \dots, z_N)$ , absorbing the remaining factor of the three-dimensional (3D) wavefunction as a normalisation coefficient. It is straightforward that the gas is kinematically effectively one-dimensional, with each individual atom only moving along the  $z$  axis, however the effect of the strong confinement on the interactions between

---

<sup>1</sup>Precautions should be taken in the vicinity of  $z_i = z_{i+1}$  where kinks appear in the many-body wavefunction as shown below.

atoms should be considered carefully.

For three-dimensional scattering, in the low-energy limit and for short-range interactions (both assumptions usually verified in the case of dilute ultracold atomic gases), a single parameter entirely contains the physics of scattering: the (3D) s-wave scattering length  $a_S$ , related to the phase shift gained by the colliding particles during the scattering event. Momentum and energy conservation laws ensure that when two particles collide in one dimension, their momenta are simply exchanged. The interaction potential can be written in terms of an effective coupling constant  $g_{1D}$  (which we assume positive, implying repulsive interactions):

$$V(\mathbf{r}) = g_{1D} \delta(\mathbf{r} - \mathbf{r}') \quad (1.3)$$

In the presence of an transverse external harmonic trapping potential of confinement frequency  $\omega_\perp$ , the effective 1D coupling is expressed with  $a_S$  as [113]:

$$g_{1D} = \frac{2\hbar a_S \omega_\perp}{\left(1 - C \frac{a_S}{l_\perp}\right)} \quad (1.4)$$

$l_\perp = \sqrt{\hbar/m\omega_\perp}$  is the transverse harmonic oscillator length, and  $C = \zeta(1/2) \approx 1.46\dots$  ( $\zeta$  being the Riemann  $\zeta$  function). If  $a_S \ll l_\perp$  (verified for weak enough interactions), the above expression takes the simpler form  $g = 2\hbar a_S \omega_\perp$ . Equation 1.4 suggests that a large coupling constant can be achieved with the so-called confinement-induced resonance, similar in nature to a Feshbach resonance: the incoming channel of two particles is coupled to a transversally excited molecular bound state. Such a resonance was experimentally implemented with Cesium atoms by Nägerl and colleagues [69] to reach strongly interacting regimes in 1D and 2D gases.

For  $^{87}\text{Rb}$  these resonances are not accessible. The ratio  $C a_S / l_\perp$  is of the order of 1 for transverse trapping frequencies in the 100 MHz range which is completely out of reach, with typical experimental transverse frequencies being around 1 kHz. Since Feshbach resonances are also out of reach (around 1000 G), we always lie in the limit where  $a_S$  is constant and  $g_{1D} \propto \omega_\perp$ . The s-wave scattering was measured to be  $a_S = 5.3$  nm [145] in the ground state  $|F = 2, m_F = 2\rangle$ . From now on, we consider such a transversally confined gas with an effective coupling constant  $g_{1D}$ .

## 1.2 Exact description and phase diagram

Just like a certain number of other one-dimensional (1D) systems, the 1D Bose gas has the remarkable property of being integrable. The models which describe the system, presented in this section, can be exactly solved and a certain number of quantities are exactly known. After presenting the  $T = 0$  and finite temperature models I will detail the interesting variety of phases the system exhibits. From a numerical point of view numerous exact methods also exist, the reduced dimensionality being a clear advantage from a computational cost point of view, and I will briefly mention the available methods most relevant to this doctoral work. However for a more comprehensive introduction to the models and methods mentioned here I refer the reader to the vast literature (see the cited documents throughout the Chapter).

### 1.2.1 Lieb-Liniger model

The Lieb-Liniger model developed in two seminal papers [100, 101] constitutes the simplest non-trivial model of interacting 1D bosons in the continuum at zero temperature. It contains two terms; kinetic energy and repulsive point-contact interactions (assumption usually verified in ultracold atomic gases) and takes the following form in second quantisation:

$$\hat{\mathcal{H}}_{LL} = -\frac{\hbar^2}{2m} \int dz \hat{\Psi}^\dagger(z) \frac{\partial}{\partial z} \hat{\Psi}(z) + \frac{g}{2} \int dz \hat{\Psi}^\dagger(z) \hat{\Psi}^\dagger(z) \hat{\Psi}(z) \hat{\Psi}(z). \quad (1.5)$$

By setting  $g$  to  $+\infty$  in equation 1.5 one recovers the so-called Tonks-Girardeau gas. Historically, Tonks first considered the classical problem of hard spheres in 1936 [139], and Girardeau [61] pointed out the one-to-one correspondance between impenetrable bosons in dimension one and spinless fermions in 1960, before Lieb and Liniger considered the quantum problem for arbitrary interaction strengths in 1963. From the parameters present in 1.5, an energy and a length scale can be built:

$$l_g = \frac{\hbar^2}{mg} \text{ and } E_g = \frac{mg^2}{2\hbar^2}. \quad (1.6)$$

Since particles are indistinguishable one can restrict the problem to a subspace  $z_1 < z_2 \dots < z_N$  and  $\hat{\Psi}$  in other regions of the multi-dimensional space can be recovered by symmetrisation. The ground state of the many-body wavefunction can be constructed using a Bethe Ansatz [101]. A set of  $N$  quantum numbers  $I_1 < \dots < I_N$  (in a system with  $N$  particles, reflecting the integrability of the problem) then completely determine the so-called quasi-momenta  $k_i$  of the system and the corresponding eigenstates: [17, 27].

$$\hat{\mathcal{H}}_{LL} \hat{\Psi}(z_1, \dots, z_N) = E(k_1, \dots, k_N) \hat{\Psi}(z_1, \dots, z_N) \quad (1.7)$$

with

$$\hat{\Psi}(z_1 < \dots < z_N) = \sum_P A_P e^{i(k_{P(1)} z_1 + \dots + k_{P(N)} z_N)} \text{ and } E = \frac{\hbar^2}{2m} \sum_i k_i^2. \quad (1.8)$$

where there are  $N!$  possible permutations  $P$  of the set  $\{1, 2, \dots, N\}$ . The Bethe wavefunction can be interpreted in the following manner: when the coordinates  $z_i$  are distinct, the Hamiltonian is reduced to a system of free particles and the many-body eigenstate is a linear combination of the free-particle plane waves. If two particles of momenta  $k_{i+1}$  and  $k_i$  collide, resulting in a permutation of momenta, the boundary condition  $z_i = z_{i+1}$  translates to:

$$A_{P'} = A_P \frac{k_{i+1} - k_i + ig}{k_i - k_{i+1} + ig}. \quad (1.9)$$

The permutation  $P'$  differs from  $P$  by exchange of  $k_i$  and  $k_{i+1}$  and the coefficient  $A_{P'}$  is thus modified as in 1.9: these coefficients are fully determined by two-body collisions. In addition, the periodic boundary conditions determine the quasi-momenta  $k_i$  so that the Bethe wavefunction is completely determined by two-body processes. The Bethe Ansatz solution is exact since no additional momenta are generated after scattering processes, feature owing to point-contact interactions. In the thermodynamic limit

$L \rightarrow \infty$  at fixed density  $n = N/L$ , the ground-state properties can be computed via the quasi-momentum distribution [101].

After rescaling all energies by  $E_g$  and lengths by  $l_g$  the ground state solely depends on a dimensionless interaction parameter  $\gamma = 1/(nl_g)$ . The form of  $\hat{\Psi}(z_1 < \dots < z_N)$  for different values of  $\gamma$  is illustrated figure 1.1. A certain number of ground state properties (energy per particle, chemical potential, ground-state energy...) were determined numerically by solving an integral equation on this single relevant parameter [101]<sup>2</sup>.



**Figure 1.1:** Schematic representation of the many-body wavefunction for weak interactions ( $\gamma \ll 1$ , or equivalently  $E/N \gg E_g$ , left), and strong interactions ( $\gamma \gg 1$ , or  $E/N \ll E_g$ , right). As interactions gain in importance the value of  $\hat{\Psi}$  at the nodes decreases to vanish at the infinite interaction limit, where the gas exhibits Pauli principle-like features (or "fermionisation"). Adapted from [21].

After determining the ground-state, Lieb (in [100]) turned to the elementary excitations of the system, revealing two branches nicknamed "type I" and "type II", or "particles" and "holes" (as an analogy to excitations in a Fermi gas, particularly striking in the strongly-interacting limit). "Type I" can be identified as Bogoliubov excitations: the numerics (figure 1.2) show that the Bogoliubov spectrum practically lies on the Lieb I excitation curve for small  $\gamma$ , however a slight discrepancy appears for larger interaction strengths. A certain number of papers suggest a correspondence between type II excitations and dark solitons for weak interactions, as in [76] or more recently [84].

### 1.2.2 Yang-Yang thermodynamics

At finite temperature, Type I and Type II excitations are thermally generated. In the thermodynamic limit, C.N. Yang and C.P. Yang derived two integral equations (from the minimisation of free energy and the continuity of the wavefunction) for the quasi-momentum distributions, from which the exact equation of state  $n(\mu, T)$  can be numerically evaluated. The existence of this exact solution is of course an tremendous advantage when it comes to measuring thermodynamic quantities experimentally (see Chapter 3 for more on this aspect).

Besides usual thermodynamic variables like the chemical potential, the entropy per particle or the internal energy, other quantities like the local pair correlations  $g^{(2)}(0)$  can be computed. It represents the probability of finding a second particle at  $z = 0$  knowing that another has been detected at this same position and defines the various phases of the 1D Bose gas (see below). We follow the approach adopted in [57] based on the Hellman Feynman theorem. For a generic hamiltonian depending on a parameter

<sup>2</sup>Many people wonder who Werner Liniger was: an acclaimed numerical physicist working at IBM research centre in New York at the time.

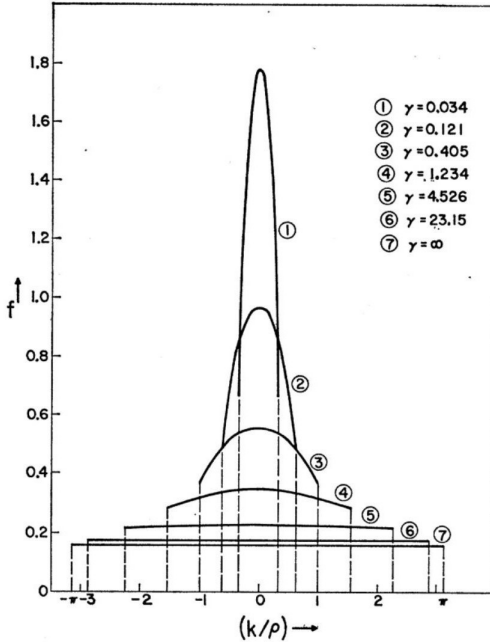


FIG. 2. The distribution function of “quasi-momenta” in the ground state for various values of  $\gamma = c/\rho$ . The vertical dashed lines are the cutoff momenta  $K$  (cf. Fig. 1). When  $\gamma = \infty$ ,  $f = (2\pi)^{-1}$ . For all  $\gamma$ ,  $\int_{-K}^K f(k) dk = \rho$ .

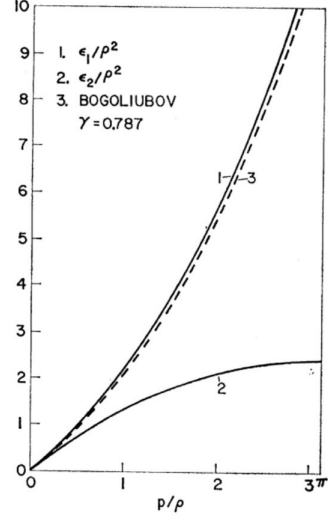


FIG. 4. A comparison plot of the two types of excitations,  $\epsilon_1$  and  $\epsilon_2$ , for  $\gamma = 0.787$ . The dashed curve is Bogoliubov's spectrum which is quite close to the type I spectrum. The type II spectrum does not exist in Bogoliubov's theory.

**Figure 1.2:** Left: figure 2 of [101], representing the quasi-momenta distributions for different interaction strengths. The most peaked distributions correspond to the smallest  $\gamma$ , while the strongly-interacting samples reveal Fermi-like distributions. Right: figure 4 of [100]. The dispersion relations of the two excitation branches are plotted, along with the Bogoliubov dispersion (dashed).

$\lambda$ , and one of its eigenstates  $|\Psi_\lambda\rangle$  depending exclusively on  $\lambda$  and the eigenenergy  $E_\lambda$  one has:

$$\frac{d}{d\lambda} E_\lambda = \langle \Psi_\lambda | \frac{d}{d\lambda} \hat{H}_\lambda | \Psi_\lambda \rangle \quad (1.10)$$

The free energy  $F$  is defined by  $F = -\beta^{-1} \ln (\sum_n e^{-\beta E_n})$  with summation over all eigenstates, so that (where  $\langle \dots \rangle$  represents an ensemble average)

$$\frac{dF}{d\lambda} = \frac{1}{\text{Tr}(e^{-\beta \hat{H}_\lambda})} \sum_n \frac{dE_n}{d\lambda} e^{-\beta E_n} = \left\langle \frac{d\hat{H}_\lambda}{d\lambda} \right\rangle \quad (1.11)$$

For the Lieb-Liniger Hamiltonian and the coupling constant  $g$ :

$$\frac{dF}{dg} = \left\langle \frac{1}{2} \int dz \hat{\Psi}^\dagger(z) \hat{\Psi}^\dagger(z) \hat{\Psi}(z) \hat{\Psi}(z) \right\rangle = L \frac{n^2}{2} g^{(2)}(0) \quad (1.12)$$

With the knowledge of the equation of state, the quantity  $g^{(2)}(0)$  is accessible, and can be computed for different regimes of gas [88].

### 1.2.3 Absence of condensation but a variety of phases

1D Bose gases present distinct coherence properties compared to their three-dimensional counterparts. Since the density of states  $\rho(\epsilon)$  scales like  $\epsilon^{-1/2}$ , the number of particles  $N - N_0$  in the excited states (where  $N_0$  denotes the occupation of the ground state and  $N$  the total number of particles) never saturates, and no macroscopic occupation of the

ground state occurs. This argument holds for the non-interacting gas, however more general arguments reveal the absence of condensation in the interacting gas also. In the constrained one-dimensional configuration, long-wavelength quantum fluctuations in the system propagate longitudinally and impose a fast decay of the one-body density matrix, preventing long-range coherence in the system: there is no Bose-Einstein condensation in dimension one.

Nevertheless, a rich variety of phases is revealed upon varying the interaction strength and temperature. We previously defined a dimensionless interaction parameter  $\gamma = 1/nl_g$ . A reduced temperature is also introduced by rescaling  $k_B T$  with  $E_g$ . The full phase diagram of the 1D Bose is then obtained by spanning the two dimensionless parameters

$$\gamma = \frac{mg}{\hbar^2 n} \text{ and } t = \frac{2\hbar^2 k_B T}{mg^2}. \quad (1.13)$$

From  $g^{(2)}(0)$ , three asymptotic phases can be identified in parameter space  $(t, \gamma)$ , separated by smooth crossovers (rather than phase transitions since no continuous symmetry can be broken in 1D).

For  $g^{(2)}(0) \approx 2$ , the gas is in the so-called ideal Bose gas regime (IBG). In this phase found in the region of the phase diagram where  $t\gamma^2 > 1$ , the particles bunch: a boson has twice the probability of finding itself at a position where there is already a boson than elsewhere. Two subregimes with such behaviour can be identified. For  $t\gamma^2 \gg 1$  the interparticle distance is much larger than the de Broglie wavelength  $\lambda_{dB}$  and the gas follows Maxwell-Boltzmann statistics. As  $\lambda_{dB}$  increases, the Bose gas becomes degenerate and no longer verifies the classical equation of state.

By further increasing the density, one gradually enters a regime where the repulsive interactions prevent bosonic bunching, so that  $g^{(2)}(0) \approx 1$ . This occurs for  $t\gamma^{3/2} \approx 1$ , or equivalently at the crossover temperature  $k_B T_{CO} = \hbar n \sqrt{gn/m}$ <sup>3</sup>. The gas is coherent from the density fluctuation's perspective (they are suppressed just as they would in a true condensate), but phase fluctuations remain, phase coherence over the complete length of the gas being forbidden. In this quasi-condensate (or qBEC, also sometimes called a phase-fluctuating condensate) two subregimes can also be distinguished, by the nature of the fluctuations in the system: when  $t\gamma \gg 1$  thermal fluctuations dominate while for denser and colder systems verifying  $t\gamma \ll 1$  quantum fluctuations take over<sup>4</sup>.

Finally, in the strong interactions limit where  $t \ll 1$  and  $\gamma \gg 1$  one enters the Tonks-Girardeau phase, where  $g^{(2)}(0) \ll 1$ . Atoms are strongly correlated, and mimic the Pauli exclusion principle of fermions.

---

<sup>3</sup>This crossover temperature can be derived by considering the condition for which density fluctuations become small, see section 1.4.3

<sup>4</sup>The characterisation of the different phases of the 1D Bose gas is considered here from the quantity  $g^{(2)}(0)$ , however for different observables this identification of phases may vary.

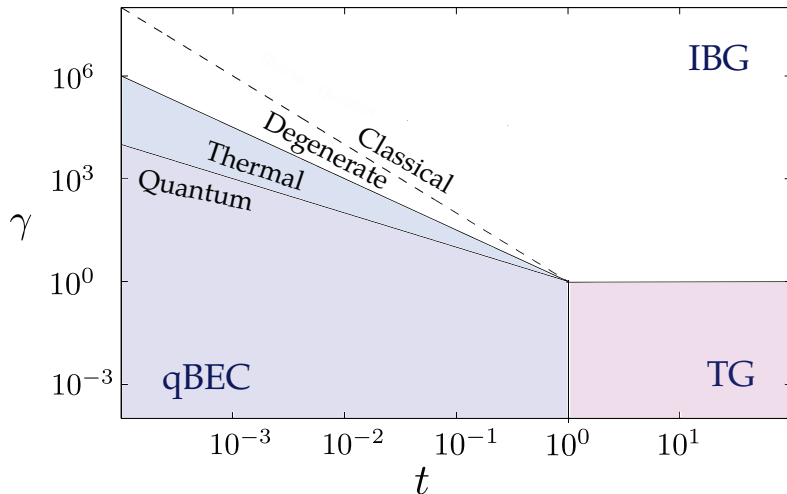


**Figure 1.3:** Phase diagram of the 1D Bose gas. There are three main phases: the ideal Bose gas (IBG), where bunching persists, the Tonks gas (TG) where fermionisation occurs and the quasi-condensate (qBEC) where bunching is suppressed. The equations of the lines separating the phases in the weakly-interacting region ( $\gamma \ll 1$ ) are  $t\gamma^2 = 1$  (dashed line in white region),  $t\gamma^{3/2} = 1$  (white to blue) and  $t\gamma = 1$  (solid line in blue region).

However powerful Yang-Yang thermodynamics may be, not all potential quantities of interest can be determined, like correlation functions. Other methods exist, and in particular a certain number of exact numerical tools can be implemented.

#### 1.2.4 Numerically exact methods

Although the Lieb-Liniger model is integrable, the general Hamiltonian of a trapped 1D Bose Gas in the grand-canonical ensemble is a numerically hard problem. Here I wish to give the idea behind some available numerical methods. Mainly three so-called exact<sup>5</sup> methods come to mind for 1D Bose gases: Exact Diagonalisation, Density Matrix Renormalisation Group (DMRG) and Quantum Monte Carlo (QMC).

Exact diagonalisation is a powerful method to calculate low-energy eigenvalues and eigenfunctions of a stationary Hamiltonian. It is applicable in a wide range of problems and was demonstrated for 1D Bose gases in [35] (amongst others). The matrix elements of each term of the Hamiltonian is expressed on a single-particle basis, chosen judiciously. Since the dimension of the Hilbert space is in general infinite, the basis is restricted to a finite number of vectors. This truncation results in deviations between the exact and numerical eigen- energies and functions, so that the accuracy of the results greatly depends on the initial choice of basis functions and their number. In this case "exact" refers to the absence of any other approximation to solve the many-body quantum problem [34]. However, the computation time and memory limits the sizes of the Hilbert spaces, scaling exponentially with the number of particles, in reach. Only small systems of a few tens of particles at most can be considered [27].

<sup>5</sup>We will see in this discussion that the exact nature of the results is not granted, but that they are in general accurate within error bars.

DMRG is a variational method first developed by S. White [149], and aiming at simplifying the task of finding accurate solutions for large Hilbert spaces rather than brute force exact diagonalisation. DMRG iteratively reduces the size of the Hilbert space by selecting effective degrees of freedom most important for the target state (like the ground state for instance). It is a renormalisation method in the sense that the system is iteratively divided into subsystems ( $M$  and  $N$ ). The reduced density matrices  $\hat{\rho}_M$ ,  $\hat{\rho}_N$  are then considered to express the target state  $|\Psi\rangle$ . This method has proven very accurate for a number of 1D problems and can be extended to time-dependent Hamiltonians [27]. For the study of 1D bosons, it was implemented for instance in [36].

The term Quantum Monte Carlo in fact encompasses a large number of methods which all aim to provide a reasonably accurate solution of quantum many-body problems. They are in principle applicable in all dimensions, to a great variety of systems, of both quantum statistics (although the infamous sign problem remains an obstacle for fermionic and spin systems). These numerical methods go well beyond mean-field and allow for instance the computation of correlation functions and offering exact solutions - within statistical error bars - for a certain number of problems (like non-frustrated bosons). Their common thread is the use of the Monte Carlo method to treat high-dimensional integrals which arise in quantum many-body problems. QMC is most powerful for non time-dependent Hamiltonians.

During my thesis we collaborated with Tommaso Roscilde of ENS de Lyon. He computed the two-body correlation function in momentum space across the quasi-condensation crossover (quantity which we measured, see Chapter 4) using the stochastic series expansion (SSE) approach, which differs from the path-integral scheme. In the latter, the Boltzmann operator  $e^{-\beta H}$  is evaluated in imaginary-time propagation using path-integral representation [132]. In the series expansion representation, the Boltzmann operator is decomposed in a Taylor series expansion as:

$$e^{-\beta H} = \sum_{n=0}^{+\infty} \frac{-\beta^n}{n!} H^n \quad (1.14)$$

Choosing a basis, the partition function can then be written as

$$Z = \sum_{n=0}^{+\infty} \sum_{\alpha_n} \langle \alpha_0 | H | \alpha_{n-1} \rangle \dots \langle \alpha_2 | H | \alpha_1 \rangle \langle \alpha_1 | H | \alpha_0 \rangle. \quad (1.15)$$

The method was applied for the computation of the momentum distribution and momentum correlations, for comparison with experimental data, detailed in Chapter 4.

### Summary

- The 1D Bose gas is an example of an integrable system and the equation of state can be computed exactly.
- Although no condensation is possible in dimension one, in the presence of repulsive interactions three main phases arise: the non-interacting ideal Bose

gas, the so-called quasi-condensate (which owes its name to the fact it verifies half of the properties of a true condensate), and the strongly interacting Tonks gas.

- Although Yang Yang thermodynamics are very powerful to determine a certain number of quantities, exact numerical methods are available where the analytical approach fails.
- These numerical methods are manifold, and in the course of this thesis we turned to Quantum Monte Carlo calculations.

### 1.3 Tools for the weakly-interacting gas

Most of the numerical methods mentioned previously are quite challenging to implement and require substantial computational power and time. However, more simple tools, although not exact, are straightforward enough and capture pertinent physics. The idea is to find strategies to solve the hard problem given, in the general case of a trapped 1D Bose gas in the grand-canonical ensemble, by:

$$\hat{\mathcal{H}} = -\frac{\hbar^2}{2m} \int dz \hat{\Psi}^\dagger(z) \left( \frac{\partial^2}{\partial z^2} + (V_{ext}(z) - \mu) \right) \hat{\Psi}(z) + \frac{g}{2} \int dz \hat{\Psi}^\dagger(z) \hat{\Psi}^\dagger(z) \hat{\Psi}(z) \hat{\Psi}(z). \quad (1.16)$$

The case of the ideal Bose gas is treated separately since the absence of interactions greatly simplifies the problem. Then, assuming  $T \ll T_{CO}$  to place ourselves in the quasi-condensate phase, two common approaches for the weakly-interacting gas (the Bogoliubov approximation and the Gross-Pitaevskii equation) are introduced. Finally, the slightly more involved classical field picture is considered: this approach can describe the quasi-condensation crossover as long the temperature is high enough. The case of strongly-interacting gases will not be mentioned in the following.

#### 1.3.1 Quick detour: the non-interacting gas

Consider  $N$  bosons in a box of length  $L$  (for simplicity the external potential is discarded in this discussion), of chemical potential  $\mu$  and temperature  $T$ . The occupation number of a mode  $k$  is given by the Bose law:

$$\nu_k = \frac{1}{e^{\beta(E_k - \mu)} - 1} \quad (1.17)$$

$E_k$  is the dispersion relation of a free particle  $E_k = \hbar^2 k^2 / 2m$ , and  $\mu < 0$ . The equation of state  $n(\mu, T)$  is obtained by integrating  $\nu_k$  over  $k$ . In the thermodynamic limit it reads:

$$n = \frac{1}{\lambda_{dB}} g_{1/2}(f). \quad (1.18)$$

$f = e^{\beta\mu}$  is the fugacity of the gas,  $\lambda_{dB} = \hbar \sqrt{2\pi/mk_B T}$  the thermal de Broglie wavelength and  $g_{1/2}(z) = \sum_{l=1}^{+\infty} z^l / \sqrt{l}$ . In 1D,  $n$  diverges when  $\mu$  approaches zero, which

prevents a saturation of the population of excited states.

In the classical and degenerate limits the equation of state takes simple forms:

- When  $|\mu| \gg k_B T$ , the Bose distribution simplifies to a Maxwell-Boltzmann distribution and the signature of the quantum nature of the considered particles disappears:

$$\nu_k = e^{-\beta(E_k - \mu)}. \quad (1.19)$$

The equation of state thus becomes

$$n = \frac{1}{\lambda_{dB}} e^{\beta\mu} \quad (1.20)$$

- In the opposite limit where  $|\mu| \ll k_B T$ , the occupation number becomes Lorentzian

$$\nu_k = \frac{1}{k^2 \frac{\lambda_{dB}^2}{4\pi} + \beta|\mu|}, \quad (1.21)$$

and correspondingly,

$$n = \frac{1}{\lambda_{dB}} \sqrt{\frac{\pi}{\beta|\mu|}}. \quad (1.22)$$

These results are valid as long as the interactions are not important enough to impose an energy cost on density fluctuations.

### 1.3.2 Gross-Pitaevskii equation

Despite the absence of true long-range order some approaches valid for three-dimensional condensates can be extended to the 1D case, such as the Gross-Pitaevskii equation. If a true condensate would exist, the approach would be to decompose the quantum field  $\hat{\Psi}$  into a complex field (representing the macroscopic condensate wavefunction) and a perturbation  $\delta\hat{\Psi}$  describing the depletion of the condensate.

$$\hat{\Psi} = \Psi_0 + \delta\hat{\Psi} \quad (1.23)$$

Injecting this form of  $\hat{\Psi}$  into hamiltonian 1.16, the energy functional of the system is found to be (neglecting high-order terms in  $\delta\hat{\Psi}$ ):

$$E = \int dz \left[ \frac{\hbar^2}{2m} |\partial_z^2 \Psi_0(z)|^2 + V_{ext}(z) |\Psi_0(z)|^2 + \frac{g}{2} |\Psi_0|^4 \right] \quad (1.24)$$

The ground-state of the condensate wavefunction is then given by the minimisation of this functional for a constant total number of particles  $N$ , and introducing the chemical

potential as a Lagrange multiplier  $E - \mu N$ . The result is the time-independent Gross-Pitaevskii equation [66, 119], which is a mean-field derivation (where correlations between particles are neglected since products of  $\delta\Psi$  were discarded) of the ground state of the system:

$$-\frac{\hbar^2}{2m} \frac{\partial^2}{\partial z^2} \Psi_0 + V_{ext}(z) \Psi_0(z) + g|\Psi_0(z)|^2 \Psi_0(z) = \mu \Psi_0(z). \quad (1.25)$$

The time-dependent Gross-Pitaevskii equation is then given by

$$i\hbar \frac{\partial \Psi_0(z, t)}{\partial t} = -\frac{\hbar^2}{2m} \frac{\partial^2}{\partial z^2} \Psi_0 + V_{ext}(z) \Psi_0(z) + g|\Psi_0(z)|^2 \Psi_0(z). \quad (1.26)$$

Exact solutions are rare and hard to compute (the most famous class of exact analytical solution are probably solitons), and in general the equation is numerically propagated. A characteristic length scale referred to as the healing length can be extracted from this equation. In a homogeneous system with boundary conditions  $\Psi_0(0) = \Psi_0(L) = 0$ ,  $\xi = \hbar/\sqrt{2mgn}$  is the typical distance over which the gas gains its bulk density  $|\Psi_0|^2$ . This length also appears in the Bogoliubov treatment (section 1.3.3), and the density correlation function (section 1.4.3).

However, the initial assumption of the reasoning leading to the Gross-Pitaevskii equation is wrong: in 1D the decomposition 1.23 *a priori* doesn't hold because of the absence of a macroscopically occupied state  $\Psi_0$ . Following the approach of Mora and Castin [108], the Gross-Pitaevskii can be recovered in a more rigorous treatment. If density fluctuations are small, the field operator may be written in phase-density representation:

$$\hat{\Psi}(z) = \sqrt{\hat{n}(z)} e^{i\hat{\theta}(z)} \quad (1.27)$$

where  $\hat{n}$  and  $\hat{\theta}$  are canonical conjugate operators. Precautions should be taken when defining these operators locally and in particular the authors of [108] discretise space. In the following I will assume they are properly defined<sup>6</sup>. In the quasi-condensate density fluctuations are small and a similar treatment as previously can then be applied, with the density operator written as:

$$\hat{n} = n_0 + \delta\hat{n}, \quad (1.28)$$

with  $\delta\hat{n} \ll n_0$  and  $\partial_z \hat{\theta} \ll n_0$ . With these two small parameters, the Hamiltonian can be expanded, which was done up to third order (necessary for the computation of the density fluctuations [108]):  $\hat{H} = \hat{H}_0 + \hat{H}_1 + \hat{H}_2 + \hat{H}_3$ . The minimisation of  $\hat{H}_0$  at fixed chemical potential recovers the Gross-Pitaevskii equation, with the current notations:

$$\left[ -\frac{\hbar^2}{2m} \partial_z^2 + V_{ext}(z) - \mu + gn_0 \right] \sqrt{n_0} = 0. \quad (1.29)$$

As a consequence the previously presented results of the Gross-Pitaevskii equation are perfectly valid. For the choice of density profile given by the Gross-Pitaevskii approximation  $H_1$  vanishes. The next order to evaluate is  $H_2$ , which gives the excitations of

---

<sup>6</sup>Y. Castin's lecture notes [24] pedagogically present the issues and how to circumvent them.

the system on top of the zeroth order result given by 5.2: in the linearised approach presented in the next section, they are the Bogoliubov excitations.

### 1.3.3 Bogoliubov transformation

The extension of the classic Bogoliubov theory [16] for condensates to lower dimensions needs to be considered carefully because of the absence of true long-range order. In [108] the authors derive an expansion of the hamiltonian with the appropriately defined small parameters  $\delta\hat{n} \ll n_0$  and  $\partial_z\theta \ll n$ .  $H_0$  was found to return the Gross-Pitaevskii equation. Consider the Heisenberg equations of motion applied to the expanded Hamiltonian  $\hat{H}$ :

$$i\hbar \frac{d\hat{\Psi}}{dt} = [\hat{\Psi}, \hat{H}]. \quad (1.30)$$

The results of this derivation are the so-called hydrodynamic equations:

$$\hbar\partial_t\hat{n} = \frac{\hbar^2}{m}\partial_z^2(\hat{\theta}\hat{n}), \quad (1.31)$$

$$\hbar\partial_t\hat{\theta} = \frac{\hbar^2}{2m}(\partial_z\hat{\theta})^2 + \frac{\hbar^2}{2m}\frac{\partial_z^2\sqrt{\hat{n}}}{\sqrt{\hat{n}}} - g\hat{n}. \quad (1.32)$$

The previous equations can be linearised in  $\delta\hat{n}$  and  $\partial_z\hat{\theta} \ll n$ :

$$\begin{aligned} \hbar\partial_t\delta\hat{n} &= 2\sqrt{n_0}\left(-\frac{\hbar^2}{2m}\partial_z^2 + gn_0 - \mu + V_{ext}(z)\right)\hat{\theta}\sqrt{n_0} \\ \hbar\partial_t\hat{\theta} &= -\frac{1}{2\sqrt{n_0}}\left(\frac{\hbar^2}{2m}\partial_z^2 + 3gn_0 - \mu + V_{ext}(z)\right)\frac{\delta\hat{n}}{\sqrt{n_0}} \end{aligned} \quad (1.33)$$

We now restrict the discussion to a homogeneous system (such that  $V_{ext} = 0$ , for simplicity). The spectrum of excitations can be derived from the two linearised hydrodynamic equations with the following transformation (diagonalising the quadratic hamiltonian associated with equations 1.33):

$$\begin{aligned} \delta\hat{n} &= \sqrt{\frac{n_0}{L}}\sum_k f_k^- \left(\hat{b}_k e^{ikz} + \hat{b}_k^\dagger e^{-ikz}\right) \\ \hat{\theta} &= \frac{1}{2i\sqrt{n_0 L}}\sum_k f_k^+ \left(\hat{b}_k e^{ikz} - \hat{b}_k^\dagger e^{-ikz}\right) \end{aligned} \quad (1.34)$$

Where  $f_k^\pm$  verify

$$\begin{aligned} f_k^+ &= \left[\frac{E_k}{E_k+2\mu}\right]^{1/4} \\ f_k^- &= \frac{1}{f_k^+}. \end{aligned} \quad (1.35)$$

$E_k$  being the dispersion relation of a free particle. With this procedure, the Hamiltonian  $\hat{H}$  takes the diagonal form

$$\text{lang}e\hat{H} = \sum_k \epsilon_k \hat{b}_k^\dagger \hat{b}_k. \quad (1.36)$$

$\epsilon_k = \hbar\omega_k = \sqrt{E_k(E_k + 2\mu)}$  is the dispersion relation of the quasi-particles created or destroyed by the operators  $\hat{b}_k^\dagger, \hat{b}_k$ .  $\epsilon_k$  takes two familiar forms in the limits  $k \ll \xi^{-1}$  and  $k \gg \xi^{-1}$  ( $\xi$  being the healing length defined above). The low-energy excitations

are phonon-like, with a linear dispersion relation  $\omega_k = ck$  ( $c = \sqrt{\mu/m}$  being the speed of sound), and the high-energy excitations are particle-like with a dispersion relation  $E_k + \mu$ . The Bogoliubov approach is linear in the sense that excitations don't interact: they all evolve independently. In this sense, the time-dependent Gross-Pitaevskii equation goes beyond this approach since quasi-particles may exchange energy during its propagation.

### 1.3.4 Classical field description

In the weakly-interacting gas, most of the features measured on the experiment are in fact classical in the sense that they are not due to the quantum fluctuations in the quasi-condensate. For instance, for our experimental temperatures, measured density fluctuations are mainly due to thermal contributions, since our pixel size is not small enough to resolve the contribution of quantum depletion [79]. Although having an integrable model at hand to describe the full quantum system is extraordinary, it is sometimes cumbersome to compute arbitrary quantities and simulate the equilibrium properties or dynamics of the gas by solving the full quantum problem. The classical field picture allows a more straightforward computation of correlation functions and is lighter to implement numerically. Indeed, for 1D systems this classical field approach does not suffer from ultraviolet divergences like in the two- and three-dimensional cases. It is also interesting to compare the results predicted by classical field with those obtained from a full resolution of the quantum problem (like in QMC), like in [80], to better understand the role of quantum effects.

The classical field method essentially amounts to neglecting the quantum nature of the field operator  $\hat{\Psi}$  and replacing it by a complex number, denoted  $\Psi$  in the following. In other words, the discrete nature of the gas is disregarded. In the grand-canonical ensemble, the energy functional (with chemical potential  $\mu$ ) results in:

$$E[\{\Psi\}] = \int_0^L dz \left[ \frac{\hbar^2}{2m} \left| \frac{d\Psi}{dz} \right|^2 + \frac{g}{2} |\Psi|^4 - \mu |\Psi|^2 \right]. \quad (1.37)$$

The thermal density operator for the quantum field is consequently replaced by the probability distribution for the classical field, a Boltzmann factor and correspondingly the partition function can be written as

$$Z = \int \mathcal{D}\Psi e^{\beta E[\Psi]}. \quad (1.38)$$

with  $\beta = 1/k_B T$ . From this, correlation functions can be computed, as for instance the first order correlations  $G^{(1)}$  given by the average of  $\Psi^*(z)\Psi(0)$ :

$$G^{(1)}(z) = \frac{1}{Z} \iint \mathcal{D}\Psi e^{-\beta E[\Psi]} \Psi^*(z)\Psi(0) \quad (1.39)$$

Castin and coworkers applied this type of correlation function calculation in the context of atom lasers [24, 26]. By defining dimensionless parameters for the classical field

problem, it appears that the state of the system is captured in a single quantity  $\eta$ . By rescaling  $\Psi$ ,  $z$  and  $E$  with a  $z_0$ ,  $\Psi_0$  and  $\beta$ , the classical field energy functional becomes:

$$\tilde{E} \left[ \left\{ \tilde{\Psi} \right\} \right] = g\Psi_0^4 z_0 \beta \int_0^{L/z_0} d\tilde{z} \left[ \frac{\hbar^2}{2mg\Psi_0^2 z_0^2} \left| \frac{d\tilde{\Psi}}{dz} \right|^2 - \frac{1}{2} \left| \tilde{\Psi} \right|^4 - \frac{\mu}{g\Psi_0^2} \left| \tilde{\Psi} \right|^2 \right] \quad (1.40)$$

By setting

$$z_0 = \left( \frac{\hbar^4 \beta}{m^2 g} \right)^{1/3}, \quad \Psi_0 = \left( \frac{m}{\hbar^2 g \beta^2} \right)^{1/6}, \quad (1.41)$$

Equation 1.40 becomes

$$\tilde{E} \left[ \left\{ \tilde{\Psi} \right\} \right] = \int_0^{L/z_0} d\tilde{z} \left[ \frac{1}{2} \left| \frac{d\tilde{\Psi}}{d\tilde{z}} \right|^2 + \frac{1}{2} \left| \tilde{\Psi} \right|^4 - \eta \left| \tilde{\Psi} \right|^2 \right]. \quad (1.42)$$

In the thermodynamic limit  $L \rightarrow +\infty$  the classical field problem thus depends on a single parameter

$$\eta = \mu \left( \frac{\hbar^2 \beta^2}{mg^2} \right)^{1/3}. \quad (1.43)$$

This approach can be applied on the complete quasi-condensation crossover and requires no other hypothesis than highly degenerate states, typically achieved for high temperatures. The validity of the approach however depends on the considered observable. For instance, Jacqmin et al. showed that for the momentum distribution a classical field description without energy cutoff fails for  $t < 10^6$ . The calculated Full Width Half Maximum (FWHM) of momentum distributions across the crossover with the classical field approach deviate from those computed with QMC for too small reduced temperatures [80].

During this doctoral work, the classical field approach was implemented numerically. One can sample a thermal field and then study the dynamics of the system using the time-dependent Gross-Pitaevskii equation (Chapter 5).

### Summary

- A number of tools based on various approximations are available to study weakly-interacting Bose gases.
- The Gross-Pitaevskii equation offers a mean-field approach where the ground state of the system may be computed, without considering the elementary excitations. The time-dependent Gross-Pitaevskii equation gives the dynamical evolution of a given complex field in a classical picture, neglecting the operator nature of the field  $\Psi$ .

- The Bogoliubov transformation derives the form of the elementary excitations of a 1D Bose gas (and coincides with one of the branches of the excitations predicted by Lieb). This linearised approach is simple enough to constitute a first theoretical calculation before turning to more involved description and often gives insight into the physics.
- The classical field formalism gives a theoretical framework in which the field operators are treated as c-numbers (the Gross-Pitaevskii equation is therefore included in this approach). It allows a more straightforward computation of correlation functions than QMC and can be implemented numerically (like in Chapter 5).

## 1.4 Equilibrium correlation functions over the crossover

### 1.4.1 Definitions

In this section, we consider a homogeneous Bose gas in a box of size  $L$ , with periodic boundary conditions.

#### First-order correlation function

The first-order correlations of a field  $\hat{\Psi}(z)$  is  $G^{(1)}(z, z') = \langle \hat{\Psi}^\dagger(z) \hat{\Psi}(z') \rangle$ . One usually considers the normalised correlation function

$$g^{(1)}(z) = \frac{\langle \hat{\Psi}^\dagger(z) \hat{\Psi}(0) \rangle}{n}, \quad (1.44)$$

where we assumed the translational invariance of the system. This function is the Fourier transform of the momentum distribution. Indeed, in second quantisation the annihilation of a particle of momentum  $k$  is, by definition of the field operator  $\hat{\Psi}$ :

$$\hat{a}_k = \frac{1}{\sqrt{L}} \int dz \hat{\Psi}(z) e^{-ikz}. \quad (1.45)$$

The momentum distribution  $\nu_k$  (or, the number of particles with momentum  $k$ ) of the gas becomes

$$\nu_k = \langle \hat{a}_k^\dagger \hat{a}_k \rangle = \frac{1}{L} \iint dz dz' \langle \hat{\Psi}^\dagger(z) \hat{\Psi}(z') e^{ik(z-z')} \rangle, \quad (1.46)$$

which, assuming translational invariance, simply gives:

$$\nu_k = n \int dz g^{(1)}(z) e^{ikz} \quad (1.47)$$

The momentum distribution is a quantity frequently measured in cold atom experiments and in particular we implemented a magnetic focussing technique to directly access this observable on our setup (see Chapter 3). The expressions of  $g^{(1)}(z)$  in the asymptotic limits are given in sections 1.4.2 and 1.4.3 (failing to give a general expression).

## Second-order correlation function

The second order normalised correlation function is expressed as (again, assuming translational invariance):

$$g^{(2)}(z) = \frac{\langle \hat{\Psi}^\dagger(z)\hat{\Psi}^\dagger(0)\hat{\Psi}(z)\hat{\Psi}(0) \rangle}{n^2} \quad (1.48)$$

The physical interpretation of this quantity is the probability to find a particle at a position  $z$ , knowing that a particle is already present at position  $z = 0$ . It is therefore intimately related to bunching. The local pair correlations  $g^{(2)}(0)$  in fact identify the various regimes of the 1D Bose gas and can be computed thermodynamically. However, in general  $g^{(2)}(z)$  is not known.

$g^{(2)}(z)$  can be accessed in a indirect manner experimentally by measuring density fluctuations. The average correlation between densities at position 0 and  $z$  is

$$\langle n(z)n(0) \rangle = \langle \hat{\Psi}^\dagger(z)\hat{\Psi}(z)\hat{\Psi}^\dagger(0)\hat{\Psi}(0) \rangle. \quad (1.49)$$

With  $\delta n(z) = n(z) - \langle n(z) \rangle$ , and applying the bosonic commutation relation verified by  $\hat{\Psi}$ , one relates the density fluctuations to the  $g^{(2)}$  function by:

$$\langle n(z)n(0) \rangle = n\delta(z) + n^2(g^{(2)}(z) - 1). \quad (1.50)$$

On our experiment, the measured quantity is in fact the atom number fluctuations  $\langle \delta N^2 \rangle$  per pixel, given by the previous expression integrated over the pixel size  $\Delta$  ( $N$  being the number of atoms per pixel). We use this experimental probe as a thermometer and a signature of the regime the gas lies in (see Chapter 3). Depending on the value  $g^{(2)}(0)$  density fluctuations will be superpoissonian (larger than the shot noise contribution  $n\delta(z)$ , when bunching is present), or subpoissonian. Just like the first-order correlation function, there is no general expression for the second-order correlations, however they can be estimated in the asymptotic regimes.

### 1.4.2 Ideal Bose Gas

Let us first consider the non-interacting ideal Bose gas phase. The  $g^{(1)}$  function could in principle be determined by taking the Fourier transform of the Bose occupation numbers. However no analytical expression of the considered integral exists and one needs to turn to the limits of classical and highly degenerate gases where the occupation numbers take simpler forms.

In the classical limit where  $k_B T \ll |\mu|$  (or equivalently  $n \ll \lambda_{dB}$ , the Bose factor simplifies as a Maxwell-Boltzmann distribution. The Fourier transform  $g^{(1)}(z)$  is then a gaussian function given by:

$$g^{(1)}(z) = e^{-\pi \frac{z^2}{\lambda_{dB}}}. \quad (1.51)$$

The correlation length is thus identified as the thermal wavelength  $\lambda_{dB}$ . As degeneracy is reached, the momentum distribution becomes lorentzian, and the  $g^{(1)}(z)$  is given by

$$g^{(1)}(z) = e^{-\frac{2\pi|z|}{n\lambda_{dB}^2}}. \quad (1.52)$$

In agreement with the increasing degeneracy compared to the classical gas, the correlation length becomes  $l_\phi = n\lambda_{dB}^2 \gg \lambda_{dB}$ . As one reaches the crossover temperature  $T_{CO}$ , one finds that the phase coherence length of the system becomes of the order of the healing length  $\xi$ .

For the non-interacting gas the Hamiltonian is quadratic in  $\hat{\Psi}(z)$  which makes Wick's theorem applicable to the computation of  $g^{(2)}(z)$ . By decomposing the mean value of the product of four field operators in products of mean values of two operators only [150], the following identity arises:

$$g^{(2)}(z) = 1 + |g^{(1)}(z)|^2. \quad (1.53)$$

This expression elegantly interprets the bosonic bunching phenomenon: the probability of finding two atoms at distances smaller than the correlation length is twice the probability of finding two atoms far apart, and especially  $g^{(2)}(0) \approx 2$ , which is a result we already encountered from Yang-Yang thermodynamics.

These results are valid as long as  $|\mu| \gg gn$  or equivalently,  $T \gg T_{CO}$  (by injecting the degenerate gas equation of state into the condition on the chemical potential).

### 1.4.3 Quasi-condensate

Now turning to the quasi-condensate phase (assuming  $T \ll T_{CO}$ , condition one can verify *a posteriori*), bunching is suppressed by the presence of repulsive interactions in the system but phase fluctuations remain. These two characteristics are present in the second and first order correlation functions respectively. The  $g^{(1)}(z)$  and  $g^{(2)}(z)$  were computed by Mora and Castin [108] without neglecting density fluctuations and including quantum fluctuations. However, most of the features of the density and phase fluctuations relevant experimentally can be captured in an approach which neglects quantum fluctuations<sup>7</sup>.

#### Density fluctuations

Density fluctuations can be conveniently estimated in the following approach. Since we cannot resolve the structure of the density-density correlation function, we restrict the discussion to the fluctuations  $\langle \delta n^2 \rangle$ , by treating the cases of low-energy (or phonon) excitations and high-energy (or particle) excitations separately. For  $k \ll \xi^{-1}$  the phase/density representation is appropriate. Following [21] and starting from the Hamiltonian of a 1D Bose gas:

$$\hat{\mathcal{H}} = \frac{\hbar^2}{2m} \int dz \left( (\partial_z \sqrt{\hat{n}})^2 + \sqrt{\hat{n}} (\partial_z \hat{\theta})^2 \sqrt{\hat{n}} \right) + \frac{g}{2} \int dz \hat{n}(z)^2, \quad (1.54)$$

---

<sup>7</sup>The condition for which quantum fluctuations can be neglected are different for first and second order correlations, they will be discussed when necessary.

and expanding up to second order in small parameters  $\delta\hat{n} = \hat{n} - n_0$  and  $\partial_z\hat{\theta}$ , one retrieves the Bogoliubov hamiltonian:

$$\hat{\mathcal{H}}_{bogo} = \frac{\hbar^2}{m} \int dz \left( \frac{1}{8mn_0} (\partial_z \delta\hat{n})^2 + \frac{n_0}{2} (\partial_z \hat{\theta})^2 \right) + \frac{g}{2} \int dz \delta\hat{n}(z)^2. \quad (1.55)$$

By expanding on sinusoidal modes<sup>8</sup>, where  $\delta n_{j,k}$  and  $\theta_{j,k}$  are conjugate variables:

$$\begin{aligned} \delta n(z) &= \sqrt{\frac{2}{L}} \sum_{k>0} (\delta n_{c,k} \cos(kz) + \delta n_{s,k} \sin(kz)) \\ \theta(z) &= \sqrt{\frac{L}{2}} \sum_{k>0} (\theta_{c,k} \cos(kz) + \theta_{s,k} \sin(kz)), \end{aligned} \quad (1.56)$$

and injecting into  $\hat{\mathcal{H}}_{bogo}$  1.55, the Hamiltonian takes a quadratic form, as a sum of uncoupled oscillators, with the dispersion relation  $\epsilon_k = \sqrt{E_k(E_k + 2\mu)}$ :

$$\hat{\mathcal{H}}_{bogo} = \sum_{i,k} \frac{g}{2} \delta n_{i,k}^2 + \frac{\hbar^2 k^2}{8mn_0} \theta_{i,k}^2. \quad (1.57)$$

Assuming a high enough temperature to apply a classical field approximation and neglecting the quantised nature of operators  $\delta n_{j,k}, \theta_{j,k}$ , and invoking the equipartition theorem, the mean values of the fluctuations of the sinusoidal modes are:

$$\begin{aligned} \langle \delta n_{j,k}^2 \rangle &= \frac{k_B T}{g} \\ \langle \theta_{j,k}^2 \rangle &= \frac{k_B T}{\hbar^2 k^2 / (4mn_0)}. \end{aligned} \quad (1.58)$$

The contribution to the total density fluctuations of these phonon modes formally reads:

$$\langle \delta n^2 \rangle_{ph} = \frac{k_B T}{Lg} \sum_{i=1}^{L/\xi} 1 : \quad (1.59)$$

We finally recover  $T_{CO}$  in the expression of the relative density fluctuations:

$$\frac{\langle \delta n^2 \rangle_{ph}}{n^2} = \frac{T}{T_{CO}}. \quad (1.60)$$

Since  $\delta n \ll n$  we find that this condition is equivalent to  $T \ll T_{CO}$ . For momenta  $k \gg 1/\xi$ , the phase-density representation is not the most appropriate. A free particle excitation with energy  $E_k = \hbar^2 k^2 / 2m$  corresponds to a plane wave  $\Psi = e^{ikz} / \sqrt{L}$  and the Bogoliubov annihilation operator  $\hat{b}_k$  identifies with the free particle annihilation operator  $\hat{a}_k$ . Just as we did for the low-energy excitations, we assume  $\hat{a}_k$  can be treated as a c-number  $a_k$  which follows a Gaussian distribution

$$\langle |a_k|^2 \rangle = k_B T / E_k. \quad (1.61)$$

---

<sup>8</sup>This expansion can be related to the transformation used in section 1.3.3: one can retrieve the previous transformation with  $a_k, a_k^\dagger$  as linear combinations of  $\delta n_{j,k}, \theta_{j,k}$ .

From the Bogoliubov transformation introduced in 1.3.3 ( $f_k^- \approx 1$  for large wavevectors),

$$\delta n_k = \sqrt{\frac{n_0}{L}} (a_k e^{ikz} + a_k^* e^{-ikz}). \quad (1.62)$$

Physically, this expression can be understood as the contribution of high-momentum atoms to density fluctuations mainly arising from interference of the atomic field  $a_k e^{ikz}/\sqrt{L}$  with low-energy spatial variations of density, of order  $\sqrt{n}$ . It leads to

$$\langle \delta n_k^2 \rangle = \frac{4mnk_B T}{L\hbar^2 k^2} \quad (1.63)$$

by injecting the equipartition relation. Incidentally,  $\xi$  is the typical distance over which density fluctuations decay like  $1/k^2$  and identifies as the density correlation length. With our typical parameters, this length is an order of magnitude below our optical resolution. By summing over all wavevectors verifying  $k \gg 1/\xi$ , the total density fluctuations from the free particle excitations are:

$$\frac{\langle \delta n^2 \rangle_{particle}}{n^2} = \frac{T}{T_{CO}}. \quad (1.64)$$

### $g^{(1)}$ function

From the phase-density representation introduced above, and neglecting density fluctuations (this is appropriate in the qBEC as we just argued), the first-order correlation function becomes  $g^{(1)}(z) = \langle e^{i(\theta(z)-\theta(0))} \rangle$  and reflects the phase fluctuations of the gas. By virtue of the applicability of Wick's theorem for a quadratic Hamiltonian, we are left to compute  $g^{(1)}(z) = e^{-\langle (\theta(z)-\theta(0))^2 \rangle / 2}$ . From the expansion on sinusoidal modes:

$$\langle (\theta(z) - \theta(0))^2 \rangle = \sum_{k>0} 2\langle \theta_{c,k}^2 \rangle (\cos(kz) - 1)^2 + \sum_{k>0} 2\langle \theta_{s,k}^2 \rangle \sin^2(kz) \quad (1.65)$$

Injecting the results of the equipartition of energy in each mode:

$$\langle (\theta(z) - \theta(0))^2 \rangle = \frac{4mk_B T}{Ln_0 \hbar^2} \sum_{k>0} \frac{1 - \cos(kz)}{k^2}. \quad (1.66)$$

Finally (after integration on  $k$ ),

$$g^{(1)}(z) \propto e^{-4\pi|z|/(n\lambda_{dB}^2)}. \quad (1.67)$$

This defines the phase correlation length in the quasi-condensate as  $l_\phi = 2n\lambda_{dB}^2$ , twice the coherence length in a degenerate Bose gas. This is compatible with the fact that in the qBEC only phase fluctuations contribute to the first-order correlations whereas in the IBG both density and phase fluctuations contribute. Although we neglected quantum fluctuations in the approach adopted here, they are generally irrelevant in experiments probing 1D Bose gases.

**Summary**

- Correlations functions are fundamental to describe many body quantum system. First-order and second-order correlations have physical interpretations and can be (more or less directly) observed in experiments.
- In the degenerate IBG gas phase the first-order correlations are exponentially decaying on typical distances which vary depending on the degeneracy of the gas. The second-order correlations can be directly related to the first-order correlation function by Wick's theorem.
- In the qBEC one can also extract an analytical (also exponentially-decaying) form for the  $g^{(1)}$  function: the phase coherence length is twice the coherence length of an IBG. As for density-density correlations, they decay on a typical distance  $\xi$  and verify  $\delta n \ll n$  as long as  $T_{CO} \ll T$ .

# CHAPTER 2

---

## Upgrade of the experimental apparatus

---

### 2.1 Overview of the experimental setup

The atom chip experiment in Palaiseau was first set up in 2003, and since the first condensate [7] several generations of students have brought technological and technical upgrades, to gradually make the study of one-dimensional Bose gases the speciality of the Atom Chip group. During the time of my PhD an important number of such changes were made to the setup. Before describing in detail each component of the experiment and the changes made, let me briefly introduce the general structure of this cold atom machine.

The heart of the experiment is the atom chip, mounted in a vacuum chamber with ultra-high vacuum (UHV,  $P < 10^{-10}$  mbar). The final ultracold cloud of  $^{87}\text{Rb}$  is magnetically trapped with current flowing in wires on this chip (see 2.3). The layout of the chip was modified for compatibility with the new imaging system at the beginning of my doctoral project, and is presented in detail in 2.3.

The vacuum chamber (a 7 cm cube) has optical access allowing the various necessary laser beams (namely the MOT beams, the repumper, the optical pumping, and imaging beam) to be shone on the atoms (2.2). The atoms come from dispensers on the chip mount. The laser system, changed during this PhD work, is detailed below. The complete vacuum system is inside a magnetic shield to avoid sensitivity of the on-chip magnetic traps to magnetic field fluctuations in the environment.

The atoms are imaged with a high-resolution objective (NA = 0.39) recently designed and installed on the experiment. After shining a resonant laser beam onto the atoms, we recover the absorption profile of the cloud on a CCD camera. The new objective is presented section 2.4 and the complete imaging setup in the next chapter.

This chapter concentrates on the various changes that were made on the experimental apparatus. The experimental cycle and measurement techniques are delegated to a subsequent chapter (Chapter 3). The changes presented here were motivated by two aspects: improvement of the stability of the experiment (less free-space propagation of laser beams, and more stable lasers which do not require frequent relocking), and improvement of the signal over noise ratio and resolution of our images (which lead to the conception of a new objective).

## 2.2 The laser system

In this section I introduce the laser system used to cool, trap, pump and image the  $^{87}\text{Rb}$  atoms. All lasers described here are in the vicinity of 780 nm, corresponding to the atomic transitions relevant to us. An additional laser (at 1530 nm) was added for a periodic potential along the longitudinal axis for an optical lattice (see Chapter 6). So-called "Master 1" remained as before but all others laser were replaced.

### 2.2.1 Implementation of a new setup: Master 1, Master 2, Repumper

The various frequencies required during the experimental sequence are achieved with three lasers. Master 1 is the absolute frequency reference, locked on the D2 line of  $^{87}\text{Rb}$ . The repumper is locked 6.6 GHz away, and is used during the MOT phase to pump the atoms back to the  $|F = 2\rangle$  state for cooling on the  $|F = 2\rangle$  to  $|F' = 3\rangle$  transition. Master 2 is also locked on Master 1 and its frequency is swept electronically for the different stages of the experimental cycle (MOT, molasses, imaging, which each require a different detuning with respect to Master 1. These steps are detailed in Chapter 3). The energy levels and corresponding transitions are represented figure 2.1.

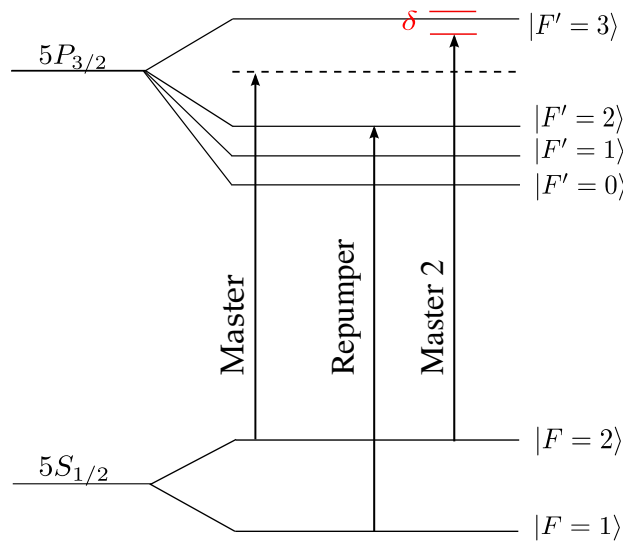


**Figure 2.1:** Level scheme of  $^{87}\text{Rb}$  and required lasers in the experimental sequence. Master 1 is locked on the level crossing between  $|F' = 2\rangle$  and  $|F' = 3\rangle$ . During the MOT phase, the  $|F = 2\rangle$  to  $|F' = 3\rangle$  is addressed, and the repumper locked 6 GHz from Master brings the atoms back to the cooling transition if they fall in the dark  $|F = 1\rangle$  state. Finally, many different frequencies slightly detuned from  $|F' = 3\rangle$  are required during the cycle. Master 2 sweeps this frequency range of about 120 MHz.

#### Master 1 and repumper servoloop

Master 1 is an extended-cavity laser based on a design by the SYRTE laboratory<sup>1</sup> [8]. In SYRTE lasers, anti-reflection coated laser diodes<sup>2</sup> are placed in a cavity of about 10 cm where the light is amplified. An interference filter in the cavity allows to roughly tune the wavelength of the emitted light. A Peltier module maintains the diode at the

<sup>1</sup>SYstèmes de Référence Temps Espace, component of the Observatoire de Paris

<sup>2</sup>Eagleyard EYP-RWE-780-02000-1300-SOT12 series

desired temperature and a piezoelectric crystal fine tunes the length of the cavity and thus allows a fine control of the frequency of the emitted light. The spectral bandwidth of these lasers is around 100 kHz. The mechanical mount is home-engineered by the mechanical workshop, and designed with Master student Aurélien Eloy and mechanical engineer André Guilbaud [41]. Master 1 is locked on the D2 transition by saturation absorption spectroscopy of  $^{87}\text{Rb}$  and a fraction of its light is taken to beat with the repumper laser on a fast photodiode.

The repump light is provided by a distributed feedback diode (DFB)<sup>3</sup>. This laser has the advantage of compactness since the DFB diode itself acts as a cavity and provides up to 100 mW of optical power at 780 nm. The TO3 mount also includes the Peltier module for temperature control. However, the bandwidth is an order of magnitude below that of a SYRTE mount (although this is not an issue for repump light), and more problematically the spatial mode has important aberrations. The coupling efficiency into an optical fibre was so low that we had to install an additional slave laser, injected by the DFB diode light. This provides a comfortable 60 mW of light in a close-to-gaussian spatial mode, sent to the auxiliary input port of the fibre cluster and mixed with the MOT light in one of the output ports (see below).

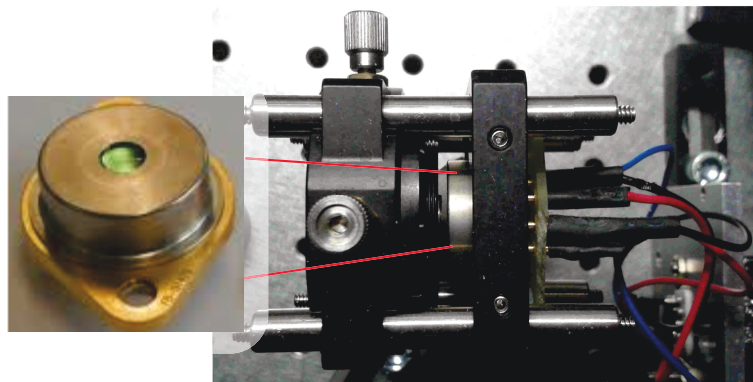


**Figure 2.2:** DFB diode mounted in a cage system. An aspheric lens shapes the strongly divergent beam, which proved strongly aberrant.

The beating of the two lasers (Master 1 + Repumper) is detected by a fast photodiode which monitors the frequency of the second laser with respect to Master 1. After beating with an additional electronic reference at 6 GHz, the frequency difference is converted to a voltage, which is the final signal sent to a lock box (after amplification, [78]) containing a PID controller. This allows to counteract the current of the DFB diode to fine tune its frequency at the required 6.6 GHz from the level crossing.

### Master 1 and Master 2 servoloop

The remaining power of Master 1 is injected into an optical fibre and brought onto the main optical table for beating with Master 2. Master 2 is a laser identical to Master 1 in its mechanical mounting, but has a more powerful laser diode to inject a tapered

<sup>3</sup>Eagleyard EYP-DFB-0780-00080-1500-TOC03-0005 series

amplifier (TA, see below). A small fraction of Master 2 is aligned onto a fast photodiode with Master 1<sup>4</sup>, which monitors (just like for the repumper loop) the frequency difference between both lasers. After amplification<sup>5</sup> the signal is sent to a home-built (by electronical engineer André Villing) lock box which counteracts the high voltage applied on the piezoelectric of the cavity. This in turn fine tunes the frequency emitted by the laser. The frequency difference between Master 1 and Master 2 is of the order of 300 MHz, which is a frequency range accessible electronically.

### Schematic of the complete setup

The following sketch gives an overview of the complete laser system (only the most important elements are depicted here). The TA light and the repumper (*i.e* the light coming from the slave laser) are injected in the fibre port cluster, which splits the light into four MOT beams (see below). The three lasers (Master 1, Master 2 and Repumper) can stay locked for a whole day.

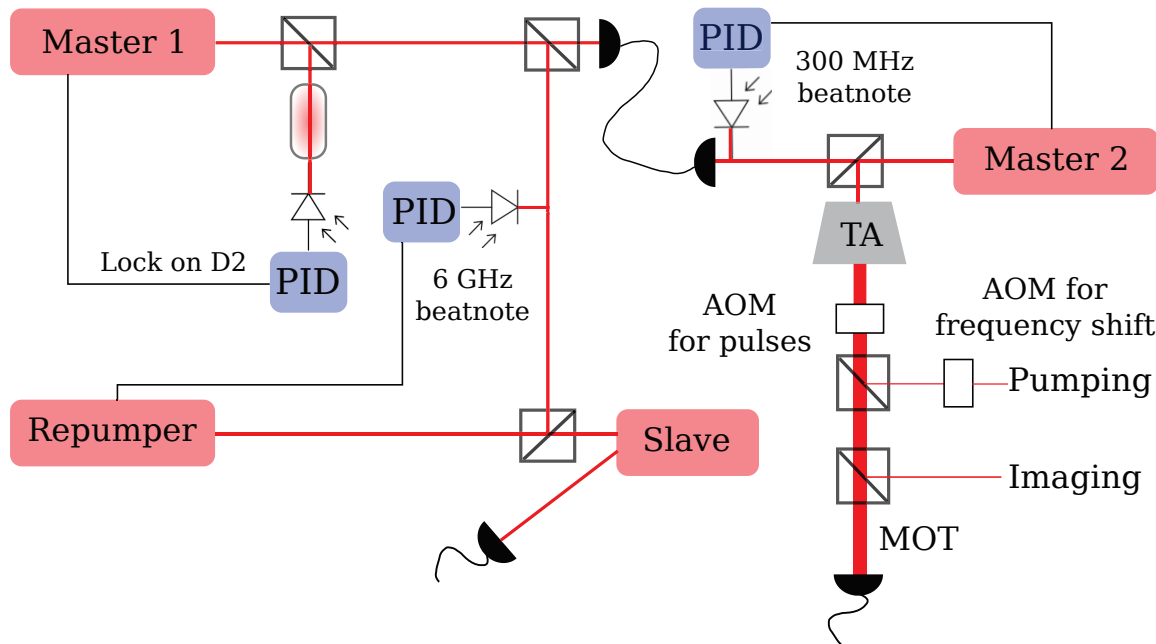


**Figure 2.3:** Schematic of the laser setup. The Master 1 laser is locked on the level crossing between  $|F = 2, F' = 2\rangle$  and  $|F = 2, F' = 2\rangle$  by saturated absorption spectroscopy through a Rb cell. A fraction of Master 1 is taken to lock the repumper 6.6 GHz away, another fraction for the lock with "Master 2". Master 2's frequency is varied during the experimental sequence for the various frequencies required from the MOT phase to the imaging through the molasses step and the optical pumping pulse. The optical power is provided by the tapered amplifier (TA), injected by Master 2.

<sup>4</sup>Thorlabs SM05PD2B

<sup>5</sup>The photodiode, reverse biased through a bias tee (Mini-Circuits ZX85-12G-S7) collects the signal which is then amplified (Mini-Circuits ZFL-500HLN+)

## 2.2.2 More power and optical fibres

### Tapered Amplifier

Master 2 injects a so-called tapered amplifier (TA), which provides the optical power necessary (about 0.6 W injected in the fibre cluster) for the complete experiment. A TA consists of a small chip with a semi-conducting medium which amplifies incoming light. Our particular chip<sup>6</sup> works at currents of the order of 1.5 A (2 A maximum) and provides a nominal optical power of 1W; more than enough for MOT light, pumping and imaging. The TA chip is mounted on a home-made mechanical setup, with temperature control and water cooling, complete with aspherical lenses at input and output. The "tapered" amplifier produces an astigmatic beam which requires shaping before diffraction by an AOM and injection into the fibre cluster. Indeed, after collimating the fast axis with the aspherical lens at the output, the beam still diverges in one of its spatial directions. We use two cylindrical lenses to collimate the slow axis at the right diameter to produce a square-shaped beam.

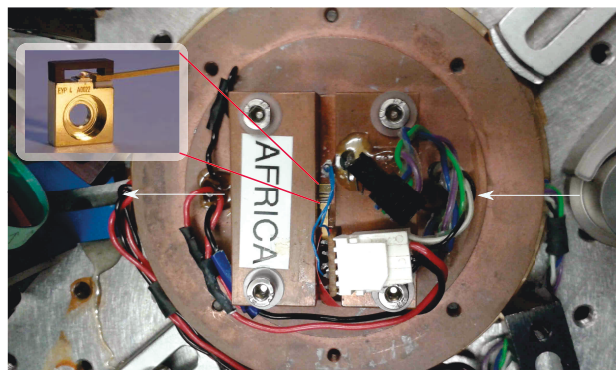


**Figure 2.4:** The TA chip is nested in a home-made mechanical mount. It contains a Peltier module for temperature control, to avoid too much heating, in addition to water cooling. There are also two aspherical lenses: one at the input to focus the beam onto the gain medium, and one at the output to collimate one of the axes of the amplified beam.

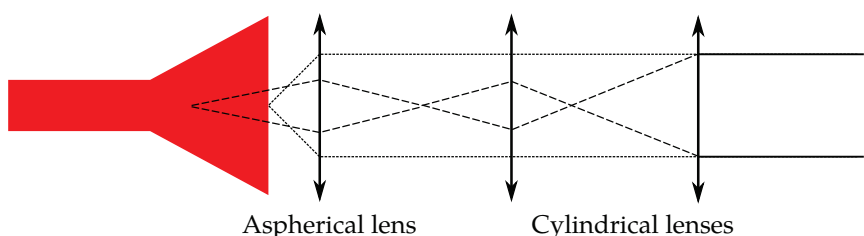


**Figure 2.5:** Shaping of the output beam. The gain medium is represented in red. The beam is astigmatic, meaning that the two axes diverge differently. The so-called fast axis is collimated with the aspherical lens on the TA mount. The remaining axis is then collimated at the desired size with a couple of cylindrical lenses, giving a square shape to the beam.

We achieved 85% diffraction efficiency and 50% coupling into the input fibre of the cluster using this shaping method. The light from the TA is separated in three paths: the injection of a fibre cluster, the light for the optical pumping and finally the beam for

<sup>6</sup>Eagleyard EYP-TPA-0780-01000-3006-CMT03-0000

the imaging probe.

Another difficulty related to the TA is the heating of the neighbouring optics: a steady state is reached after about 30 minutes, with water cooling.

### Fibre cluster and MOT light

Previously the optical power was provided by a single slave diode, but the MOT beams were propagating over a large distance before reaching the atoms. To improve the stability of the experiment and avoid painful alignment, we installed a Schäfter & Kirchhoff fibre cluster<sup>7</sup>.

After injection into the input port, the fibre cluster splits the light in four output ports (our MOT beams reflect off the chip surface, such that four beams are required for the trap rather than the usual six, see below). The coupling efficiency from the input fibre to each output fibre is of the order of 80 %, and the balance of the output power in each port can be controlled with  $\lambda/2$  plates included in the cluster. Each output fibre is connected to 2 inch fibre outcoupplers<sup>8</sup> installed close to the vacuum chamber, thus minimising free propagation and sensitivity to a slight misalignment upstream. The repump light injected in the auxiliary input port is mixed into one of the output ports, and finally on the atoms.

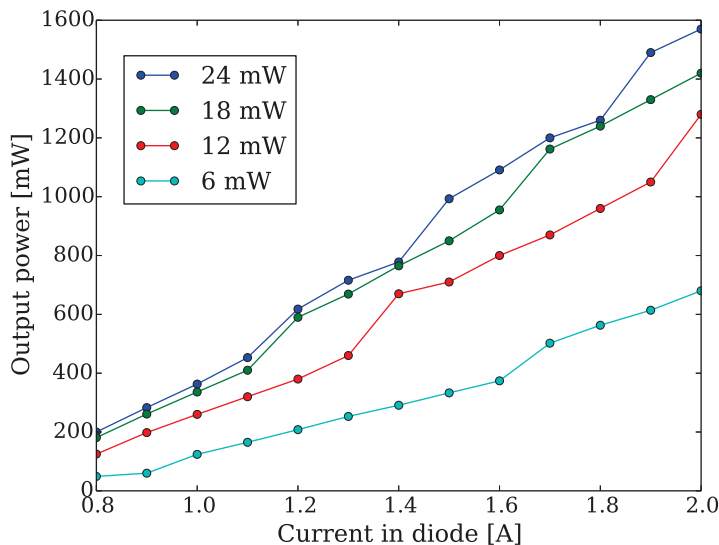


**Figure 2.6:** Output power of the TA for different injection powers from Master 2. To reach the nominal 1 W, the amplifier needs to be injected with about 20 mW of power. We usually work at 1.5 A current.

<sup>7</sup>Fibre Port Cluster FPC

<sup>8</sup>60FC-0780-4-M125-54. These outcoupplers include an optional  $\lambda/4$  plate built-in to directly produce circular polarisation.

### Summary

- The laser system was almost completely upgraded for more power and stability.
- For stability, a DFB diode (whose wavelength is very stable compared to an extended-cavity) is used for the repumping light, and an electronic control of the wavelength of Master 2 (rather than a double-pass acousto-optical modulator like before) was implemented. So far these upgrades have proven useful as the lasers seldom require relocking.
- Also for stability, we decided to install optical fibres for the MOT beams (rather than free space propagation). We now hardly realign those beams, however the price to pay is more optical power to inject the optical fibres.
- For power, we installed a TA. The MOT seems to contain more atoms than before (although we have no quantitative measurement of atom number).

## 2.3 The heart of the experiment: the atom chip

Atom chips were first developed in the late 1990s with the idea of integrating and miniaturising matter-wave optics: they consist in a small electronic circuit printed on a surface, containing nanofabricated wires used to engineer magnetic potentials. The first attempts were to guide atoms along macroscopic wires to trap them in simple geometries [39], and gradually with fabrication methods the wires became micro-wires [54] and atom chips appeared along with their versatility of magnetic potentials [53]. After a first condensate on a micro-device in 2001 [70, 115], a certain number of atom chip experiments were developed and now routinely exploit ultra-cold atomic gases for various purposes [55]. Because the atomic cloud can be brought very close to the microwires, large trapping frequencies can be achieved which makes them ideal for the study of one-dimensional systems [125].

### 2.3.1 Chip layout and trap configurations

#### Principle of magnetic trapping

Consider a  $^{87}\text{Rb}$  atom in a magnetic field  $\vec{B}$ . A neutral atom interacts with an external magnetic field via its magnetic moment  $\vec{\mu}_m$ . The magnetic moment  $\vec{\mu}_m$  rapidly precesses around the magnetic field axis at angle  $\theta$  at the Larmor frequency  $\omega_L$ . The atoms adiabatically follow changes in the magnetic potential if the field's direction changes slowly compared to the Larmor frequency  $\omega_L = \mu_m |\vec{B}| / \hbar$  (typically 1 MHz). In these conditions  $\vec{\mu}_m$  stays aligned with  $\vec{B}$  and the potential felt by the atoms is:

$$V = -|\vec{\mu}_m| \cdot |\vec{B}|, \quad (2.1)$$

Quantum mechanically, the energy levels of an atom with angular momentum  $F$  in an external field  $\vec{B}$  are  $V(m_F) = g m_F \mu_B |\vec{B}|$ ,  $m_F$  being the component of  $F$  along the

quantisation axis defined by the direction  $\theta$  of the field. The ratio  $m_F/F$  replaces the classical interpretation of scalar product  $\vec{\mu}_m \cdot \vec{B} = \mu_m B \cos\theta$ . Depending on the sign of  $g m_F$ , the atoms will seek maximal or minimal  $|\vec{B}|$ . However, since a maximum of magnetic field is forbidden in free space (according to Maxwell's equations), only states with positive  $g m_F$  can be trapped. The larger this product, the stronger the potential, so we chose  $|F = 2, m_F = 2\rangle$ : with  $g = 1/2$  in  $F = 2$  only positive  $m_F$  states can be trapped.

Magnetic traps existed before the idea of atom chips appeared; with coils quadrupolar or Ioffe-Pritchard traps can easily be implemented (for instance to reach condensation [42]). However, the main advantage of trapping with microwires is that important confinement strengths can be achieved with reasonable currents, by bringing the atoms close to trapping wires. The potential strength near its minimum is indeed given by the gradient of  $\vec{B}$ , naturally inversely proportional to the distance from the wire squared.

### Loading traps: U, Z configurations

Several classic (U and Z) trap configurations and an original type of AC trap is implemented with the current atom chip on our setup. The base ingredient of U and Z traps is the wire guide, which consists of a wire and a transverse homogeneous magnetic field. This produces a transverse quadrupole at a height  $h_0$  above the wire:

$$h_0 = \frac{\mu_0}{2\pi} \frac{I_0}{B_0} \quad (2.2)$$

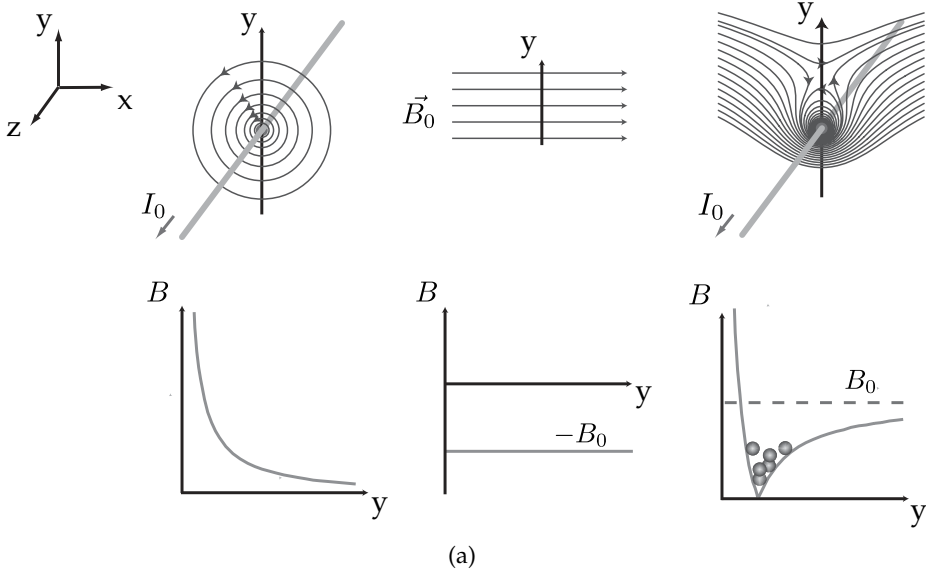


**Figure 2.7:** Principle of the wire guide. A current  $I_0$  flowing through an infinite wire creates a rotationally invariant field, whose intensity is inversely proportional to the distance from the wire. By adding a perpendicular bias field, the field cancels at a certain height  $h_0$  above the wire, and around this minimum the field is quadrupolar. Figure adapted from [125].

A longitudinal component can be added to  $\vec{B}$  by bending the wire to break the translational symmetry along z. Typical shapes are so-called "U" and "Z" configurations.

Whether the wire is U or Z shaped determines, with the current flowing in the perpendicular bars, if the trap is a quadrupole (with a zero magnetic field minimum), or an Ioffe-Pritchard trap (with a finite  $|\vec{B}|$  at the bottom of the trap).

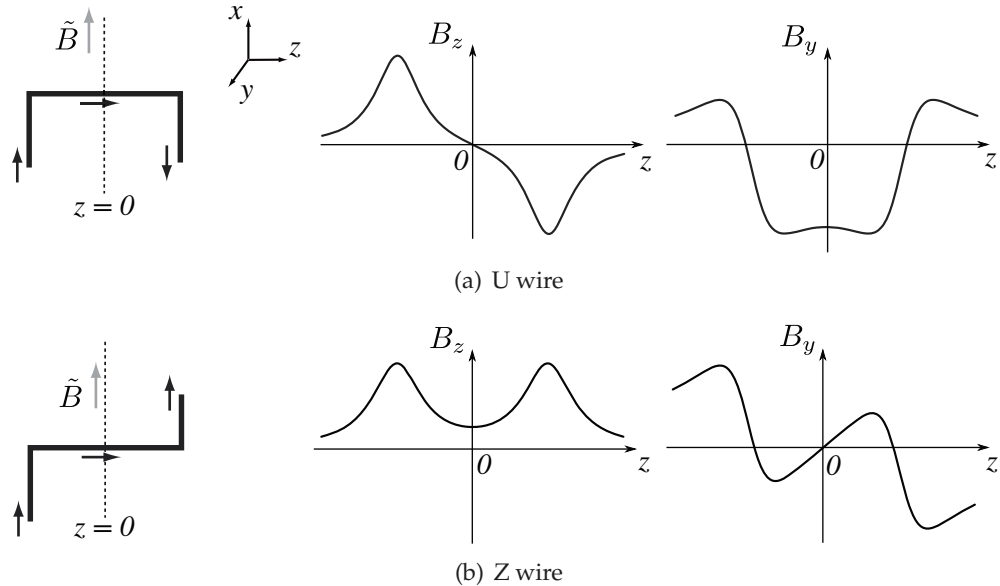


**Figure 2.8:** Adapted from [125]: magnetic field components along the trap axis. In the U configuration, the  $z$  component to the field cancels at the centre of the central bar, and since the current in the side bars flows in opposite directions a locally quadrupolar field is created. In the Z trap, with the current flowing in the same directions in both side bars, the  $z$  component of the magnetic field has a non-zero minimum.

The U wire is used to create the quadrupole field for the on-chip MOT, and is a  $500\text{ }\mu\text{m}$  thick strip. This creates a quadrupole at a height of about 0.5 to 1 mm for a bias field of a few Gauss and a current of about 5 A. The Z trap is an intermediate loading step before the final modulated guide, with a wire thickness of  $100\mu\text{m}$ . The atoms are trapped about 200 to 500  $\mu\text{m}$  above the chip for currents of 3 to 5 A and a bias fields ranging from 10 to 40 G. The role of these two traps will be detailed in Chapter 3.

### Final trap: modulated guide

The Ioffe-Pritchard already produces an elongated cloud (the aspect ratio is quite large with  $\omega_{\perp} \approx 1\text{ kHz}$  vs  $\omega_z \approx 5\text{ Hz}$ ). To achieve higher trapping frequencies the cloud needs to be brought closer to the wires, which would require to further increase the bias field or further reduce the current flowing in the wire. However, to reach more strongly interacting regimes, the linear density must be decreased (since  $\gamma$  is inversely proportional to  $\rho$ ). At these rather small chemical potentials the density profile is sensitive to the roughness of the micro-fabricated wires. To overcome this issue, a new type of trap was implemented on the experiment, initially in 2007 during J.B Trebbia's PhD [141, 142], and in 2011 in its current form [3, 78]. Another interesting feature of this novel trap is the independence of longitudinal and transverse confinements.

Although fabrication techniques evolved to improve the quality of the wires (using for instance evaporation instead of electrodeposition), imperfections remain, slightly distorting the magnetic field lines and roughening the trap bottom by adding a noisy longitudinal component  $\delta B_z$  to the field [45]:

$$V(z) = \mu_B(B_0 + \delta B_z) \quad (2.3)$$

If the current in the wire creating  $\delta B_z$  is reversed, the potential roughness is also reversed [93]. By running an AC current trough the wire, the atoms see a time-averaged potential where the roughness is suppressed:

$$\langle V(z) \rangle = \mu_B B_0. \quad (2.4)$$

In practice, the modulated guide consists of three wires connected in series (see figure 2.9) along with a longitudinal bias field  $B_0$ . This creates a two-dimensional quadrupole at a certain height  $h_0$  above the wires. The three wires are equally spaced, the current in the two outer wires is  $-I(t)$ , and  $I(t)$  in the central wire, creating a tight trap at a distance  $h_0 = d/2$  above the chip plane, where  $d$  is the distance separating the two most distant wires (see figure 2.9). The current is modulated at 400 kHz. Strong transverse confinements (up to 100 kHz in principle) can be reached for currents of the order of 1 A with  $h_0 = 15 \mu\text{m}$  [79].

The longitudinal confinement comes from four additional lateral wires, creating a locally harmonic trap of a few Hz. This is the final trap in which we take data. For the weakly interacting regime we typically use  $\omega_{\perp} = 2 \text{ kHz}$  and  $\omega_z = 6 \text{ Hz}$ . In practice, we use currents such that the trap is harmonic around its centre but in principle different configurations like quartic traps are accessible<sup>9</sup>.

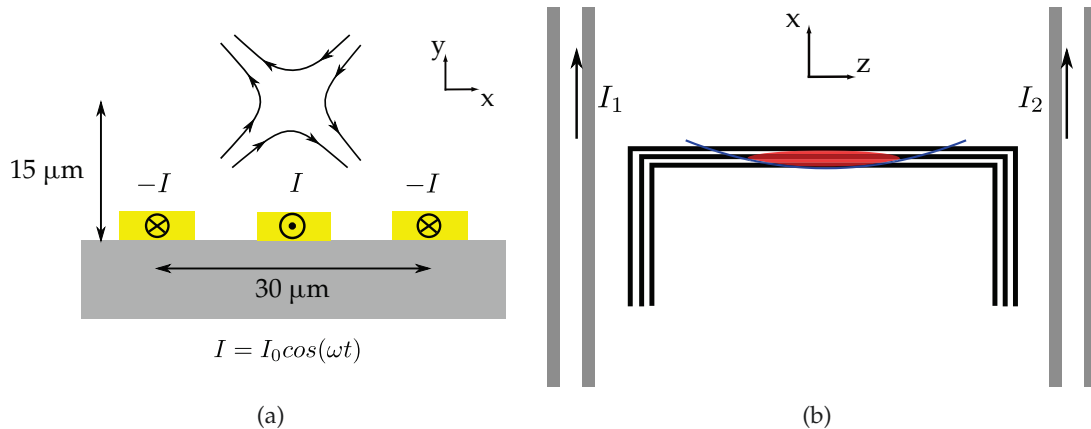


**Figure 2.9:** Left: view of the quadrupole trap above the small wires. The field created by the central wire cancels exactly the field created by the two outer wires where current flows in the opposite direction. With the three wires in series this configuration is easily achieved and the position of the modulated trap is stable. Right: view of the small wires and the additional wires for longitudinal trapping. The latter is independent of the transverse trap and can be engineered with the four wires available.

<sup>9</sup>The possibility of a quartic trap was interesting to decrease the effect of an external potential. However we now plan to install a Digital Micromirror Device (DMD) which could be used to create a homogeneous optical confinement, see the last chapter for more on this aspect.

### Choice of the modulation frequency

We recently installed a new power supply for the small wires: previously the current was modulated at  $f_m = 2\omega_m/2\pi = 200$  kHz, we now modulate at  $2\omega_m/2\pi = 400$  kHz with a home-designed and produced power supply (courtesy Frédéric Moron). The lower bound for  $f_m$  is given by the stability condition of the trap: modulation needs to be faster than the transverse motion at  $\omega_\perp$ , typically in the kHz range for weakly-interacting samples [20]. The upper bound for  $f_m$  is given by the adiabaticity condition: the atomic spin should follow the instantaneous magnetic field orientation to prevent losses via spin-flip transitions, or equivalently:  $2\omega_m \ll \omega_L$ . These qualitative arguments show that modulation frequencies in the 100 kHz range are suitable.

Now consider a weak radio-frequency field added to the modulated trap, polarised along  $\vec{x}$ , like during evaporation for instance. The atomic Larmor frequency  $\omega_L$  is now modulated in time, or, equivalently, the RF field is frequency modulated at a given position in the trap (in the rotating wave approximation, [20]). The RF field contains a carrier plus sidebands at multiples of  $2\omega_m$ , and coupling to untrapped states are resonant at positions  $r_n$  which verify ( $b'$  being the quadrupole gradient at peak current):

$$\hbar\omega_{RF} = \mu_B B_0 + \frac{\mu_B b'^2 r_n^2}{4B_0} - 2n\hbar\omega_m \quad (2.5)$$

The RF field is thus resonant for different trap locations with energies every  $2\hbar\omega_m/k_B$ . The potential energy difference between two resonances for a 200 kHz modulation is  $3 k_B \mu\text{K}$ . For temperatures above this limit, resonances inside the cloud induce loss by spin-flip. For this reason, precooling before loading the modulated guide is necessary, and increasing  $f_m$  to 400 kHz gives more margin for loading and cooling, by increasing the frequency window in which evaporation without hitting a resonance is possible.

### New chip layout

A new chip mask was designed for compatibility with the new imaging system (see following section for more on the new objective). On the previous chip the final trap was not centered on the optical axis. The new objective installed on the experiment has a much smaller field of view, the price to pay for a larger numerical aperture. For this reason the final trap had to be shifted to the centre of the chip, which itself coincides with the centre of the vacuum chamber and the optical axis.

The following figure shows three zoom levels of the chip mask. Indeed, over the experimental sequence the idea is to gradually bring the atoms closer to the chip and trap them in smaller volumes: from the MOT to the modulated guide, through the Z trap.

#### 2.3.2 From the cleanroom to the vacuum chamber

##### A word on the fabrication

The current generation of chips on this particular experiment are Aluminium-Nitride (AlN) based, chosen for its remarkable heat-conducting properties [4]. The wires are deposited by evaporation on the AlN substrate, and then covered by an insulating layer

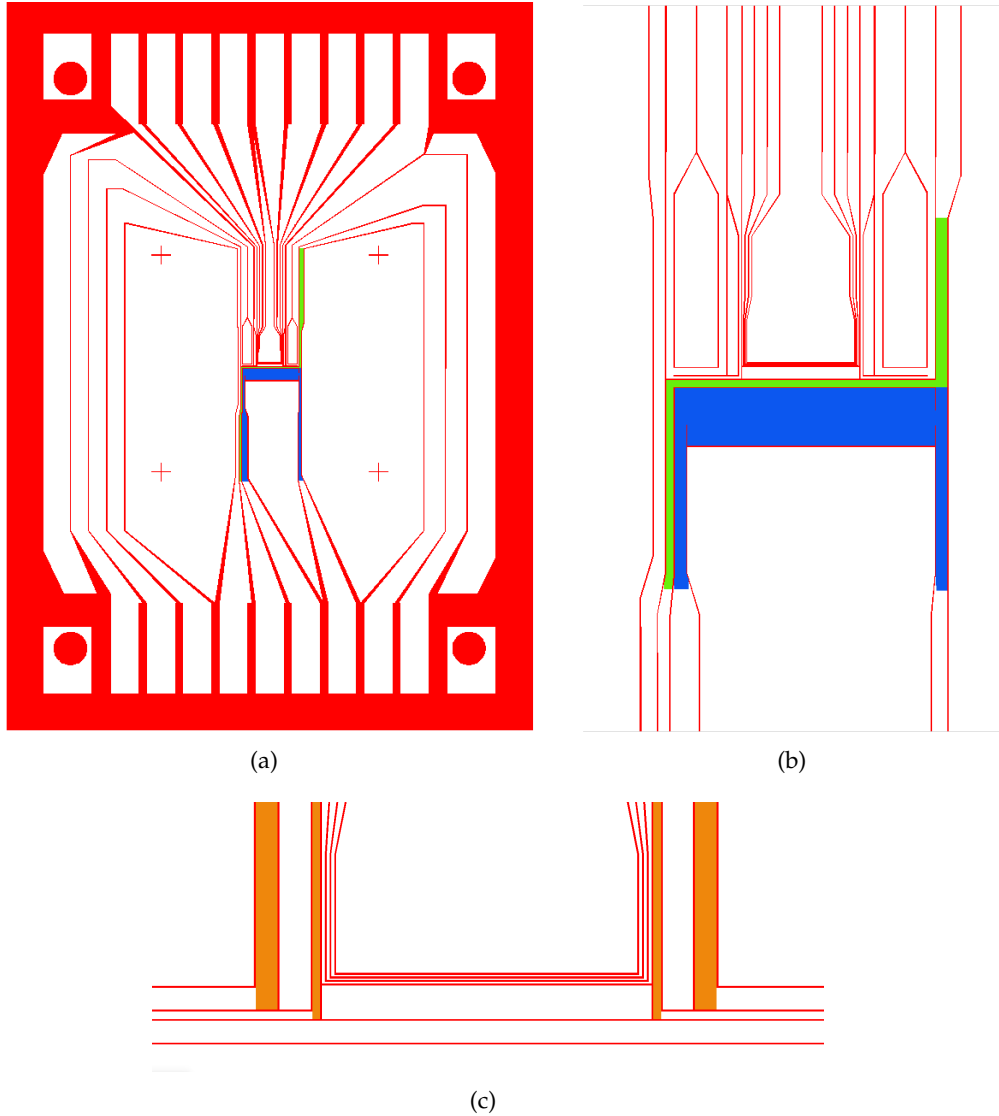


**Figure 2.10:** (a): Complete chip layout ( $2.5 \times 3.5$  cm), the conducting wires are shown in white. There are eighteen connections in total, nine at each extremity (two extra connections are required for the dispensers, adding up to the twenty connections in total on the electrical feedthrough), several wires share connections. The U-wire (blue), Z-wire (green) and modulated guide are highlighted. (b) Zoom on the central region: the U-wire, the Z-wire, and wires for the final trap. (c) Close-up of the final trap: three so-called small wires form the modulated guide used for the transverse confinement, and four vertical wires (orange) add a slowly-varying longitudinal confinement. The small wires are 1.5 mm long and the final cloud extends over less than  $200 \mu\text{m}$  in the centre of the smallwire region.

(the resist we use is BCB <sup>10</sup>). Finally, a thin layer of gold is evaporated on the surface. This layer acts as a mirror for infrared light, and is required for the mirror MOT phase and the imaging. Since the probe beam to image the cloud is reflected off this mirror the surface quality of the chip and is quite crucial, meaning that the insulating layer should have as little defects as possible.

<sup>10</sup>Benzocyclobutene, chosen for its resistance to heat and weak surface tension for spin coating, as well as its good planarisation properties

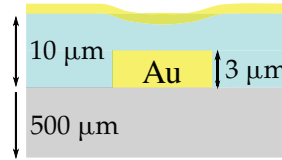


**Figure 2.11:** Simplified sketch of the layers of the atom chip: on the heat-conducting AlN wafer ( $500\text{ }\mu\text{m}$  thick), the wires are evaporated and then covered by an insulating layer of BCB and finally a thin mirror of gold. The chip surface has depressions where the wires lie, which is a drawback for the quality of the images, but allows us to image the wires on the chip with incoherent white light, when installed on the experiment. This is of great help for alignment and focussing of the imaging system.

The fabrication is carried out by Isabelle Bouchoule and Sophie Bouchoule, with the help of undergraduate students, at LPN cleanroom<sup>11</sup> and Thalès cleanroom<sup>12</sup>, the two institutions having different types of equipment available. During this PhD project a new chip was installed on the experiment, with similar technology as previously but a different layout of the wires. A new fabrication process with a Silicium-carbide base (SiC) is currently under investigation, for better heat conductivity and a better control of roughness (since AlN is a ceramic it is formed by micron-sized grains which vary from one batch to another). Unfortunately this new generation of chips could not be installed yet due to technical complications.

Typically, the chip needs to be replaced every two years. One reason is that the dispensers we get our  $^{87}\text{Rb}$  atoms from run out, but another less controllable phenomenon is that the surface of the chip degrades over time: the atoms stick to the surface, affecting the quality of the mirror and creating a slight rough potential which cannot be suppressed by modulating the current in the wires.

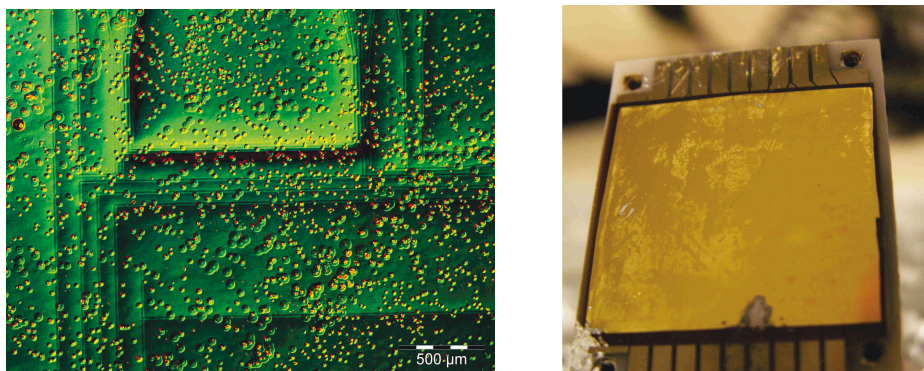


**Figure 2.12:** Left: image of adsorbed Rb on the surface. This reduces the quality of the mirror as can be seen on the picture shown right.

### Mounting the chip on the experiment

After fabrication is complete the chip is soldered to a gold-plated copper mount which acts as a heat sink (see figures 2.13 and 2.14 for photographs of the mounted chip).

<sup>11</sup>Laboratoire Photonique et Nanostructures, based in Marcoussis, about 20 km from Palaiseau.

<sup>12</sup>In their research centre just across the street from us in Palaiseau.

Since 2010 Indium is used to solder the AlN wafer to the copper for good heat dissipation from the wires to the heat sink, which is necessary since currents up to 6 A flow in the micro-fabricated wires. The copper mount itself is connected to a CF40 flange with an electrical feedthrough. The wires which connect the electrical feedthrough to the wires on the chip have Brass-Beryllium strips, and electrical contact is done with a PEEK<sup>13</sup> grating screwed down onto the strips against the terminations of the wires on the chip. The Rubidium dispersers (two altogether) are placed on the sides of the copper mount. They release a vapor of <sup>87</sup>Rb when a large enough current flows in them.

The vacuum chamber simply consists of a small cubic (7 cm) chamber, an ion getter pump and an additional Ti sublimation pump, the complete system having a relatively small volume ensuring efficient pumping and bake-out. The simplicity of the vacuum setup is crucial since the chip needs to be replaced at least every two years (or more frequently if a technical problem arises), but is also an advantage stemming from the smaller size of atom chip experiments compared to standard cold atom experiments.

### Summary

- Our experiment has the specificity of using an atom chip to trap the atoms and create one-dimensional ultracold samples.
- The atom chip is micro-fabricated in a clean room and consists in a electronic circuit which allows to engineer magnetic potentials. Several trapping configurations are implemented, corresponding to different stages in the experimental sequence from the MOT phase to the final gas.
- The layout of the chip was adapted for compatibility with the new imaging objective.

---

<sup>13</sup>Polyether Ether Ketone, a polymer with good resistance to heat.

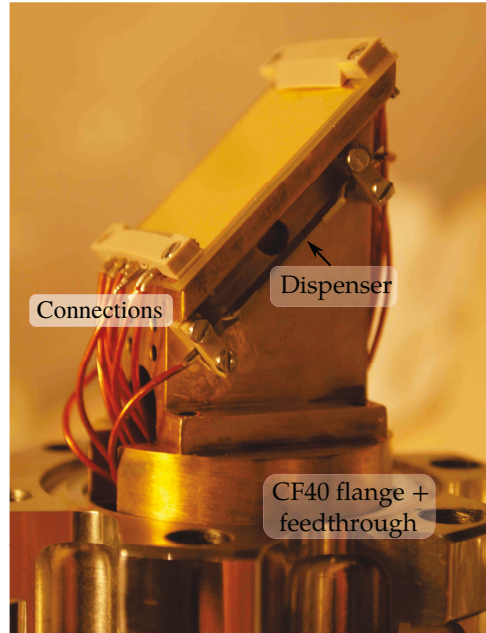


**Figure 2.13:** Left: chip mount with electrical feedthrough, dispensers and connections. The copper mount is covered with gold.

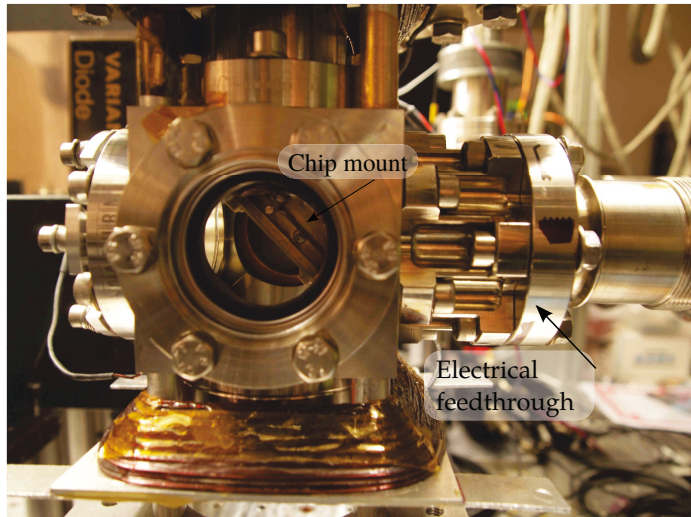


**Figure 2.14:** View of the chip mount in the vacuum chamber. The chip is facing downwards at a 45°. There are four windows altogether: one visible on the picture, one opposite this window, one beneath the chamber and one on the left of the image. The electrical feedthrough is connected to all the necessary current supplies. The bias coils and MOT coils were removed for bake-out when the picture was taken. The flange on the left is "reentrant" for the new imaging objective to be close enough to the atoms, as detailed in the next section.

## 2.4 The imaging system

### 2.4.1 A new high-resolution objective

The reason for the new chip layout is the installation of a new imaging objective with a larger numerical aperture. After a short description of its technical specifications, I'll describe some further changes which had to be brought to the setup to integrate this new objective.

#### Technical specifications

The objective was home-designed, mounted and tested by former PhD student Bess Fang, with the help of Yvan Sortais (assistant professor at Institut d'Optique), the optical workshop (Christian Beurthe) and the mechanical workshop (André Guilbaud). It was inspired by the objective currently in use on our neighbouring experiment "Pince" (supervised by Vincent Josse, also part of the Atom Optics group at Institut d'Optique), itself inspired by the objective in use on the BEC experiment in M. Oberthaler's group in Heidelberg [116]. The lenses were manufactured by LensOptics. Details can be found in B. Fang's PhD thesis [49] but here I will give a quick overview of its characteristics for consistency.

The objective consists of three lenses mounted in a custom (and home-built in the mechanical workshop) tube. The choice of the curvature radii came from an optimisation procedure with optical design software OSLO. The main difficulty in this procedure comes from the BK7 3 mm thick window between the lenses and the vacuum: the aberrations introduced by this glass cell need to compensated for.

The final objective was tested with performances reaching expectations (working distance is 26.5 mm): Numerical Aperture (N.A) of 0.39, point spread function radius (PSF)  $1.2 \mu\text{m}$  and a field of view of  $\pm 380 \mu\text{m}$ . Figures 2.15 and 2.16 (taken from [49]) summarise the testing of the objective with a pinhole.

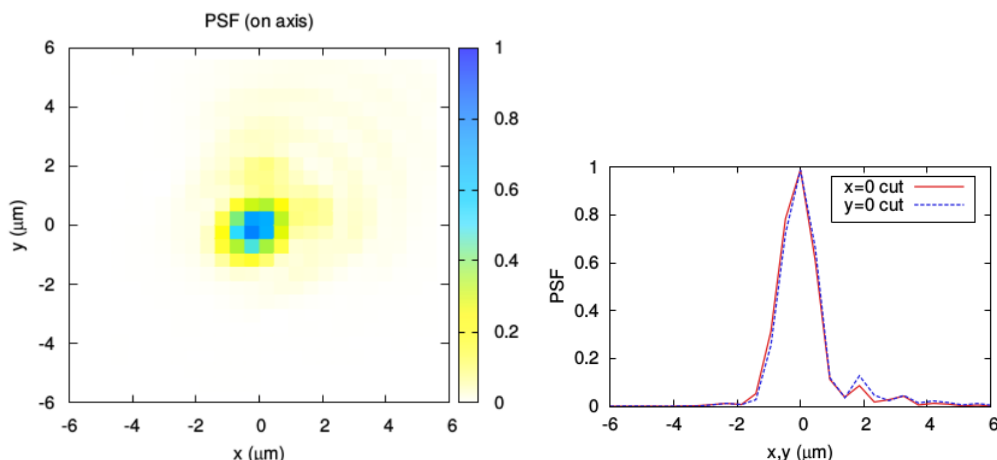


**Figure 2.15:** Measured PSF on axis (left) and cuts along  $x = 0$  and  $y = 0$ , adapted from [49]. The measured radius of the PSF is  $1.2 \mu\text{m}$ . The remaining decentering coma was found to be uniform throughout the field.

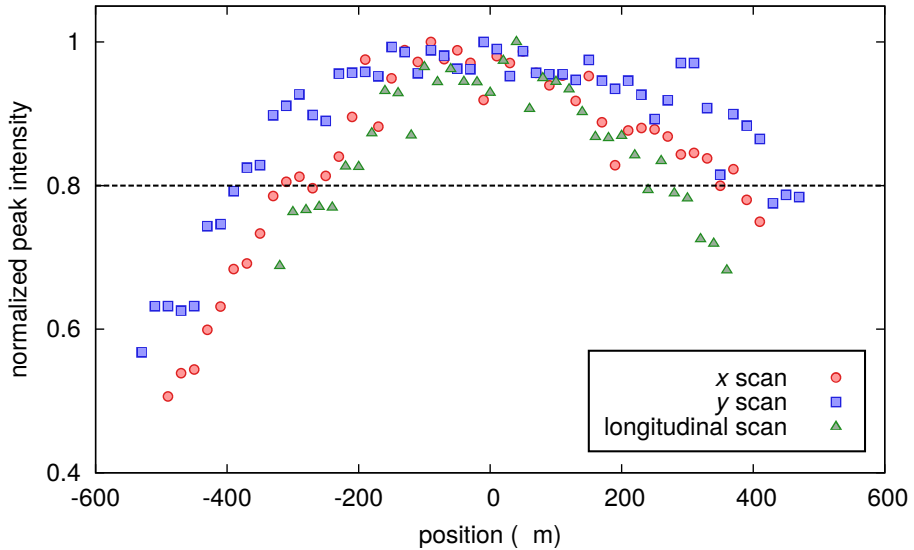


**Figure 2.16:** Normalised peak intensities off axis (with slight decentering along  $x$  or  $y$ ), and on-axis in the vicinity of the focal point. The horizontal dashed line corresponds to the PSF intensity reduced by 20%. The imaging is close to diffraction limited up to  $350 \mu\text{m}$  off-axis, and the longitudinal working distance is around  $\pm 200 \mu\text{m}$ .

## 2.4.2 Required changes to the setup

### Vacuum system

To achieve a higher numerical aperture, the objective needs to be brought closer to the atoms. For this purpose a reentrant flange with an indium seal replaced a standard CF flange with a window. The objective mount is then installed inside the reentrant flange and the distance between the objective and the atoms is greatly reduced. The flange is vacuum tight by the sole pressure difference between atmospheric pressure and UHV. Before installation on the vacuum chamber, the indium wire is pressed between the window and the edge of the flange, and mechanically held by screws. After installing on the vacuum chamber, bake-out can be carried out as usual and once the pressure is low enough the mechanical mount maintaining the window and the seal can be removed.

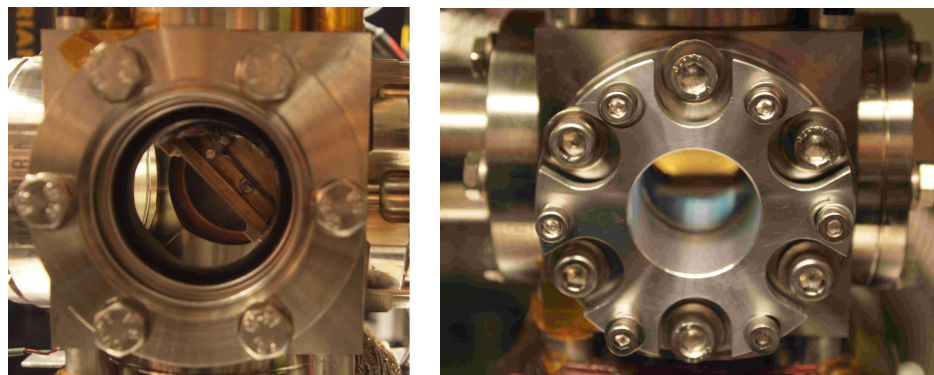


**Figure 2.17:** View of the reentrant flange along with the mechanical system (a tube screwed on the flange) which initially presses the window against the indium wire. After bake-out, the tube is removed and replaced by the objective.

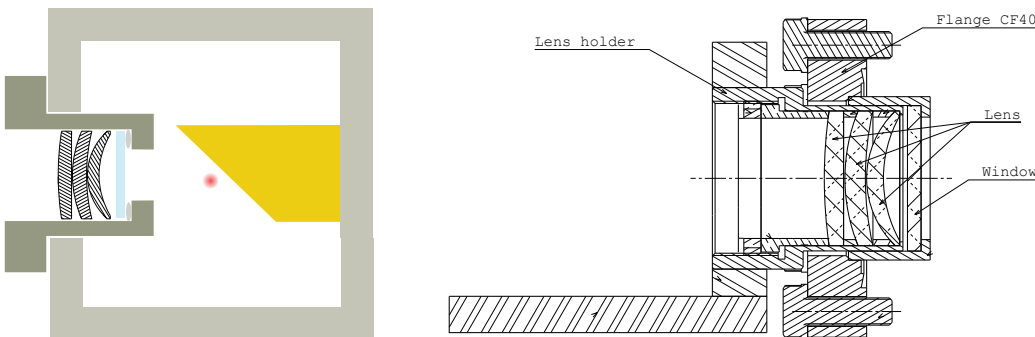


**Figure 2.18:** Sketch of the vacuum system, with the objective inside the reentrant flange (left). Technical drawing of the reentrant flange (right). The lens holder is designed to be on a translation stage.

The new vacuum seal requires some caution during bake-out: since indium melts around  $140\text{ }^{\circ}\text{C}$  we decided to heat the chamber only up to about  $110\text{ }^{\circ}\text{C}$ , so that the chamber had to be kept hot for longer than before to achieve similar pressures (about  $4.10^{-11}\text{ mbar}$ ). In fact during our first bake-out attempt with the new seal a small leak appeared after some time, limiting the pressure in the chamber to  $3.10^{-10}\text{ mbar}$ .

### Optical system

The tube containing the objective is fixed on a translation stage, for precise focussing on the atoms. Because of the large numerical aperture of the objective, it strongly focusses the MOT beam reflecting off the chip (see figure 2.19). To recover a reasonable beam diameter at the position of the MOT, an achromat doublet is added on the optical path just before the objective, inside the magnetic shielding. However, this lens should not be used to image the atoms since the ideal imaging configuration (*i.e* diffraction limited) is the infinite-conjugate configuration through the objective. For this reason, we placed the "MOT" lens on a vertical translation stage to remove the lens from the optical path during imaging. Since this lens needs to be very close to the objective, we had no choice but to place the translation stage inside the magnetic shield. The translation stage we purchased<sup>14</sup> works with piezoelectric crystals: successive stick-slip translates the device over macroscopic distances, in our case almost 10 cm, in times of the order of a second. It was crucial that the translation stage wouldn't work with conventional (magnetic) motors.

The complete translation mount is fixed on the ion pump by a large cylinder tightly maintained by two screws on the base (visible at the top of the photograph figure 2.19). We gradually found that the repetitive movement of the translation stage makes the large ring move downwards, affecting the alignment of the MOT, so that current mechanical mount is slightly different than what is presented here. In the following chapter, the testing of the objective on the atom cloud will be presented along with the experimental sequence and measurement methods available to us.

<sup>14</sup>SmarAct series, sold by Trioptics in France

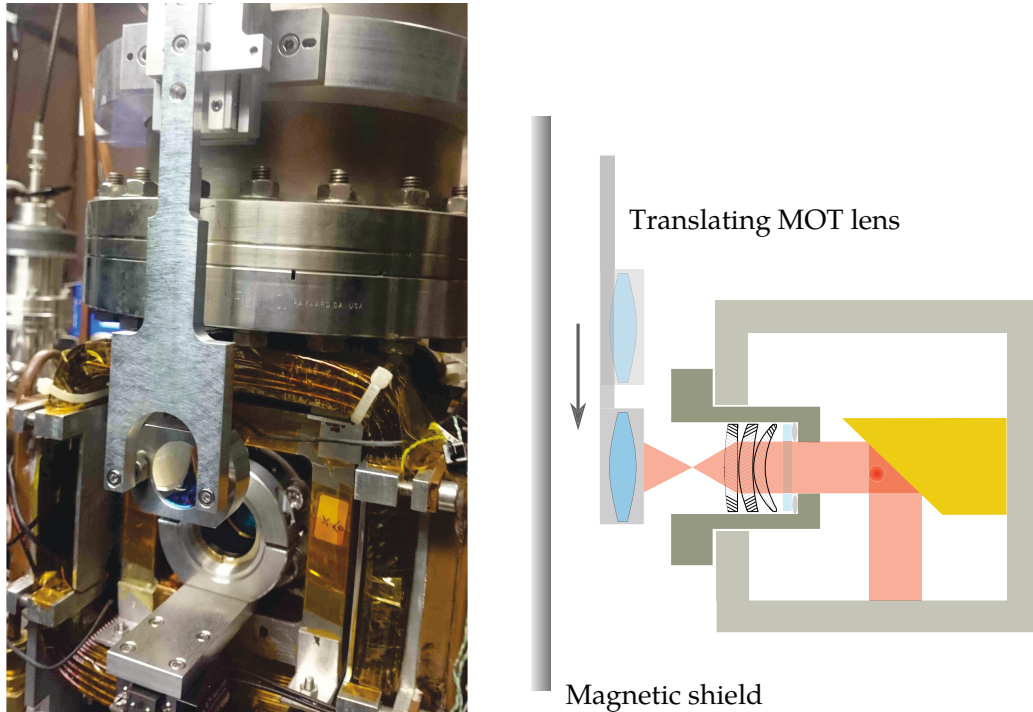


**Figure 2.19:** Left: photograph of the lens on the translation stage. Usually this part of the setup is inside the magnetic shield, which lead to important space constraints when conceiving the optical system. Right: sketch of the side view of the MOT lens and the vacuum chamber. The translation stage removes the additional lens for the imaging. The thick beam represents the MOT light, coming from the left side.

### Summary

- A new more performant objective was installed on the experiment. This required some adapting of the experimental setup.
- The vacuum system was modified with the use of a reentrant flange and an Indium seal, to bring the objective closer to the atoms.
- The optics for the MOT was also adapted: for a collimated MOT beam an additional lens is required, but only for the MOT phase. The lens is fixed onto a vertical stage and removed from the path of probe beam during the imaging phase.



# CHAPTER 3

---

## Producing, probing and understanding the one-dimensional Bose gas

---

In this chapter I introduce in more detail the experimental sequence, the imaging of the final atomic cloud and the measurement tools available.

### 3.1 Producing: the experimental cycle

To produce a highly-degenerate ultracold cloud starting from an atomic vapour at room temperature, a certain number of steps are implemented. The synchronisation of the events is controlled by a home-made sequencer (introduced section 3.1.1). I then describe the stages of the experiment up to the loading of the final trap and finally detail the characteristics of this modulated guide, the final trap used for the study of one-dimensional (1D) Bose gas.

#### 3.1.1 The sequencer: computer-experiment interface

Since the ultracold gas is destroyed after imaging (we employ a destructive absorption imaging technique), the sample needs to be produced anew in identical experimental conditions many times for statistics and pertinent measurements. The synchronisation of all events in the experimental sequence is assured by a home-made (by electrical engineer André Villing) "sequencier" which receives instructions from a Matlab programme and, in turn, sends signals to all power supplies and electronics on the experiment. This home-made interface contains a certain number of TTL and analog (ramp) cards, as well as a Direct Digital Synthesizer (DDS) for the additional RF field employed during the evaporation phases. The sequencer and the related code were developed in the very first stages of the Atom Chip experiment, and details on the architecture can be found in [44]. The structure nowadays is essentially identical, except many upgrades have been brought to accompany the increasing complexity of the setup.

The upgrades brought during my doctoral project are essentially of two types. Firstly, the number of output channels per digital card was increased from 8 to 16, and similarly the number of output channels on the analog cards was upgraded from 4 to 8. Secondly, the maximal number of points (or bytes) to program the cards was increased from 32 to 256, allowing to program more complicated ramps throughout the sequence. These hardware changes implied some changes in the programme also.

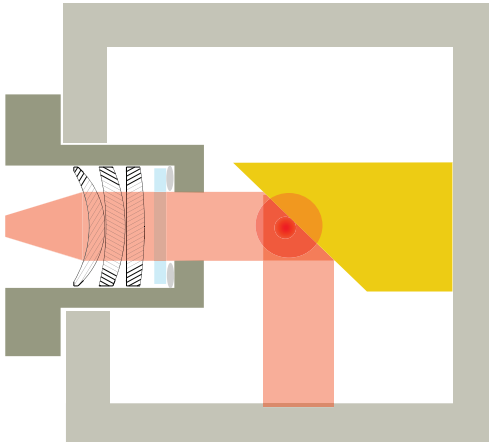


**Figure 3.1:** Configuration of the MOT beams. The vacuum chamber (a cube) contains four optical accesses: one beneath the cube, two facing each other perpendicular to the page plane and finally the objective (on the left on this sketch). The  $45^\circ$  angle of the chip allows to have the beams parallel or perpendicular to the optical table rather than at a more awkward angle.

### 3.1.2 Towards loading the final trap

#### External and on chip MOT

At the very beginning of the sequence, a vapour of  $^{87}\text{Rb}$  is released from the dispensers. From this room-temperature vapour atoms are captured by an external magneto-optical trap (MOT). In this initial trap, the magnetic fields are produced by external coils as opposed to fields created by on-chip wires. The 9 A current in the anti-Helmholtz coils produces a 30 G/cm field gradient, creating a trap when combined with circularly polarised laser beams detuned 15 MHz below the  $|5S_{1/2}, F = 2\rangle$  to  $|5P_{3/2}, F' = 3\rangle$  transition. The specificity of this MOT is that the beams reflect off the chip surface, such that only four of them are necessary to trap the atoms (figure 3.1). The few  $10^8$  atoms in the cloud are cooled down to a temperature of about  $200 \mu\text{K}$ , a few mm away from the chip. This initial step of the experiment proved crucial for all the following steps in the sequence. Indeed, with the 2" fibre outcouplers the MOT beams are significantly larger than before, greatly increasing the capture volume of the trap. We also have more optical power available. Although we have no quantitative measurement of the number of atoms in the MOT, its size increased after the upgrades brought to the experiment, and this lead to an apparent increase of the number of atoms in the next steps too.

The atoms are then transferred to a second MOT where the quadrupolar field is now created by the U wire on the chip with an additional bias field as explained in Chapter 2. The atoms are captured from the external MOT with a large current (5 A) in the U wire, and by compressing the trap (lowering the current in the wire down to 2 A and increasing the bias field) the atoms are brought 500  $\mu\text{m}$  from the trap surface. The number of atoms in this second MOT phase is of the order of several  $10^7$ .

#### Optical Molasses and pumping

The temperature achieved with the MOT is not low enough to directly load a magnetic trap. An additional molasses phase where sub-Doppler cooling occurs cools the atoms down to temperatures low enough for subsequent magnetic trapping. By ramping the

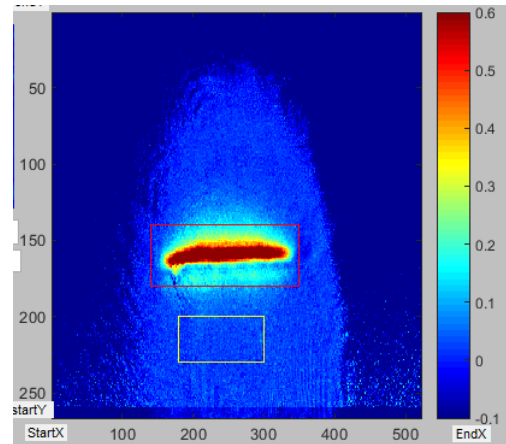


**Figure 3.2:** Screenshot of the compressed Z trap. The pixels are scaled such that the cloud is more elongated than it appears. The colour bar gives the optical density and reveals the high density of the gas. This image was taken with a pixel size of the order of  $8 \mu\text{m}$ , much larger than the ultimate pixel size used to image the final samples, because the cloud extends over several mm.

detuning of the light down to far red-detuned values (about  $-80 \text{ MHz}$ ) the cloud is cooled down to several tens of  $\mu\text{K}$ . After this phase the atoms are to be transferred into a purely magnetic trap. However, they are equally distributed in the five Zeeman sublevels of the  $F = 2$  hyperfine state. Since we chose to trap the  $m_F = 2$  sublevel, we optically pump the atoms into this Zeeman substate. A circularly polarised beam (along the quantisation axis) addresses the  $F = 2 \rightarrow F' = 2$  transition in a few hundred  $\mu\text{s}$  long pulse, during which the number of atoms captured in the trap increases by a factor of about 3<sup>1</sup>.

### Z trap and ACDC trap

After the molasses phase light is no longer used to trap the atoms. They are transferred into a magnetic trap produced by the Z-shaped wire on the surface on the chip (along with a homogeneous bias field). The  $\approx 10^7$  atoms of the molasses are almost entirely transferred to a first Z trap configuration,  $500 \mu\text{m}$  from the chip. This first deep Z trap ( $600 \mu\text{K}$  deep) is created with a maximal current of  $6 \text{ A}$  and a relatively low bias field of  $13 \text{ G}$ . With a decrease of the current flowing in the Z wire and an increase of the bias field, the trap is transversely compressed and the height of the trap is decreased to  $150 \mu\text{K}$ , with a corresponding current of  $3 \text{ A}$  and a bias field of  $40 \text{ G}$ . The compressed Z trap is very elongated in shape, the transverse frequency being of the order of  $3 \text{ kHz}$  compared to a longitudinal frequency of a few Hz.

A first RF-induced evaporation stage cools the cloud in the compressed Z trap down to a few  $\mu\text{K}$  with a remaining  $3.10^5$  atoms. The AC trap is then switched on and superimposed with the Z trap (to create the so-called ACDC trap<sup>2</sup>). By matching the positions of the Z trap and AC trap, and then lowering the DC potential, about  $10^5$  atoms are

<sup>1</sup>In principle since there are five sublevels we should gain a factor five but in practice the configuration which optimises atom number later corresponds to a factor 3 of increase.

<sup>2</sup>The atoms are on the highway to degeneracy

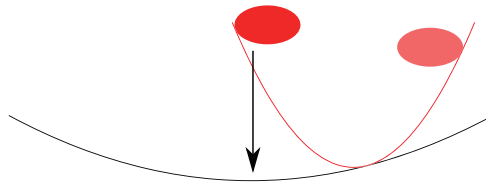


**Figure 3.3:** Illustration of "catching". The initial and final trap is the loose confinement represented in black. When the cloud's centre of mass oscillations brings the atoms to the far right, the potential is quickly changed to the tighter and displaced red one. The cloud continues to oscillate in this second potential and when it reaches the oscillation maximum on the far left, we switch the potential back to the initial black configuration and the cloud falls, at rest, into the final trap.

finally loaded into the pure AC trap, also referred to as the modulated guide. The preliminary evaporation stage is necessary: because of the modulation of the magnetic field the evaporation window available is very small (see Chapter 2 for more on this).

### 3.1.3 The final trap

#### Loading method

A total of  $10^5$  atoms are finally loaded into the modulated guide. This final loading stage is quite delicate since any stray homogeneous fields will displace the centre of the trap, creating a strong force on the atoms and heating the cloud [78]. Especially in the last steps of the ramp decreasing the current in the Z wire and the bias fields, the slightest remaining homogeneous components tend to excite oscillations of the cloud. To prevent this, we implement a "catching" scheme, illustrated figure 3.3. After identifying the center and frequency of the centre of mass oscillations appearing when the DC trap is switched off, the longitudinal trap is quickly turned tighter and displaced, such that the new maximum of oscillation (where the cloud is at rest) coincides with the previous centre of the looser trap. When the cloud reaches this position the longitudinal trap is quickly switched back to its original configuration, and the atoms fall, at rest, in the centre. This is possible thanks to the decoupled longitudinal and transverse confinements of the AC trap: the scheme can easily be implemented by controlling the current in the lateral wires which produce the longitudinal confinement.

After the catching scheme, a second evaporation stage cools the atoms to a final temperature in the 100 nK range, with an atom number ranging from  $10^3$  to  $10^4$  depending on the desired experimental configuration. For transverse trapping frequencies around a few kHz corresponding to weak effective coupling constants (see below), we can access the ideal Bose gas regime, as well as deeply quasi-condensed gases, and explore the broad crossover between these two asymptotic phases.

The experiment has proven to be quite stable so far: the number of atoms loaded in the AC trap varies from one shot to another by 10 %. However, optimisation and readjustments of loading parameters are required because of long-term drifts.

### Characteristics: trapping frequencies

After loading the final trap, we can turn to its characterisation and in particular the measurement of the longitudinal and transverse trapping frequencies.

The longitudinal confinement is provided by the lateral wires (baptised "d", "d'" and "D", "D'" wires), which are perpendicular to the modulated guide on the chip. We have four wires available, so that in principle one can engineer traps that take the form of any arbitrary fourth-order polynomial. Except for measurements in momentum space where the trap is required to be as harmonic as possible, we only use two wires to create a locally harmonic confinement. Indeed, the final cloud extends over maximum  $200 \mu\text{m}$ , whereas the lateral wires are separated by a distance of 3 mm, leaving some margin for the range over which the trap can be considered harmonic. A typical slowly-varying trap is achieved with a current of 0.4 A in the D, D' wires and a longitudinal  $\tilde{B} = 1 \text{ G}$ . By measuring center of mass oscillations (triggered by a kick in the longitudinal potential), we get 8.6 Hz.

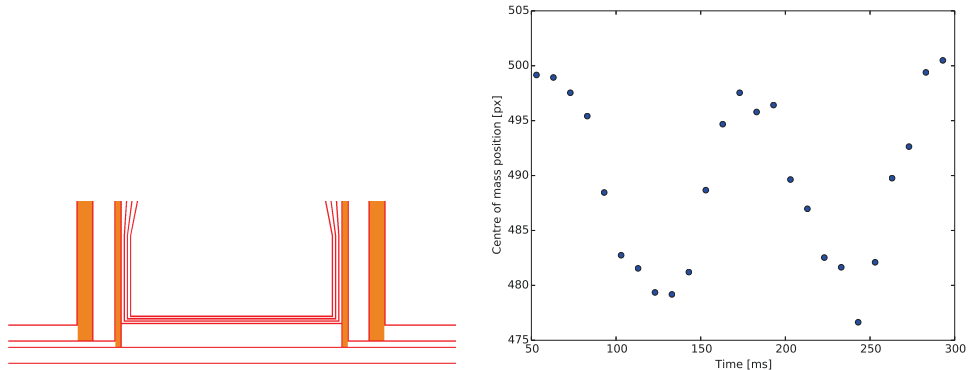


**Figure 3.4:** Left: reminder of the position of the wires providing the longitudinal confinement. Right: center of mass oscillations in the trap. A fit gives a longitudinal trapping frequency  $\omega_z/2\pi = 8.6 \text{ Hz}$ .

The transverse confinement is provided by the modulated guide: three parallel wires with alternating current at 400 kHz flowing through them. To access the transverse frequency experimentally, several methods are available. One can do parametric heating, where the idea is to modulate the transverse trapping frequency. For modulation frequencies verifying  $f_{mod} = 2f_{\perp,AC}/n$  with  $n$  integer, parametric resonances will result in a sharp dip in atom number. Experimentally, we observe such a dip at a frequency  $f_{\perp} = 8.7 \text{ kHz}$  (figure 3.5).

The measured trapping frequencies are important in the characterisation of the ultracold samples: they will be used later for thermometry. The longitudinal frequency is required to fit the longitudinal density profile with an equation of state in the local density approximation while the transverse frequency directly gives the effective coupling constant  $g_{1D} = 2a_S\hbar\omega_{\perp}$  (with  $a_S$  the s-wave scattering length).

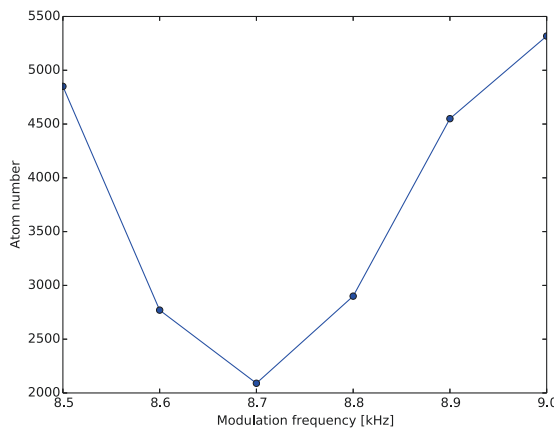


**Figure 3.5:** Parametric heating of the cloud to measure the transverse confinement: a clear dip in a atom number appears around 4.35 kHz.

### Summary

- The first steps of trapping and cooling are the now classic MOT and molasses phase. The atoms are gradually cooled and brought closer to the chip surface to then be confined in on-chip magnetic traps.
- However at this stage they are not yet cold enough to be loaded in the final modulated guide. For this reason we first compress (to bring the atoms yet closer to the surface) and cool the atoms by RF-induced evaporation in the so-called Z trap.
- Finally, when the atoms are at a temperature of a few  $\mu\text{K}$  and about  $10 \mu\text{m}$  from the chip surface, they are loaded in the AC trap (or modulated guide).
- In this trap, after a second cooling phase the 1D Bose gas reaches quantum degeneracy. The high transverse trapping frequency (about 4 kHz) ensures the sample is 1D.

## 3.2 Probing: absorption imaging

Now that we presented the protocol to produce the ultracold 1D Bose gas, in this section I will present the method used to image the produced cloud: absorption imaging. This technique is very common in the cold atom community [86] and presents better signal over noise when the resolution of the imaging system is improved, which I will discuss after presenting the general method. I will then present the very first images of the cloud made with the new objective, to discuss calibration of atom number and optical resolution.

### 3.2.1 Principle

After conducting the desired experiment (produce a cloud at equilibrium, or excite the cloud in any manner and then letting the system evolve), the integrated two-dimensional density distribution is recorded by shining a resonant laser beam onto the atomic cloud, and measuring the absorption profile on a CCD camera after being reflected off the chip surface (figure 3.6). In other words, the less photons collected locally, the more important the local optical density. The decrease of intensity along the line of sight is, according to the Beer-Lambert law:

$$\frac{dI}{dz} = -\rho(x, y, z)\sigma(I)dz. \quad (3.1)$$

$\sigma(I)$  is the absorption cross-section, in general dependent on the probe intensity  $I$ , and  $\rho$  the three-dimensional density. If the interparticle distance becomes of the order of the probe wavelength, this expression no longer holds as non-trivial reabsorption events effectively reduce the absorption signal.

The absorption cross-section  $\sigma(I)$  not only depends on the probe beam intensity, but also on the atomic level structure, and a possible Zeeman effect which shifts the levels and the polarisation of the probe beam. For a two-level atom (in our case  $|F = 2, m_F = 2\rangle$  and  $|F' = 3, m_{F'} = 3\rangle$ , addressed with  $\sigma^+$  light), the absorption cross-section takes the form

$$\sigma(I) = \frac{\sigma_0}{1 + I/I_{sat}}, \quad (3.2)$$

where

$$\sigma_0 = \frac{3\lambda^2}{2\pi} \quad (3.3)$$

is the low-intensity cross-section and the saturation intensity reads

$$I_{sat} = \Gamma \frac{\hbar\omega}{2\sigma_0}. \quad (3.4)$$

$\Gamma = 2\pi \times 5.7$  MHz is the natural linewidth of the considered transition. In general, the cross-section is not straightforward to determine and in principle one must solve the optical Bloch equations describing the light-matter interactions [78]. In an approximate model [126] corrections including effects of a more complex level structure, an external magnetic field and arbitrary polarisation of light, deviations from above expressions are included in a dimensionless parameter  $\alpha$ :

$$\sigma_{eff} = \frac{\alpha\sigma_0}{1 + I/I_{sat}}. \quad (3.5)$$

In addition, on our setup the cloud is so close to the chip that it sees both direct and reflected light with different polarisations. We determine this parameter experimentally. To account for deviations from the Beer-Lambert law in the case of dense clouds, we also implement a scheme which will be detailed in the relevant sections below (3.2.3 and 3.3.1).

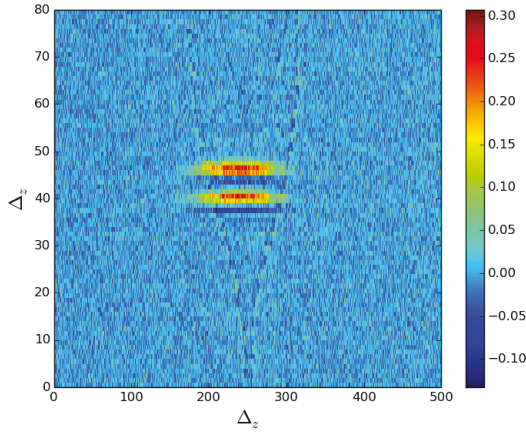


**Figure 3.6:** Example of an image. Its reflection in the chip surface (which acts as a mirror for the imaging probe) is also visible. The colour bar shows optical density.

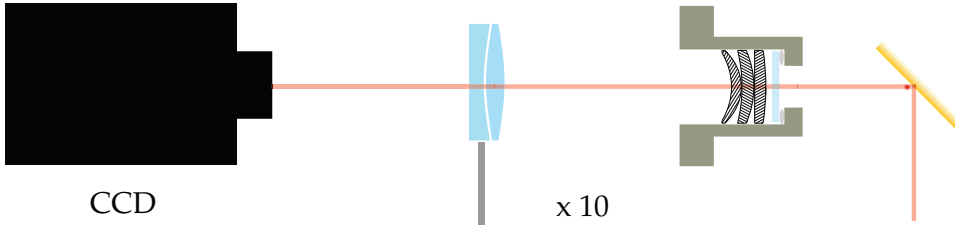


**Figure 3.7:** After the light crosses the atomic cloud the photons are collected on a Charged Coupled Device (CCD) camera. The image is formed at a distance  $f'$  from the achromat doublet. The camera and doublet are mounted on translation which in principle allow for different imaging configurations. For instance, a smaller magnification (corresponding to a smaller  $f'_{doublet}$ ) is useful to image the optical molasses, in which case we adjust the position of the camera.

The complete imaging system consists of the previously described imaging objective (Chapter 2), and a doublet, which sends the image of the cloud on a CCD. For in situ imaging, the cloud is at the focal point of the objective and we image in infinite conjugation. However, we also take images after a time-of-flight where the cloud is no longer at the focal point of the objective. This imaging configuration is less performant, this is considered section 3.3.2. The working distance of the objective being 20.5 mm, with  $f'_{doublet} = 250$  mm the pixel size in the imaging plane is  $\Delta_z = 1.8 \mu\text{m}$ .

Since the imaging probe reflects off the chip surface a good surface quality is crucial for clean imaging. The probe beam is in fact an imaging sheet to match the very elongated shape of the imaged cloud and ensure a relatively homogeneous intensity over the sample.

### 3.2.2 Improving the SNR

The motivation for replacing the imaging objective was the improvement of the signal over noise ratio (SNR) of our absorption imaging. The resolution of the optical system is  $\max(\delta, \Delta_z)$ ,  $\delta$  being the radius of the point spread function (PSF, the response of the optical system when imaging a point).

Consider the absorption signal of a single atom detected on a CCD. The photon count on a single pixel for an intensity  $I$ , and pulse time  $\tau_p$  is:  $N_{ph} = I\tau_p\Delta_z^2\lambda/hc$  and the corresponding absorption signal (if the complete signal is collected on the considered single pixel) is  $\sigma/\Delta_z^2N_{ph}$ .

The technical noise of the camera<sup>3</sup> is negligible so that the only remaining source of noise is the photonic shot noise directly given by  $\sqrt{N_{ph}}$ . The SNR is then simply expressed by [49]:

$$\text{SNR} = \sqrt{\frac{3\lambda^2\Gamma}{4\pi}} \frac{\sqrt{\tau_p}}{\Delta_z} \frac{\sqrt{I/I_{sat}}}{1 + I/I_{sat}} \quad (3.6)$$

It appears that better SNRs are achieved for long pulse times and small pixel sizes. However there is a lower bound for the pixel size for a given pulse length, since the atoms diffuse during the imaging pulse. Their movement can be modelled as a random walk in momentum space and the resulting displacement is [80]:

$$\langle \delta z^2 \rangle = \frac{h^2\Gamma}{6m^2\lambda^2} \frac{I/I_{sat}}{1 + I/I_{sat}} \tau_p^3. \quad (3.7)$$

The condition for the resolution not to be degraded by the diffusion of atoms during the imaging pulse is thus  $\sqrt{\langle \delta z^2 \rangle} < \Delta_z$  (condition shown in red on the following figure). In practice we may use  $I < I_{sat}$  and longer imaging pulses.

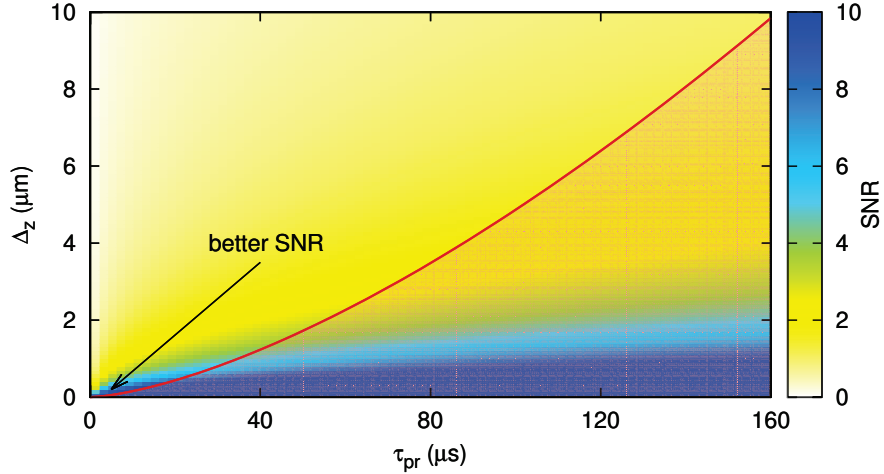


**Figure 3.8:** Colour map of the dependance of SNR on pixel size  $\Delta_z$  and length of imaging pulse  $\tau_p$ , taken from [49]. The best SNR is for smaller pulse lengths and pixel sizes, however a lower bound of pixel size is imposed by the diffusion of atoms during the imaging pulse.

### 3.2.3 Testing the objective with the atoms

Here I present the very first images of the atomic cloud made with the new imaging system. I discuss two calibration measurements: an independent determination of the effective optical resolution and the calibration of atom number.

<sup>3</sup>Pixis-1024BR

### Determining the resolution from pixel correlations

As explained above, for a small enough pixel size and short enough imaging pulse, the optical resolution is directly given by the point spread function of the imaging objective. This quantity can be accessed by measuring correlations between pixels. Indeed, if the pixels are small enough compared to the RMS width  $\delta$  of the imaging response function, but larger than the density-density correlation length  $\xi$  (typically  $\xi \ll \Delta_z \lesssim \delta$ ), the degree of correlation between adjacent pixels depends only on  $\delta$ . By assuming a Gaussian Point Spread Function (PSF), the calculation of these correlations can be conducted analytically, as we do for first-neighbour pixels and second-neighbours [78]. The expression of the PSF is:

$$\mathcal{A}(\alpha, p) = \frac{e^{-z^2/(2\delta^2)}}{\delta\sqrt{2\pi}} \quad (3.8)$$

We measure correlations between pixels and compare the measurements to the expected correlations from the analytical expression, as a function of  $\delta$ . The experimental correlations (left panel of figure 3.9) are plotted as a function of density, in atoms per pixel. They rapidly saturate to their maximal value, the correlations for low densities being limited by the signal from the most dilute regions of the cloud. We extract the degree of first- and second-neighbour correlation from this measurement and compare to the plot of the right panel of figure 3.9: the measured correlation values correspond to a certain resolution  $\delta_{\text{eff}}$ . From the right panel of figure 3.9, we thus find the  $\delta_{\text{eff}}$  which best reproduces the measured correlations. In the case where the imaging pulse slightly blurs the image and reduces the resolution, the method is also applicable and the measured resolution  $\delta_{\text{eff}}$  is then slightly larger than the ideal resolution  $\delta$ . In the figure below, measured correlations with the new imaging objective are represented. The extracted resolution of  $\delta_{\text{eff}} \approx 1.5 \mu\text{m}$  is better than what we achieved with our previous objective (around  $3 \mu\text{m}$ ), but can in principle still be improved, since the expected performance is around  $\delta = 1 \mu\text{m}$ : the imaging pulse possibly introduced some blurring and could be shortened.

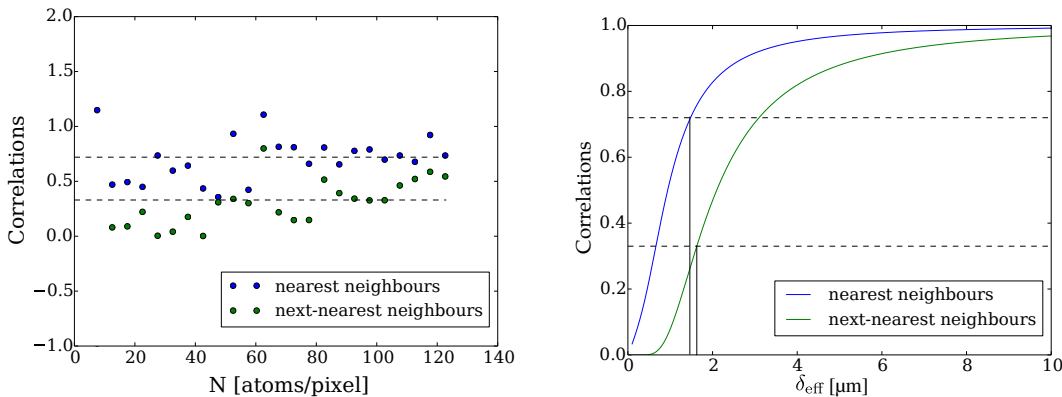


**Figure 3.9:** Left: experimental correlations between pixels for the atomic cloud shown figure 3.6. The degree of correlations between pixels can be translated to the effective optical resolution with the figure shown in the right panel. The measured correlations for nearest neighbours matches the analytical correlations for  $\delta_{\text{eff}} \approx 1.4 \mu\text{m}$ , while the second-neighbour correlations yield a slightly larger value of  $1.6 \mu\text{m}$ .

### Atom number calibration

As mentioned before, there are two difficulties in determining the atom number in an absolute manner. Firstly, the absorption cross-section can be complicated to estimate, and secondly for high atomic densities (when non-trivial reabsorption events happen) the validity of the Beer-Lambert law breaks down, leading to an underestimate of atom number. The solution to the first problem is to use high intensity probes; at large intensities, the cross-section does not require the knowledge of the sublevel structure nor the Zeeman shift or polarisation of light and absolute atom number can be calibrated this way [153]. Indeed, if enough photons reach the atoms they will each scatter  $\Gamma/2$  photons per second no matter the probe and measurement condition [80].

The solution to the problem of high optical densities is to perform a time of flight before imaging. Transverse expansion makes the cloud more dilute and prevents reabsorption events. In addition, after these 13 ms of TOF the cloud is far enough from the chip to be crossed by the probe beam once which excludes double-counting. An external magnetic field aligns the magnetic moment of the atoms along the quantisation axis and the  $\sigma^+$  addresses the closed  $|F = 2, m_F = 2\rangle$  to  $|F' = 3, m_F = 3\rangle$  transition. For the experimental situation presented above (figure 3.6), the number of atoms directly extracted from this *in situ* image is about  $2.10^3$ . Atom number calibration gives a much larger number around  $9.10^3$ .

#### Summary

- The method used to probe the cloud is absorption imaging, with a high-resolution optical system.
- We recently replaced this optical system to increase the SNR and resolve smaller structures.
- The resolution of the optical system can be determined independently by imaging an ultracold cloud and measuring correlations between pixels, and we find a PSF of RMS width  $\delta_{\text{eff}} = 1.5\mu\text{m}$ .
- Atom-number calibration requires some caution and is performed with high-intensity resonant light after 13 ms time of flight.

### 3.3 Understanding: analysis methods

On the experimental setup we can take images of the cloud in real as well as in momentum space. For data *in situ*, we take several types of images for different diagnoses, from which we extract thermodynamic quantities (temperature, chemical potential) thanks to the exact equation of state available.

### 3.3.1 Real space diagnoses

#### Modified equation of states in the 1D-3D crossover

Although the transverse confining potential is very tight to ensure a large transverse ground state energy  $\hbar\omega_{\perp}/2$ , in typical experimental situations a small fraction of transverse excited states should be taken into account on top of the 1D Yang-Yang (YY) equation of state (EoS)  $\rho_{YY}(\mu, T)$  as the gas may lie on the 1D-3D crossover with  $k_B T \approx \mu$ . The few percent of atoms in these excited states are treated as a correction to the YY EoS as an ideal gas, with a shifted chemical potential  $\mu(j) = \mu - j\hbar\omega_{\perp}$  for the  $j$ th excited state [144]. The corresponding equation of state for the excited fraction is

$$\rho_{TE}(\mu(j), T) = \frac{1}{\lambda_{dB}} g_{1/2} \left( e^{\mu(j)/k_B T} \right). \quad (3.9)$$

Finally the total linear density becomes

$$\rho(\mu, T) = \rho(\mu, T)_{YY} + \sum_{j=1}^{+\infty} (j+1) \rho_{TE}(\mu(j), T). \quad (3.10)$$

In practice, we truncate the sum at about  $j = 35$ . This constitutes the Modified Yang-Yang (MYY) equation of state.

MYY allows to correct the EoS for samples with relatively large temperatures. For samples with a chemical potential of the order of  $\hbar\omega_{\perp}$ , the Thomas-Fermi EoS  $\mu = gn$  is modified in the 1D-3D crossover, to take the form

$$\mu_{3D} = \hbar\omega_{\perp} (\sqrt{1 + 4\rho a_S} - 1) \quad (3.11)$$

This accounts for the integration of a three-dimensional density profile and the resulting swelling of the wavefunction [58].

#### Local Density Approximation

The presence of a slowly-varying longitudinal trap may also be accounted for as a shift in the chemical potential. The quantisation of the longitudinal energy levels may usually be neglected since  $\mu$  is orders of magnitude larger than  $\hbar\omega_z$ . In the local density approximation (LDA), the total system is divided in small slices  $\delta z$ . In each of these slices, density can be considered homogeneous, and the subsystem is at thermal equilibrium with its neighbours.  $\delta z$  should verify  $\xi \ll \delta z \ll L$  where  $\xi$  is the typical density correlation length. The system size being roughly given by  $\omega_z$ , the LDA is applicable for small trapping frequencies. The chemical potential at position  $z$  is then expressed as

$$\mu(z) = \mu_{\text{centre}} - \frac{1}{2} m \omega_z z^2. \quad (3.12)$$

Consequently, a single realisation of a gas spans a whole range of chemical potentials and explores different regions of the EoS.

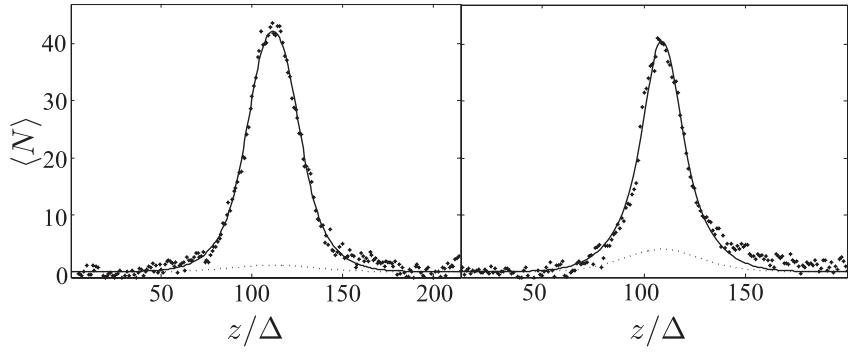


**Figure 3.10:** Two examples of in situ profiles (figure adapted from [80]): the left profile is in the quasi-condensate regime, while the profile represented right is in the ideal Bose gas phase. The solid lines represent fits of the Yang-Yang equation of state, which allows to extract temperature. For these sets of data, we found 111 nK and 76 nK for the profiles shown left and right respectively. The contribution of transverse excited states is also shown (dotted lines).

### Longitudinal density profile

By integrating a two-dimensional absorption image along the vertical direction, we extract the longitudinal density profile  $N(z)$ , in units of atom number per pixel. To image the density profile, one is interested in the shape of the atomic cloud. Saturation of the signal in the centre of the cloud where atomic density is the largest should thus be avoided: when the Beer-Lambert law is no longer verified the absorption signal is reduced and the measured optical density underestimated. To prevent this, after the sample is produced the cloud is released and slightly expands in a short 1 ms time of flight. The probe beam is slightly detuned to reduce the absorption cross-section. The profile measurements are then renormalised by the total atom number determined from a careful calibration as described in 3.2.3. The intensity of the probe beam is low ( $I/I_{sat} \approx 0.05$ ) to avoid saturation of the transition.

With the knowledge of the external trapping potential ( $\omega_z, \omega_\perp$ ), the temperature and chemical potential of the sample is extracted by applying the modified Yang-Yang equation of state in the local density approximation, since the density profile is completely determined by these quantities. A complete set of data in all parameter regimes was provided by K. Kheruntsyan and a numerical interpolation routine allows to extract all desired thermodynamic quantities. The method works best for samples whose temperatures are not too low. Indeed, the information on the temperature is found in the wings of the profile and as temperature decreases the density distribution approaches the Thomas-Fermi inverted parabola,

$$\rho_{TF}(z) = \rho_0 \left( 1 - \left( \frac{z}{R_{TF}} \right)^2 \right), \quad (3.13)$$

$$R_{TF} = \sqrt{\frac{2\rho_0 g}{m\omega_z^2}}$$

and correspondingly the EoS becomes independent of temperature:  $\mu = gn$ . It is also important that the chemical potential shouldn't exceed  $\hbar\omega_\perp$ , otherwise the density profile requires the correction to  $\mu$  mentioned in 3.3.1.

### Atom number fluctuations

The quasi-condensation crossover can be identified by observing the saturation of atom number fluctuations at high densities. This measurement was performed on our experiment [6,79], and implemented as an independent thermometry of the gas performant in regimes where profile fits become less reliable. We now routinely use this quantity as a calibration of the produced samples. In addition, since they are related to the compressibility of the gas, we envision to use atom number fluctuation measurements in the context of the Mott transition (see Chapter 6).

The atom number fluctuations  $\langle \delta N^2 \rangle = \langle \delta N^2 \rangle - \langle \delta N \rangle^2$  (where  $N$  designates a number of atoms per pixel) are related to the temperature by a fluctuation-dissipation relation:

$$\langle \delta N^2 \rangle = k_B T \Delta_z \frac{\partial n}{\partial \mu} \quad (3.14)$$

This relation is valid in the thermodynamic limit which requires the pixel size to be much larger than the density-density correlation length  $\xi$ :  $\Delta_z \gg \xi$ .

The signal in neighbouring pixels is slightly correlated because the effective optical resolution  $\delta_{\text{eff}}$  (effective resolution which takes into account a possible blurring during the imaging pulse) spreads over several pixels:  $\Delta_z \lesssim \delta_{\text{eff}}$ . The image of a single atom is spread over several pixel which results in a reduction of the fluctuation signal by a factor  $\kappa$  compared to the physical fluctuations:

$$\langle \delta N^2 \rangle_{\text{mes}} = \kappa \langle \delta N^2 \rangle. \quad (3.15)$$

For a pixel size well below the optical resolution and weak optical densities,  $\kappa$  is simply expressed by  $\kappa \approx \Delta_z / 2\sqrt{\pi}\delta_{\text{eff}}$  [43]. In practice,  $\delta_{\text{eff}}$  and  $\kappa$  are found measuring correlations between pixels as in 3.2.3: the determined  $\delta_{\text{eff}}$  gives the corresponding reduction factor  $\kappa$ .

The compressibility of the gas  $\partial n / \partial \mu|_T$  is known from the MYY EoS and an interpolation routine with the available numerical MYY data fits the best  $(\mu, T)$  to the measured fluctuations. The protocol to measure and extract atom number fluctuations from in situ images is as follows:

- To measure fluctuations a large number of images (200 – 300) is required. In a complete data set, we alternate the different types of images we wish to acquire. Typically, we take six fluctuation images for one atom number calibration and one profile calibration. The different types of images are "interlaced" to account for slow technical drifts.
- The imaging pulse is short ( $30 \mu\text{s}$ ) and intense ( $0.15 I_{\text{sat}}$ ) to minimise motion of the atoms and blurring and to maximise signal. Time of flight is reduced to  $50 \mu\text{s}$ , and the atoms are very close to the chip surface and see both incident and reflected probes. The probe is resonant and the cross-section follows the effective relation 3.5, where the correction  $\alpha$  was found to be 0.8 experimentally (see Supplemental Material of [5]). To account for effects beyond the Beer-Lambert law at high

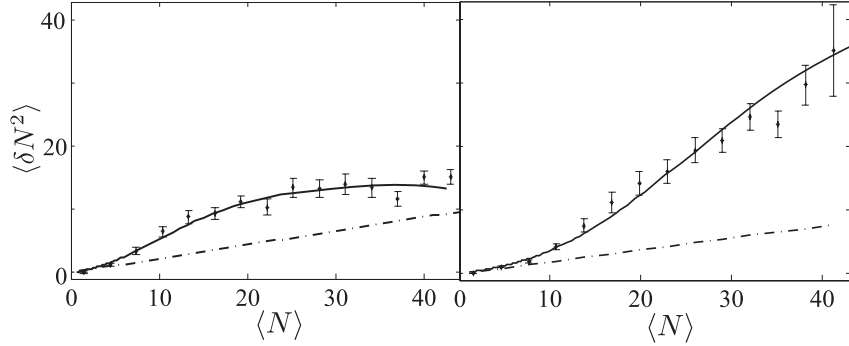


**Figure 3.11:** Experimental atom number fluctuations for the same data sets as in figure 3.10. On the left panel, the density fluctuations saturate, indicating that the gas indeed lies in the quasi-condensate regime, where density fluctuations are suppressed compared to the ideal Bose gas phase (as can be observed in the right panel). The solid lines are Yang-Yang fits, with determined temperatures of 72 and 84 nK respectively. Dash-dotted curves give the shot-noise limit.

atomic densities, a second-degree polynomial  $F_p(N)$  is determined by comparison with the renormalised profile measurement to correct the measured density profile extracted from the fluctuation images [5].

- Photon shot noise  $\langle \delta N_{ph}^2 \rangle$  contributes to the measured fluctuation signal and is subtracted. It reads [78]:

$$\langle \delta N_{ph}^2 \rangle = \left( \frac{\Delta_z}{\sigma_{\text{eff}}} \right)^2 F'_p(N) \sum_x \left( \frac{1}{N_1(x, z)} + \frac{1}{N_2(x, z)} \right). \quad (3.16)$$

The number of recorded photons in a given empty pixel in image  $i = (1, 2)$   $N_i(x, z)$  is integrated over a column of the two-dimensional image. As an alternative to the MYY EoS, one can also fit the data in the dense centre of the cloud with the modified qBEC equation of state on  $\mu_{3D}$ .

We thus have two independent thermometry methods in real space: a first method which relies on fits of in situ linear density profiles, and a second method where atom number fluctuations are fitted with the Yang-Yang equation of state. Some disagreement between the temperatures given by both methods are often found for samples deeply one-dimensional, and this point will be extensively discussed in Chapter 5.

### 3.3.2 Momentum space measurements

The velocity distribution of the atomic cloud is equivalent to the first-order correlation function (they are related by Fourier transformation, see Chapter 1): by measuring this quantity experimentally one directly accesses the coherence length of the cloud. A measurement of the momentum distribution by Bragg Spectroscopy of an atomic cloud gave the first experimental evidence of phase coherence over the system size in a BEC [135]. Signatures of phase transitions present in the  $g^{(1)}$  function were brought to light experimentally, like for the Mott transition for instance [62]. For these reasons diagnostics in momentum space are ubiquitous in the ultracold gas community. In 1D, two methods can be implemented: Bragg Spectroscopy [46, 59, 127], or long times of

flight where the far-field regime is reached, so that the measured spatial density distribution maps the initial velocity distribution of the cloud provided the interactions are switched off upon releasing the atoms. The advantage of the second technique compared to the first is to access the momentum distribution in a single experimental shot. However, its implementation is complicated by weak longitudinal confinements. Indeed, the times required to reach the far-field regime become too long and the cloud would extend over distances which would require unrealistic fields of view. The so-called focussing method surpasses this experimental issue by accelerating the focussing of the cloud to the Fourier plane.

### Magnetic focussing - principle

This method was first implemented to probe the coherence length of an elongated Bose gas, initially in a shock-cooling context [134], and more recently on an atom chip experiment in Amsterdam [37] for the study of 1D gases much like our own setup. It can also be implemented in 2D [143]. The best way to understand the method is by analogy with optics. An object at an infinite distance can indeed be brought to the Fourier plane at the focal point of a converging lens. In the case of atomic clouds, the converging lens is mimicked by a parabolic kick given to the trapped cloud. This harmonic kick gives a velocity to the atoms, proportional to the distance from the centre of the trap. After the impulsion, the confining potential is switched off and after a time  $\tau_f$  of free fall (equivalent to the focal distance in optics), the atoms focus and their spatial distribution reflect the initial velocity distribution.

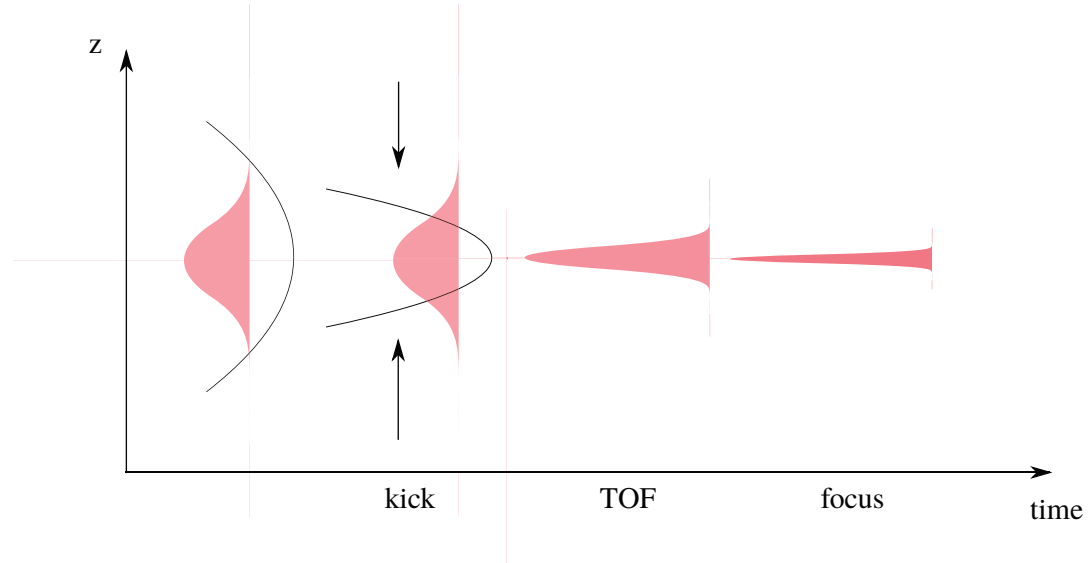


**Figure 3.12:** Illustration of the focussing technique. After applying a longitudinal kick to the cloud in the initial trap, the confinement is switched off and the atoms are released. After a time  $\tau_f$  of flight, the spatial distribution of the atoms reflect the initial velocity distribution of the cloud.

- The short kick ( $\tau_{\text{kick}} \approx 0.7$  ms) gives a momentum shift to the atoms given by  $\delta p = -m\omega_f^2 \tau_{\text{kick}} z$ . Typically,  $\omega_f = 2\pi \times 40$  Hz (whereas  $\omega_z \approx 2\pi \times 7$  Hz). Movement of the atoms can be neglected during the kick if  $\omega_f \tau_{\text{kick}} \ll 1$ . The gas is interacting, and it can be shown using the scaling approach that the effect of the interactions

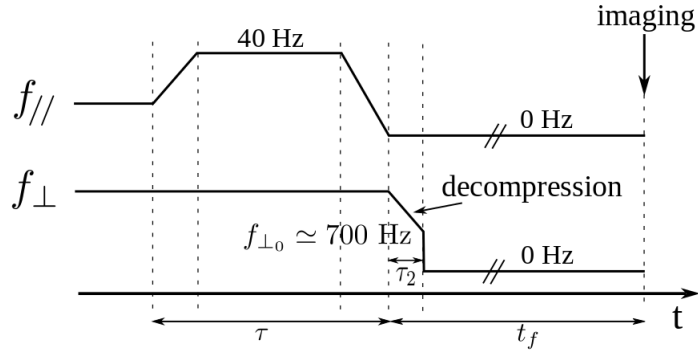


**Figure 3.13:** Focussing sequence of the longitudinal and transverse trappings, taken from [78].

can be neglected if  $\omega_z \tau_{kick} \ll 1$  [25, 80]. To give an impulsion to the atoms we necessarily have  $\omega_f > \omega_z$  and the condition  $\omega_f \tau_{kick} \ll 1$  is sufficient for the second condition  $\omega_z \tau_{kick} \ll 1$  to also be verified.

- The focussing potential should be as harmonic as possible for the imprinted velocity to be proportional to  $z$  (in other words, to avoid aberrations). Four wires are used to create this focussing potential (rather than two only for the slowly-varying longitudinal trap), to create a potential harmonic up to fifth order.
- After the kick, an additional decompression of the transverse trap reduces (represented figure 3.13) transverse spreading of the cloud which would in turn reduce the signal.
- The focussing time  $\tau_f \approx 1/(\omega_f^2 \tau_{kick})$  is about 25 ms for the considered  $\omega_f$  and  $\tau_{kick}$ . The resolution of the measurement is given by the pixel size in momentum space  $\Delta_p/\hbar = \Delta_z m/(\tau_f \hbar) \approx 0.15 \mu\text{m}^{-1}$ , for the older imaging configuration where the pixel size was larger at  $\Delta_z = 2.7 \mu\text{m}$ .

### Momentum distribution measurements

When the focussing scheme was first realised on the experimental setup in 2012, T. Jacqmin and co-workers measured the evolution of the momentum distribution across the quasi-condensation crossover, and compared the experimental results to Quantum Monte-Carlo simulations [79]. This method is now routinely used in the group, and here I present an example of such a measurement. The results presented here were obtained with the previous experimental setup, since (unfortunately) the focussing method has not been implemented yet in the new setup. We take about 30 images in the same experimental conditions, to measure the mean momentum distribution. Using this method we revealed novel features like self-reflection of the breathing mode [50], unobserved in previous (similar) measurements [67] because they performed simple time-of-flight, not quite reaching the far-field regime. A direct application of this focussing method will be developed in Chapter 4.

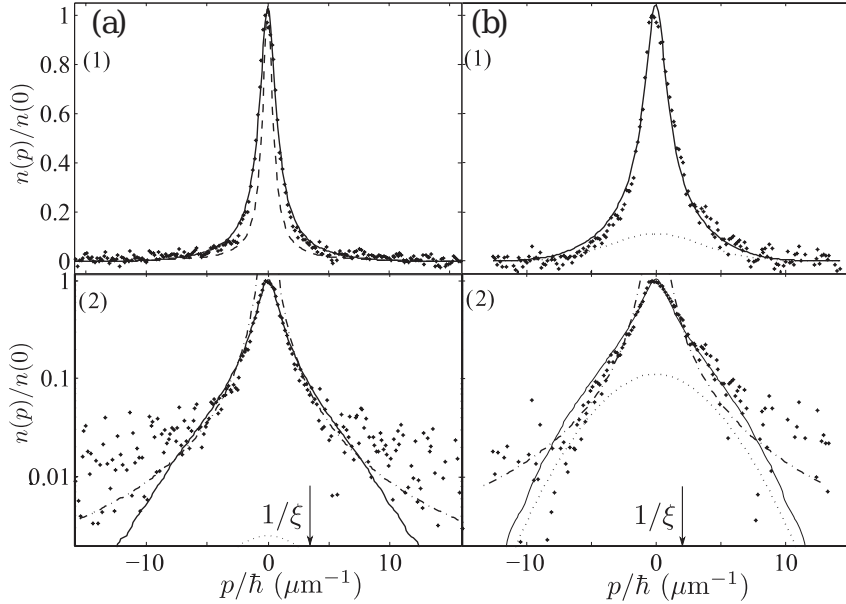


**Figure 3.14:** Measured momentum distributions, reproduction of figure 5 of [80] (the represented data sets are the same as those shown in figures 3.10 and 3.11). The normalised momentum distributions are represented in linear (1) and log (2) scales, for data sets in two different regimes: far in the qBEC (a) and in the ideal Bose gas (b). The measurement points are fitted with QMC (solid line) and the Lorentzian predicted in the qBEC (dashed lines). The dotted lines represent the contribution of transverse excited states and dash-dotted lines indicate the  $1/p^2$  behaviour. Fitting the experimental data with QMC, the temperatures of the samples can be extracted and agree with the temperatures fitted to the atom number fluctuations.

### Imaging in non-infinite conjugation

An imaging objective reaches its optimal performance when the object is in the focal plane of the optical system, and with its larger numerical aperture, the new objective has a reduced depth of field compared to the previous one. After 25 ms of free fall the atoms are displaced by 3 mm, which brings them out of focus. To image in optimal conditions, both the objective and the achromat doublet would have to be displaced to compensate for this fall, which is not possible in the current experimental configuration: the achromat doublet is fixed on the vertical translation stage whose position along the optical axis is fixed. Master student Aghilas Aoudia considered this problem and studied the decrease in performance of the objective when the atoms are several millimetres away from the focal point.

The aberrations introduced when imaging in this non-optimal conditions arise from the extremal rays. The trick to minimise these aberrations is then to reduce the diameter of the objective by placing a diaphragm on the optical path. For a given defocussing distance  $d$  and a given diaphragm diameter  $D$ , one can find the optimal working distance, *i.e* the position which minimises the diameter of the point spread function. The optimisation procedure was conducted using software CODE V and the result of the study is shown figure 3.15.

This study is quite pessimistic, in the sense that we would have to greatly reduce the numerical aperture (the optimisation procedure suggests a diaphragm diameter as

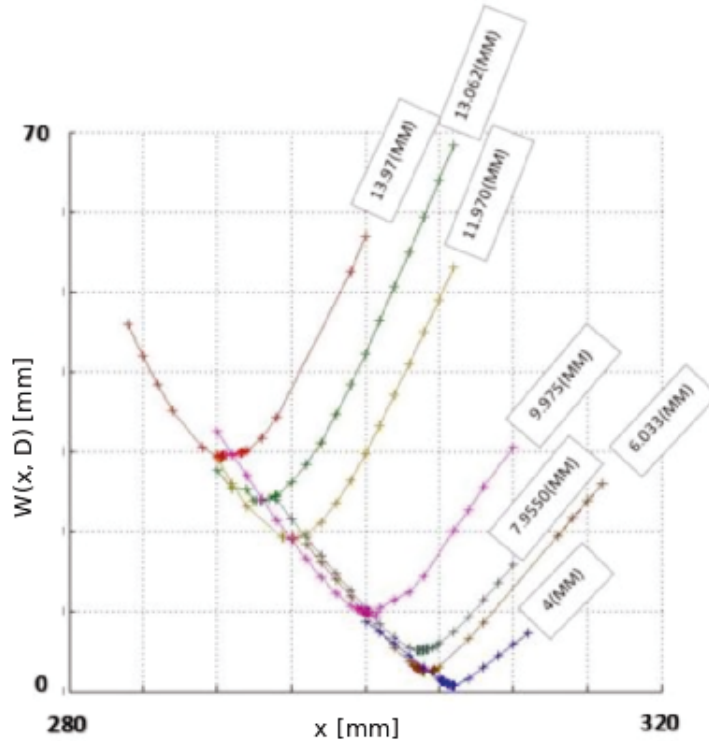


**Figure 3.15:** Evolution of the position of optimum performance for different diaphragm diameters  $D$  at defocussing  $d = 4\text{mm}$ , for different positions  $x$  along the optical axis. The optimal performance corresponds to the minima of the plotted curves, the  $y$ -axis representing the size of the point-spread function. The best performance (or smallest spot size  $W$ ) is achieved with the smallest diaphragm diameter of 4 mm.

small as 4 mm) to achieve a reasonable performance of the imaging system for atoms several mm away from the focal point. This was not tested experimentally yet.

### Summary

- A certain number of experimental tools were developed to characterise the produced 1D Bose gases at- and out-of-equilibrium.
- In real space, density profile measurements give direct access to thermodynamic quantities.
- Also in real space, atom number fluctuations not only consist in a measurement of the compressibility of the gas, they also allow an independent temperature measurement. With the better resolution now available, we could even attempt measurements of (integrated) correlations in real space, although the density correlation length (the healing length  $\xi$ ) remains below our resolution.
- Finally, a focussing technique allows us to probe the momentum distribution (or equivalently the  $g^{(1)}$  function), potentially unveiling novel features previously unobserved because the far-field regime was not reached.

- The first experimental project conducted during my doctoral work directly implemented the method to probe momentum-space correlations.

# CHAPTER 4

## Momentum-space correlations of a one-dimensional Bose Gas

Correlation functions are an essential tool to describe the physics of isolated many-body quantum systems like ultracold atomic gases. They contain valuable information on the quantum statistics [83, 131] and thermodynamics, allowing for instance to characterise different phases and states of matter [1, 2, 56]. Measuring correlation functions is especially relevant for one-dimensional (1D) Bose gases where the role of fluctuations is enhanced by the constrained nature of the system. The different phases of the 1D Bose gas are indeed defined by the local two body correlations, or equivalently, the behaviour of density fluctuations [79, 91], and the natural presence of phase fluctuations can be exploited as a temperature probe [75, 104]. Correlations not only inform on equilibrium states, they also contain information on the excitations of the system [29, 82] and propagate after driving a system out of equilibrium [30, 97]. Moreover, at a phase transition the scaling of correlations identifies its universality class and can be used to characterise classical or quantum phase transitions [111]. Finally, high-order correlation functions recently revealed non-thermal features [96], compatible with the generalised Gibbs ensemble formalism. Such correlations can be measured in standard cold atom experiments thanks to high precision imaging. They unveil information about these complex correlated systems beyond the possibilities of numerical simulations.

Most previous studies focussed on either equilibrium real-space correlations or out-of-equilibrium correlations in momentum space. Here, we report on the measurement of the equilibrium two-body correlations in momentum space, of a 1D Bose gas, throughout the quasi-condensation crossover. We define the correlations as

$$\mathcal{G}(k, k') = \langle \delta\hat{n}_k \delta\hat{n}_{k'} \rangle = \langle \hat{n}_k \hat{n}_{k'} \rangle - \langle \hat{n}_k \rangle \langle \hat{n}_{k'} \rangle, \quad (4.1)$$

where  $\delta\hat{n}_k = \hat{n}_k - \langle \hat{n}_k \rangle$  and  $n_k$  is the population of mode  $k$ . This type of measurement is possible on our experimental setup because we can measure the complete momentum distribution in a single shot, contrary to Bragg spectroscopy like for instance in [135]. Also, although previous experiments have reported momentum distribution measurements in 1D [67], reaching the far-field regime<sup>1</sup>, for such weak longitudinal traps requires some caution, and the focussing method ensures we truly measure the velocity distribution of our samples. Another strength of our experimental setup is the realisation of a single condensate at a time, rather than an ensemble of gases like in 2D lattice

<sup>1</sup>Far-field, in analogy with Fraunhofer diffraction in optics, in which the spatial distribution of atoms is homothetic to their initial velocity distribution.

experiments [67]: their imaging automatically averages over an ensemble of clouds. For these reasons we were in a good position for such measurements which had never been performed before, and establish a benchmark for future dynamical studies on our setup, after an interaction quench for instance.

This study was conducted at the beginning of my doctoral studies, before modifications were made to the experimental setup. For instance the optical resolution is lower than for the imaging system previously presented and the atom numbers typically smaller.

## 4.1 Predictions

In this work we focus on the weakly-interacting Bose gas, and more precisely the crossover between the ideal Bose gas (IBG) and the quasi-condensate (qBEC). In the homogeneous system, a certain number of analytical calculations can be carried out deep in both asymptotic regimes, as published by Isabelle Boucouse and co-workers in [18]. For comparison with the experiment we then apply the local density approximation (LDA, see below) and consider the effect of a finite optical resolution on the correlation map.

### 4.1.1 Predictions for the homogeneous gas

#### General form of $\mathcal{G}(k, k')$

Consider a uniform gas of 1D bosons, interacting via repulsive short-range interactions in a box of length  $L$ . As a reminder, in the grand-canonical ensemble the hamiltonian of the system reads:

$$\hat{\mathcal{H}} = -\frac{\hbar^2}{2m} \hat{\Psi}^\dagger \frac{\partial^2}{\partial z^2} \hat{\Psi} + \frac{g}{2} \hat{\Psi}^\dagger \hat{\Psi}^\dagger \hat{\Psi} \hat{\Psi} - \mu \hat{\Psi}^\dagger \hat{\Psi}, \quad (4.2)$$

$\hat{\Psi}^\dagger, \hat{\Psi}$  being field operators satisfying the bosonic commutation relations, and  $g$  the effective coupling constant. The density of the system is fixed by temperature  $T$  and chemical potential  $\mu$ .

In real space, the (non-normalised) first and second order correlation functions of the (bosonic) field  $\hat{\psi}$  are defined by:

$$G_1(z_1, z_2) = \langle \hat{\Psi}^\dagger(z_1) \hat{\Psi}(z_2) \rangle \quad (4.3)$$

$$G_2(z_1, z_2, z_3, z_4) = \langle \hat{\Psi}^\dagger(z_1) \hat{\Psi}(z_2) \hat{\Psi}^\dagger(z_3) \hat{\Psi}(z_4) \rangle \quad (4.4)$$

Since the momentum distribution  $\langle n(k) \rangle$  is the Fourier transform of  $G_1(z_1, z_2)$ ,  $\mathcal{G}(k, k')$  according to definition 4.1 becomes:

$$\mathcal{G}(k, k') = \frac{1}{L^2} \iiint_0^L d^4 z e^{-ik(z_1-z_2)} e^{-ik'(z_3-z_4)} [G_2(z_1, z_2, z_3, z_4) - G_1(z_1, z_2) G_1(z_3, z_4)]. \quad (4.5)$$

### Quasi-condensate regime: Luttinger liquid approach

In the qBEC phase, where the correlation length  $l_\phi$  of  $G_1$  is much smaller than the system size  $L$ ,  $\mathcal{G}(k, k')$  can be decomposed into a singular term and a regular term [18]:

$$\mathcal{G}(k, k') = (\langle \hat{n}_k \rangle + \langle \hat{n}_k \rangle^2) \delta_{k, k'} + \tilde{\mathcal{G}}(k, k'). \quad (4.6)$$

The regular term  $\tilde{\mathcal{G}}(k, k')$  arises from momentum exchanges in the interacting gas and therefore vanishes in the IBG.  $\langle \hat{n}_k \rangle$  is the shot noise contribution and  $\langle \hat{n}_k \rangle^2$  the bosonic bunching term, both diagonal. This shows that contrary to real space, bosonic bunching remains in momentum space in the qBEC. An analytical expression can be found for the regular term in the limit where low-energy excitations dominate (which is the case in a qBEC). The Hamiltonian then reduces to the so-called Luttinger liquid Hamiltonian [27]:

$$\mathcal{H}_{\mathcal{L}} = \frac{g}{2} (\delta \hat{\rho})^2 + \frac{\hbar^2 \rho}{2m} (\partial_z \hat{\phi})^2, \quad (4.7)$$

$\delta \hat{\rho}$  and  $\hat{\phi}$  being canonically conjugate and representing the density operator and the phase operator respectively. The density fluctuations being small (in real space) in the qBEC regime, they can be neglected for the calculation of  $G_1$  and  $G_2$  as long as the considered relative distances are larger than  $\xi$ , the density correlation length. As a reminder (more details can be found in Chapter 1) the correlation function  $G_1$  takes the exponentially decaying form

$$G_1(z_1, z_2) = \rho e^{-|z_1 - z_2|/2l_\phi}. \quad (4.8)$$

$l_\phi = \hbar^2 \rho / (mk_B T)$  is the phase correlation length, and the corresponding (via Fourier transformation) momentum mode occupation numbers are Lorentzian:

$$\langle \hat{n}_k \rangle = \frac{4\rho l_\phi}{1 + (2l_\phi k)^2} \quad (4.9)$$

In addition, the two-body correlations  $G_2$  can be expressed in terms of first-order correlations only according to:

$$G_2(z_1, z_2, z_3, z_4) = \frac{G_1(z_1 - z_2)G_1(z_3 - z_4)G_1(z_2 - z_3)G_1(z_1 - z_4)}{G_1(z_1 - z_3)G_1(z_2 - z_4)} \quad (4.10)$$

The substitution of the above forms of  $G_1$  and  $G_2$  into 4.5, leads, by identification of the regular term, to:

$$\tilde{\mathcal{G}}(k, k') = \frac{l_\phi}{L} (\rho l_\phi)^2 \mathcal{F}(2l_\phi k, 2l_\phi k'), \quad (4.11)$$

$\mathcal{F}$  being a dimensionless function expressed by

$$\mathcal{F}(q, q') = \frac{256[(q^2 + 3qq' + q'^2)qq' - 2(q^2 - qq' + q'^2) - 7]}{(q^2 + 1)^2(q'^2 + 1)^2[(q + q')^2 + 16]}. \quad (4.12)$$

The regular part of the correlations is mainly negative (see figure 4.1), and can be thought of as a reduction of the total correlations to compensate the positive bunching which remains in momentum space although greatly reduced in real space.  $\mathcal{F}$  decays to zero on a typical distance of the order of the inverse phase coherence length  $kl_\phi \sim 1$ .

The validity of this expression relies on the negligible nature of the density fluctuations in the system, or in other terms, that the temperature  $T$  is much lower than the crossover temperature  $T_{CO}$ .

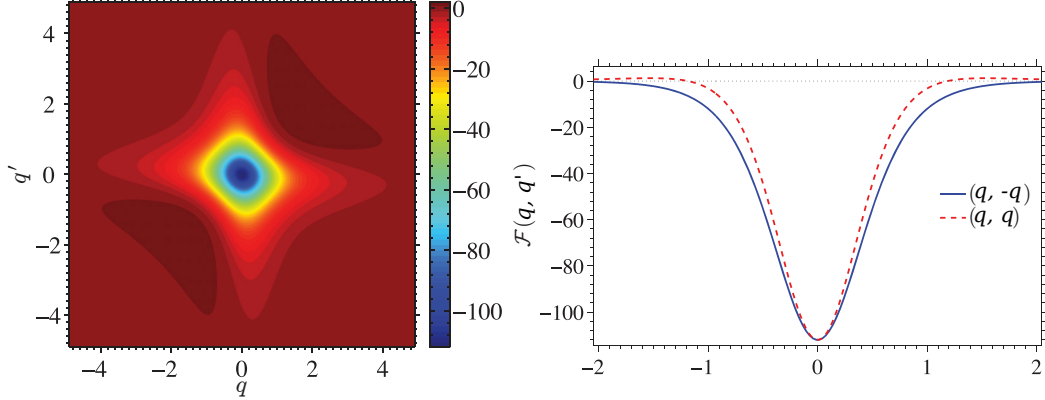


**Figure 4.1:** Left: regular part of the two-body correlations in momentum space, deep in the qBEC regime. It is defined negative, thus partly compensating the positive contribution of bosonic bunching still present in momentum space and is spread over an area of typical size  $1/l_\phi^2$ , which is the typical length scale of the  $G_1$  function. Right: cuts along the diagonal and antidiagonal. Adapted from [18].

### True condensate vs quasi-condensate behaviour

The general form of the expected momentum correlations is very different if one has phase coherence over the whole length of the system. However, some reminiscent features of true long range are present in the computed regular function.

For a one-dimension Bose gas at  $T = 0$ , the first-order correlations  $G_1$  decay algebraically rather than exponentially, as:

$$G_1 \approx (\xi/|z_1 - z_2|)^{\sqrt{\gamma}/2\pi}, \quad (4.13)$$

with a corresponding exponentially large correlation length  $l_{\phi,0} \approx \xi e^{2\pi/\sqrt{\gamma}}$ . This algebraic decay remains as long as  $|z|$  is smaller than the thermal phonon wavelength, which we assume here to retain true long-range order and use Bogoliubov theory to predict the form of the momentum correlations in the system, as was done in [106]. Here I just give the main results, for details of derivation please refer to the original publication.

In a true BEC, the correlation function  $\mathcal{G}(k, k')$  is non-zero for  $k = k'$  and  $k = -k'$  only. On the diagonal, the correlations are the bunching term for an IBG:

$$\mathcal{G}(k, k') = (\langle n_k \rangle + \langle n_k \rangle^2) \delta_{k,k'} \quad (4.14)$$

with the occupation numbers  $\langle n_k \rangle$  given by:

$$\langle n_k \rangle = (1 + 2n_{k,bogo}) \frac{E_k + g\rho}{2\epsilon_{k,bogo}} - \frac{1}{2}. \quad (4.15)$$

$\epsilon_{k,bogo}$  is the Bogoliubov dispersion relation,  $n_{k,bogo}$  the occupation numbers of the Bogoliubov modes, and  $E_k$  the free particle dispersion relation. For opposite momenta,  $\mathcal{G}(k, -k)$  reads

$$\mathcal{G}(k, -k) = (1 + 2n_{k,bogo}) \left( \frac{g\rho}{2\epsilon_{k,bogo}} \right) \quad (4.16)$$

At zero temperature, correlation between opposite momenta is maximal, due to the creation of pairs of excitations in the Bogoliubov vacuum (the quantum depletion of the condensate). For high-energy particle modes, opposite momenta are less correlated with increasing temperature due to thermal depletion of the condensate.

In the qBEC,  $l_\phi \ll L$  and the previous statements no longer hold. However remnants of opposite momenta correlations are present in the structure of  $\tilde{\mathcal{G}}$ . By dividing the system of length  $L$  into small slices where the phase is homogeneous, one can apply the Bogoliubov approach to each independent domain. Consider the normalised regular part of the two-body correlation function:

$$\tilde{g}^{(2)}(k, k') = \frac{\tilde{\mathcal{G}}(k, k')}{\langle \hat{n}_k \rangle \langle \hat{n}_{k'} \rangle} \quad (4.17)$$

Which can also be written in terms of the previously defined regular part of the correlation function:

$$\tilde{g}^{(2)}(k, k') = \frac{l_\phi}{L} (1 + (2l_\phi k)^2) (1 + (2l_\phi k')^2) \frac{\mathcal{F}((2l_\phi k), (2l_\phi k'))}{16}. \quad (4.18)$$

One recovers positive correlations around the anti-diagonal, scaling with  $l_\phi/L$  and thus gaining in importance as phase coherence appears over distances of the order of the system size  $L$ .

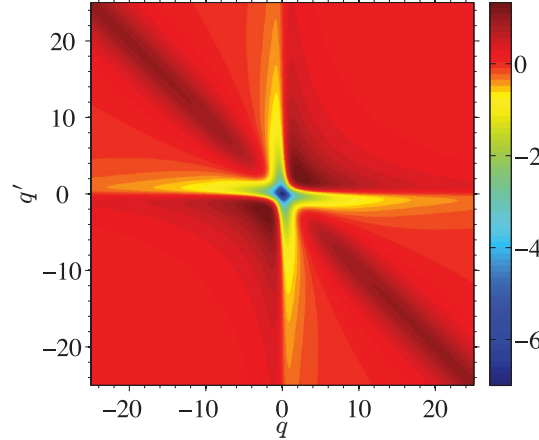


**Figure 4.2:** Normalised regular part of the correlation function,  $\tilde{g}^{(2)}(k, k')$ . A positive anti-diagonal is revealed by the normalisation of the correlation function, feature which arises from local phase coherence in the system like what is expected for a system with true long range order (although in the latter the amplitude of these anti-correlations is much larger relative to the positive term).

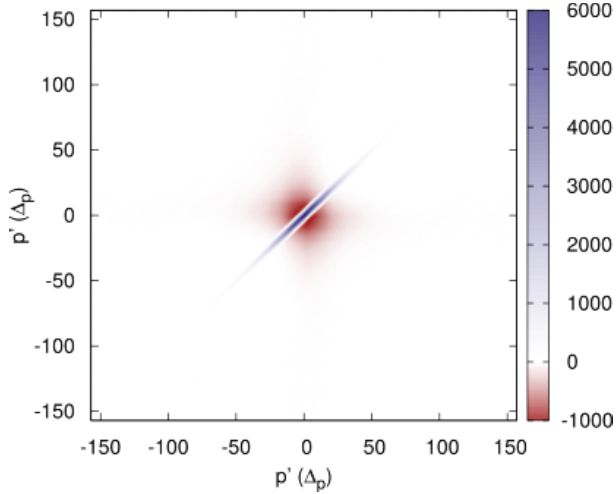


**Figure 4.3:** Example of a QMC simulation of a gas on the quasi-condensation crossover, in a trap (using the local density approximation). The two contributions to the momentum correlations are clearly visible: a bunching term on the diagonal (the width of the diagonal is finite because the trap imposes a system size  $L$ ), and a negative regular contribution.

### Quantum Monte Carlo on the crossover

In general, there is no analytical formula available for momentum correlations of a repulsive 1D Bose gas. Over the crossover, when neither of the asymptotic predictions are expected to hold, we turned to Quantum Monte Carlo simulations performed by our colleague Tommaso Roscilde from ENS de Lyon. Starting from a certain configuration computed with the stochastic series expansion, a so-called directed-loop algorithm is implemented. More precisely, to compute the  $g^{(1)}$  function (and equivalently the momentum distribution), a so-called "worm" is introduced in the following manner.

After generating a certain configuration with a stochastic series expansion (SSE), a particle is created on site  $i$  with the operator  $a_i^\dagger$  (also referred to as the tail of the worm), later destroyed with  $a_i$  (the head of the worm). The directed-loop algorithm moves the head (or the tail) away from the tail (respectively the head). Some SSE configurations where both  $a_i^\dagger$  and  $a_j$  (where  $j \neq i$ ) are present are generated, thus contributing to  $g^{(1)} = \langle a_i^\dagger a_j \rangle$ . In other terms, the head and the tail of the worm move away from each other spatially, with  $g^{(1)}$  the probability distribution of the distance between head and tail.

Now, to compute  $\mathcal{G}(k, k')$  one needs to evaluate the double Fourier transform of  $\langle a_i^\dagger a_j a_l^\dagger a_m \rangle$ . To sample this four-point quantity a double worm, with two heads ( $a_i^\dagger$  and  $a_l^\dagger$ ) and two tails ( $a_j$  and  $a_m$ ) is required. This was programmed by our colleague Tommaso. An example of a computed momentum correlation map is shown above (figure 4.3).

These simulations are performed in the local density approximation to take into account the trapping potential. However, for the analytical considerations above the gas was assumed homogeneous. To compare these previous calculations to experimental results the external (slowly-varying) trapping potential needs to be taken into account.

This is done in the local density approximation. The finite resolution of our measurements also affect the form of the measured correlations. These two effects are accounted for and detailed in the following section.

#### 4.1.2 Effects of an external trapping potential and finite resolution

##### Trapped gas in the local density approximation

As shown above, the momentum correlations can be written as the sum of three contributions (in terms of momentum  $p = \hbar k$  as probed in the experiment):

$$\langle \delta n_p \delta n_{p'} \rangle = S(p, p') + B(p, p') + \langle \delta n_p \delta n_{p'} \rangle_{reg} \quad (4.19)$$

$S(p, p')$  labels the shot noise contributions and  $B(p, p')$  the bunching term. In a trap, for a given  $p$  contributions from different regions of the confinement (and therefore different densities) to  $n_p$  need to be taken into account. The local density approximation relies on a small phase correlation length  $l_\phi$  compared to the system size  $L$ . If  $\nu_{\rho(z)}^{(h)}((p+p')/2)$  is the momentum distribution of a homogeneous gas of density  $\rho(z)$ , the complete bunching term in the LDA is expressed as an integral over the local bunching term  $\langle \nu_{\rho(z)}^{(h)}(p) \rangle^2 \delta(p - p')$  and yields (see Appendix A for more details on the derivation):

$$B(p, p') = \left| \frac{1}{\hbar} \int dz \langle \nu_{\rho(z)}^{(h)}((p+p')/2) \rangle e^{i(p-p')z/\hbar} \right|^2 \quad (4.20)$$

The width of  $B(p, p')$  is of the order of  $\hbar/L$ . For a condensate length of about  $100 \mu\text{m}$  and a resolution in momentum space (see next section) of  $\Delta_p/\hbar \approx 0.15 \mu\text{m}^{-1}$ , we cannot resolve the structure inside the diagonal and we write the bunching term as a singular function

$$B(p, p') \approx \delta(p - p') \mathcal{B}(p), \quad (4.21)$$

$\mathcal{B}$  being  $2\pi\hbar \int dz \langle \nu_{\rho(z)}^{(h)}(p) \rangle^2$ . Generally the shot-noise term can be neglected since we consider highly-degenerate gases, so the only remaining term to evaluate in the local density approximation is the regular function. Again, the result is an integration over the local contribution of a homogeneous gas of density  $\rho(z)$ , in this case expressed by the dimensionless function  $\mathcal{F}$ . Along with dimensional analysis to determine the prefactor, one finds:

$$\langle \delta n_p \delta n_{p'} \rangle_{reg} = \int dz \frac{l_\phi^3 \rho^2}{(2\pi\hbar)^2} \frac{\mathcal{F}\left(\frac{2l_\phi p}{\hbar}, \frac{2l_\phi p'}{\hbar}; t, \gamma\right)}{8}. \quad (4.22)$$

Here  $l_\phi$  is  $z$ -dependent via  $\rho(z)$ . Details of derivation can be found in Appendix A.

For comparison with the experiment, one finally needs to take into account the finite imaging resolution on our experiment, together with the pixelisation due to the camera. These both affect the form of the measured correlations  $\mathcal{G}(p, p')$

### Convolution with the imaging response function

In the experiment, the accessible quantity is a number of atoms in a given pixel (indexed by integer  $\alpha$ ) <sup>2</sup>  $N_\alpha = \int dp n(p) \mathcal{A}(\alpha, p)$ .  $\mathcal{A}(\alpha, p) = \int_{\Delta_\alpha} dq e^{-(p-q)^2/(2\delta^2)} / (\delta \sqrt{2\pi})$  is the contribution of an atom in  $p$  to the signal in pixel  $\alpha$ , function of width  $\delta$  integrated over a pixel  $\Delta_\alpha$ . Pixel  $\Delta_\alpha$  has a size  $\Delta_p$  in momentum space, which depends on the focussing time  $\tau$  and the pixel size in real space  $\Delta_z$ , via:  $\Delta = m\Delta_z/\hbar\tau$ . For the data presented here,  $\tau = 25$  ms, and  $\Delta_p/\hbar = 0.15 \mu\text{m}^{-1}$ .

The discretised correlation map  $\langle \delta N_\alpha \delta N_\beta \rangle$  is then:

$$\langle \delta N_\alpha \delta N_\beta \rangle = \int dp dp' \mathcal{A}(\alpha, p) \mathcal{A}(\beta, p') \langle \delta n_p \delta n_{p'} \rangle. \quad (4.23)$$

Typically in the following  $\delta \approx \Delta_p/\hbar$ . Unlike in Chapter 3,  $\delta$  is a width in momentum space, related to the width to the width of the response function in real space by  $\delta/\hbar = \delta_z m / (\tau_f \hbar)$ . With these two experimental artefacts (trap and finite resolution) taken into account, we can now turn to the experimental results and their comparison with the expected correlations.

#### Summary

- The two-body correlation function  $\mathcal{G}(k, k')$  can be analytically calculated in the asymptotic regimes (IBG and qBEC).
- It contains a singular positive bunching term (the only non-vanishing contribution in the IBG), and a regular negative contribution stemming from momenta exchanges in the interacting phase.
- In general  $\mathcal{G}(k, k')$  needs to be numerically evaluated and numerics reveal both bunching and regular contributions.
- In order to compare the theoretical predictions to experimental data, the effect of the external trapping potential and the finite resolution are taken into account.

## 4.2 Experimental results

We measured correlations in momentum space over the quasi-condensation crossover, and present three data sets: one in the IBG phase, one deeply qBEC and finally an intermediate set of data on the crossover to illustrate that the measured features vary continuously over the smooth change from a non-interacting gas to the interacting qBEC.

### 4.2.1 Experimental protocol and data analysis

Each of the presented data sets consists of about 50 shots in momentum space, along with calibration data taken in real space to determine the thermodynamic quantities

---

<sup>2</sup>All pixels are identical, the index  $\alpha$  is necessary later when the correlations  $\langle \delta N_\alpha \delta N_\beta \rangle$  are considered.

and the position in the phase diagram of the samples, as explained in Chapter 3. For these experiments the longitudinal frequency was  $\omega_z/(2\pi) = 7$  Hz, and the transverse frequency  $\omega_\perp = 1.9$  kHz. Over the course of a measurement sequence, shot-to-shot atom number fluctuations range from 4% for the highest densities to about 40% for the lower densities. With a pixel size in the imaging plane of  $\Delta = 2.7 \mu\text{m}^3$ <sup>3</sup> and a time of flight  $\tau$  of 25 ms, the pixel size in momentum space is  $\Delta_p/\hbar = 0.15 \mu\text{m}^{-1}$ . The 50 shots in momentum space are measured using the focussing method which assures that we truly measure the velocity distribution of our sample. Averaging over the data set, the mean momentum distribution  $\langle N_\alpha \rangle$  is deduced and for each shot we compute the quantity  $\delta N_\alpha = N_\alpha - \langle N_\alpha \rangle$ .

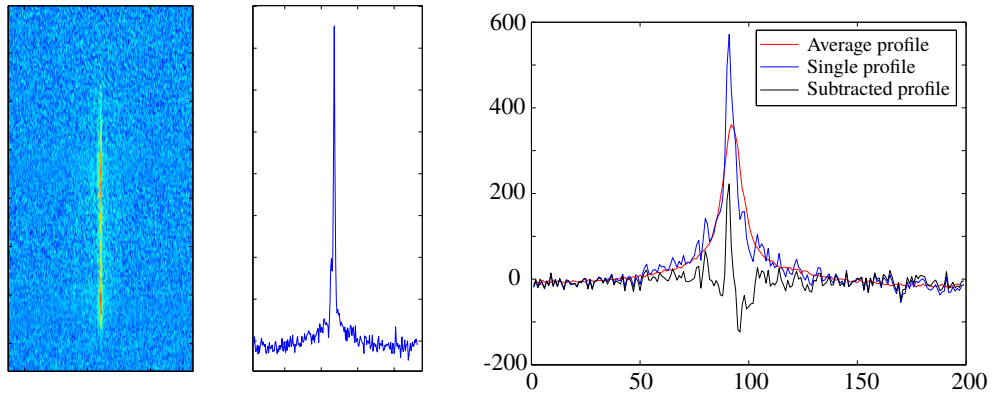


**Figure 4.4:** A single shot of momentum distribution: on the very left the absorption imaging signal, and the corresponding integrated distribution (middle), of lorentzian shape as expected. On the right,  $\delta N_\alpha$  is shown in black, as the difference between the single shot profile (blue) and the mean profile (red).

The mean correlation matrix  $\langle \delta N_\alpha \delta N_\beta \rangle$  is then deduced for data sets in different regions of the phase diagram.

#### 4.2.2 Presentation of the three data sets

We label the three data sets A, B and C, and their position in the phase diagram is shown below (figure 4.5).

Data A is in the IBG regime, with a measured temperature of 144 nK (with an accuracy of about 20 %), and a peak density of 50 atoms per pixel ( $1.8 \cdot 10^7 \text{ m}^{-1}$ ). The density fluctuations are in agreement with the temperature extracted from fitting the profile with the Modified Yang Yang equation of state (figure 4.6).

Data C lies deep in the qBEC regime, with a measured temperature of about 75 nK (according to density fluctuations) and a peak density of 250 atoms per pixel (or  $1 \cdot 10^8 \text{ m}^{-1}$ ). Profile thermometry yields a higher temperature of 100 nK, however with the

<sup>3</sup>These measurements were made with the older imaging system.

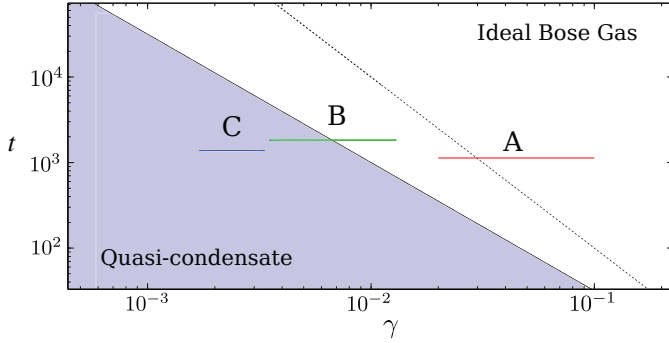


**Figure 4.5:** The three data sets presented in this chapter. Data A is in the so-called degenerate IBG regime, where atoms don't interact and strongly bunch. Data C is far in the qBEC regime, while data B is on the smooth crossover between A and C. This figure is a zoom of the complete phase diagram which was introduced in Chapter 1.

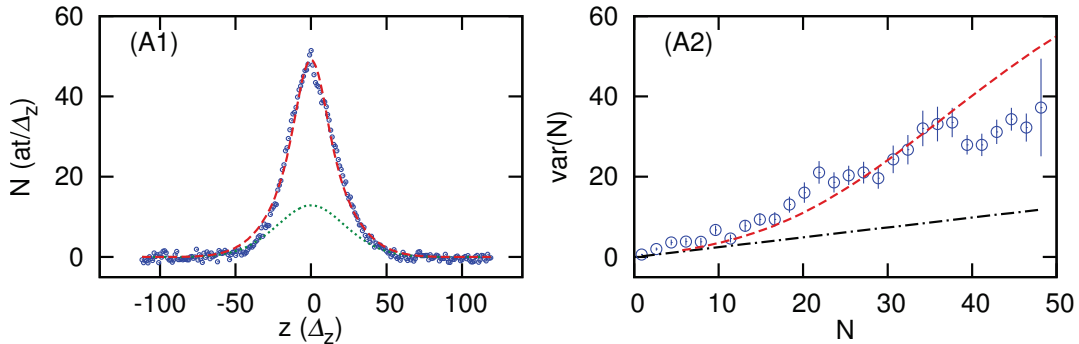


**Figure 4.6:** Calibration measurements of data A. The density fluctuations do not saturate at high densities which is a signature that the sample lies in the IBG regime. The shot noise level shown in dash-dotted line is well below the level of density fluctuations indicating that the sample is indeed highly degenerate.

rather small wings of the Yang Yang profile the fluctuation temperature is more reliable and perfectly fits with the qBEC equation of state  $\mu = g\rho$ <sup>4</sup>.

For data B, with the same methods as previously, we measure a temperature around 144 nK, and a peak density of  $5 \cdot 10^7 \text{ m}^{-1}$ .

### 4.2.3 Measured correlation maps for each set of data

#### Correlations for data A - IBG

In this regime, the measured momentum correlations  $\langle \delta N_\alpha \delta N_\beta \rangle$  are essentially positive and diagonal, in very good agreement with the expected theoretical correlations. The non-zero correlations in the rest of the plane are much smaller than the signal on the diagonal. The results are consistent with what is expected for the trapped IBG in the grand-canonical ensemble: since the single-particle states have well-defined momenta, correlations of the diagonal are vanishing. The grand-canonical description holds since each pixel can be considered independently (in other terms  $\hbar/L \ll \Delta_p \ll \hbar/l_\phi$ ) and for each pixel the rest of the cloud acts as a reservoir. The question of correlations in the

<sup>4</sup>We also suspect that the sample is not in thermal equilibrium since the system is close to integrable, and relate this discrepancy to a dissipative evaporation mechanism detailed in Chapter 5.

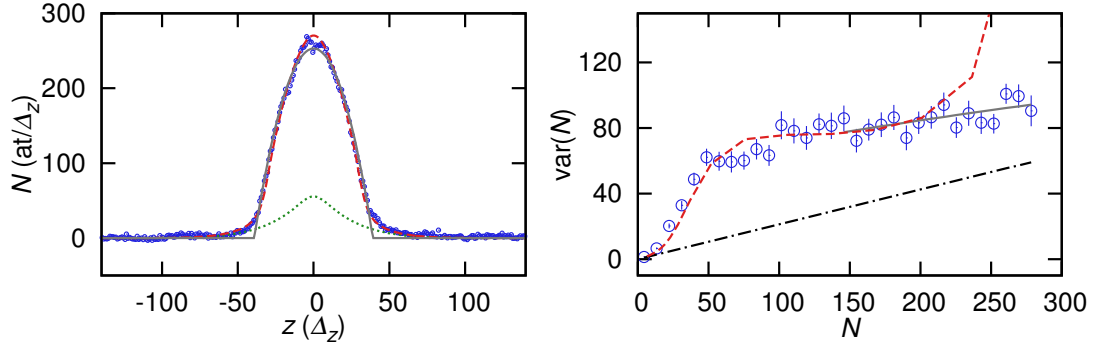


**Figure 4.7:** Calibration measurements of data C. Density fluctuations saturate at high densities and follow the prediction from the Thomas-Fermi equation of state, which gives us a temperature measurement with good precision. On the other hand, the profile fitting with the Yang-Yang equation of state is expected to be less reliable since the wings can barely be distinguished from the zero-temperature Thomas-Fermi profile (solid line).

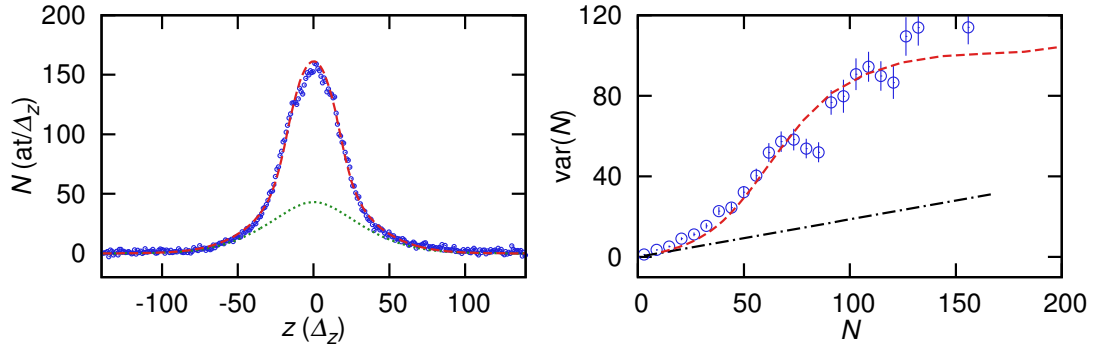


**Figure 4.8:** Calibration of data B. The onset of saturation in the density fluctuations indicate that data B lies on the crossover between an IBG and a qBEC.

canonical ensemble where atom number is fixed is considered in section 4.3.1.

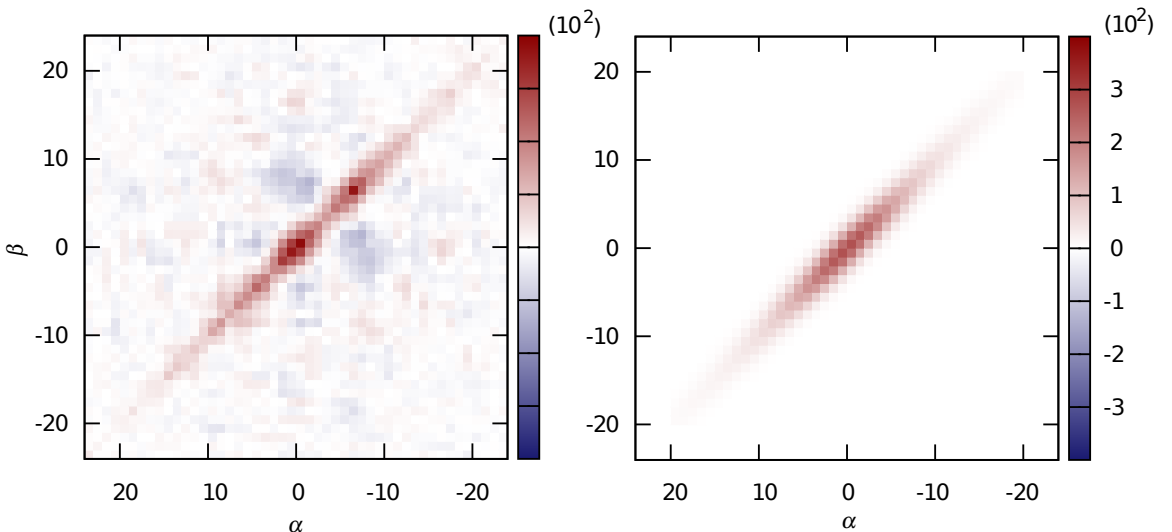


**Figure 4.9:** Correlations maps in the IBG: measured (left) compared to the IBG theory (right).

For more quantitative comparison, we plot the diagonal cuts of the correlation maps

(figure 4.10). Agreement is fairly good despite the relatively low signal for the low densities of this experimental condition.

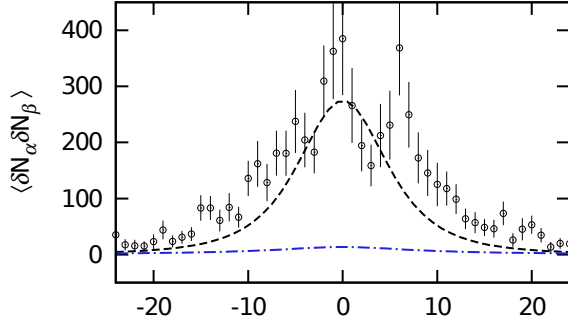


**Figure 4.10:** Cut along the diagonal of the measured data (circles) and the theory (dashed line). The shot noise level is represented as the blue dash-dotted curve which lies well below the measured signal.

### Quasi-condensate: Data C

In the qBEC regime, we observe the expected regular negative contribution (figure 4.11). The experimental data qualitatively fits the expected correlation map computed from theoretical predictions: positive correlations remain on the diagonal while a negative regular part appears off the diagonal. The pixelisation of the data alters the qualitative form of the correlations: in this regime  $l_\phi$  is so large that the momentum distribution is only spread over several pixels, making the shape of the correlations barely recognisable compared to section 4.1.1. Again, for a more qualitative comparison than colourmaps, cuts along the diagonal and anti-diagonal are represented (figure 4.12).

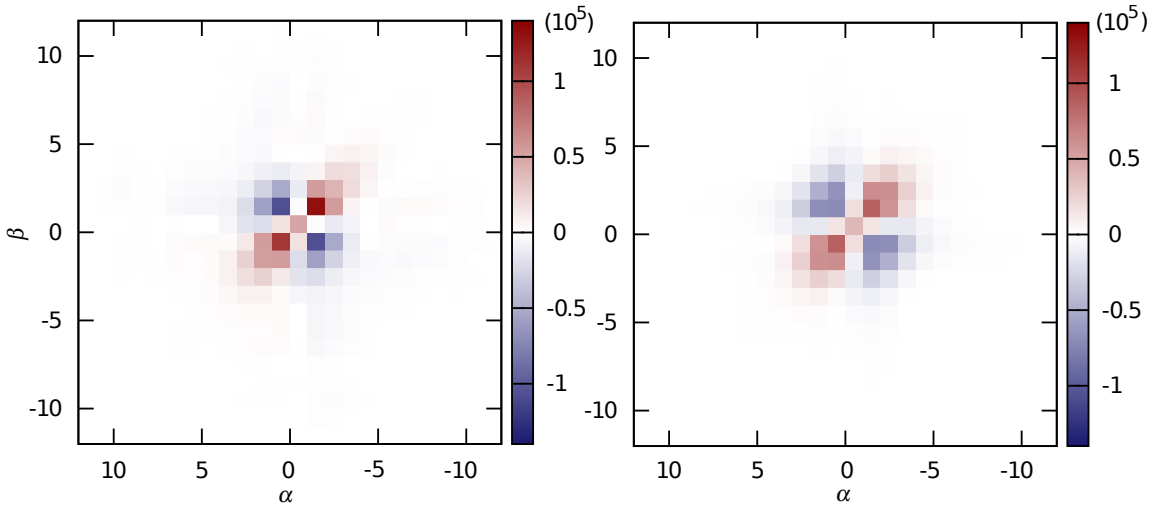


**Figure 4.11:** Experimental correlation map (left) and theoretical correlation map. Qualitatively the agreement is good.

Atom-number fluctuations are strongly reduced in the qBEC regime because of repulsive interactions, as can be seen on the calibration figure (where density fluctuations saturate at high densities). However in momentum space bunching remains: the curves lie well above the shot-noise limit (figure 4.12). The negative contribution

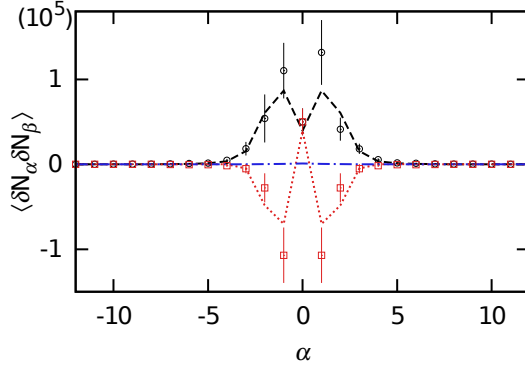


**Figure 4.12:** Cuts along the diagonal and anti-diagonal directions for experimental data (circles) and theory. The agreement is again very satisfying, given the resolution of the measurement. The blue dashed-dotted curve give the shot noise limit.

$\mathcal{F}$ , spread over a region  $\hbar/l_\phi$ , reduces the total fluctuation signal and is thus a consequence of the repulsive interactions which drive the quasi-condensation crossover. The situation is very different from the case of a system with true long range order. This measurement is the first experimental proof that bunching remains in momentum space. The very good agreement with the theoretical regular contribution is ensured by the fact that  $\langle \delta n_p \delta n_{p'} \rangle$  is dominated by contributions from the central region of the cloud where  $l_\phi$  is the largest, as extensively discussed in section 4.3.1. It is well described in the grand-canonical ensemble since the rest of the cloud acts as a reservoir, and the measured correlations are much smaller than those expected from the renormalisation by total atom number.

### On the crossover: Data B

The difference between the IBG data and qBEC data is striking: first of all in the IBG correlations are only on the diagonal and positive, whereas negative regions appear in the qBEC off the diagonal, and secondly the correlations spread over a much smaller region in the qBEC because the momentum distribution is much thinner. The crossover from an IBG to a qBEC is smooth and in the third set of data, the slow change from the IBG to qBEC is visible. Negative regions start to appear around the anti-diagonal, signature of the appearance of repulsive interactions in the system. The positive diagonal remains, and the area of the correlation region is intermediate, larger than data C in the qBEC but thinner than data A. This is because  $l_\phi$  slowly increases as one enters the qBEC regime. The experimental data is compared to QMC in the figure below (figure 4.13).

The agreement between data and QMC is more visible on the cuts of the diagonal and anti-diagonal as shown below. This excellent matching between data and numerics was not granted a priori because as mentioned above, the computation of this fourth-order quantity is challenging. Moreover, the numerical error performed needs to be very low in order to recover a reasonable uncertainty after binning and blurring the numerical data to match the experimental resolution: the washed-out physical structures are indeed much smaller than what can be probed experimentally.

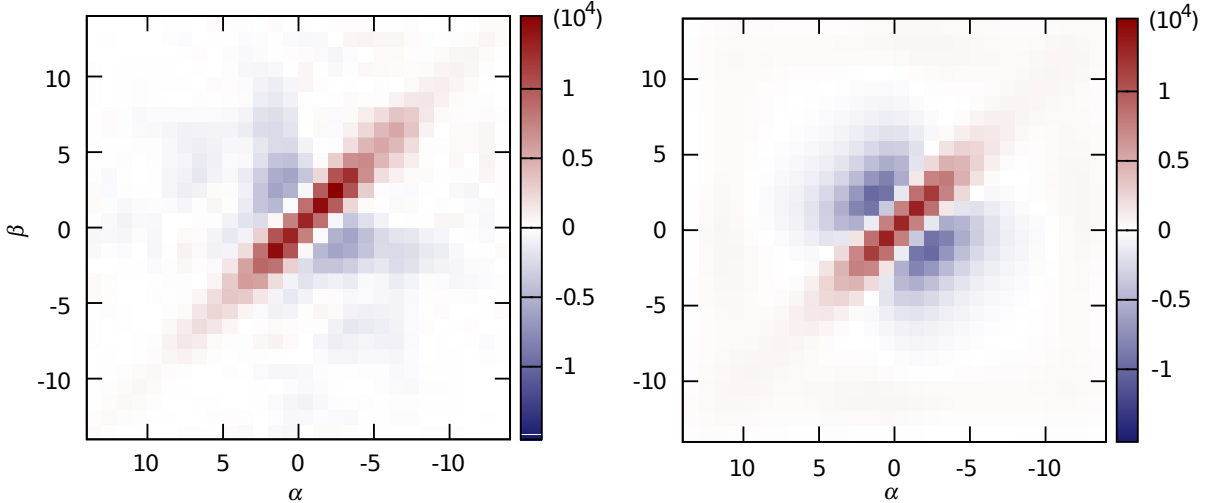


**Figure 4.13:** Comparison between the experimental (left) correlations with QMC simulations (right) for data B. Apart from an asymmetry on the experimental data, the agreement is excellent.

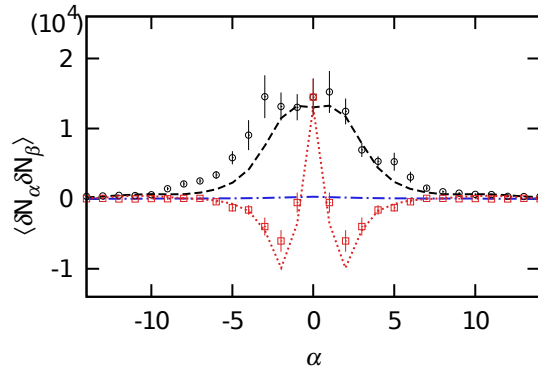


**Figure 4.14:** Diagonal and anti-diagonal of the above correlation maps, revealing very good agreement.

We measured the momentum correlations for three data sets over the crossover, and observed the onset of negative correlations off the diagonal as one reaches the qBEC regime. We also observed that the positive diagonal, namely the bunching contribution, remains in the qBEC in momentum space when it disappears in real space. We now attempt to describe these features of the crossover in a single quantity called  $C$ .

### A single intensive quantity to summarise the data

Because of the resolution of the measurements, the main structure of the correlations are washed out and the bunching contribution can no longer be distinguished from the regular (negative) contribution. For this reason we cannot measure the evolution of  $\mathcal{F}$  over the crossover for its characterisation. We thus considered the following experimental quantity:

$$C = \sum_{\alpha} \langle \delta N_{\alpha} \delta N_{-\alpha} \rangle / \langle N_0 \rangle \quad (4.24)$$

$C$  is an intensive quantity, and one can show that in the limits  $\delta, \Delta_p \gg \hbar/l_\phi$  and  $\delta \gg \Delta_p$ , only depends on  $t$  and  $\gamma_0$  ( $\gamma$  in the centre of the cloud). Proof of this is delegated to Appendix A, to focus on the main results. We found the following expressions in the asymptotic regimes of the phase diagram:

- In the degenerate IBG, the equation of state is  $\rho \approx k_B T \sqrt{m}/(\hbar \sqrt{2|\mu|})$ , and  $\nu_{\rho,T}^{(h)}(0) \approx \hbar\rho/(mk_B T)$ , and one finds:

$$C \approx 0.54 \frac{\hbar^2 \rho^2}{mk_B T} = \frac{1.08}{t\gamma_0^2} \quad (4.25)$$

- In the qBEC,  $\mu = g\rho$  and  $\nu_{\rho,T}^{(h)}(0) \approx 2\hbar\rho/(mk_B T)$  so that:

$$C \approx -1.14 \frac{\hbar^2 \rho^2}{mk_B T} = \frac{-2.28}{t\gamma_0^2} \quad (4.26)$$

We computed this newly defined intensive quantity for each of our data sets and plotted (figure 4.15) its values along with the asymptotic predictions.

The agreement is not so good. First of all, this is because the initial hypothesis ( $l_\phi \ll \hbar/\delta \ll \hbar/\Delta_p$ ) is not quite valid for this experiment. Moreover,  $C$  depends on the two intensive quantities  $\delta l_\phi/\hbar$  and  $\delta/\Delta_p$ . Since the resolution remains the same from one data set to another they correspond to different  $\delta l_\phi/\hbar$  so a quantitative comparison should be done cautiously.

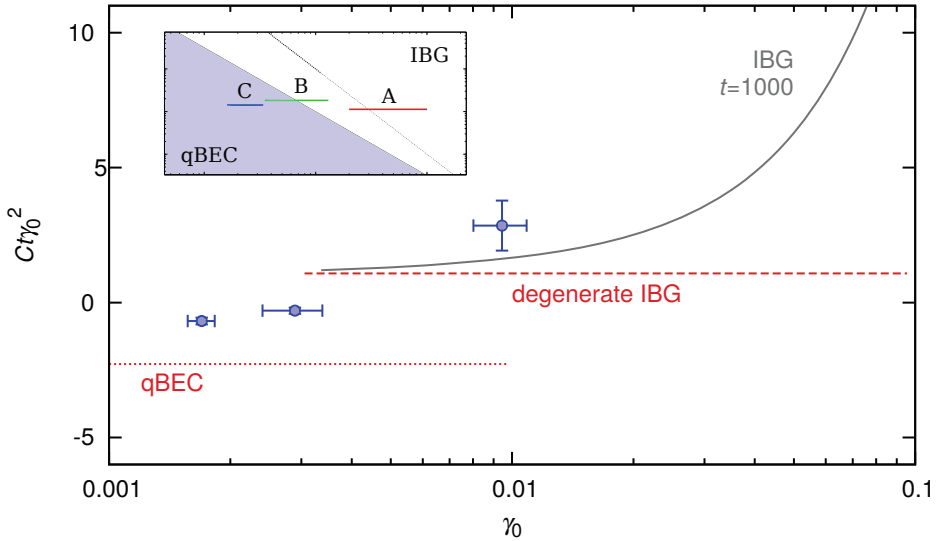


**Figure 4.15:**  $C$ -value plotted for the three data sets. Their position in the phase diagram is reminded in the inset. The calculated asymptotic values as well as the prediction for a classical Bose gas are plotted alongside. The agreement is not perfect, because the assumptions made to compute the asymptotic values of  $C$  are not reached, and moreover each data set has a different  $\delta l_\phi/\hbar$  which makes a direct comparison rather tricky.

### Summary

- We measured momentum correlations of three data sets realising the complete crossover from an IBG to a qBEC.
- For each data set agreement with analytical calculations or numerical simulations was quantitatively good.
- However the attempt at defining a single quantity to characterise the crossover (since a lot of information is lost in the experimental sampling) was not so conclusive.

## 4.3 Discussions

The presented correlation measurements are quite challenging from an experimental point of view because a number of precautions should be taken to rule out all possible artefacts on the measured signal. In particular, extra correlations could be introduced in the data analysis procedure. We found that for instance a small centre jitter could slightly change the results (although fortunately the centre is stable in our experiment, with a jitter of maximum two pixels). Our measurements were robust against changes in the data analysis method (like recentring the profiles, or normalising/ordering the atom number, etc.) which gave us confidence that the measured correlations were physical.

However the fact that the negative regions we observe are mainly related to the absence of true long-range in the system should be discussed to reinforce our statement. Firstly, we rule out the effect of normalising atom number in the data analysis, which introduces negative correlations but not enough to reproduce the experimental signal. Secondly, we return to the long-range order prediction and show that the Bogoliubov prediction in the canonical ensemble (and therefore with negative correlations present) do not match the measured correlations, to contrast with the results of [106].

### 4.3.1 Effect of normalising atom number

From an experimental shot to another, the total number of atom varies relatively from 4 to 40 % and these fluctuations are related to the preparation procedure. In the data analysis, we remove shot-to-shot atom number fluctuations to place ourselves in a fixed atom number ensemble, by renormalising each momentum profile to the mean atom number. This would be without effect on the momentum distribution if there were a scaling of the form  $n(p; N_1)/N_1 = n(p; N_2)/N_2$ . This is not the case since the width of the momentum distribution scales with  $1/\rho$ . The normalisation therefore introduces extra fluctuations, typically of the order of the variance of the atom number fluctuations in the given set of data. Normalising the profile is also expected to introduce negative correlations for large  $p - p'$  since the normalisation procedure especially affects the wings of the distributions. More importantly, by fixing the atom number and placing ourselves in the canonical ensemble, the total sum of the correlations  $\sum_{\alpha,\beta} \langle N_\alpha N_\beta \rangle$

vanishes. With a positive signal on the diagonal, negative correlations appear to compensate the positive ones, as soon as atom number is kept constant. In the following we estimate this last effect on our data.

### Homogeneous gas

We first consider a homogeneous gas confined in a box potential, of length  $L$ , and suppose that the momentum correlations are solely due to bosonic bunching. The effect of optical resolution is disregarded and we take  $\delta = 0$ , however keeping pixelised data (with a pixel size  $\Delta_p$ ). The number of momentum states in a given pixel is  $M = \Delta_p L / (2\pi\hbar)$  such that (with  $\Delta_p \gg \hbar/L$ ) the total atom number fluctuations fulfill

$$\langle \delta N_\alpha^2 \rangle = (\langle N_\alpha \rangle + \langle N_\alpha^2 \rangle) / M \ll \langle N_\alpha^2 \rangle. \quad (4.27)$$

Normalising the momentum distribution to  $N$  changes  $\langle N_\alpha \rangle$  to

$$\langle \tilde{N}_\alpha \rangle = \langle N_\alpha^2 \rangle + \langle \delta N_\alpha^2 \rangle - \frac{\langle N_\alpha^2 \rangle}{N} \sum_\beta \langle N_\beta^2 \rangle, \quad (4.28)$$

and the resulting momentum correlations are:

$$\langle \delta \tilde{N}_\alpha \delta \tilde{N}_\beta \rangle = \langle \delta N_\alpha^2 \rangle \delta_{\alpha,\beta} - \frac{\langle N_\alpha \rangle}{N} \langle \delta N_\alpha^2 \rangle - \frac{\langle N_\alpha \rangle \langle N_\beta \rangle}{N} \sum_\gamma \langle \delta N_\gamma^2 \rangle. \quad (4.29)$$

Just as to compute the  $\mathcal{F}$  function previously, as one replaces  $\langle \tilde{N}_\alpha \rangle$  by a Lorentzian of FWHM  $2\hbar/l_\phi$ , the resulting correlations can be written as a function of  $\mathcal{F}_n$ :

$$\langle \delta \tilde{N}_\alpha \delta \tilde{N}_\beta \rangle = \langle \delta N_\alpha^2 \rangle \delta_{\alpha,\beta} + (\Delta_p L / (2\pi\hbar))^2 \mathcal{F}_n(2l_\phi p/\hbar, 2l_\phi p'/\hbar) (\rho l_\phi^3 / N), \quad (4.30)$$

where

$$\mathcal{F}_n(q, q') = \frac{-64(1+q^2) - 64(1+q'^2) + 16(1+q^2)(1+q'^2)}{(1+q^2)^2(1+q'^2)^2}. \quad (4.31)$$

$\mathcal{F}_n$  is plotted figure 4.16, along with  $\mathcal{F}$  which are the expected negative correlations for a homogeneous qBEC in the grand-canonical ensemble. Although the two functions differ slightly in shape, it would be very difficult to distinguish between experimentally. They have the same integral and their central value  $q = q' = 0$  is identical.

In our experiment, the gas is trapped, which (fortunately) completely changes the picture.

### Inhomogeneous cloud

Here we show, despite the pessimistic estimations of the previous paragraph, that the measured negative correlations are not due to renormalisation effects. Indeed, in a trap the negative correlations are dominated by those introduced by the central region of the cloud where  $l_\phi$  is the largest, as shown by equation 4.22. Data C (in the qBEC regime) was newly analysed without the renormalisation procedure, and the result is shown in the left panel of figure 4.17. The result differs only slightly with the correlations

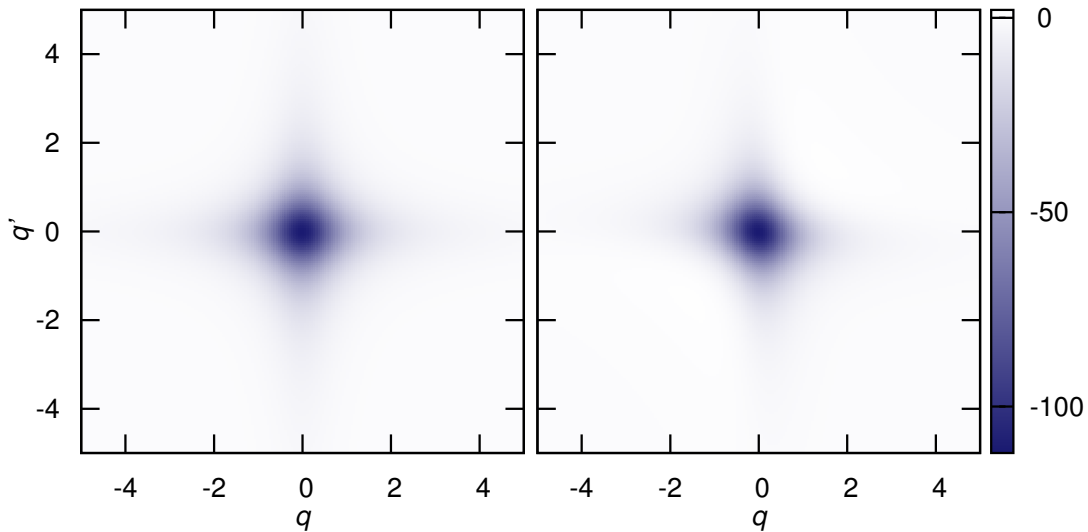


**Figure 4.16:** Function  $\mathcal{F}_n$  describing the effect of normalising all momentum distributions of a data set to an atom number  $N$ , for a homogeneous gas with bosonic bunching only.  $\mathcal{F}_n$  is different from  $\mathcal{F}$  (plotted right) since it is even in both  $q, q'$ , however both functions are very similar and given the resolution of the experimental data they would be difficult to distinguish in practice.

presented above. Finally, we bin and blur data A (in the IBG regime, and spread over a much larger number of pixels than data C), to reach the same  $\Delta_p l_\phi/\hbar$  as data C for quantitative comparison. Since this data lies in the IBG regime without normalisation only bunching on the diagonal would be present. We then analyse binned data A with atom-number normalisation and show the result in the right panel of figure 4.17.

We therefore conclude that the negative correlations measured in the qBEC do not arise from the normalisation procedure.

### 4.3.2 Contrast with true long-range order

At the beginning of this chapter we discussed the difference between expected correlations for true-long-order and a qBEC. As well as a positive diagonal and anti-diagonal, Mathey et al. predict negative correlations along  $k = 0$  and  $k' = 0$ . However these correlations are of different nature from those measured in our experiment. They arise from the conservation of particle number in their calculation and the presence of a positive diagonal (bosonic bunching) and anti-diagonal (pairs depleted from the condensate): in order for the total sum of correlations to vanish these negative correlations appear. To confirm the different nature of these correlations compared to our results and show that our observed negative correlations are truly a signature of the absence of long-range order, we took the situation of data C (the qBEC data), and computed the expected correlation map with the prediction of equation (62) from reference [106]. The resulting correlation map is shown figure 4.18.

For our experimental situations the temperature is high enough for  $l_\phi$  to be much smaller than the system size and prevent the absence of even quasi long-range order (when the temperature is low enough  $l_\phi$  may reach the system size). This is compatible

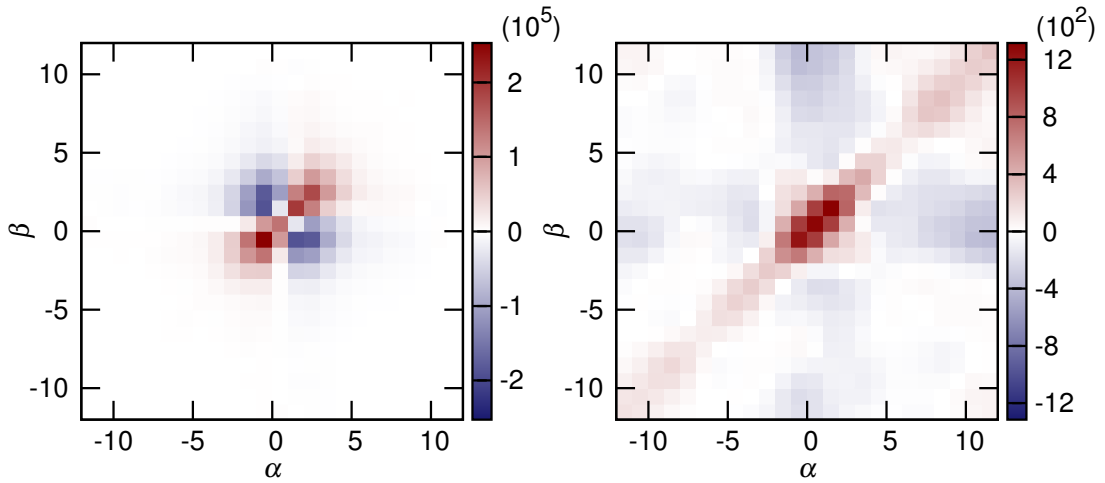


**Figure 4.17:** Left: data C analysed without renormalisation. The negative correlations are about as large in amplitude as the positive contribution. Right: data A binned to compare A and C on equal footing (with similar  $\Delta_p l_\phi / \hbar$ ). The normalisation procedure introduces negative correlations on the  $\alpha = 0$  and  $\beta = 0$  axis, however they remain much smaller in amplitude than the bunching contribution, contrary to the negative correlations on the left.

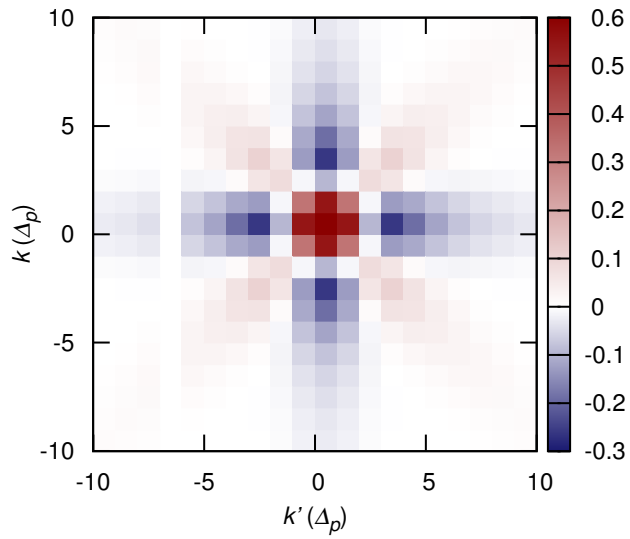


**Figure 4.18:** Correlation map expected from the results of [106]. Negative correlations come from the conservation of atom number. The result is qualitatively different from the shape of the measured correlations of data C, with positive correlations along the anti-diagonal and negative contributions along  $k, k' = 0$ .

with the fact that the results of Mathey and colleagues does not predict the correlations we measure.

**Summary**

- The fact that the measured negative correlations are solely a consequence of absence of long-range order in the experimental system should be taken with caution so we performed several checks to prove the robustness of our experimental observation.
- Firstly the effect of normalising atom number in the data analysis and forcing additional negative correlations in was ruled out.
- Secondly the prediction of true-long range order in the canonical ensemble (reference [106]) also predict negative correlations: they do not match the experimental correlations however.

# CHAPTER 5

---

## Non thermal states resulting from atom losses

---

In this chapter, a cooling mechanism via uniform atom loss in a one-dimensional Bose gas is considered. This scheme was proposed and demonstrated experimentally by colleagues in Vienna [65, 124]. Using classical field simulations, we show that such a mechanism indeed induces a reduction of energy in the excitations of the gas, but to a non-thermal state: modes of different energy are not "cooled" at the same rate. This is in agreement with some experimental observations of our setup. We relate the resulting cooling of the modes in the gas to its integrable nature: adding a perturbation which breaks the integrability destroys the non-thermal state resulting from atom loss. Finally, by taking into account the quantised nature of the field, the temperature decay is limited by long-wavelength fluctuations excited by the removal of atoms. We extend the classical field picture by modelling the system with a stochastic Gross-Pitaevskii equation, to modelise the discrete nature of the atomic field. All the work presented in this Chapter is ongoing: some conclusions or results are not complete and we are still investigating many aspects.

### 5.1 Context: cooling via uniform atom loss

#### 5.1.1 The cooling paradox of 1D gases

Evaporative cooling in atomic clouds allows to reach temperatures well below the limit of quantum degeneracy [87]. It relies on the removal, via a radio-frequency driving field or the lowering of an optical potential, of the most energetic atoms in the system, leaving the remaining particles to thermalise to a lower temperature by atomic collisions [102, 137]. Such a scheme reduces the temperature from the  $\mu\text{K}$  range to the  $\text{nK}$  range in a few seconds. In the one-dimensional magnetic traps engineered with atom chips, RF-induced evaporation lead to temperatures as low as  $\hbar\omega_{\perp}/10$  [79] on our experimental setup. However, the cooling mechanism in the one-dimensional regime remained unclear at the time of the publication of those results. Standard evaporative cooling indeed relies on energy selection, which is ruled out if all atoms lie in the ground state of the transverse trap. Moreover, since the one-dimensional gas is not ergodic, collisions between particles are not sufficient to redistribute the energy after removal of atoms and thermalise the system. As a side remark, an alternative cooling scheme leading to very low temperatures is reported in [112], but their system is not one-dimensional.

### 5.1.2 Origins of the dissipative cooling mechanism

#### Observations

The cooling process implemented in [124] relies on continuous outcoupling of atoms to an untrapped state by a radio-frequency transition. The atoms, in  $|F = 2, m_F = 2\rangle$ , are weakly driven into an untrapped Zeeman state, by setting the RF on resonance, at a low amplitude. Starting from a quasi-condensate (7000-10000 atoms, 30-100 nK, very similar to the experimental situations realised on our own setup), they slowly drive the atoms to remove them in an unselected manner, and probe the resulting temperature of the cloud. Performing experiments in different conditions, they showed that the data collapses, revealing a linear scaling between temperature and atom number:

$$\frac{T}{T_0} = \frac{N}{N_0} \quad (5.1)$$

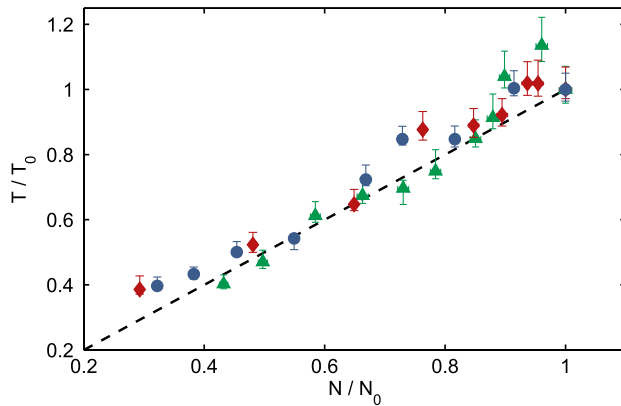


**Figure 5.1:** Scaling of temperature with atom number (taken from [124]). The proposed evaporation scheme leads to a linear scaling of temperature with the remaining number of atoms in the trap. The different curves correspond to different experimental situations: the blue circles are data with a colder initial temperature than the green triangles, and the red diamonds were acquired through a procedure where the atoms are outcoupled to a different untrapped state.

This type of scaling is not expected in conventional evaporation and the cooling proved very efficient, the reported temperatures being as low as  $k_B T / \mu \approx 0.25$ <sup>1</sup>.

#### Model

To attempt to explain how the cloud's temperature can be reduced by simple atom loss, one can consider the Luttinger liquid picture, where the elementary excitation modes are non-interacting phonons. Each of these modes contributes to the fluctuations of the gas through a phase and density quadrature, and the free evolution of each mode  $k$  is the rotation in phase space of the corresponding Wigner function at  $\omega_k$ . Essentially, by removing atoms from the gas, the energy in the density quadrature of each mode is reduced. Consequently, after many-body dephasing and redistribution of the energy with the phase quadrature, the energy of each phonon mode is reduced, leading to a

<sup>1</sup>This however is incompatible with the following statement in the theoretical publication [65]: if the discrete nature of the field is taken into account, the limiting temperature is  $k_B T = \mu$ , see below.

colder system. A similar linearised approach is introduced as the starting point of our study in 5.2.1.

The dissipation of atoms is represented by the addition of a loss term in the Gross-Pitaevskii equation:

$$i\hbar \frac{\partial \hat{\Psi}}{\partial t} = -\frac{\hbar^2}{2m} \frac{\partial^2}{\partial z^2} \hat{\Psi} - g \hat{\Psi}^\dagger \hat{\Psi} \hat{\Psi} - \mu \hat{\Psi} - i\hbar \frac{\Gamma}{2} \hat{\Psi} \quad (5.2)$$

Grišins and colleagues modelled this dissipative outcoupling of atoms, taking into account a quantum noise term  $\hat{\zeta}$  on top of the quasi-condensate wave-function evolution. This noise represents the quantisation of the atomic field, beyond the classical-field approach given by a Gross-Pitaevskii equation, thereby limiting the temperature to which the system can be cooled. In the absence of this term the scaling between temperature and atom number leads to an asymptotically vanishing temperature in the limit of very small atom numbers, while the limiting temperature in the presence of this term is  $k_B T_{min} = \mu$ . As an individual atom is removed from the cloud, low-energy excitations are induced, limiting the energy extraction of the dissipative mechanism.

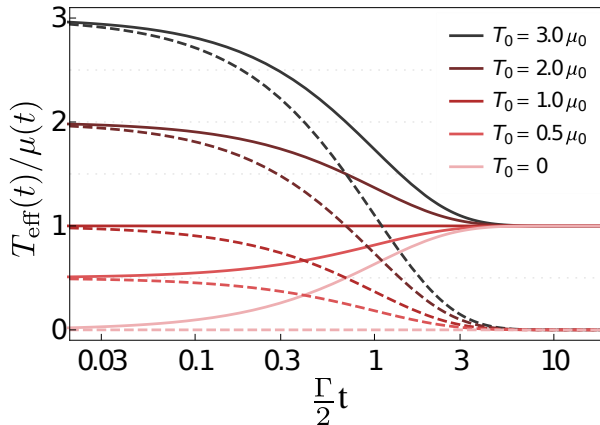


**Figure 5.2:** Temperature to chemical potential ratio for different initial temperatures (from [65]). The dashed lines represent the classical mean-field result, compared with the solid line prediction taking into account the quantised nature of the field. The asymptotic temperature is limited by low-energy excitations generated as atoms are outcoupled.

The authors of [65] emphasized results for low-energy excitations, since the associated experiment essentially probes those: they measure density fluctuations which develop from the initial phase fluctuations in their gas, after time of flight. This method is sensitive to long-wavelength modes.

### Summary

- Until recently, the mechanism by which one-dimensional Bose gases could be cooled down to temperatures as low as  $\hbar\omega_\perp/10$  was unclear. Conventional evaporative cooling based on energy selection is indeed inhibited in 1D.
- The dissipation mechanism proposed in [65, 124] convincingly leads to substantial cooling in such systems.

- This cooling mechanism, as we discuss later in this Chapter, is believed to occur on our own setup: we indeed reached comparable temperatures in very similar experimental conditions.

## 5.2 Emergence of non-thermal states: a classical field study

### 5.2.1 Toy model: linearised approach in homogeneous systems

The authors of the study presented in the section above speak of cooling in the "universal phonon limit", arguing that the Luttinger liquid picture accurately describes the observations of the experimental study in the sense that only low-energy excitations are relevant. However, this dissipative mechanism leads to an out-of-equilibrium state, since Bogoliubov modes of different energies are expected to suffer energy decay at different rates. In other words, the resulting temperature in the phononic limit should be different than the temperature of higher-energy excitations<sup>2</sup>. This can be shown using the following model, in the linearised Bogoliubov approach.

The uniform and constant dissipation is expressed as  $\hat{\Psi}(t) = \hat{\Psi}(0)e^{-\Gamma t/2}$ , where  $\hat{\Psi}$  designates the field operator of the one-dimensional quasi-condensate, and the density accordingly decreases like  $n(t) = n(0)e^{-\Gamma t}$ . We start from a phase-density representation of the field  $\hat{\Psi} = \sqrt{n}e^{i\hat{\theta}}$ . In the quasi-condensate, density fluctuations  $\delta\hat{n} = \hat{n} - n_0$  are small and phase fluctuations are of long wavelength, and the equations of motion can be linearised, as was presented in Chapter 1. Expanding  $\hat{n}(z)$  and  $\hat{\theta}(z)$  on sinusoidal modes:

$$\hat{\theta}(z) = \sum_{k>0} \sqrt{2} (\hat{\theta}_{c,k} \cos(kz) + \hat{\theta}_{s,k} \sin(kz)), \quad (5.3)$$

and similarly

$$\delta\hat{n}(z) = \sum_{k>0} \sqrt{2} (\hat{n}_{c,k} \cos(kz) + \hat{n}_{s,k} \sin(kz)). \quad (5.4)$$

$\hat{\theta}_{j,k}$  and  $\hat{n}_{j,k}$  are conjugate variables verifying the canonical commutation relation

$$[\hat{\theta}_{j,k}, \hat{n}_{j,k}] = \frac{i}{L} \delta_{j,j'} \delta_{k,k'} \quad (5.5)$$

and  $j$  an index designating the cosine or sine contributions to the sum. Each mode  $k$  then evolves independently according to the Bogoliubov Hamiltonian

$$H_{j,k} = L \left[ \left( \frac{g}{2} + \frac{\hbar^2 k^2}{8mn_0} \right) \hat{n}_{j,k}^2 + \frac{\hbar^2 k^2}{2m} n_0 \hat{\theta}_{j,k}^2 \right] \equiv E_n + E_\theta, \quad (5.6)$$

---

<sup>2</sup>In the following, for practical reasons, we will use the word "temperature" although the existence of a unique temperature to describe the gas is ruled out to start with.

at a frequency (we recover the previously encountered Bogoliubov dispersion relation):

$$\omega_k = \sqrt{\frac{\hbar^2 k^2}{2m} \left( \frac{\hbar^2 k^2}{2m} + 2gn_0 \right)} \quad (5.7)$$

In this linearised form, the effect of atom loss can be investigated for each mode separately. Consider a given mode of wavevector  $k$  and let us assume its temperature is large enough so that it can be treated classically. The distributions of  $\theta_{j,k}$  and  $n_{j,k}$  are thus Gaussian, and verify the equipartition relations

$$\frac{k_B T}{2} = \left( \frac{g}{2} + \frac{\hbar^2 k^2}{8mn_0} \right) \langle n_{j,k}^2 \rangle = \frac{\hbar^2 k^2}{2m} n_0 \langle \theta_{j,k}^2 \rangle. \quad (5.8)$$

The uniform dissipation affects each density quadrature  $n_{j,k}$  equally, at the same rate  $\Gamma$ , as well as the quasi-condensate density  $n_0$ : they decay as  $e^{-\Gamma t}$ . The decrease in energy of a given mode  $j, k$  after a infinitesimal time  $\delta t$  writes

$$\delta E = -\Gamma \delta t \left[ \left( \frac{\hbar^2 k^2}{8mn_0} + g \right) \langle n_{j,k}^2 \rangle + n_0 \frac{\hbar^2 k^2}{2m} \langle \theta_{j,k}^2 \rangle \right]. \quad (5.9)$$

If the loss is slow enough compared to the frequency  $\omega_k$  of the considered mode, the equipartition of energy between the two conjugate variables is always verified. Therefore  $\delta E = k_B \delta T$  and the cooling of each mode can be expressed explicitely. Replacing  $\theta_{j,k}$  and  $n_{j,k}$  by their expression according to equation 5.8,

$$k_B \delta T = -\Gamma \delta t k_B T \frac{3 + \hbar^2 k^2 / 2n_0 mg}{2 + \hbar^2 k^2 / 2n_0 mg}. \quad (5.10)$$

From this expression it is clear that the temperature of each mode decreases, however the rate explicitely depends on  $k$ . In the phonon limit where  $k \ll 1/\xi$  ( $\xi = \hbar/\sqrt{2mgn}$  being the healing length),

$$\frac{dT}{dt} = -\frac{3\Gamma}{2} T, \quad (5.11)$$

while in the opposite (particle) limit, one finds

$$\frac{dT}{dt} = -\Gamma T. \quad (5.12)$$

All modes suffer energy decay, at a certain rate which depends explicitely on  $k$ . In a harmonic trap, the density profile is (as a first approximation) the Thomas-Fermi inverted parabola and total atom number scales with density as  $N \propto n^{3/2}$ , leading to a loss at the same rate as the temperature decrease  $dN/N = -3 \Gamma/2dt$  in the phonon limit. In other terms we recover the linear scaling observed by [124] experimentally. Despite limitations discussed below, this rather simple approach nonetheless suggests the emergence of a non-thermal state in a quasi-condensate with atoms lost at a constant rate  $\Gamma$ , meaning that the system cannot be described by a Gibbs ensemble. This could not be observed in the experimental study described above since their thermometry probes low-energy excitations: after time-of-flight the phase fluctuations of the trapped quasi-condensate develop into density fluctuations. Their thermometry scheme is based on a fit of the resulting interference pattern [75].

A more general description than this linearised approach is advisable. Firstly, in this model each mode evolves independently. In the following section we will show that despite coupling between modes the non-thermal state is robust. This is not obvious *a priori* and in a further section we will discuss that the integrability of the model is responsible for this out-of-equilibrium cooling. Secondly, the classical field picture completely neglects the quantised nature of the field. In reality, atoms are lost in a discrete manner and the introduction of poissonian noise will be considered in a final section, where we recover the results by Grišins and coauthors [65].

### 5.2.2 Non-linear Schrödinger equation with losses

The first step beyond the linearised classical field approach presented above is to consider a time evolution of the quasi-condensate field  $\hat{\Psi}$  according to a Gross-Pitaevskii (or non-linear Schrödinger) equation. In this non-linear picture Bogoliubov modes are coupled. The presented approach thus goes beyond the Luttinger liquid for two reasons: the coupling between excitations and the inclusion of the complete spectrum of excitations (and not only the low-energy phonon limit). For a quasi-condensate in a box of length  $L$ , the non-linear Schrödinger equation (NLSE) with an additional loss term is given by equation 5.2, as a reminder:

$$i\hbar \frac{\partial \hat{\Psi}}{\partial z} = -\frac{1}{2m} \frac{\partial^2}{\partial z^2} \hat{\Psi} - g \hat{\Psi}^\dagger \hat{\Psi} \hat{\Psi} - \mu \hat{\Psi} - i\hbar \frac{\Gamma}{2} \hat{\Psi}. \quad (5.13)$$

In the classical field framework, the field operator  $\hat{\Psi}$  is considered as a complex number. To prepare the initial state at temperature  $T$  and chemical potential  $\mu$ , the Bogoliubov modes are populated according to the equipartition relation, each quadratic degree of freedom contribution for  $k_B T/2$ :

$$E_n = E_\theta = \frac{k_B T}{2} \quad (5.14)$$

This leads to the following relations in terms of variables  $n_{j,k}$  and  $\theta_{j,k}$ :

$$\langle n_{j,k}^2 \rangle = \frac{k_B T}{g + \hbar^2 k^2 / 4m n_0} \quad (5.15)$$

$$\langle \theta_{j,k}^2 \rangle = \frac{k_B T}{\hbar^2 k^2 n_0 / m} \quad (5.16)$$

Numerically, the  $n_{j,k}$  and  $\theta_{j,k}$ s are generated randomly, with Gaussian distributions of variances given by 5.15 and 5.16. The initial wavefunction

$$\Psi_0 = \sqrt{n(z)} e^{i\theta(z)} \quad (5.17)$$

of a single realisation is developed on the sinusoidal modes, with the generated coefficients  $n_{j,k}$  and  $\theta_{j,k}$ .  $\Psi_0$  is then propagated in the NLSE, using a generic time-split method <sup>3</sup>, with the additional loss term  $\Psi e^{-\Gamma t/2}$ . A complete simulation typically contains a few tens of realisations <sup>4</sup>. Typical parameters of the numerical simulation are the following:

<sup>3</sup>This method is very common to propagate the Gross-Pitaevskii equation. It is explicated in B.

<sup>4</sup>The numerics were performed on GMPCS in Orsay - Groupement Massivement Parallèle de Calcul Scientifique.

- The initial temperature is  $T = 0.05T_{CO}$ . This represents a sample deeply quasi-condensate, where dissipative cooling is expected to take over the usual energy-selective evaporation ( $T_{CO}$  is the crossover temperature introduced in Chapter 1). In the classical field approximation, a single parameter completely determines the many-body state: in Chapter 1 (section 1.3.4) we introduced the parameter  $\eta$  which emerges when introducing dimensionless variables for the classical-field energy functional. However, as discussed in [19, 26], one can equivalently consider the dimensionless parameter  $T/T_{CO}$ .
- The atom loss rate is  $\Gamma = 2 \times 10^{-3}ng/\hbar$ . This corresponds to a slow outcoupling rate, adiabatic with respect to the evolution of each Bogoliubov mode.

Over time  $t$ , the energy in each Bogoliubov mode is newly computed, by projecting the wavefunction  $\Psi(t)$  on the Fourier components of the decomposition 5.3, 5.4. In the following, the evolution of the energy in three Bogoliubov modes in different regimes of the dispersion relation are plotted: a first simulation highlights the exponential decay of the energy in each mode, but at different rates, while in the second dissipation was interrupted and the system was let to evolve. Each mode retains its energy from the end of the dissipation: the produced non-thermal state is robust.

These simulations show, despite possible coupling between modes in the NLSE, that the generated non-thermal state is maintained after dissipation stops: the phonon modes have lower energies than the particle-like excitations. This system can be described in a generalised Gibbs ensemble, with a  $k$ -dependent temperature. In the next section, we relate this result to past experimental observations. As a consistency check, the numerics were also performed at higher temperatures, and the same behaviour arised: the fact this non-thermal state is stationary is related to the integrability of the one-dimensional NLSE (see 5.3.2 for more on this), despite the fact that the considered Bogoliubov modes are not the conserved quantities of the problem (see Chapter 1, section 1.2.1). In fact, it was recently shown in numerical simulations that phonons have a short lifetime in finite temperature Gross-Pitaevskii simulations, and the excitations are rapidly scrambled in the thermal bath represented by the quasi-condensate [95]. To conclude, the emergence of such a stationary non-thermal state is non-trivial.

### 5.2.3 Trapped systems

Since the non-thermal signature of the out-of-equilibrium state is in the energy of the different excitation modes, its experimental detection is difficult. Incidentally, the experiment reported in [124] does not provide such non-thermal features, since, as we already discussed, they can only access low-energy excitations. However, in a trap, there exists a spatial separation of modes of different energies: the low-energy excitations occupy the centre of the trap, where the trapping potential is the lowest. Higher-energy modes are present in the edges, where the potential energy is the largest.

#### Experimental observation

Chapter 3 presented the thermometry methods available to us in detail. They are both implemented in the trapped gas, from in situ images, unlike the thermometry used in

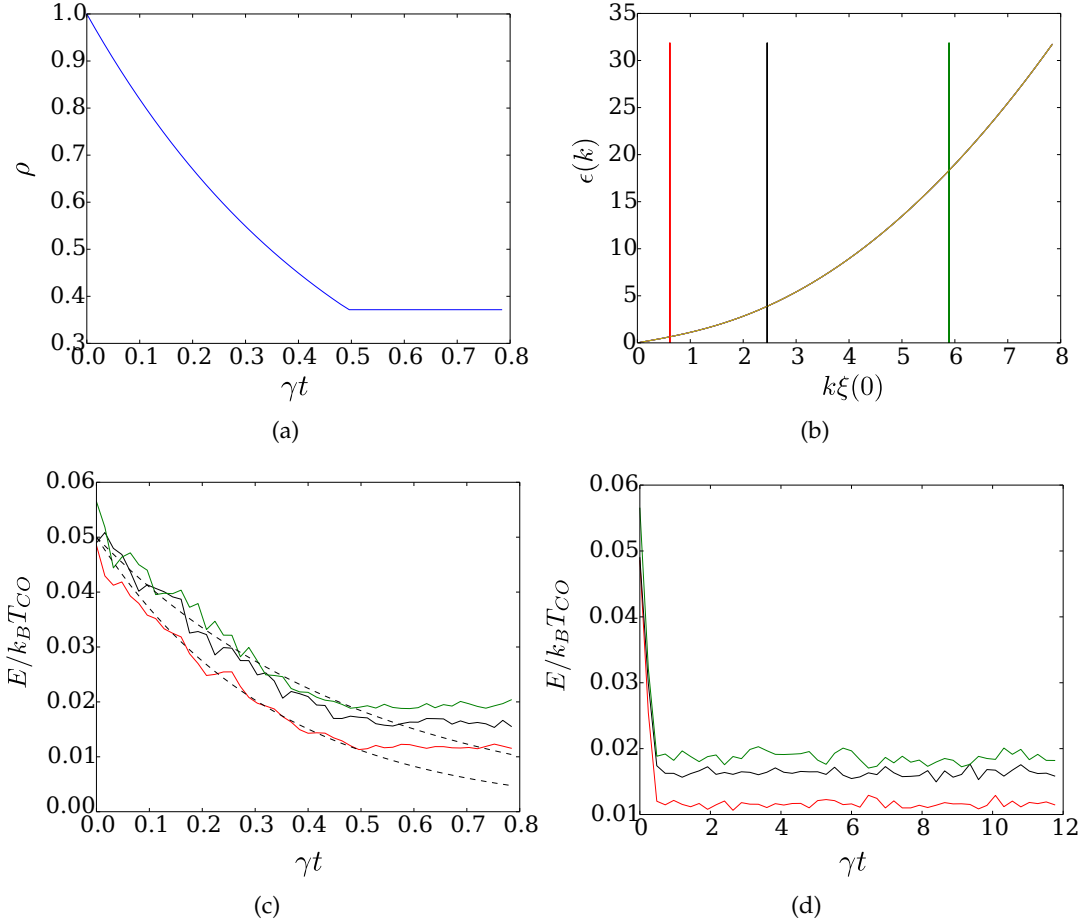


**Figure 5.3:** Panel (a): evolution of total density in the first simulation: dissipation is stopped towards the end of the simulation after 70 % of atoms are lost. Panel (b): Bogoliubov dispersion relation, and markers indicating the position of the modes considered below (with matching colours). Panel (c): short-time evolution, with dissipation, of the three considered Bogoliubov modes. The dashed lines indicate the equipartition prediction:  $e^{-3\Gamma t/2}$  for low-energy modes and  $e^{-\Gamma t}$  for high-energy modes. Panel (d): longer time evolution than the simulation shown in (c): each Bogoliubov mode retains its energy, meaning that the resulting non-thermal state is robust.

Vienna [75]. The first method relies on a fit of the in situ density profile, in the local density approximation (LDA), using the exact Yang-Yang equation of state. This thermometry is more sensitive to the edges of the density profile: the information on the temperature indeed lies in the thermal wings, where the finite-temperature profile deviates from the zero-temperature Thomas-Fermi parabola. The second method probes density fluctuations, related to the temperature by the compressibility. This also requires the knowledge of the equation of state, which depending on the experimental conditions can be taken as the general Yang-Yang description, or the quasi-condensate equation of state valid for dense and cold samples. In the quasi-condensate, the density fluctuations saturate at high densities, so that the temperature is essentially given by the asymptotic level of fluctuations in the high density region. An illustration of the thermometry methods is shown below.

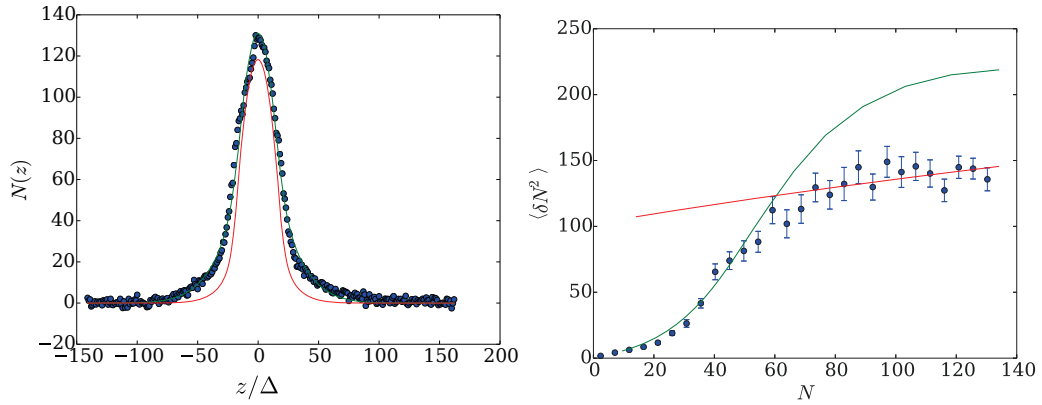


**Figure 5.4:** Illustration of the two thermometry methods accessible: profile fit with the Yang-Yang equation of state (left), and fit of the atom number fluctuations (right). On the figure left, the green profile is the best fitted profile to the data, giving a temperature  $T_{prof} = 140$  nK. On the figure right, the temperature is determined from the fit done using the quasi-condensate equation of state  $\mu = \hbar\omega_\perp(\sqrt{1 + 4na} - 1)$  (straight red line). This yields a second temperature  $T_{fluc} = 80$  nK. On the left panel, the green line represents the profile corresponding to  $T_{fluc}$ , while on the right panel, the red line shows the expected fluctuations for  $T_{prof}$ . The nicely follow the measured fluctuations in the low density region, in other terms the wings of the profile.

In this set of data, the two thermometries clearly give different results, well beyond the uncertainty on the temperature which is believed to be of the order of 10 to 20 %. The fluctuation temperature, which probes the centre of the trapped cloud, is  $T_{fluc} = 80$  nK, compared to the temperature determined from a fit of the profile  $T_{prof} = 140$  nK, probing the edge of the cloud. In fact, profile fits are poor for certain sets of data, certainly because of their out-of-equilibrium nature. In [80], thermometry in momentum space is also considered: we can perform Quantum Monte Carlo fits of the momentum distributions and for the sets of data presented in that publication, the temperatures measured in momentum agree with the temperature extracted from atom number fluctuations. This is in accordance with the fact that low-energy excitations are probed in momentum space: the high energy excitations are far in the wings of the profile and the QMC fit is more sensitive to the width of the momentum distribution  $1/l_\phi$ , the inverse of the phase coherence length. In the qBEC regime  $l_\phi \gg \xi$ .

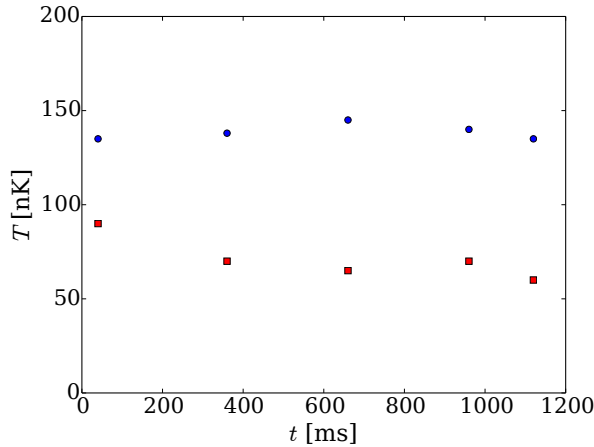


**Figure 5.5:** Time evolution of the temperatures extracted from the profile (blue circles) and density fluctuations respectively. Both temperatures do not evolve significantly. The error on these temperatures range from 10 to 20% depending on the considered data set, which is much smaller than the difference in the result between fluctuation and profile thermometries.

This "two-temperature" state is not only frequently observed on our experimental setup, it is also robust in time. We performed a simple experiment, where the cloud is held in the trap for different times up to one second, and measure the temperature after holding. The protocol is the following: after the usual evaporation ramp where the frequency is reduced exponentially, the radio-frequency is slightly increased by 30 kHz as a shield to eliminate the most energetic atoms, like those involved in three-body recombinations. With this shield on, the cloud is then held for the desired time in the trap before measuring. The result is shown figure 5.5: both temperatures are constant over time.

This experiment was not performed in the scope of implementing dissipative cooling: it was rather an attempt to understand the emergence and dynamics of this observed out-of-equilibrium state without having a physical explanation at hand. It appears that the observations are compatible with the non-thermal state predicted in the context of uniform atom loss from the system: the low-energy excitations (probed by density fluctuations) appear colder than the high-energy modes (accounting for the profile temperature), and moreover this state is robust after evaporation is complete.

## Simulation

To relate the experimental observations with the dissipative cooling mechanism, we performed, with Stuart Szigeti of the University of Queensland, classical field simulations in a trap. The principle of the simulation is identical to those in the homogeneous system: a quasi-condensate is prepared at a certain temperature, and the initial state is then propagated with a NLSE containing the additional term accounting for atom loss.

The approach used to generate the initial state is the Stochastic Projection Gross-Pitaevskii Equation (SPGPE), briefly introduced in Appendix C, and also used in [19]. The state

is then propagated using the Projected Gross-Pitaevskii Equation (PGPE), see e.g Appendix C and [11, 12]. For the purpose of this study, the PGPE contains an additional loss term  $i\hbar\Gamma/2\hat{\Psi}$ , just as in the simulation for homogeneous systems. Here I present the very first results of the simulation, performed in the following conditions:

- The loose trapping frequency is  $\omega_z = 20$  Hz (slightly tighter than the experimental value of 6 Hz).
- The tight trapping frequency is  $\omega_{\perp} = 2$  kHz (which is a typical experimental value).
- The initial temperature of the cloud is  $k_B T = 200\hbar\omega_z$ , corresponding to a typically low temperature on the experiment.
- The chemical potential  $\mu = 0.8k_B T$  also corresponds to a typical experimental configuration.
- Finally the outcoupling rate was taken identical to the simulation in the homogeneous case, as  $\Gamma = 0.002ng/\hbar$ .

The initial state is shown below, with the computed mean density profile (and corresponding Yang-Yang fit) and fluctuations.

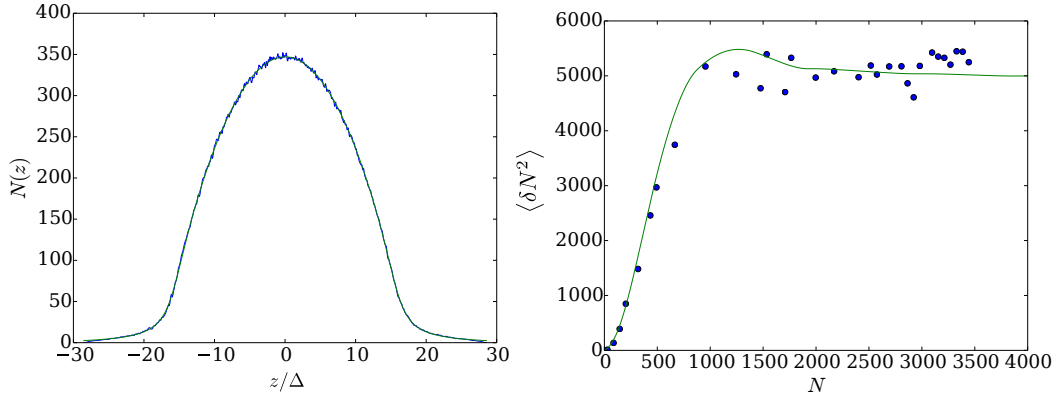


**Figure 5.6:** Initial conditions of the simulation. Observables of interest are  $T_{prof} = 210$  nK, compatible with  $T_{fluc} = 212$  nK.

After a large fraction of atoms are lost, we perform the same analysis as for experimental data: the profile and density fluctuations are fitted using a Yang-Yang equation of state, and the results are shown in the following figure. To compute atom number fluctuations, the data is binned to pixels whose size is an order of magnitude above the healing length, just like the experimental pixels. The results of this analysis are represented figure 5.7.

Although the fits are not perfectly accurate the results convey observations compatible with the experiment: temperature provided by atom number fluctuations is lower than the best fitted temperature from the profile. Unfortunately we do not yet have an experimental knob which deliberately controls the emergence of such a non-thermal

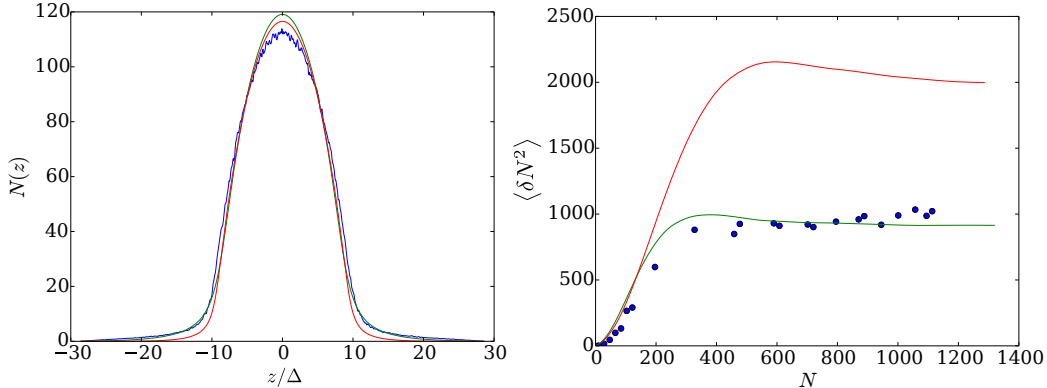


**Figure 5.7:** Best fits for the density profile (left, in green) and density fluctuations (right, in green). It appears that the profile is not accurate, revealing the out-of-equilibrium character of the system after loss. This feature was also reported in our experiment. The fluctuations associated with the best profile fit are shown in red on the right panel. The profile corresponding to the best fluctuation fit is also represented in red, on the left panel. The fitted temperatures are  $T_{prof} = 80$  nK and  $T_{fluc} = 30$  nK respectively. This is qualitatively in agreement with experiment results. Density fluctuations saturate after decreasing from a local maximum, which differs from the experimental behaviour. This is because the simulation is purely one-dimensional while the experimental data lies on the 1D-3D crossover where the chemical potential behaves as  $\sqrt{1 + 4na}$ .

state: up to now we can only rely on their natural (and uncontrolled) appearance. We fitted the classical field results with the exact Yang-Yang equation of state for convenience (and immediate availability of Yang-Yang data), however for self-consistency we plan to fit with the classical field equation of state, which we yet have to compute numerically.

As a final remark on the relation with what we observe on the experiment, the predicted lower bound for the temperature does not match experimental results: observed temperatures are as low as  $\mu/4$  [79, 124], well below the computed bound of  $\mu$ . To briefly conclude, the role played by this dissipation during the cooling of our gas is not clear: to reach lower temperatures there would have to be some type of energy selection. We currently believe that this dissipation does occur on our experiment, but this mechanism doesn't seem to give the complete picture.

### Summary

- As a first approach, our linearised toy model showed that the energy of Bogoliubov modes in different regions of the dispersion relation are not equally affected by atom loss: their energies all decay exponentially but at different rates, creating a state which is clearly out-of-equilibrium.
- We then performed non-linear Schrödinger equation simulations with an additional term modelling constant atom loss, in the homogeneous case. This revealed that the behaviour predicted by the linearised approach was robust against the non-linearity introduced by the considered partial differential equation: the phononic energy decays faster than the energy of the particle modes, leading to a stationary non-thermal state.

- Finally, this result is compatible with past experimental observations, which we show by performing identical simulations, but in a trapped system. The temperatures extracted by our two methods (in situ atom number fluctuation measurements and in situ profile fits) are indeed different in the numerical data after dissipation, which is in agreement with the reported experimental observation.

## 5.3 Relation with integrability

Up to now we have shown that in the one-dimensional Bose gas, uniform and constant atom loss alone significantly cools the gas, at the cost of driving the system in a stationary out-of-equilibrium state. The stationary non-thermal property is clearly related to the integrable nature of the considered system. We first derive some simple thermodynamic arguments, to show that in an ergodic system cooling is far from granted if atoms are removed from the system, and we then simulate atom loss in a non-integrable problem to highlight the different dynamics compared to the single NLSE.

### 5.3.1 Thermodynamic arguments

Consider a generic thermodynamic system, submitted to atom loss in a non-selective manner. We assume one can apply usual thermodynamic reasoning to the system of interest, namely that it is ergodic and that it rapidly relaxes to an equilibrium state after removal of atoms. If the number of atoms decreases by  $\delta N < 0$ , the energy variation is the mean energy per particles times the number of atoms lost:

$$\delta E = \frac{E}{N} \delta N \quad (5.18)$$

Using  $E = -pL + TS + \mu N$  leading to  $dE = TdS - pdL + \mu dN$ , one has  $\delta S = [(-\mu + E/N)/T] \delta N$  since  $dL = 0$ . Introducing the intensive variable  $s = S/N$ <sup>5</sup>, the variation of entropy per particle is:

$$\delta s = -\frac{p}{Tn} \frac{\delta N}{N}. \quad (5.19)$$

These relations show that during the loss process the entropy per atom is increased. We are more interested in the sign of  $\delta T$ : by writing that

$$\delta T = \left[ \frac{\partial T}{\partial E} \Big|_{N,L} \frac{E}{N} + \frac{\partial T}{\partial N} \Big|_{E,L} \right] \delta N, \quad (5.20)$$

$\delta T$  is expressed as:

$$\delta T = \frac{1}{C_V} \left( \frac{E}{N} - \frac{\partial E}{\partial N} \Big|_{T,L} \right) \delta N \quad (5.21)$$

---

<sup>5</sup>For an intensive variable  $a$ ,  $\frac{\partial(Na)}{\partial N} \Big|_{N,L} = a + n \frac{\partial a}{\partial n}$

$C_V$  is the heat capacity at constant volume, positive for stable materials and  $\partial E/\partial N$  is the chemical potential. The sign of  $\delta T$  therefore relies on the behaviour of the internal energy of the system with particle number. For non-degenerate gases for instance,  $\partial E/\partial N|_{T,L} = E/N$ , so that  $\delta T = 0$ .

More relevant for this study, let us consider degenerate gases. For an ideal Bose gas, the chemical potential is negative so that  $\delta T$  has the same sign as  $\delta N$ . This translates into cooling when atoms are removed from the system. However, if (repulsive) interactions are considered, the energy (in 1D) of the quasi-condensate is approximately given by  $E = gN^2/(2L)$ . The expected temperature change becomes:

$$\delta T = -\frac{\delta N}{C_V} \frac{gn}{2}, \quad (5.22)$$

which is positive: losses appear to induce heating in the system. These arguments somehow illustrate how counter-intuitive and peculiar the presented cooling mechanism is, but should be taken with precaution since they are not expected to hold in our integrable system of interest.

### 5.3.2 Breaking the integrability: coupled NLSE

Integrable systems exhibit particular dynamics, in the sense that they do not, in general, relax to a Gibbs ensemble. To check that the non-thermal state observed and described above is indeed related to the integrable nature of the considered system, we performed numerical simulations in a one-dimensional Bose gas with a non-integrable perturbation. There are many ways to break the integrability, however a non-integrable perturbation may not be sufficient to completely alter the dynamics on numerically accessible time scales. In classical mechanics, the Kolmogorov-Arnold-Moser theorem states that under some perturbations, the closed orbits of an integrable system may survive. Discussions on a quantum analog of the KAM theorem are ongoing, such as for instance in this paper which considers the 1D Bose gas as a test model [22]. In the current classical field study, a reliable manner to break the integrability in our system of interest is to introduce a two-component gas, with an interspecies interaction, and two different masses [73,74]. The case of a two-component system with interspecies interaction but identical masses was shown to be Bethe-Ansatz solvable, which is equivalent to stating that the problem is integrable [152].

We therefore consider two masses  $m_1, m_2 = 2m_1$  each interacting via a repulsive delta-potential. We assume that the single-species interactions are equal:  $g_{11} = g_{22} = g$ . The two species interact with each other through a coupling constant  $g_{12}$ . This interspecies interaction is considered as a perturbation of the uncoupled Hamiltonian, in other terms we fix  $g_{12} \ll g$ . The complete Hamiltonian of the system contains three terms:

$$\hat{\mathcal{H}}_{coupled} = \hat{\mathcal{H}}_1 + \hat{\mathcal{H}}_2 + \hat{\mathcal{H}}_{12} \quad (5.23)$$

with:

$$\hat{\mathcal{H}}_i = -\frac{\hbar^2}{2m_i} \int dz \hat{\Psi}_i^\dagger(z) \frac{\partial}{\partial z} \hat{\Psi}_i(z) + \frac{g}{2} \int dz \hat{\Psi}_i^\dagger(z) \hat{\Psi}_i^\dagger(z) \hat{\Psi}_i(z) \hat{\Psi}_i(z). \quad (5.24)$$

and

$$\hat{\mathcal{H}}_{12} = g_{12} \int dz \hat{\Psi}_1^\dagger(z) \hat{\Psi}_2^\dagger(z) \hat{\Psi}_1(z) \hat{\Psi}_2(z) \quad (5.25)$$

The dynamics of the coupled system obeys the coupled time-dependent Gross-Pitaevskii equations (in the homogeneous system) given by:

$$\begin{cases} i\hbar \frac{\partial \Psi_1}{\partial t} = \left( -\frac{\hbar^2}{2m_1} \frac{\partial^2}{\partial z^2} + g|\Psi_1|^2 + g_{12}\Psi_1^\dagger\Psi_2 \right) \Psi_1 \\ i\hbar \frac{\partial \Psi_2}{\partial t} = \left( -\frac{\hbar^2}{2m_2} \frac{\partial^2}{\partial z^2} + g|\Psi_2|^2 + g_{12}\Psi_2^\dagger\Psi_1 \right) \Psi_2 \end{cases} \quad (5.26)$$

As a first (preliminary) test, by taking  $g_{12}$  sufficiently small, it is not necessary to diagonalise the resulting Hamiltonian of the coupled system using a generalised Bogoliubov approach. We considered each species separately, populating the initial state as was done above for the single-component simulations. In this case the problem reduces to two independent quadratic Hamiltonians, each quadratic term contributing to the total energy of the system by  $k_B T/2$ . The initial state is then propagated using the split-time algorithm, including the coupling term (which is possible since the two-species contribution is of the same form as the intra-species interaction). After letting the system evolve with loss, dissipation is stopped and the system is left to propagate without atoms being removed, but with the slight coupling. After a relatively long propagation time (since  $g_{12}$  is small the effects of non-integrability take a while to kick in), the observations are as depicted in figure ???. During evolution, the energies in the Bogoliubov modes (of the uncoupled two-component system, to avoid solving the complete coupling problem) are newly computed. We compare the results with an identical simulation, but without the integrability-breaking coupling.

Unfortunately the simulation could not be run for longer times, with drifts appearing in the non-coupled simulation: for instance the dashed-red (phonon) curve in the left panel starts to slowly increase in time, when it should remain stable. The above graphs nevertheless show that the dynamics are different in presence of the coupling term: the system appears to evolve towards a state where the energy of phonons increases. Whether the system relaxes to a Gibbs ensemble (with equipartition between modes) or if it continues to heat is not clear. We hope to solve this question by diagonalising the coupled Hamiltonian to a quadratic form as was done for instance in [98]. Observation of heating would relate to the thermodynamic arguments presented above.

### Summary

- The one-dimensional non-linear Schrödinger equation has the particular property of being integrable (or non-ergodic), which explains the stationary non-thermal states emerging after atom loss.

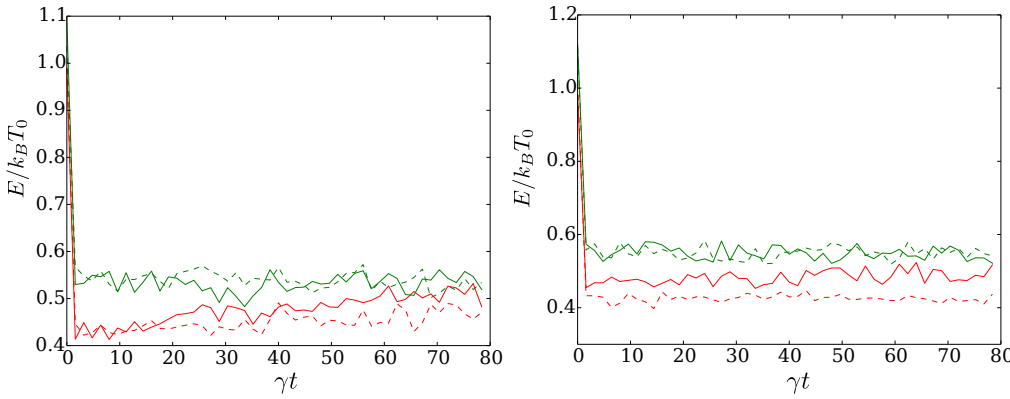


**Figure 5.8:** Energies of a particle-like Bogoliubov mode (green) and phonon-like mode (red) in each of the components of the gas (referred to as 1 and 2). The solid line represents the evolution with coupling  $g_{12}$  and the dashed line the evolution without the coupling for comparison. With coupling, the system appears to evolve towards an equipartition of energy.

- Although thermodynamic arguments are in principle not applicable in non-ergodic problems, simple arguments show that a quasi-condensate should heat up when atoms are removed. Such a result underlines the non-intuitive nature of the cooling mechanism at play.
- When an integrability-breaking perturbation is added (in this case two-body coupling between components of distinct masses), the dynamics of the system after atom loss is strongly affected: a long term heating of the lower energy modes appears. However the outcome of the simulation is not clear and the added perturbation should be made stronger to conclude. This was not yet implemented to date, but will be after submission of the current manuscript.

## 5.4 Beyond classical field: effect of atom quantisation

In the above treatment, loss is considered as a continuous process and the quantised nature of the field (in the form of atoms) is ignored. Taking into account the discretised nature of the outcoupling process amounts to adding shot noise associated with the loss of atoms, which heats the system and imposes a lower bound to the accessible temperature with the dissipative evaporation mechanism.

### 5.4.1 Modelling the quantised losses

#### Stochastic Gross-Pitaevskii equation

For convenience and since the study is partly numerical, we first discretise the problem. One-dimensional space is discretised on a grid of spacing  $\delta z$ . The annihilation operator

$\hat{\Psi}$  satisfies the bosonic commutation relation in cell  $j$ :  $[\hat{\Psi}(j)^\dagger, \hat{\Psi}(j)] = 1$ .  $\tilde{g}$  denotes the rescaled coupling constant  $g/\delta z$ .

By writing the Lindblad equation for the dissipative problem, and then using a Wigner representation, we recover (this proof is delegated to Appendix D, to ensure the continuity of the discussion) the stochastic Gross-Pitaevskii equation considered in [65].

$$i\hbar d\Psi = \left( -\frac{\hbar^2}{2m} \partial_j^2 \Psi + \tilde{g} |\Psi|^2 \Psi - i\hbar \frac{\Gamma}{2} \Psi \right) dt + d\xi, \quad (5.27)$$

This equation is essentially classical, and the quantised nature of the field appears as an additional noise term. We recover a classical-field like approach after applying the truncated Wigner approximation (see Appendix D). This stochastic partial differential equation is the starting point of the model taking into account the discretised nature of the field: however this numerical hack to introduce noise gives physical results after averaging over many realisations.

### Evolution of the Bogoliubov modes

We now consider a linearised model, like in 5.2.1, where each excitation evolves independently. The field operator is expressed, like above, in the field-density representation, namely  $\Psi = \sqrt{n}e^{i\theta(z)}$ . Separating the real and imaginary parts of the stochastic Gross-Pitaevskii equation, and linearising in density fluctuations and phase gradient, we get the following system for the evolution of the phase and density fields:

$$\begin{cases} d\delta n = -\frac{\hbar^2 n}{m} \partial_z^2 \theta dt - \Gamma dt \delta n + \sqrt{n} d\eta \\ d\theta = -(\tilde{g} + \frac{\hbar^2}{4mn} \partial_z^2) \delta n dt + \frac{1}{2\sqrt{n}} d\nu \end{cases} \quad (5.28)$$

where  $d\nu$  et  $d\eta$  are random gaussian variables of mean value equal to 0 and variances

$$\langle d\eta^2 \rangle = \langle d\nu^2 \rangle = \delta_{z,z'} \Gamma dt. \quad (5.29)$$

Expanding over sinusoidal modes (as in 5.2.1, in other terms we take the Fourier transform), we obtain an evolution equation for each mode:

$$\begin{cases} dn_{j,k} = \frac{\hbar^2 k^2 n}{m} \theta_{j,k} dt - \Gamma dt n_{j,k} + \sqrt{n} d\eta_{j,k} \\ d\theta_{j,k} = -(\tilde{g} + \frac{\hbar^2 k^2}{4mn}) n_{j,k} dt + \frac{1}{2\sqrt{n}} d\nu_{j,k} \end{cases} \quad (5.30)$$

For a vanishing loss rate, this system of equations derive from the harmonic oscillator Hamiltonian, which we already encountered in our toy model:

$$H_{j,k} = L \left[ \left( \frac{\tilde{g}}{2} + \frac{\hbar^2 k^2}{8mn_0} \right) n_{j,k}^2 + \frac{\hbar^2 k^2}{2m} n_0 \theta_{j,k}^2 \right] \quad (5.31)$$

A single stochastic trajectory does not contain a physical meaning: one needs to average over many realisations to recover the physical behaviour of our conjugate variables in the process. Since an initially Gaussian distribution retains its Gaussian form under the stochastic process above, the distribution of each mode is completely determined by its average and variance. In accordance with the Wigner function approach explained

Appendix D, quantum expectation values are simply obtained by averaging the corresponding classical quantities over the Wigner distribution. Averaging over stochastic trajectories, from Eq. 5.30 we obtain:

$$\begin{cases} \frac{d}{dt}\langle n_{j,k}^2 \rangle = 2\frac{\hbar^2 k^2 n}{m} \langle \theta_{j,k} n_{j,k} \rangle - 2\Gamma \langle n_{j,k}^2 \rangle + n\Gamma \\ \frac{d}{dt}\langle \theta_{j,k}^2 \rangle = -2(\tilde{g} - \frac{\hbar^2 k^2}{4mn}) \langle \theta_{j,k} n_{j,k} \rangle + \frac{\Gamma}{4n} \\ \frac{d}{dt}\langle n_{j,k} \theta_{j,k} \rangle = \frac{\hbar^2 k^2 n}{m} \langle \theta_{j,k}^2 \rangle - \left( \tilde{g} - \frac{\hbar^2 k^2}{4mn} \right) \langle \theta_{j,k}^2 \rangle \end{cases} \quad (5.32)$$

As in the treatment in 5.2.1, if one assumes loss is adiabatic with respect to the free evolution of each mode, then equipartition of energy between the two conjugate variables  $\theta_{j,k}$  and  $n_{j,k}$  is ensured. The Wigner function is then solely determined by the energy  $E$  in the mode, and from 5.32 we find:

$$\frac{d}{dt}\tilde{E} = \Gamma(-\tilde{E} + B) \quad (5.33)$$

where  $B = (1/2 + gn/k^2)/\sqrt{1 + 4gn/k^2}$  and  $\tilde{E} = E/\omega$ . The solution to this first-order differential equation is

$$\tilde{E} = \tilde{E}(0)e^{-\Gamma t} + \int_0^t \Gamma d\tau B(\tau)e^{-(t-\tau)\Gamma}. \quad (5.34)$$

For phonons, one has  $B \simeq \sqrt{gn}/(2k)$ , such that the previous equation predicts an asymptotic value of  $gn E = \omega(t)\tilde{E}$ . Since  $gn$  is much larger than the ground state energy  $\hbar\omega/2$ , this corresponds to a thermal equilibrium at a temperature

$$T_{\text{phonon}} \underset{t \rightarrow \infty}{\simeq} ng. \quad (5.35)$$

For modes with  $k \gg \sqrt{ng}$  on the other hand, using an expansion of  $B$  in powers of  $gn_0/k^2$ , one finds

$$\tilde{\epsilon} \simeq \left( \frac{gn_0}{k^2} \right)^2 e^{-\Gamma t} (1 - e^{-\Gamma t}) + \tilde{\epsilon}_0 e^{-\Gamma t} \quad (5.36)$$

where  $\tilde{\epsilon} = \tilde{E} - 1/2$  is the excess of energy above the quantum ground state energy of the mode. At large times,  $\tilde{\epsilon}$  becomes much smaller than one. This corresponds to a temperature  $T \simeq (k^2/2) \ln(\tilde{\epsilon})$ , much smaller than  $\omega_k$ . At large times, we find

$$T_{\text{part}} \underset{t \rightarrow \infty}{\simeq} \frac{k^2}{2} \frac{1}{\Gamma t}. \quad (5.37)$$

The temperature of those modes explicitly depends on  $k$ <sup>6</sup> and takes much larger values than  $T_{\text{phonon}}$ . Eq. 5.36 shows that modes with small enough initial temperatures suffer an increase in energy at short times.

#### 5.4.2 Simulation

In order to test the quantitative predictions of the linearised approach, we numerically simulated the evolution given by the stochastic GPE. The initial state (here the starting

---

<sup>6</sup>Again, for clarity we use the word "temperature" but of course there is no true thermodynamic temperature in the particle limit because of this explicit dependence in  $k$ .

temperature is  $T = 3ng$  and  $g = 10^{-5}$ ) is prepared by applying equipartition of energy

$$E_{th} = \hbar\omega_k \left( \frac{1}{2} + (e^{\hbar\omega_k/k_B T} - 1)^{-1} \right) \quad (5.38)$$

between quadratures  $\delta n_{j,k}$  and  $\theta_{j,k}$ : they each contribute for  $E_{th}/2$ . The atomic field  $\Psi$  is then evolved and for different evolution times we compute the energy in each Bogoliubov mode and by averaging over many realisations we associate the mean energy in a given mode  $\langle E_k \rangle$  to a "temperature"  $T_k$ , given by:

$$k_B T_k = \frac{\hbar\omega_k}{\ln((2E_k + \omega_k)/(2E_k - \omega_k))}. \quad (5.39)$$

In the left panel of the figure below, the evolution of the energy of a mode deep in the phonon regime is represented, and compared to the classical prediction (smooth solid line)  $e^{-3\Gamma t/2}$ . The temperature converges to the expected  $n(t)g$  at long times. The right panel represents the evolution of the "temperature"  $T_k$  vs  $k$  for different times. The apparent heating of the high-energy modes is probably a numerical artefact.

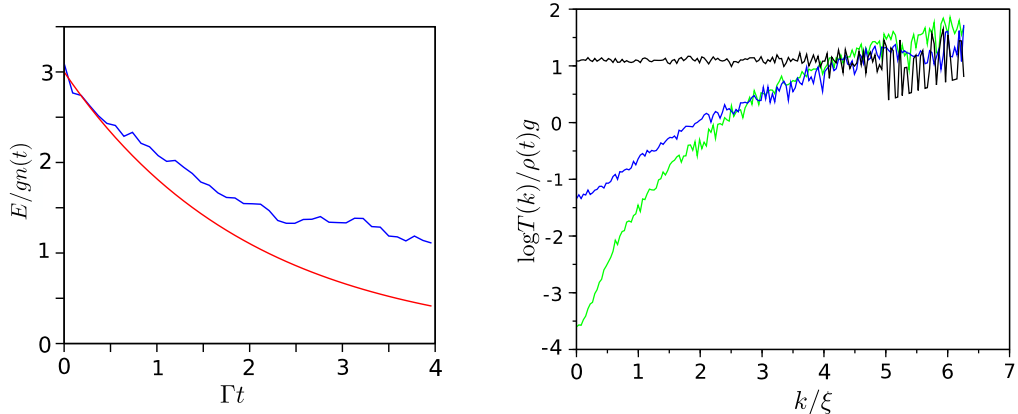


**Figure 5.9:** Left: temperature decaying to  $n(t)g$  in the phonon limit. Right: convergence the energies of modes in the phononic regimes towards the asymptotic limit  $\rho g$ , where different colours correspond to modes of different initial energies.

### Summary

- In this section, we complete our previous classical field description by adding a stochastic term in the Gross-Pitaevskii equation: this accounts for the quantised nature of the field.
- A linearised approach recovers the following result of [65]: the addition of this noise term limits the asymptotic temperature in the low-energy limit of excitations to  $gn$ .
- In the high-energy limit of the dispersion relation, the energy of the modes explicitly depends on  $k$ , which compromises the definition of a temperature.

- Numerical simulations, beyond the linearised approach, show that the energy of phonon modes indeed decay to the expected  $gn$ , and that the atom loss generates a non-thermal state, with an explicit dependance of  $T_k$  for modes which are not in the phonon limit.

# CHAPTER 6

---

## Perspective: a one-dimensional lattice for a magnetically trapped one-dimensional Bose gas

---

### 6.1 Physical background: Mott transition and specificities of 1D

The Mott transition is a prime example of how the cold atom community exchanges with condensed matter physics. In the latter, it designates a metal-nonmetal transition. This transition occurs in a variety of condensed matter systems and is related to the electron-electron interactions and the opening of a gap due to many-body effects [109]. A number of phenomena can drive the transition like doping, ferromagnetism or the presence of disorder [110]. Mott-type transitions with bosonic particles were first studied theoretically in the context of experiments with liquid helium [52]. For cold atoms, attention was brought to this quantum phase transition with its experimental realisation with bosons in 2002 [63] following a theoretical proposal [81]: in this case the material goes from being superfluid to "insulating". The transition is said to be of Mott-Hubbard type [155], with no long range interactions involved. The experimental realisation of correlated states of matter like the Mott insulator is of interest in the quantum simulation context: the mere presence of such correlations defies numerical simulations with classical computers.

In this chapter I introduce the physical context of prospective projects on our experiment. We started installing a longitudinal optical lattice to create a periodic potential along the  $z$  axis in addition to the magnetic confinement provided by the chip. I first give some theoretical background on lattice physics in 1D, and after introducing the experimental setup I will describe the questions we wish to consider along with the specificities of our experiment.

#### 6.1.1 Generalities on the Mott transition

Consider bosons with repulsive interactions hopping through a three-dimensional lattice potential. Two energy scales in the system compete: the on-site interaction  $U$  and the tunneling between the lattice sites  $J$ . If particles may hop easily from a site to another the system is in a superfluid state where the wavefunction is delocalised over all lattice sites. If on-site interaction prevails, when hopping is suppressed by a deep enough lattice depth, the atoms localise in the lattice sites where density takes integer

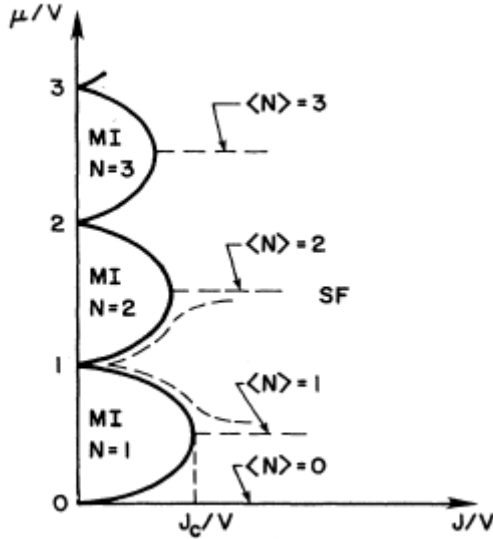


**Figure 6.1:** Three-dimensional zero-temperature phase diagram of the Bose-Hubbard model. The MI phase is incompressible: the number of atoms per site (or density) is fixed. One may cross from one phase to another by increasing the chemical potential or the hopping, at fixed on-site interaction. Figure taken from [52].

values, creating an insulating phase. In this state with a fixed number of atoms per site the phase strongly fluctuates and coherence is lost: the system becomes a so-called Mott insulator (MI). This phase transition is quantum, characterised by the opening of an energy gap in the excitation spectrum and occurring at zero temperature, since quantum fluctuations drive the phase change.

The physics of the transition is captured by the three-dimensional Bose-Hubbard hamiltonian [60], containing two competing terms: the on-site (interaction) energy and the hopping (kinetic) term.

$$\hat{\mathcal{H}}_{BH} = -J \sum_{\langle i,j \rangle} \hat{b}_i^\dagger \hat{b}_j + \frac{1}{2} V \sum_i \hat{n}_i (\hat{n}_i - 1) \quad (6.1)$$

Here  $\hat{b}_{i,j}^\dagger, \hat{b}_{i,j}$  are the bosonic creation and annihilation operators (on sites  $i$  and  $j$  respectively), and  $\hat{n}_i$  the number operator. This model is valid for a deep enough lattice where particles occupy the lowest band. The zero-temperature phase diagram was first discussed in [52]. The critical point is reasonably well described in the mean-field approximation, with a critical ratio  $(U/zJ)_c = 5.827$ ,  $z$  being the number of nearest neighbours in the considered lattice geometry [52]. The first experimental observation of the transition confirms the accuracy of the mean-field prediction [63]. The phase diagram takes the form of insulating lobes with commensurate densities, with the superfluid phase in the high  $J$  region of parameter space.

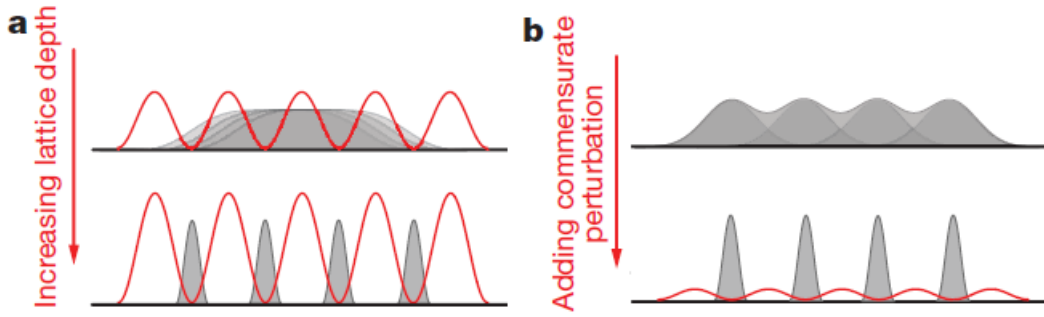


**Figure 6.2:** Illustration of the two transitions from a superfluid to an insulator in 1D, taken from [68]. On the left, in the Bose-Hubbard model where the lattice is deep the many-body wavefunction is delocalised up to a critical potential depth. On the right, in the sine-Gordon model, the homogeneous gas itself is strongly correlated and a commensurate perturbation suffices to localise the many-body wavefunction.

### 6.1.2 Mott physics in dimension one

#### Two models: sine-Gordon vs Bose-Hubbard

The one-dimensional Bose-Hubbard (BH) model also predicts a Mott transition, analogous to the three-dimensional phenomenon [94]. The critical point was numerically determined to be  $(U/J)_c = 3.85$  with DMRG. However, in 1D for strong enough interactions the homogeneous system is strongly correlated, so that an arbitrarily low periodic potential is enough to crystallise the gas: this transition specific to 1D is called the Pinning transition, captured by a Hamiltonian of sine-Gordon (sG) form:

$$H_{sG} = \frac{\hbar v_s}{2\pi} \int dz [(\partial_z \theta)^2 + (\partial_z \phi)^2 + V(\sqrt{4K} \cos \theta)] \quad (6.2)$$

$K$  is a dimensionless parameter which can be mapped onto the interaction parameter  $\gamma$ .  $v_s$  the sound velocity and  $V$  the potential depth. The first term represents the interaction energy dependent on the density field  $\partial_z \theta$  while the second accounts for the kinetic energy proportional to phase fluctuations in this hydrodynamic description of the 1D liquid. Such a model is valid for strongly interacting gases, in contrast with the Bose Hubbard model valid in the weakly-interacting system [23].

For the Bose-Hubbard model, the gas goes from being superfluid to insulating when the depth of the (deep) periodic potential  $V$  is increased <sup>1</sup>, at commensurate densities. For the sine-Gordon model, a sinusoidal perturbation, commensurate to the density ( $n \sim 1/a = 2/\lambda$  where  $a$  is the lattice spacing and  $\lambda$  the wavelength of the lattice laser), on top of the strongly-interacting gas is enough to localise the system [23] if the interaction parameter  $\gamma$  exceeds  $\gamma_c = 3.5$ . The pinning transition was observed experimentally, as well as the change of regime to the conventional Bose-Hubbard transition in [68], and further investigated experimentally alongside numerical results in [15].

<sup>1</sup>It was however recently shown with QMC calculations that the Bose-Hubbard model holds to relatively low potential depths [15]

To simplify the discussion, let us discriminate between two types of transitions: the generic Mott transition with a phase diagram qualitatively similar to its three-dimensional counterpart (with parameters  $\mu$  and  $J$ ), and the commensurate-incommensurate transition. Both phase diagrams meet at the multi-critical Pinning transition point [52].

### Bose-Hubbard model and generic Mott transition

Consider the Bose-Hubbard limit of a deep potential  $V$  of fixed value. In analogy to the 3D phase diagram presented above (figure 6.1), one can construct the phase diagram of the BH model with parameters  $\mu$  and  $J$ , as shown below for the first lobe (one atom per site). DMRG calculations [94] revealed a reentrant behaviour of the superfluid phase and a critical point at  $(U/J)_c = 3.85$ :

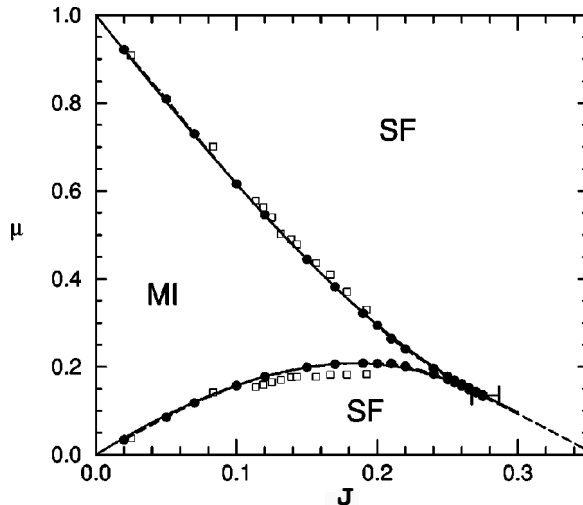


**Figure 6.3:** Phase diagram for one atom per site, at fixed potential depth. Adapted from [94] and computed with DMRG. Along the dashed line the density is exactly one atom per site.

The transition by crossing the tip of the MI lobe has a different universality class than the transition varying  $\mu$  (introduced below): this transition is of Berezinskii-Kosterlitz-Thouless (BKT for short) type, when the rest of parameter space has a generic first-order critical behaviour. The Mott transition can therefore be characterised (numerically or experimentally) by a diverging density correlation length, or a diverging compressibility.

### Commensurate/incommensurate and Pinning transitions

Büchler et al considered the Mott transition from the complementary point of view of parameters  $U$ ,  $\gamma$  (interaction strength) and  $Q$  (commensuration,  $Q = 2\pi(n - 2/\lambda)$ ), reformulating in the cold atom context results from the condensed matter community. Let us first assume a fixed commensurate density  $n = 1/a$ , or equivalently  $Q = 0$ . For strong enough interactions in the homogeneous system, the addition of an arbitrarily low lattice potential suffices to localise the gas. This is depicted in panel b of the figure below (6.4). The point  $\gamma = 3.5$  and  $V = 0$  is the Pinning transition. Now if one changes the commensurability of the gas in the weak periodic potential, the crystalline order is locked in a certain range of chemical potentials (the phase is incompressible), until broken at a critical incommensurability  $Q_c$ , as shown in the three-dimensional phase

diagram panel a. This commensurate-incommensurate transition has similar physical features to the transition of the same name of adsorbates on periodic structure, once again illustrating analogies with condensed matter physics [120].

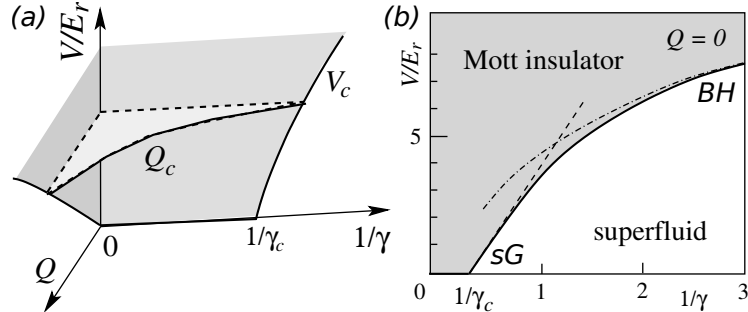


**Figure 6.4:** Commensurate/incommensurate (a) and one atom per site (b) phase diagrams, adapted from [23]. In b, the gas is insulating above critical values of  $V$ . The stronger the interactions (the smaller  $1/\gamma$ ), the smaller the critical value  $V_c$  to localise the gas, until the Pinning transition at  $1/\gamma_c$ , which joins the  $V = 0$  line ( $V$  is an alternative notation for the  $U$  use until now). sG stands for sine-Gordon (dashed line), model applicable at weak lattice depths  $V$ , and BH stands for Bose-Hubbard (dash-dotted), applicable in the opposite limit where the potential is deep enough for the atoms to be in the lowest band.  $E_r$  stands for recoil energy, referring to optical lattices used to produce the periodic potential in ultracold atom experiments (see below).

The transition represented by a solid line at fixed commensurate density  $Q = 0$  is part of the BKT universality class [23, 94] and the tip of the insulating lobe figure 6.3 lies on the solid line in panel b of figure 6.4.

The presented results were computed at zero temperature, without external trapping potential. Both a finite temperature and harmonic confinement should be considered to draw a parallel with experiments. The Bose-Hubbard transition from a superfluid to a Mott insulator was first observed in a one-dimensional gas by [136], followed by the Pinning transition in [68].

### 6.1.3 Effects of finite temperature and trapping potential

#### Trapped systems

In trapped gases, the density spans different values, leading to a possible coexistence of the superfluid and insulating phases. For harmonic confining potentials, one can define a rescaled density:

$$\tilde{n} = Na\sqrt{\frac{V_z}{J}} \quad (6.3)$$

Rigol and colleagues computed, using QMC, the state diagrams of confined one-dimensional bosons in optical lattices [129], and the related observables in real and momentum space, accessible experimentally. The rescaled density allows to compute a state diagram in  $(\tilde{n}, U/t)$  parameter space, independent of total atom number and curvature of the potential [128]. The critical point is shifted to larger potential depths with  $(U/J)_c = 5.5$ . For the deepest lattice, at a given chemical potential, the superfluid phase is only

found at the edges of the sample, with a related non-vanishing compressibility (figure 6.5). As the potential depth is reduced, a superfluid fraction appears in the central region, gaining in importance as the potential  $U$  is lowered.

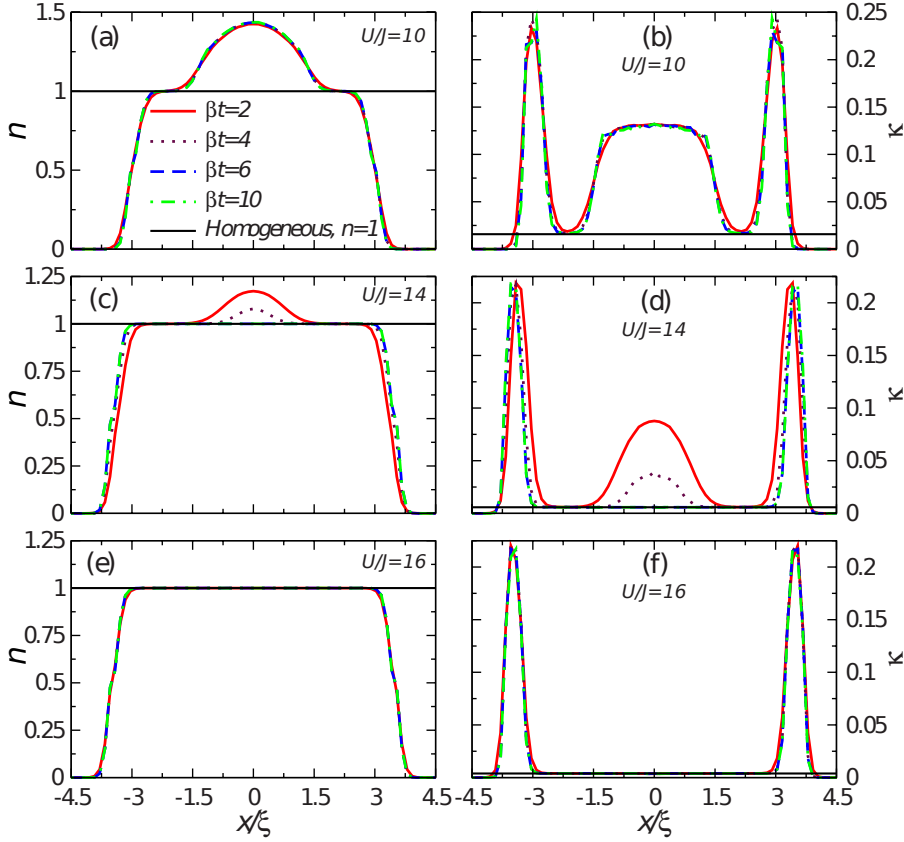


**Figure 6.5:** Figure taken from [129]. The right column represents the linear density, with flat regions translating the locally homogeneous gas in the Mott insulating phase. The left column shows the compressibility  $\kappa$  of the gas. It decays to zero in the regions where the density  $n$  is flat, showing the incompressibility of the Mott phase.  $U/J = 16$  corresponds to a typically very deep lattice, requiring high laser power experimentally. This supposes that our experimental configuration will be closer to the situations represented panels (a) and (b).

The simulations were performed for non-zero, although very low, temperatures. For  $U/t = 14$ , the superfluid barely appears for the lowest temperatures  $T = J/6k_B$  and  $T = J/10k_B$ . Thermally induced hopping enforces the superfluid in the centre as temperature is increased to  $T = J/2k_B$ . However, the considered temperatures are well below typical experimental values.

### Finite temperature

More realistic temperatures are considered in [123], illustrating that the zero-temperature phase transition becomes a smooth crossover as temperature is increased, smearing the sharp behaviour of density and compressibility at the Mott transition. In their Monte-Carlo numerics, they investigated a quasi-1D system ( $V_z = 15E_r$ ,  $V_\perp = 40.5E_r$ ) at temperatures ranging from  $3J/k_B$  to  $24J/k_B$ . They show that the thermally-induced excitations is translated by the presence of atomic pairs with neighbouring empty sites, for otherwise uniformly distributed site occupations of unity. The resulting density distribution and compressibility are plotted below:

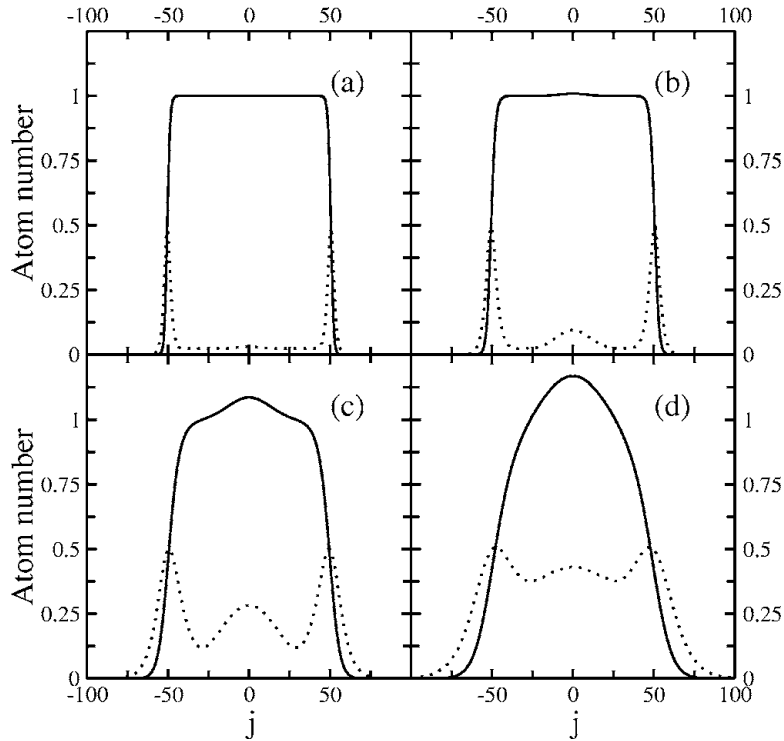


**Figure 6.6:** Density distribution (solid line) and compressibility (dotted line) of the finite-temperature state for the quasi-1D gas. Temperature is increased from (a) to (d) following:  $k_B T/J = 3$  (a), 5 (b), 12 (c) and 24 (d). As temperature is increased, the signal is clearly smeared: the thermally-promoted atoms to the superfluid phase in the centre gain in importance, until the density plateau of the Mott insulator is barely perceptible. Correspondingly, the compressibility takes larger values in the central region.

### Summary

- In 1D there exists a Mott transition, mapped by the Bose-Hubbard model, just as in three dimensions.
- Unlike the 2D or 3D model, the transition at commensurability is of BKT type.
- For high enough interactions, an arbitrarily low periodic potential suffices to enter the insulating phase: this is referred to as the Pinning transition. The generic Mott and Pinning transitions have been observed experimentally.
- On the theoretical side, efforts to understand the effects of an external trapping potential and temperature showed the possibility of coexistence of the superfluid and insulator phases. The characteristics of the Mott insulating phase (flat density distribution and vanishing compressibility) are accordingly smeared out.
- At this early stage of the experiment, it is not obvious to determine exactly in which parameter regime ( $T$ ,  $U$ , etc.) we will lie, the presented results in a trap and at finite  $T$  just give a qualitative indication on their effect.

## 6.2 Experimental setting up of the lattice

The setup of the lattice is not complete to this day, but all the equipment is ready and the first stages of installation and alignment were performed. Unfortunately we could not finalise the alignment on the atoms yet, but this should be achieved in the next months.

### 6.2.1 Lattice setup

The optics for the lattice are on two separate optical tables. On the first, a 1530 nm laser diode<sup>2</sup> injects an Erbium Doped Fibre Amplifier (EDFA)<sup>3</sup>, providing a nominal 1W of optical power. After passing through an acousto-optical modulator, the infrared light is injected into an optical fibre, to the main optical table. On this second table, containing the science chamber, the laser is first shaped to the desired size and then reflected off a dichroic plate into the vacuum, on the same path as the horizontal MOT beams. After crossing the chamber, a cat's eye configuration retro-reflects the beam back onto its incident path, creating a standing wave of periodicity  $a = \lambda/2 = 765$  cm. The cat's eye (a mirror placed at the focal point of a lens) is more stable than a simple reflection on a mirror. With a retro-reflecting configuration, any frequency fluctuation will result in lattice shaking [118]. However, it has the advantage of requiring less optical power than a counter-propagating disposition where the initial power would be split and injected into two optical separate fibres, placed in front of each other to create the standing wave. The complete optical setup is presented figure 6.7. The grazing lattice beam is reflected off the chip at a small angle  $\theta$  (inset b).

For the alignment of the lattice, the Stark effect induced by the electrical field of the laser shifts the atomic transition, an effect visible on the imaging: the imaging resonance is sensibly shifted and peak in atom number is expected to be displaced by about 10 MHz. Our experimental setup would then allow us to image the optically trapped cloud *in situ* or in momentum space, permitting different diagnoses of the superfluid and Mott insulating phases (see below for more details on the planned measurements).

### 6.2.2 Digital micromirror device

With the help of research engineer Florence Nogrette, we plan to install a Digital Micromirror Device (DMD)<sup>4</sup> on the experiment. Each micromirror in the 1024 times 768 array can be individually switched between an "on" and "off" state by tilting the axis of the mirror, to reflect the light in the desired direction ("on"), or out of the optical path ("off").

The problem with the harmonic trapping potential is that the Mott insulating and superfluid phases can coexist in the trap. After time-of-flight such as during focussing, the signal we are searching for will be smeared from the presence of the competing phase. With such a device, one can post-select atoms in the desired state by pumping the atoms into a dark state ( $|F = 1\rangle$ ) in a certain spatial region. For instance if we wish

<sup>2</sup>Fitel, 50mW max optical power, 10 MHz linewidth.

<sup>3</sup>Keopsys KPS-CUS-OEM-C-30-SLM-PM-111-FA-FA

<sup>4</sup>DLP 7000 of Texas Instruments

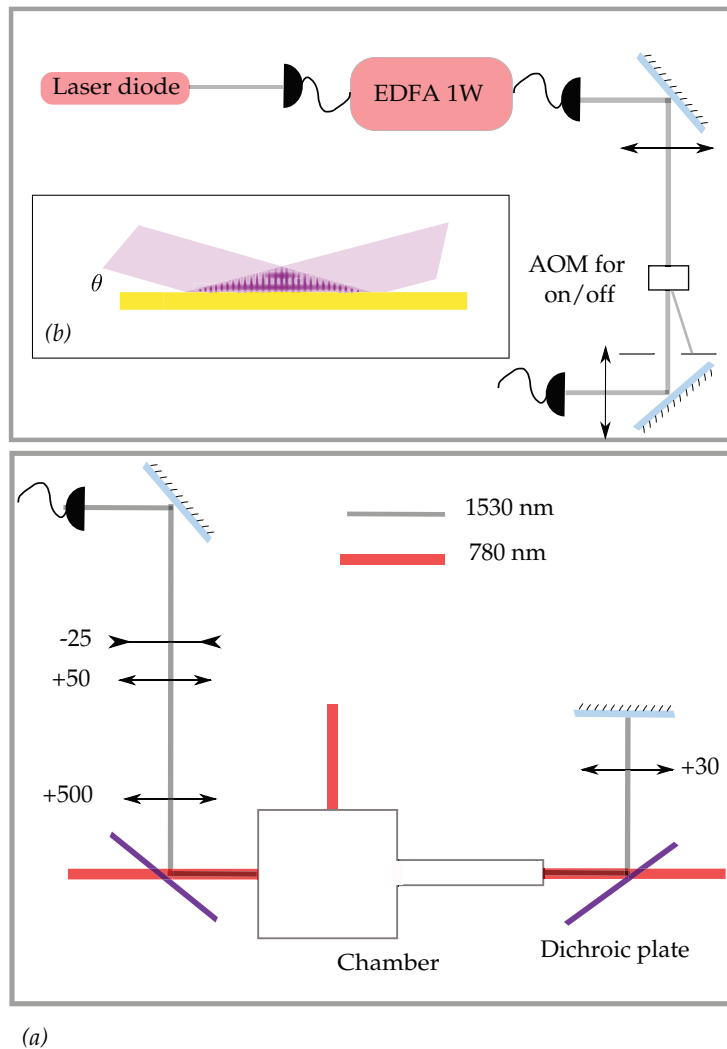


**Figure 6.7:** Optical setup: first optical table with the laser (top), second optical table with the science chamber (bottom), and reflection of the infrared beam off the chip at a small angle (inset). The chamber is seen from above, and the MOT beams represented in red.

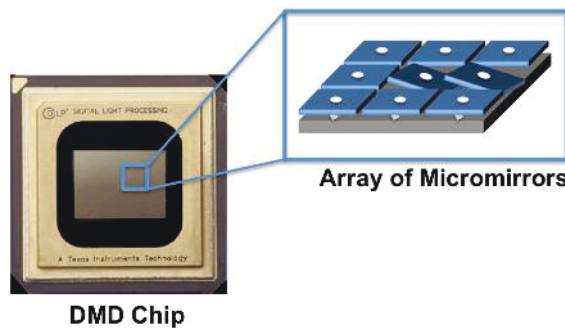


**Figure 6.8:** Figure taken from Texas Instruments, illustration of the tilting micro-mirrors.

to image the Mott insulator in the central region of the trap, after identifying its spatial extent we can programme the DMD to be "on" only on the edges of the trap and send

light to pump the atoms in the superfluid state into  $|F = 1\rangle$ . Another possible application of the DMD is the engineering of a trapping box, using a repulsive blue-detuned laser, not unlike [31], where the DMD is replaced by an intensity mask.

### Summary

- A 1530 nm laser is used to create a longitudinal periodic optical potential, on top of the magnetic confinements provided by the chip.
- The setup is almost complete, and we hope to align the lattice on the atoms in the upcoming months.
- We also expect to complete our setup with a DMD in the process, which would finalise the upgrading of our experiment to tackle new physics.

## 6.3 Experimental constraints

Although the setting up of the lattice is not complete, in this section I present the questions raised to motivate the choices for the previously presented setup.

### 6.3.1 Optical power to reach the Mott transition

For small enough interactions ( $\gamma < \gamma_{c,pinning}$ ) and at commensurability, the Mott insulating phase is reached for a minimal optical potential depth. Since the depth of the lattice is directly related to the optical power of the beam used to trap the atoms, a minimal optical power is required to cross the transition. Here we consider the transition for a deep lattice, in the Bose-Hubbard limit. The optical potential created by two counter-propagating beams is [13, 107]:

$$V_{lat}(0, 0, z) = V_0 \cos^2(kz) \quad (6.4)$$

with

$$V_0 = \alpha \left( \frac{4P_{beam}}{2\epsilon_0 c \pi w_0^2} \right) \quad (6.5)$$

$\epsilon_0$  is the vacuum permittivity,  $w_0$  the waist of the laser beam and  $c$  the speed of light. In the tight-binding approximation, the hopping term  $J$  is expressed as

$$J = \frac{4}{\sqrt{\pi}} \frac{V}{E_r} E_r \exp^{-2(V/E_r)^{1/2}}. \quad (6.6)$$

And the strength of the on-site interaction  $U$  reads [81]:

$$U = \sqrt{2\pi} \frac{g_{1D}}{\lambda} \left( \frac{V}{E_r} \right)^{1/4} \quad (6.7)$$

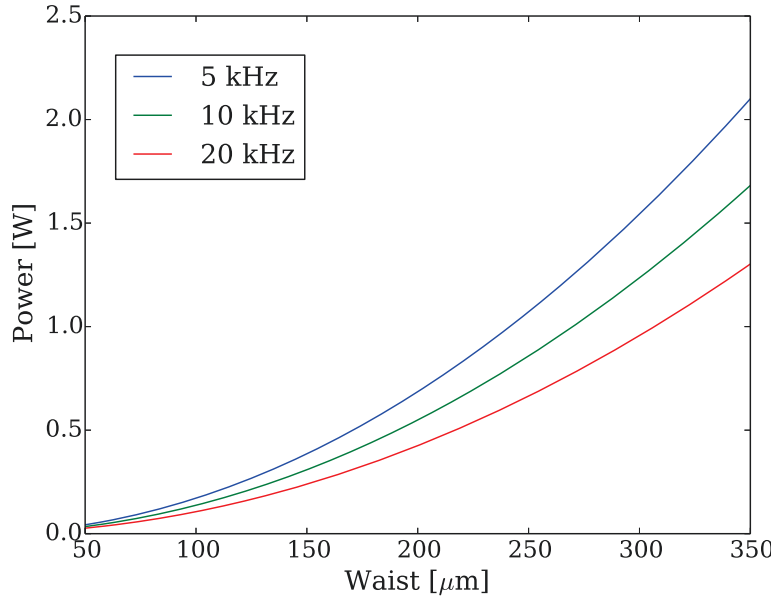


**Figure 6.9:** Power to reach the critical point, for different transverse confinements. Since the amplifier provides a maximal 1W, the effective power reached on the atomic cloud cannot reasonably exceed 500 mW, which indicates that the waist should not be larger than about 200  $\mu\text{m}$ .

The condition  $(U/J)_c = 3.85$  to cross the Mott transition can be translated to a condition on  $V_0$ , itself only dependent on the power  $P_{beam}$  and the waist  $w_0$ . Finally,  $V_{0,c}$  is the solution to the implicit equation [23]

$$4 \frac{V_{0,c}}{E_r} = \ln^2 \left[ \frac{1}{\gamma} 2\sqrt{2}\pi \left( \frac{U}{J} \right)_c \left( \frac{V_{0,c}}{E_r} \right) \right], \quad (6.8)$$

$\gamma$  being the Lieb-Liniger interaction parameter

$$\gamma = \frac{mg_{1D}}{\hbar^2 n}, \quad (6.9)$$

and, as a reminder,  $g_{1D} = 2\hbar a_S \omega_\perp$ . The required power depends on the transverse confinement  $\omega_\perp$  via the interaction parameter, and waist  $w_0$ . Figure 6.9 depicts the minimal optical power in mW, vs waist, for three typical transverse trappings. Essentially, stronger trappings would lead to lower linear densities (and higher  $\gamma$ ), and lower power to cross the critical point. Since the first lobes of the phase diagram correspond to 1, 2 or 3 atoms per site, the corresponding linear densities verifying  $\lambda n/2p \sim 1$ , where  $p = \{1, 2, 3\}$ . With  $\lambda = 1530$  nm the linear densities should be between  $2.10^6$  and  $1.10^7 \text{ m}^{-1}$ . Typically, the aimed transverse confinements will be higher than the previous studies in more weakly-interacting regimes. A landmark for comparison is the first realisation of a strongly-interacting gas on the experiment in 2011 [79], where the largest published transverse confinement of 18.8 kHz lead to a peak linear density of about  $10^6 \text{ m}^{-1}$ . In the figure below, the considered trapping frequencies are 5 kHz, 10 kHz and 20 kHz.

The laser amplifier provides a maximal optical power of 1 W. With the various sources of power loss (diffraction by an AOM, injection of a fibre, and so on), one can hope

for several hundreds of mW on the atoms, which should be sufficient, given our other experimental parameters (read below). However, a number of other experimental constraints should be taken into account to verify the feasibility of the experiment.

### 6.3.2 Geometrical constraints on the beam

Since the modulated guide is a few microns above the chip surface, rather than having a horizontal standing wave parallel to the trap axis which would cause the laser light to diffract off the edges of the chip, the beams will reflect off its surface at a small angle  $\theta$ . With this configuration, we listed four geometrical constraints on our optical setup.

The first constraint comes from this reflection of the lattice beam: the grazing incident angle could induce loss if the beam is truncated by the edge of the chip. The intensity of the gaussian beam decreases as

$$\frac{I(R, z)}{I_{max}} = \left( \frac{w_0}{w(z)} \right)^2 \exp \left( \frac{-2R^2}{w^2(z)} \right). \quad (6.10)$$

$w_0$  designates the minimum waist, and  $w(z)$  its spatial dependence,  $R$  and  $z$  are the radial and longitudinal coordinates respectively.

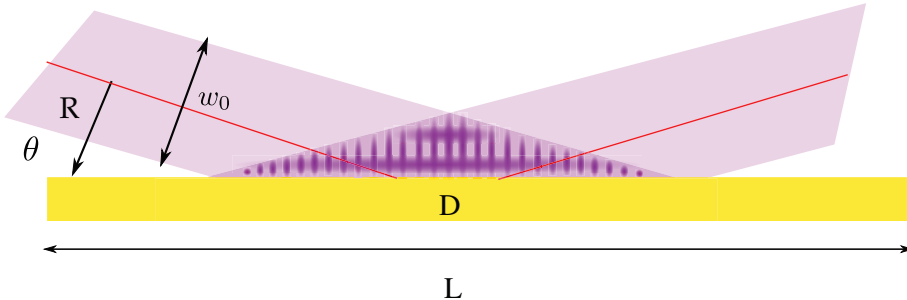


**Figure 6.10:** The maximum (central) intensity is represented in red, and decays as  $R$  increases. A region of size  $D$  is illuminated by the incident light, giving the spatial extent of the one-dimensional lattice.  $L$  is the total width of the chip. In the chamber, the chip is facing downwards at a 45° angle.

Noticing that  $R = (L/2)\sin(\theta)$  and assuming  $I(R, z) \approx I(R, 0)$  for simplicity,  $\sin(\theta)$  is related to the beam properties by

$$\sin(\theta) = \sqrt{-\left(\frac{4}{L^2}\right) \frac{w^2(z)}{2} \ln \left( \frac{I(R, z)}{I_{max}} \left( \frac{w(z)}{w_0} \right)^2 \right)}. \quad (6.11)$$

$L$  is much smaller than the Rayleigh length of the lattice beam so that we can additionally consider  $w(z) \approx w_0$ . Even a slight intensity loss by diffraction on the edge reduces the accessible  $(\theta, w_0)$  parameter space. Figure 6.11 summarises all the geometrical constraints, and the plotted excluded region (denoted A) is for a beam being at the position where the intensity is 1% of the central intensity. Naturally, this excludes too large waists.

The smaller the angle  $\theta$ , the larger the illuminated region  $D = w_0/\sin(\theta)$  of the chip, at fixed waist  $w_0$ . The length of our one-dimensional gas rarely exceeds 200  $\mu\text{m}$ . On

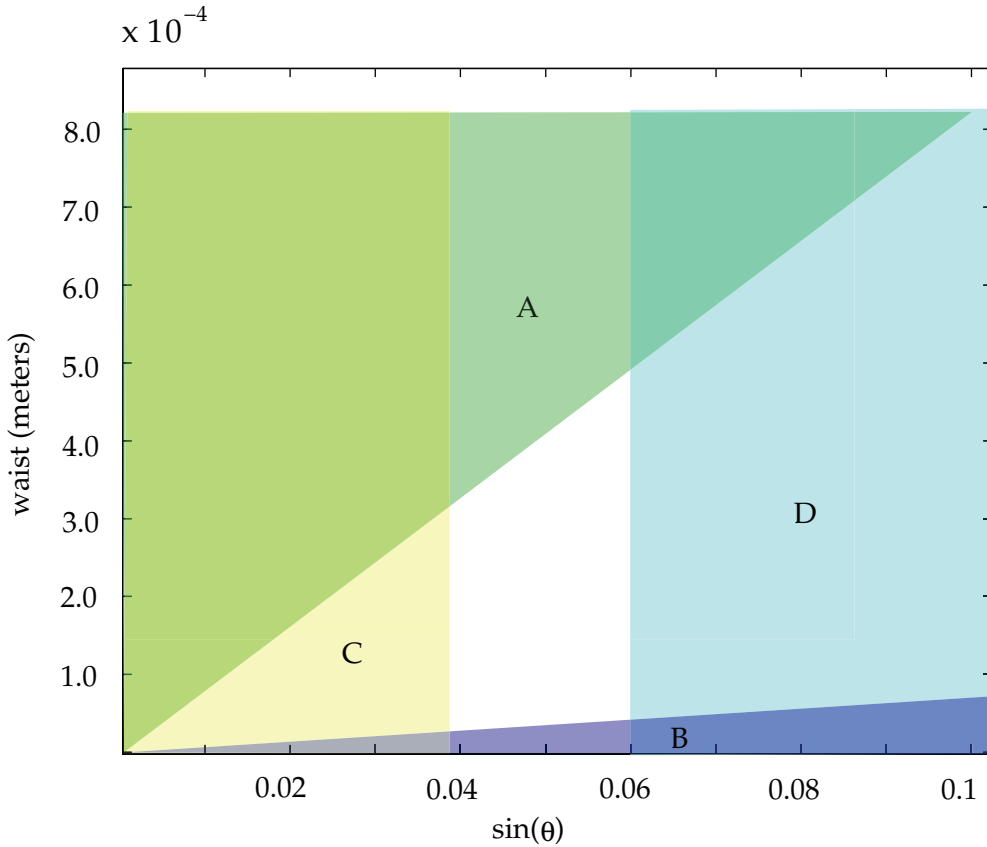


**Figure 6.11:** Summary of the geometrical constraints, represented in parameter space  $\theta, w_0$ .

this length scale, the optical power of the gaussian beam shouldn't vary too much, so that all the atoms roughly see the same lattice depth. In the parameter space diagram 6.11 (region B), the constraint chosen is that the optical power change over the cloud size shouldn't exceed 10%, which leads to an exclusion of the smallest waists. As an example, with  $w_0 = 200 \mu\text{m}$  and  $\sin(\theta) \approx 0.06$ ,  $D = 3.3 \text{ mm}$  and the atoms see very little intensity variation.

As the beam crosses the vacuum chamber, it also crosses a long tube (not represented to scale on figure 6.7) which limits the angle  $\theta$  at which the beam may arrive. The distance between the centre of the chip and the end of the tube is roughly 25 cm, and the opening is a CF40 flange. The maximum angle is  $\sin(\theta) \approx 0.06$ , by considering a window diameter of 3 cm (excluding region D of parameter space).

Since the lattice beam arrives at an angle  $\theta$ , a transverse lattice is created in addition to the desired longitudinal lattice, of periodicity  $d_{\perp} = \lambda/(2\sin(\theta))$ . Atoms are  $4 \mu\text{m}$  above the chip surface, distance at which the transverse spatial power modulation should be around its maximum. Ideally,  $d_{\perp}$  should be  $8 \mu\text{m}$ , and  $\sin(\theta) = 0.047$ . But with the experimental tolerance, if we allow for  $1 \mu\text{m}$  margin, the angle corresponding to  $d_{\perp} = 10 \mu\text{m}$  is  $\sin(\theta) = 0.0325$ . For smaller  $d_{\perp}$ , the values become larger than the already determined upper bound  $\sin(\theta) = 0.06$  (D). Naturally, if the atoms are not exactly at the maximum of the transverse lattice, the required total optical power to cross the transition will be consequently increased.

It appears that any waist between  $50 \mu\text{m}$  and  $200 \mu\text{m}$  is suitable. On the practical side, larger waists correspond to smaller numerical apertures, ensuring more homogeneous optical power in the vicinity of the atoms (this effect was neglected in the previous calculations since we crudely assumed  $w(z) = w_0$ ). With a larger waist we would also be less sensitive to the alignment. A possible set of parameters is  $w_0 = 150 \mu\text{m}$ , with an angle  $\sin(\theta) = 0.05$  (or  $d_\perp \approx 8 \mu\text{m}$ ). The power to cross the Mott transition would then range, depending on the transverse confinement  $\omega_\perp$ , from 200 to 400 mW.

### Summary

- The optical power required to cross the Mott transition is of the order of several hundreds of mW, but is strongly dependent on the transverse confinement  $\omega_\perp$  and the waist of the lattice beam  $w_0$ .
- Several constraints on our setup reduce the accessible range of parameters, and we are left with some margin for the final choice of our laser waist.

## 6.4 Prospective studies

### 6.4.1 Context

A certain number of experimental setups by colleagues have explored lattice physics with bosons in dimension one, all of which use a deep two-dimensional optical lattice to create independent parallel tubes of one-dimensional gases, with an additional weaker longitudinal periodic potential.

The first observations of the Mott and Pinning transitions in 1D made use of this experimental technique [68, 136]. A deep two-dimensional lattice along with a weaker longitudinal lattice was also used to produce a strongly-interacting Tonks-Girardeau gas: the periodic potential was used to initially pin down the atoms. The presence of the periodic potential increases the effective mass of the atoms, which results in an increase of the interaction parameter  $\gamma \propto m$  [117]. A similar experimental setup in Florence used Bragg spectroscopy to probe excitations in the superfluid and Mott insulating phases [33, 48].

Despite the remarkable results obtained, this type of setup suffers from one main drawback: in a single experimental shot a statistical ensemble of gases is produced, so that probing a single gas at a time and measuring statistical fluctuations by isolating single realisations of the gas is greatly complicated (but not impossible, [147]). By using an atom chip to produce a single one-dimensional cloud, and with our measurement methods in real and momentum space, we expect to bring new insight on the correlated phases in 1D. The planned measurements are of two types: equilibrium physics in the lattice, and out-of-equilibrium dynamics using the lattice as a tool.

### 6.4.2 Equilibrium physics

A phase transition is characterised by the evolution of correlations across the phase change, and the behaviour of a one-dimensional Bose in a periodic potential is rich,

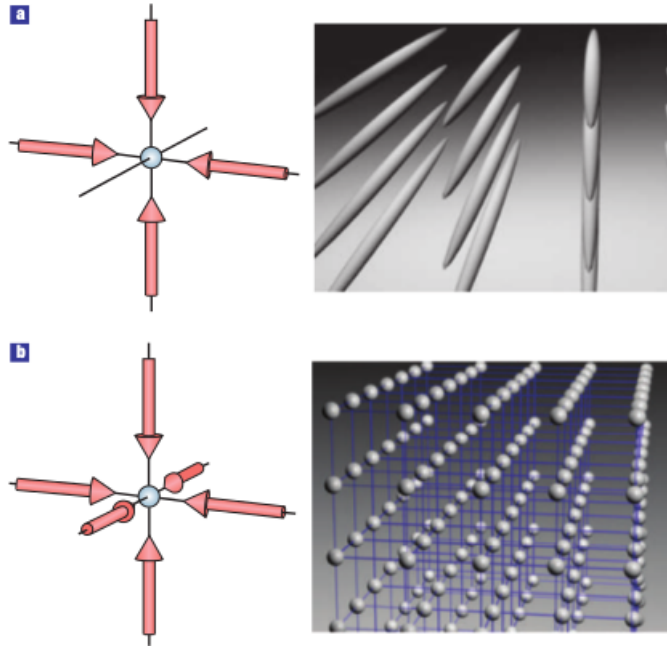


**Figure 6.12:** Two- and three-dimensional optical lattices. If the transverse lattice is much tighter than the longitudinal confinement, the tubes are decoupled and one can explore Mott physics in dimension one. Figure adapted from [13].

allowing to the occurrence of phase transitions of different universality classes. Generally speaking, our experimental setup will allow us to probe and characterise strongly-correlated phases, including the Tonks-Girardeau gas.

With our focussing method, we can access the first-order correlation function. For the Mott transition at commensurability, of BKT type, first-order correlations go from an exponential to algebraic behaviour across the transition. This feature has never been observed experimentally in the case of the Pinning transition. Alongside the momentum distributions, we can access the compressibility of the gas by probing density fluctuations. This will allow us to identify the Mott insulating phase. Similarly, the critical commensurate/incommensurate transition may be identified by the abrupt increase of the density correlation length: with the help of our new high-resolution objective this phenomenon may be accessible. The critical regime is very narrow, happening over a small range of chemical potentials: the slowly-varying potentials created with the atom chip are therefore adapted for this measurement.

Similar studies can be performed at strong interactions in homogeneous systems. So far, we could reach interaction parameters of the order of  $\gamma = 1$  [79]. However heating due to three-body losses induced by the strong confinements used (up to 50 kHz) limited the strength of interactions which could be reached. We envision to use the longitudinal optical lattice to attempt to reach more strongly interacting samples. The better signal over noise ratio achieved with the new imaging system should assist us in this task, since the desired linear densities are smaller than what we currently explore on the experiment. The lattice will also be a tool to reach more strongly-interacting regimes of the homogeneous Lieb-Liniger model, namely the Tonks gas.

### 6.4.3 Out-of-equilibrium dynamics

The Lieb-Liniger model of repulsive bosons on a continuum is an example of an integrable system, which we routinely realise on our experimental setup (the presence of slow external longitudinal potential only slightly breaks the integrability and features due to this property survive). The model is an ideal playground for the study of out-of-equilibrium dynamics in isolated quantum systems: integrable models are not expected to relax to a thermal distribution as was discussed in Chapter 5. So far, as well as extensive studies of the Lieb-Liniger model at equilibrium [5, 6, 79, 80], we began investigating physics out-of-equilibrium with the case study of the breathing mode [50]. Installing an optical lattice opens up new perspectives with the possibility of breaking the integrability by adding a periodic potential on top of the Lieb-Liniger gas. Indeed, the mechanisms leading to the equilibration of a closed quantum system are still an open question. The Eigenstate Thermalisation Hypothesis (ETH) is a strong candidate [40] as a relaxation mechanism, demonstrated numerically [130] and, very recently, experimentally [85]. This scheme is expected to fail in integrable systems.

The integrability notably translates to the existence of long-lived excitations, as was illustrated by the experiment described in [92], coined as a "quantum Newton's cradle". Oscillations of two separate clouds prepared with different velocities, in a trap, were shown to be undamped over experimental time scales. In our breathing mode study [50], we also reported that the collective excitations were long-lived. Adding a lattice to break the integrability would allow to observe whether such long-lived excitations survive or alternatively how their lifetime evolves in the non-integrable system..

One of the first experiments we wish to perform with the lattice relates to the Kibble-Zurek mechanism. When crossing a phase transition by rapidly varying the control parameters, topological defects are created [154]. In the case of the Mott transition, the defects are sine-Gordon solitons and antisolitons, and they have been studied theoretically in [38, 121]. The Kibble-Zurek mechanism relates the speed at which the phase transition is crossed to the number of defects, as long as the crossing is non-adiabatic. Our setup would allow us to study the emergence of those topological defects across the transition of interest.

#### Summary

- With the lattice, the spectrum of physical phenomena accessible on our experiment is greatly broadened.
- A quantitative characterisation of the different phase transitions (Pinning, commensurate/incommensurate) still lacks, and our experiment is well suited for this type of measurement with a direct measurement of the first-order correlation function in a single shot, and high-resolution compressibility measurements.

- Many questions regarding the equilibration of closed quantum systems remain open, and having a knob (the lattice) to turn the integrability on or off could help shed light on the underlying relaxation dynamics.



---

## Conclusions

---

The doctoral work presented in this document can be divided in three distinct projects, which in chronological order, consisted in:

- the study of momentum-space correlations of the one-dimensional Bose gas,
- significant changes brought to the experimental setup,
- and the study of the dissipative evaporation mechanism and its generation of non-thermal states.

In the very first months of my PhD, the previous version of the experimental setup routinely produced one-dimensional Bose gases and we took data for the study of momentum-space correlations. These measurements were the first of the sort: they could be performed thanks to the acquisition of the complete momentum distribution of a single 1D Bose gas in a single shot. This contrasts with experiments performing Bragg spectroscopy (where the excitations are probed one by one), or producing their 1D samples in two-dimensional lattices (where the presence of tubes with different thermodynamic quantities destroy the information on correlations in an individual tube). We demonstrated that bosonic bunching is still present in momentum space, while negative off-diagonal correlations emerge in the quasi-condensate phase. These measurements were in very good agreement with analytical calculations (in the asymptotic limits of the ideal Bose gas and the quasi-condensate) and ab initio QMC simulations (valid over the complete quasi-condensation crossover). Such measurements open the way to characterisation of many-body systems in and out-of-equilibrium. We envision to perform such measurements to study the dynamics of our 1D samples after a quench (or ramp) of the coupling parameter  $g \propto \omega_{\perp}$ . This experimental protocol can be performed on our setup thanks to the independent control of the transverse and longitudinal confinements. We already took preliminary data in this direction: the momentum correlations proved to be strongly influenced by such a quench, with the emergence of off-diagonal features non-existing at equilibrium. However since we undertook important changes on the setup we did not take more data in this direction and the study remains at a very preliminary stage yet.

In late spring of my first year, we decided to proceed to changes on the experimental setup, having to break the vacuum to replace the  $^{87}\text{Rb}$  dispensers which had run out (this was expected, given the life span of about two years of those dispensers). These changes were of various nature, motivated by two main improvements: a better stability of the experiment, and a larger numerical aperture for the imaging system. The improvement of the stability mostly implied changes in the laser setup and optics: we replaced the repumper and changed the laser configuration, with a new so-called

"Master 2" beating with "Master 1", spanning the different frequencies required during the experimental cycle. Regarding the optics, we also fibred the MOT beams, so that more optical power was required. For this purpose a Tapered Amplifier was added to provide the necessary light. Changing the imaging objective (designed and tested by former PhD student Bess Fang and colleagues) also implied a number of upgrades. It lead to the replacement of the chip, with the design of a new electronic circuit (or mask), which I drew in the first months of my PhD. At first, we wished to install a chip with a different substrate (SiC rather than AlN), but difficulties in the fabrication process made us turn back to the previous well-understood technology. Since the imaging objective had to be brought closer to the atoms, we also modified the vacuum setup, with the introduction of an indium seal. Another number of small changes also happened, like the installation of new-generation cards for the home-made sequencer or the replacement of the control computer. At the time when these lines are being written, we now have a functioning experiment which can produce dense and cold samples. We are now looking forward to implementing the focussing technique for the measurement of momentum distributions, before installing the optical lattice and DMD.

After having made significant progress on the setup, I dedicated the final months of my PhD to a more theoretical project, but not unrelated to experimental observations. Indeed, a "two-temperature" state has been regularly observed on the experiment. In short, the density fluctuations measurements are fitted with a first temperature for low densities, and a second (lower) temperature for high densities. We related this observation to a dissipative cooling mechanism, recently proposed and implemented by our colleagues in Vienna. The study was not only dedicated to the explanation of the two-temperature observation; our theoretical study goes beyond the model proposed in Vienna by taking into account the complete spectrum of excitations and coupling between modes. This showed the emergence of a stationary, non-thermal state: in the trapped system this leads to a state compatible with our experimental observation. We also studied the role of integrability in the process: by introducing two coupled masses the system seems to evolve towards an equipartition of energy, which underlines the role of integrability in the emergence of the non-thermal state. However, we need to perform more calculations to see a possible heating of the non-integrable gas, by completely solving the coupled Bogoliubov Hamiltonian. A paradox indeed remains: thermodynamic arguments predicts a heating of the quasi-condensate, while the classical field approach shows a reduction of energy in each mode. This inconsistency may be partly resolved by including poissonian noise, materialising the quantised nature of the field. Numerical simulations showed that high-energy modes indeed heat when atoms are lost. Finally, the evaporation mechanism in the one-dimensional Bose gas is not completely elucidated: it appears that the observed temperatures may be lower than the theoretical limit  $k_B T = \mu$  with a regular observation of temperatures around  $k_B T = \mu/2$  on our experiment and on the setup of our colleagues in Vienna.

# APPENDIX A

---

## More detailed calculations for the momentum correlations

---

### A.1 Correlations in the local density approximation

In this section we derive the expressions used for the bunching and regular contributions to the momentum correlations, in a trap. The general form of the second-order correlation function in momentum space is as follows:

$$\mathcal{G}(p, p') = \frac{1}{(2\pi\hbar)^2} \int d^4z e^{-ip(z_1-z_2)/\hbar} e^{-ip'(z_3-z_4)/\hbar} \left( \langle \Psi_1^\dagger \Psi_2 \Psi_3^\dagger \Psi_4 \rangle - \langle \Psi_1^\dagger \Psi_2 \rangle \langle \Psi_3^\dagger \Psi_4 \rangle \right), \quad (\text{A.1})$$

where  $d^4 \equiv dz_1 dz_2 dz_3 dz_4$ , and  $\Psi_i$  is a short-hand notation for  $\Psi(z_i)$ . Assuming that the gas has a finite correlation length  $l_c$ , the authors of [18] decomposed the four-point correlation function as:

$$\langle \Psi_1^\dagger \Psi_2 \Psi_3^\dagger \Psi_4 \rangle \langle \Psi_1^\dagger \Psi_2 \rangle \langle \Psi_3^\dagger \Psi_4 \rangle = \langle \Psi_1^\dagger \Psi_4 \rangle \delta(z_2 - z_3) + \langle \Psi_1^\dagger \Psi_4 \rangle \langle \Psi_3^\dagger \Psi_2 \rangle + \tilde{G}_2(1, 2, 3, 4). \quad (\text{A.2})$$

We already encountered this form in the main text of Chapter 4. As a reminder, the first term is the shot noise, the second term the bunching contribution and the final contribution is a regular function which describes the binary elastic processes in the interacting gas. The bunching term in the local density approximation (which we calculate by injecting the bunching expression of A.2 into the integral above) becomes:

$$B(p, p') = \left| \frac{1}{2\pi\hbar} \int d^2z e^{-i(pz_1 - p'z_4)} \langle \Psi_1^\dagger \Psi_4 \rangle \right|^2. \quad (\text{A.3})$$

By introducing the variables  $z_c = (z_1 + z_4)/2$  and  $u = z_1 - z_4$ , as well as  $(p + p')/2$  and  $(p - p')/2$ , the expression to evaluate can be reformulated as:

$$B(p, p') = \left| \frac{1}{2\pi\hbar} \int dz_c du \langle \Psi_1^\dagger \Psi_4 \rangle e^{-i\frac{p+p'}{2}u} e^{-i\frac{p-p'}{z_c}} \right|^2. \quad (\text{A.4})$$

Bearing in mind that  $l_\phi$  (typical length scale of  $\langle \Psi_1^\dagger \Psi_4 \rangle$ ) is much smaller than the system size, one can integrate only  $u$ , assuming the integrand does not depend on  $z_c$  (at this

point we apply the local density approximation), which then gives the final expression:

$$B(p, p') = \left| \frac{1}{\hbar} \int dz \nu_{n(z)}^{(h)}((p + p')/2) e^{i(p-p')z/\hbar} \right|^2, \quad (\text{A.5})$$

by identification of the momentum distribution (occupation number, without dimension) with the Fourier transform of the first-order correlation function. Let us now turn to the computation of the regular term in the LDA:

$$\langle \delta n_p \delta n_{p'} \rangle_{reg} = \frac{1}{(2\pi\hbar)^2} \int d^4 z e^{-ip(z_1-z_2)/\hbar} e^{-ip'(z_3-z_4)/\hbar} \tilde{G}_2(1, 2, 3, 4). \quad (\text{A.6})$$

$\tilde{G}_2(1, 2, 3, 4)$  is non-zero if the  $z_i$  are close ( $\ll L$ ). By considering the centre of mass coordinate  $z_{CM}$  such that  $z_1 + z_2 + z_3 + z_4 = 0$ , we reformulate the integral as:

$$\langle \delta n_p \delta n_{p'} \rangle_{reg} = \frac{1}{(2\pi\hbar)^2} \int dz_{CM} \int dz^3 e^{-ip(z_1-z_2)/\hbar} e^{-ip'(z_3-z_4)/\hbar} \tilde{G}_2(1, 2, 3, 4). \quad (\text{A.7})$$

The second integrand is a known result of [18] since one can assume the system as locally homogeneous, with  $z_1, z_2, z_3 \ll L$ . The result of integration over  $d^3 z$  is  $l_c^3 n(z_{CM}) \mathcal{F}_{partial}$  where  $\mathcal{F}_{partial} = \mathcal{F}_{hom}/8$ ,  $\mathcal{F}_{hom}$  being the expression of the regular function found in [18]. Finally:

$$\langle \delta n_p \delta n_{p'} \rangle_{reg} = \int dz \frac{l_\phi^3 n^2}{(2\pi\hbar)^2} \mathcal{F}_{partial} \left( \frac{2l_\phi p}{\hbar}, \frac{2l_\phi p'}{\hbar}; t, \gamma \right). \quad (\text{A.8})$$

## A.2 The intensive quantity C and its relevant limits

We previously defined the following quantity to study the behaviour of the correlations over the crossover:

$$C = \sum_\alpha \langle \delta N_\alpha \delta N_{-\alpha} \rangle / \langle N_0 \rangle \quad (\text{A.9})$$

Let us assume that  $\hbar/L$  is much smaller than the experimentally accessible momentum scales. The momentum correlations then read:

$$\langle \delta n_p \delta n_{p'} \rangle = \delta(p - p') (\langle n_p \rangle + \mathcal{B}(p)) + \langle \delta n_p \delta n_{p'} \rangle_{reg}. \quad (\text{A.10})$$

Separating the bunching and regular contributions, we define  $C$  as  $C \langle N_0 \rangle = U_i + U_r$  where

$$U_i = \int dp \mathcal{R}(p, p) (\langle n_p \rangle + \mathcal{B}(p)), \quad (\text{A.11})$$

$$U_r = \int \int dp dp' \langle \delta n_p \delta n_{p'} \rangle_{reg}, \quad (\text{A.12})$$

and

$$\mathcal{R}(p, p') = \sum_\alpha \mathcal{A}(\alpha, p) \mathcal{A}(-\alpha, p'). \quad (\text{A.13})$$

Note that  $\mathcal{R}(p, p')$  is periodic in  $p$  such that  $\mathcal{R}(p + \Delta, p' - \Delta) = \mathcal{R}(p, p')$ . In the relevant limit  $\delta, \Delta_z \ll \hbar/\phi$ :

$$U_r \approx \Delta \int dp \langle \delta n_p \delta n_{-p} \rangle_{reg}, \quad (\text{A.14})$$

$$U_i \approx \Delta (\langle n_0 \rangle + \mathcal{B}(0)) \int dp \frac{\mathcal{R}(p, p)}{\Delta} \quad (\text{A.15})$$

The integral  $\mathcal{I} = \int dp \mathcal{R}(p, p)/\Delta$  present in equation A.15 takes the asymptotic value  $\mathcal{I} \approx 1/2$  in the second relevant limit  $\delta \gg \Delta$ , such that finally:

$$C = \frac{1 + \mathcal{B}(0)/\langle n_0 \rangle}{2} + \int dp \langle \delta n_p \delta n_{-p} \rangle_{reg} / \langle n_0 \rangle. \quad (\text{A.16})$$

With the local density approximation and a transformation to integrate over the chemical potential  $\mu$  instead of  $z$ ,  $C$  appears as an intensive quantity which depends exclusively on  $\gamma_0$  ( $\gamma$  in the centre of the trap/cloud) and  $t$ .



## APPENDIX B

---

### Split-time method

---

The split-time method is a typical numerical method used to propagate any generic Hamiltonian which can be written in the form

$$\hat{\mathcal{H}} = \hat{V} + \hat{K}. \quad (\text{B.1})$$

$\hat{V}$  is the potential term, diagonal in real space, and  $\hat{K}$  the kinetic term, diagonal in Fourier space. Therefore the method relies on choosing the most convenient representation for each of these terms: space representation for the first and momentum representation for the second. The Hamiltonian associated with the non-linear Schrödinger equations falls in this category of problems. The evolution operator, by definition, acts on the wavefunction  $\Psi$  as:

$$U(\Delta t) = e^{-\frac{i}{\hbar} \hat{\mathcal{H}} \Delta t} = e^{-\frac{i}{\hbar} (\hat{V} + \hat{K}) \Delta t} \quad (\text{B.2})$$

The idea of the splitting method is to appropriately write the exponentiated sum of operators  $e^{A+B}$  to perform the smallest numerical error. A first possibility is to simply consider  $e^{A+B} = e^A e^B$ , in other terms write:

$$U(\Delta t) \approx e^{-\frac{i}{\hbar} \hat{V} \Delta t} e^{-\frac{i}{\hbar} \hat{K} \Delta t} \quad (\text{B.3})$$

This is of course not accurate in general, according to the Baker-Haussdorf formula:

$$e^{\epsilon(A+B)} = e^{\epsilon A} e^{\epsilon B} e^{-\epsilon^2/2[A,B]} e^{\mathcal{O}(\epsilon^3)} \quad (\text{B.4})$$

Using this relation, it appears that the error made when writing B.3 is:

$$\frac{e^{-\frac{i}{\hbar} \hat{V} \Delta t} e^{-\frac{i}{\hbar} \hat{K} \Delta t} - U(\Delta t)}{U(\Delta t)} = \mathcal{O}(\Delta t^2). \quad (\text{B.5})$$

A smarter way of decomposing the product of exponentials is the split the effect of the term  $\hat{V}$  in the following manner:

$$U(\Delta t) \approx e^{-\frac{i}{\hbar} \hat{V} \Delta t/2} e^{-\frac{i}{\hbar} \hat{K} \Delta t} e^{-\frac{i}{\hbar} \hat{V} \Delta t/2} \quad (\text{B.6})$$

The error performed using this so-called split-time algorithm has a more advantageous scaling in time step  $\Delta t$ :

$$U_{\text{splitting}}(\Delta t) = e^{-\frac{i}{\hbar} \hat{\mathcal{H}} \Delta t} e^{\mathcal{O}(\Delta t^3)} e^{-\frac{1}{2} \left( \frac{\Delta t}{\hbar} \right)^2 [\frac{V}{2}, K]} e^{\mathcal{O}(\Delta t^3)} e^{-\frac{1}{2} \left( \frac{\Delta t}{\hbar} \right)^2 [K, \frac{V}{2}]} \quad (\text{B.7})$$

So that

$$\frac{U_{\text{splitting}}(\Delta t) - U(\Delta t)}{U(\Delta t)} = \mathcal{O}(\Delta t^3). \quad (\text{B.8})$$

Using this decomposition of the evolution operator, the algorithm to propagate the wavefunction over a time step  $\Delta t$  is as follows:

- Compute  $\Psi_1 = \Psi(z)e^{-\hat{V}(z)\Delta t/2}$ ,  $V(z)$  being diagonal in space representation.
- Take the Fourier transform  $\tilde{\Psi}$
- Compute  $\tilde{\Psi}_2 = \tilde{\Psi}_1 e^{-\hat{K}(k)\Delta t}$ ,  $\hat{K}(k)$  being diagonal in momentum representation.
- Transform back to  $\Psi_2$
- Compute  $\Psi_3 = \Psi_2 e^{-\hat{V}(z)\Delta t/2}$
- Repeat.

The split-time method can also be used to propagate the coupled non-linear Schrödinger equation since the coupling term is of the same form as the same-species interaction term.

## APPENDIX C

---

### Numerical methods for the trapped gas

---

The following section is based on references [11,12,19], and briefly introduces the methods used to prepare the initial state for the classical field simulation in the trap, and its propagation: the so-called stochastic projected GPE and projected GPE.

The initial state is prepared with a stochastic projected Gross-Pitaevskii equation (SPGPE). The classical field approach by definition considers the field operators as c-numbers  $\Psi_C$ , approximation valid as long as the occupation numbers  $n_i = k_B T / \epsilon_i$  ( $\epsilon_i$  being the energy of mode  $i$ ) are large. In the trapped system, the highly-occupied modes are treated in this manner, while the more sparsely populated, non-classical modes are considered separately as a static finite temperature reservoir. The simple-growth SPGPE is given by:

$$d\Psi_C(z, t) = \mathcal{P}_C \left\{ \left[ -\frac{i}{\hbar} \mathcal{L}_C + \kappa_{th}(\mu - \mathcal{L}_C) \right] \Psi_C(z, t) dt + \sqrt{\kappa_{th} k_B T} dW(z, t) \right\}. \quad (\text{C.1})$$

$\mathcal{P}_C$  is the projector onto the subspace of classical (highly-populated) modes, and the operator  $\mathcal{L}_C$  describes the usual Gross-Pitaevskii dynamics:

$$\mathcal{L}_C \Psi_C = \left( -\frac{\hbar^2}{2m} \frac{\partial^2}{\partial z^2} + \frac{1}{2} \omega_z^2 z^2 + g |\Psi_C|^2 \right) \Psi_C. \quad (\text{C.2})$$

$dW(z, t)$  verifies

$$\langle W^*(z, t) W(z', t + dt) \rangle = \delta_C(z - z') dt, \quad (\text{C.3})$$

$\delta_C$  being the kernel of the projection operator  $\mathcal{P}_C$ , which essentially represents a Dirac distribution. The growth rate  $\kappa_{th}$  represents the strength of the thermal and diffusive damping experienced by the classical modes in the presence of the non-classical bath.  $\kappa_{th}$  is chosen for computational convenience rather than physical arguments, since its value has no consequence on equilibrium configurations.

The dynamics of the system under atom loss (or any other perturbation of the system, like a longitudinal quench for instance in the case of [19]) is then given by the Projected Gross-Pitaevskii equation (PGPE), which can be deduced from the SPGPE by setting  $\kappa_{th} = 0$ .

All numerical calculations are performed in the Hermite-Gauss basis, which is the single-particle eigenstates for the trapped Bose gas. The basis cutoff is in direct proportion to the energy cutoff that defines the classical region: it should be chosen such that the average occupation number of those modes are larger than unity. The Hermite-Gauss basis is the most cost-efficient choice: it approximates the more sparsely occupied modes well, thereby allowing a smooth transition between the classical and non-classical regions.

## APPENDIX D

---

### Recovering the stochastic GPE in the truncated Wigner approach

---

For dissipative quantum systems a common approach is to invoke the master equation, which gives the evolution of the density matrix of the dissipative system. It is a statistical approach, in the sense that the method describes the behaviour of the system after many realisations. In this appendix, we derive the stochastic Gross-Pitaevskii equation used in the last section of Chapter 5 from the master equation. In the Wigner representation a Fokker-Planck equation is recovered. After applying the truncated Wigner approximation the stochastic classical field equation is derived.

Consider the density operator of the system  $S \rho$ . The evolution of the complete system ( $S$  and bath) can be written in terms of the density matrix: this is the quantum Liouville equation, replacing the Schrödinger equation for the wavefunction  $\Psi$ :

$$i\hbar \frac{\partial \rho}{\partial t} = [H_{tot}, \rho], \quad (\text{D.1})$$

Where  $H_{tot}$  is the Hamiltonian of the complete system.  $H_{tot}$  contains two terms: the Lieb-Liniger Hamiltonian and the Hamiltonian describing the coupling of the system with the bath. We assume this coupling is weak so that it can be treated perturbatively, and that the spectrum of the bath is a very broad continuum so that the dynamics of the system is irreversible. The dynamics of our subsystem of interest (the quasi-condensate in our case) is given by the following equation on the density matrix, a master equation referred to as the Lindblad equation:

$$\frac{d\rho}{dt} = \frac{1}{i\hbar} [H, \rho] + \mathcal{L}[\rho] \quad (\text{D.2})$$

$\mathcal{L}$  is the term which takes into account the dissipation while the commutator represents the usual Hamiltonian evolution of a closed quantum system. The former depends on the density matrix  $\rho$ , and the master equation takes the following form<sup>1</sup>, expliciting the

---

<sup>1</sup>Having realised that the appendix is already quite lengthy, I decided to directly write down the final form of this operator. An excellent introduction which entirely derives the Lindblad equation can be found in [105], sorry.

second term [105, 148]:

$$\frac{d}{dt}\rho(t) = \frac{1}{i\hbar} [H, \rho] + \frac{\Gamma}{2} \sum_j \left( 2\Psi(j)\rho\Psi(j) - \Psi(j)^\dagger\Psi(j)\rho - \rho\Psi^\dagger(j)\Psi(j) \right) \quad (\text{D.3})$$

Here the system has been discretised on a grid of spacing  $\delta z$ . The annihilation operator  $\Psi$  satisfies the bosonic commutation relation in cell  $j$ :  $[\Psi(j)^\dagger, \Psi(j)] = 1$ .  $\tilde{g}$  denotes the rescaled coupling constant  $g/\delta x$ . This equation describes the non-hermitian evolution of the open quantum system  $S$ , with dissipation into a large reservoir.  $H$  is the Lieb-Liniger Hamiltonian, which takes the following form with the discretised variables:

$$H = \sum_j \left( -\Psi(j)^\dagger \frac{\hbar^2}{2m} \partial_j^2 \Psi(j) + \frac{\tilde{g}}{\Psi} (j) \Psi^\dagger(j) \Psi(j) \Psi(j) \right) \quad (\text{D.4})$$

$\partial_j^2$  denotes the second-order finite difference. A convenient way to describe the system is to use the Wigner representation of the density matrix  $\rho$ , which writes:

$$W(\Psi(j)) = \int \prod_j d^2\lambda(j) \frac{e^{-(\lambda(j)\Psi^*(j)+\lambda^*(j)\Psi(j))}}{\pi^2} \chi(\lambda(j)), \quad (\text{D.5})$$

where

$$\chi(\lambda) = \text{Tr} \left( \rho e^{\sum_j (\lambda\Psi^+ - \lambda^*\Psi)} \right). \quad (\text{D.6})$$

The idea is now to write the Lindblad equation in this phase-space formalism. Let us first ignore the free evolution of  $\rho$  due to the Hamiltonian  $H$  and focus on the effect of atom loss captured in the second term of the Lindblad equation. The action of the creation and annihilation operators  $\Psi(j)$ ,  $\Psi^\dagger(j)$  on the density matrix  $\rho$  take the following form in terms of the Wigner representation [148]:

$$\begin{aligned} \Psi(j)\rho &\rightarrow \left( \Psi(j) + \frac{1}{2} \frac{\partial}{\partial\Psi(j)} \Psi(j) \right) W[\Psi] \\ \Psi^\dagger(j)\rho &\rightarrow \left( \Psi(j) - \frac{1}{2} \frac{\partial}{\partial\Psi(j)} \Psi(j) \right) W[\Psi] \\ \rho\Psi(j) &\rightarrow \left( \Psi(j) - \frac{1}{2} \frac{\partial}{\partial\Psi(j)} \Psi(j) \right) W[\Psi] \\ \rho\Psi^\dagger(j) &\rightarrow \left( \Psi(j) + \frac{1}{2} \frac{\partial}{\partial\Psi(j)} \Psi(j) \right) W[\Psi] \end{aligned} \quad (\text{D.7})$$

From these correspondance relations giving the Wigner representation of the action of  $\Psi(j)$ ,  $\Psi^\dagger(j)$  on  $\rho$ , we find:

$$\frac{\partial W}{\partial t} = \frac{\Gamma}{2} \sum_j \left( -\frac{\partial}{\partial\Psi(j)} (\Psi(j)) + \frac{\partial}{\partial\Psi^*(j)} (\Psi^*(j)) + \frac{\partial}{\partial\Psi(j)} \frac{\partial}{\partial\Psi^*(j)} \right) W(\Psi, \Psi^*). \quad (\text{D.8})$$

This equation, of Fokker-Planck type, is itself sampled by a stochastic process

$$d\Psi = -\frac{\Gamma}{2} \Psi dt + d\xi, \quad (\text{D.9})$$

$d\xi$  being a gaussian random variable, of vanishing mean value and of variance

$$\langle d\xi^*(x)d\xi(x') \rangle = \frac{\Gamma}{2} dt \delta_{x,x'}. \quad (\text{D.10})$$

The evolution of the Wigner function under the Lieb-Liniger Hamiltonian is non trivial, since  $H$  is non-quadratic in the field operators: the evolution contains higher-order derivative terms in  $\Psi$  such that the time evolution of the Wigner function does not reduce to a Fokker-Planck equation and cannot be represented by a stochastic process. However, for weakly interacting highly degenerate gases, the truncated Wigner approximation, which amounts to neglecting the higher order derivative terms, is a good description. Under this assumption, the Hamiltonian evolution of the Wigner function is a drift process corresponding to the dynamical equation for the classical field  $\Psi$ , whose discretised version is

$$i\hbar \frac{\partial \Psi}{\partial t} = -\frac{\hbar^2}{2m} \partial_j^2 \Psi + \tilde{g} |\Psi|^2 \Psi. \quad (\text{D.11})$$

Combining this with [D.9](#), we get:

$$id\Psi = \left( -\frac{\hbar^2}{2m} \partial_j^2 \Psi + \tilde{g} |\Psi|^2 \Psi - i \frac{\Gamma}{2} \Psi \right) dt + d\xi. \quad (\text{D.12})$$

We recover the stochastic Gross-Pitaevskii equation considered as the starting point of the study presented in the last section of Chapter 5.



## APPENDIX E

---

### Résumé en français

---

Ce manuscrit présente mes travaux de thèse, effectués dans l'équipe Puce Atomique. Nous utilisons une micro-structure, qui comporte des micro-fils à sa surface, permettant de créer des pièges magnétiques. Avec cette puce, nous confinons des atomes bosoniques ( $^{87}\text{Rb}$ ) dans une géométrie uni-dimensionnelle. Cela signifie qu'en pratique, les atomes se trouvent dans l'état fondamental de l'oscillateur harmonique transverse. C'est une réalisation expérimentale d'un modèle intégrable: le modèle dit de Lieb-Liniger [100, 101]. La physique des bosons est particulière en dimension une, en particulier il n'existe pas de condensation à proprement parler. Cependant, les interactions répulsives présentes induisent un "crossover" (par opposition à une transition de phase), avec la présence d'une phase dite de "quasi-condensat", qui ne comporte pas d'ordre à longue portée. Le travail effectué lors de cette thèse peut être divisé en trois parties bien distinctes.

Dans un premier temps, nous avons mesuré les corrélations dans l'espace des vitesses de nos échantillons uni-dimensionnels, à travers le crossover de quasi-condensation. Sur notre expérience, grâce à une technique présentée dans [80], nous pouvons mesurer la distribution complète en vitesse de notre système en un coup. En acquérant un ensemble de telles images, nous pouvons en déduire les corrélations définies par

$$\mathcal{G}(k, k') = \langle \delta \hat{n}_k \delta \hat{n}_{k'} \rangle = \langle \hat{n}_k \hat{n}_{k'} \rangle - \langle \hat{n}_k \rangle \langle \hat{n}_{k'} \rangle, \quad (\text{E.1})$$

où  $k$  représente le vecteur d'onde et  $n_k$  la population du mode  $k$ . Nos mesures ont été systématiquement comparées à des calculs analytiques (dans les régimes asymptotiques où le gaz est profondément quasi-condensat ou idéal) ou à des simulations numériques exactes. Nous avons mis en évidence la présence de corrélations négatives hors de la diagonale. Ces anti-corrélations sont une signature de l'absence de l'ordre à longue portée dans notre système et cette mesure constitue leur première mise en évidence.

Ces mesures ont été effectuées sur le montage expérimental, avant d'entreprendre de nombreuses modifications. Ces changements ont été motivés par deux aspects: l'amélioration de la stabilité de l'expérience et l'installation d'un système d'imagerie avec une plus grande ouverture numérique. Pour cette première motivation, les changements concernaient principalement le système laser. Presque tous les lasers ont été remplacés, nous avons changé le système d'asservissement et nous avons installé un

amplificateur pour sensiblement augmenter la puissance optique disponible. En effet, l'amélioration de la stabilité est aussi passée par l'installation de fibres optiques pour diminuer la propagation de nos faisceaux en espace libre. Ces fibres nécessitent une plus grande puissance en raison des pertes à l'injection. Pour le changement de système optique, nous avons dû modifier le schéma électronique de la puce pour déplacer le piége uni-dimensionnel, et enfin cela a aussi nécessité un changement de bride pour notre chambre à vide: pour amener notre objectif au plus près des atomes il a fallu installer une bride rentrante avec un joint en Indium. Ces changements sont désormais effectués, et l'expérience produit de façon régulière des quasi-condensats froids et denses. Après la calibration des mesures de distributions en impulsions, nous pourrons passer à l'étude de "quench" en interaction: l'idée est d'étudier la réponse du système intégrable à une variation brutale d'un paramètre du Hamiltonien, ici le couplage entre atomes.

Après avoir travaillé sur le montage expérimental pour apporter ces modifications, la fin de ma thèse était axé sur un projet plus théorique: l'étude d'un nouveau mécanisme de refroidissement des gaz uni-dimensionnels. Habituellement, pour refroidir des atomes à des températures bien en-deçà de la limite de dégénérescence, les atomes sont soumis à une évaporation. L'idée est d'enlever les atomes les plus énergiques, pour que les atomes restantes thermalisent à une température plus faible. Cependant, comme en 1D tous les atomes occupent le même état transverse, il n'est pas attendu que ce mécanisme fonctionne. Pourtant, des températures aussi faibles que  $E_{0,\perp}/10 = \hbar\omega_\perp/10$  ont été observées sur notre expérience et par d'autres [79]. L'idée du nouveau mécanisme (proposée dans [65] et testée expérimentalement dans [124]) est d'éliminer les atomes du gaz sans sélection aucune, de façon continue, uniforme et constante. Ainsi, cela diminue l'énergie dans les modes d'excitation du système et par conséquent la température. Nous avons effectué des simulations numériques en champ classique pour montrer que cela mène à un état hors d'équilibre où chaque mode subit une décroissance à un taux différent, menant à un état final, robuste dans le temps, où chaque mode à une température différente. En particulier, les modes de basse énergie ont une "température" plus faible que les modes de haute énergie. Nous avons relié ces résultats à des observations expérimentales faites par le passé.

En fonction de la méthode utilisée pour mesurer la température, les valeurs de  $T$  trouvées peuvent être très différentes, bien au-delà de l'incertitude sur la mesure. La première méthode utilise le profil de densité linéaire *in situ*: avec la connaissance l'équation d'état (dite de Yang-Yang), nous pouvons déduire une température, connaissant la distribution de densité et de potentiel chimique. Cette méthode donne une première température  $T_{prof}$  et sonde les bords du piége, où les excitations sont de plus grande énergie. La seconde méthode relie les fluctuations de nombre d'atoms au sein d'un pixel  $\Delta$  à la température: les deux sont proportionnels par la compressibilité du système. Cette compressibilité est connue avec la connaissance d'une équation d'état, et de même, nous pouvons extraire une température. Cette méthode, qui donne  $T_{fluc} < T_{prof}$ , sonde plutôt les modes de faible énergie comme  $\Delta \ll \xi$ . Nous avons vérifié la compatibilité avec les résultats théoriques en effectuant de nouvelles simulations, dans un piége cette fois. Ces simulations ont donné lieu à des observations similaires. En plus de ces simulations, nous avons aussi considéré un système non-intégrable en

introduisant un couplage entre deux masses différentes, et ce système s'équilibre au contraire du système intégrable. Enfin, le champ classique prédit des températures qui décroissent vers zéro dans la limite des faibles densités, ce qui n'est pas physique. Pour palier à cette incohérence, il faut considérer une équation d'évolution stochastique, dont le terme de bruit modélise la nature discrète du champ. Ce terme limite la température asymptotique à une valeur non-nulle.

Par la suite, un réseau optique longitudinal sera installé sur l'expérience pour ajouter un potentiel périodique en plus du confinement magnétique. Cela permettra de nombreuses études nouvelles avec cet ingrédient physique qui enrichit le système expérimental.



---

## Bibliography

---

- [1] A. PERRIN, R. BÜCKER, S. MANZ, T. BETZ, C. KOLLER, T. PLISSON, T. SCHUMM, AND J. SCHMIEDMAYER, *Hanbury Brown Twiss Correlations Across the Bose-Einstein Condensation Threshold*, Nat. Phys., 8 (2012).
- [2] E. ALTMAN, E. DEMLER, AND M. D. LUKIN, *Probing Many-body states of Ultracold Atoms via Noise Correlations*, Phys. Rev. A, 70 (2004).
- [3] J. ARMIJO, *Fluctuations de densité dans des gaz de bosons quasi-unidimensionnels*, PhD thesis, Université Paris Sud, 2011.
- [4] J. ARMIJO, C. L. GARRIDO-ALZAR, AND I. BOUCHOULE, *Thermal Properties of AlN-based Atom Chips*, EPJD, 56 (2010).
- [5] J. ARMIJO, T. JACQMIN, K. KHERUNTSYAN, AND I. BOUCHOULE, *Probing Three-body Correlations in a Quantum Gas using the Measurement of the Third Moment of Density Fluctuations*, Phys. Rev. Lett., 105 (2010).
- [6] ——, *Mapping out the Quasi-Condensation Transition Through the Dimensional Crossover from One to Three Dimensions*, Phys. Rev. A, 83 (2011).
- [7] C. AUSSIBAL, *Réalisation d'un condensat de Bose-Einstein sur une micro-structure*, PhD thesis, Université Paris Sud, 2003.
- [8] X. BAILLARD, A. GAUGUET, S. BIZE, P. LEMONDE, P. LAURENT, A. CLAIRON, AND P. ROSENBUSCH, *Interference-filter-stabilized External-cavity Diode Lasers*, Optics Communications, 266 (2006).
- [9] J. BERGES, S. BORSÁNYI, AND C. WETTERICH, *Prethermalization*, Phys. Rev. Lett., 93 (2004).
- [10] H. BETHE, *Zur Theorie der Metalle*, Z. Phys., 71 (1931).
- [11] P. B. BLAKIE, A. S. BRADLEY, M. J. DAVIS, R. J. BALLAGH, AND C. W. GAR DINER, *Dynamics and Statistical Mechanics of Ultra-cold Bose Gases using C-Field Techniques*, arXiv, 0809.1487 (2008).
- [12] P. B. BLAKIE AND M. J. DAVIS, *Projected Gross-Pitaevskii Equation for Harmonically Confined Bose Gases at Finite Temperature*, Phys Rev. A, 72 (2005).
- [13] I. BLOCH, *Ultracold Quantum Gases in Optical Lattices*, Nat. Phys., 1 (2005).
- [14] M. BOCKRATH, D. COBDEN, J. LU, A. RINZLER, R. SMALLEY, L. BALENTS, AND P. L. MC EUEN, *Luttinger-Liquid Behaviour in Carbon Nanotubes*, Nature, 397 (1999).

- [15] G. BOERIS, L. GORI, M. HOOGERLAND, A. KUMAR, E. LUCIONI, L. TANZI, M. INGUSCIO, T. GIAMARCHI, C. D'ERRICO, G. CARLEO, G. MODUGNO, AND L. SANCHEZ-PALENCE, *Mott Transition for Strongly Interacting One-Dimensional Bosons in a Shallow Periodic Potential*, Phys. Rev. A, 93 (2016).
- [16] N. BOGOLIUBOV, *On the Theory of Superfluidity*, J. Phys. (USSR), XI (2013).
- [17] I. BOUCHOULE, *1D Bose gases and Cold Atom Experiments*, Les Houches Lecture Notes, (2013).
- [18] I. BOUCHOULE, M. ARZAMAZOV, K. KHERUNTSYAN, AND D. GANGARDT, *Two-body Momentum Correlations in a Weakly Interacting One-dimensional Bose Gas*, Phys. Rev. A, 86 (2012).
- [19] I. BOUCHOULE, S. S. SZIGETI, M. J. DAVIS, AND K. KHERUNTSYAN, *Finite-temperature Hydrodynamics for One-dimensional bose Gases: Breathing Mode Oscillations as a Case Study*, arXiv, 1602.07889 (2016).
- [20] I. BOUCHOULE, J.-B. TREBBIA, AND C. L. GARRIDO ALZAR, *Limitations of the Modulation Method to Smooth Wire-guide Roughness*, Phys. Rev. A, 77 (2008).
- [21] I. BOUCHOULE, N. VAN DRUTEN, AND C. WESTBROOK, *Ch.11: Atom Chip and One-Dimensional Bose Gases*, Wiley-VCH, 2010.
- [22] G. P. BRANDINO, J.-S. CAUX, AND R. M. KONIK, *Glimmers of a Quantum KAM Theorem: Insights from Quantum Quenches in One-Dimensional Bose Gases*, Phys. Rev. X, 5 (2015).
- [23] H. BÜCHLER, G. BLATTER, AND W. ZWINGER, *Commensurate-Incommensurate Transition of Cold Atoms in an Optical Lattice*, Phys. Rev. Lett., 90 (2003).
- [24] Y. CASTIN, *Simple Theoretical Tools for Low-dimensional Bose Gases*, Les Houches Lecture Notes, (2004).
- [25] Y. CASTIN AND R. DUM, *Bose-Einstein Condensates in Time-dependent Traps*, Phys. Rev. Lett., 77 (1996).
- [26] Y. CASTIN, R. DUM, E. MANDONNET, A. MINGUZZI, AND I. CARUSOTTO, *Coherence Properties of a Continuous Atom Laser*, Journal of Modern Optics, 47 (2000).
- [27] M. A. CAZALILLA, R. CITRO, T. GIAMARCHI, E. ORIGNAC, AND M. RIGOL, *One dimensional Bosons: From Condensed Matter Systems to Ultracold Gases*, Reviews of Modern Physics, 83 (2011).
- [28] A. M. CHANG, L. N. PFEIFER, AND K. W. WEST, *Observation of Chiral Luttinger Behavior in Electron Tunneling into Fractional Quantum Hall Edges*, Phys. Rev. Lett., 97 (1996).
- [29] D. CHEN, M. WHITE, C. BORIES, AND B. DEMARCO, *Quantum Quench of an Atomic Mott Insulator*, Phys. Rev. Lett., 23 (2011).
- [30] M. CHENEAU, P. BARMETTLER, D. POLETTI, M. ENDRES, P. SCHAUSS, T. FUKUHARA, C. GROSS, I. BLOCH, C. KOLLATH, AND S. KUHR, *Light-cone-like Spreading of Correlations in a Quantum Many-body System*, Nature, 481 (2012).

- [31] L. CHOMAZ, L. CORMAN, T. BIENAIMÉ, R. DESBUQUOIS, C. WEITENBERG, S. NASCIMBÈNE, J. BEUGNON, AND J. DALIBARD, *Emergence of Coherence via Transverse Condensation in a Uniform Quasi-two-dimensional Bose Gas*, Nat. Comm., 6 (2015).
- [32] J.-H. CHU, J. G. ANALYTIS, K. DE GREVE, P. L. MCMAHON, Y. YAMAMOTO, AND I. R. FISHER, *In-Plane Resistivity Anisotropy in an Underdoped Iron Arsenide Superconductor*, Science, 329 (2010).
- [33] D. CLÉMENT, N. FABBRI, L. FALLANI, C. FORT, AND M. INGUSCIO, *Exploring Correlated 1D Bose Gases from the Superfluid to the Mott-Insulator State by Inelastic Light Scattering*, Phys. Rev. Lett., 102 (2009).
- [34] M. COMINOTTI, *Mesoscopic Physics of a One-dimensional Bose gas: Persistent Currents and Collective Dipole Excitations*, PhD thesis, Université de Grenoble, 2015.
- [35] M. COMINOTTI, F. HEKKING, AND A. MINGUZZI, *Dipole Mode of a Strongly Correlated One-dimensional Bose Gas in a Split Trap: Parity Effect and Barrier Renormalisation*, arXiv, 1503.07776 (2015).
- [36] M. COMINOTTI, D. ROSINI, M. RIZZI, F. HEKKING, AND A. MINGUZZI, *Optimal Persistent Currents for Interacting Bosons on a Ring with a Gauge Field*, Phys. Rev. Lett., 113 (2014).
- [37] M. J. DAVIS, P. B. BLAKIE, A. H. VAN AMERONGEN, N. J. VAN DRUTEN, AND K. V. KHERUNTSYAN, *Yang-Yang Thermometry and Momentum Distribution of a Trapped One-dimensional Bose Gas*, Phys. Rev. A, 85 (2012).
- [38] C. DE GRANDI, V. GRITSEV, AND A. POLKOVNIKOV, *Quench Dynamics near a Quantum Critical Point: Application to the Sine-Gordon Model*, Phys Rev. B, 81 (2010).
- [39] J. DENSCHLAG, D. CASSETTARI, AND J. SCHMIEDMAYER, *Guiding Neutral Atoms with a Wire*, Phys. Rev. Lett., 82 (1999).
- [40] J. M. DEUTSCH, *Quantum Statistical Mechanics in a Closed System*, Phys. Rev. A, 43 (1991).
- [41] A. ELOY, *Construction d'un système laser pour une expérience d'atomes froids*, 2013.
- [42] T. ESSLINGER, I. BLOCH, AND T. W. HÄNSCH, *Bose-Einstein Condensation in a Quadrupole-Ioffe-Configuration Trap*, Phys. Rev. A, 58 (1998).
- [43] J. ESTÈVE, J.-B. TREBBIA, T. SCHUMM, A. ASPECT, C. I. WESTBROOK, AND I. BOUCHOULE, *Observations of Density Fluctuations in an Elongated Bose Gas: Ideal Gas and Quasicondensate Regimes*, Phys. Rev. Lett., 96 (2006).
- [44] J. ESTÈVE, *Du miroir au guide d'onde atomique : effets de rugosité*, PhD thesis, Université Paris Sud, 2004.
- [45] J. ESTÈVE, C. AUSSIBAL, T. SCHUMM, C. FIGL, D. MAILLY, I. BOUCHOULE, C. I. WESTBROOK, AND A. ASPECT, *Role of Wire Imperfections in Micromagnetic Traps for Atoms*, Phys. Rev. A, 70 (2004).

- [46] N. FABBRI, D. CLÉMENT, L. FALLANI, C. FORT, AND M. INGUSCIO, *Momentum-resolved Study of an Array of One-dimensional Strongly Phase-fluctuating Bose Gases*, Phys. Rev. A, 83 (2011).
- [47] N. FABBRI, D. CLÉMENT, L. FALLANI, C. FORT, M. MODUGNO, K. VAN DER STAM, AND M. INGUSCIO, *Excitations of Bose-Einstein Condensates in a One-dimensional Periodic Potential*, Phys. Rev. A, 79 (2009).
- [48] N. FABBRI, S. D. HUBER, D. CLÉMENT, L. FALLANI, C. FORT, M. INGUSCIO, AND E. ALTMAN, *Quasiparticle Dynamics in a Bose Insulator Probed by Interband Bragg Spectroscopy*, Phys. Rev. Lett., 109 (2012).
- [49] B. FANG, *Equilibrium and Non-equilibrium Behaviours in 1D Bose Gases*, PhD thesis, Institut d'Optique Graduate School, 2014.
- [50] B. FANG, G. CARLEO, A. JOHNSON, AND I. BOUCHOULE, *Quench-Induced Breathing Mode of One-Dimensional Bose Gases*, Phys. Rev. Lett., 113 (2014).
- [51] B. FANG, A. JOHNSON, T. ROSCILDE, AND I. BOUCHOULE, *Momentum-Space Correlations of a One-Dimensional Bose Gas*, Phys. Rev. Lett., 116 (2016).
- [52] M. FISHER, P. WEICHMANN, G. GRINSTEIN, AND D. FISHER, *Boson Localization and the Superfluid-Insulator Transition*, Phys. Rev. B, 40 (1989).
- [53] R. FOLMAN, P. KRÜGER, D. CASSETTARI, B. HESSMO, T. MAIER, AND J. SCHMIEDMAYER, *Controlling Cold Atoms using Nanofabricated Surfaces: Atom Chips*, Phys. Rev. Lett., 84 (2000).
- [54] J. FORTAGH, A. GROSSMANN, C. ZIMMERMANN, AND T. W. HÄNSCH, *Miniatrized Wire Trap for Neutral Atoms*, Phys. Rev. Lett., 81 (1998).
- [55] J. FORTÁGH AND C. ZIMMERMANN, *Magnetic Microtraps for Ultracold Atoms*, Reviews of Modern Physics, 79 (2007).
- [56] S. FÖLLING, F. GERBIER, A. WIDERA, O. MANDEL, T. GERICKE, AND I. BLOCH, *Spatial Quantum Noise Interferometry in Expanding Ultracold Atom Clouds*, Nature, 434 (2005).
- [57] D. GANGARDT AND G. SHLYAPNIKOV, *Stability and Phase Coherence of Trapped 1D Bose Gases*, Phys. Rev. Lett., 90 (2003).
- [58] F. GERBIER, *Quasi-1D Bose-Einstein Condensates in the Dimensional Crossover Regime*, Europhysics Letters, 66 (2004).
- [59] F. GERBIER, J. H. THYWISSEN, S. RICHARD, M. HUGBART, P. BOUYER, AND A. ASPECT, *Momentum Distribution and Correlation Function of Quasicondensates in Elongated Traps*, Phys. Rev. A, 67 (2003).
- [60] H. GERSCH AND G. KNOLLMAN, *Quantum Cell Model for Bosons*, Phys. Rev., 129 (1963).
- [61] M. GIRARDEAU, *Relationship between Systems of Impenetrable Bosons and Fermions in One Dimension*, Journal of Mathematical Physics, 1 (1960).

- [62] M. GREINER, O. MANDEL, T. ESSLINGER, T. W. HÄNSCH, AND I. BLOCH, *Quantum Phase Transition from a Superfluid to a Mott Insulator in a Gas of Ultracold Atoms*, *Nature*, 415 (2002).
- [63] ———, *Quantum Phase Transition from a Superfluid to a Mott Insulator in a Gas of Ultracold Atoms*, *Nature*, 415 (2002).
- [64] M. GRING, M. KUHNERT, T. LANGEN, T. KITAGAWA, B. RAUER, M. SCHREITL, I. MAZETS, D. ADU SMITH, E. DEMLER, AND J. SCHMIEDMAYER, *Relaxation and Prethermalization in an Isolated Quantum System*, *Science*, 337 (2012).
- [65] P. GRIŠINS, B. RAUER, T. LANGEN, J. SCHMIEDMAYER, AND I. E. MAZETS, *Degenerate Bose Gas with Uniform Loss*, *Phys. Rev. A*, 93 (2016).
- [66] E. GROSS, *Structure of a Quantized Vortex in Boson Systems*, *Il Nuovo Cimento*, XX (1961).
- [67] E. HALLER, M. GUSTAVSSON, M. J. MARK, J. G. DANZL, R. HART, G. PUPILLO, AND H.-C. NÄGERL, *Realization of an Excited, Strongly-Correlated Quantum Gas Phase.*, *Science*, 466 (2010).
- [68] E. HALLER, R. HART, M. J. MARK, J. G. DANZL, L. REICHSSÖLLNER, M. GUSTAVSSON, M. DALMONTE, G. PUPILLO, AND H.-C. NÄGERL, *Pinning Quantum Phase Transition for a Luttinger Liquid of Strongly Interacting Bosons*, *Nature*, 466 (2010).
- [69] E. HALLER, M. MARK, R. HART, J. DANZL, J. REICHSSÖLLNER, V. MELEZHIK, P. SCHMELCHER, AND H. NÄGERL, *Confinement-Induced Resonances in Low-Dimensional Quantum Systems*, *Phys. Rev. Lett.*, 104 (2010).
- [70] W. HÄNSEL, P. HOMMELHOFF, T. W. HÄNSCH, AND J. REICHEL, *Bose–Einstein Condensation on a Microelectronic Chip*, *Nature*, 413 (2001).
- [71] A. J. HEEGER, S. KIVELSON, J. R. SCHRIEFFER, AND W.-P. SU, *Non-equilibrium Coherence Dynamics in One-dimensional bose gases*, *Rev. Mod. Phys.*, 60 (1988).
- [72] S. HOFFERBERTH, I. LESANOVSKY, B. FISCHER, T. SCHUMM, AND J. SCHMIEDMAYER, *Non-equilibrium Coherence Dynamics in one-dimensional Bose Gases*, *Nature*, 449 (2007).
- [73] P. I. HURTADO AND S. REDNER, *Simplest Piston Problem. i. Elastic Collisions*, *Phys. Rev. E*, 73 (2006).
- [74] Z. HWANG, F. CAO, AND M. OLSHANII, *Traces of Integrability in Relaxation of One-Dimensional Two-Mass Mixtures*, *J. Stat. Phys.*, 161 (2015).
- [75] A. IMAMBEKOV, I. E. MAZETS, D. S. PETROV, V. GRITSEV, S. MANZ, S. HOFFERBERTH, T. SCHUMM, E. DEMLER, AND J. SCHMIEDMAYER, *Density Ripples in Expanding Low-dimensional Gases as a Probe of Correlations*, *Phys. Rev. A*, 80 (2009).
- [76] M. ISHIKAWA AND H. TAKAYAMA, *Solitons in a one-dimensional Bose System with the repulsive Delta-function Interaction*, *J. Phys. Soc. Jap.*, 49 (1980).

- [77] Z. ISING, *Beitrag zur Theorie des Ferromagnetismus*, Z. Phys., 31 (1925).
- [78] T. JACQMIN, *Probing Correlations in a One-Dimensional Gas of Bosons on an Atom Chip*, PhD thesis, Université Paris Sud, 2012.
- [79] T. JACQMIN, J. ARMijo, T. BERRADA, K. KHERUNTSYAN, AND I. BOUCHOULE, *Sub-Poissonian Fluctuations in a 1D Bose Gas: From the Quantum Quasicondensate to the Strongly Interacting Regime*, Phys. Rev. Lett., 106 (2011).
- [80] T. JACQMIN, B. FANG, T. BERRADA, T. ROSCILDE, AND I. BOUCHOULE, *Momentum Distribution of One-dimensional Bose gases at the Quasicondensation crossover: Theoretical and Experimental Investigation*, Phys. Rev. A, 86 (2012).
- [81] D. JAKSCH, C. BRUDER, J. I. CIRAC, C. W. GARDINER, AND P. ZOLLER, *Cold Bosonic Atoms in Optical Lattices*, Phys. Rev. Lett., 81 (1998).
- [82] J. JASKULA, J. PARTRIDGE, M. BONNEAU, R. LOPES, J. RUAUDEL, D. BOIRON, AND C. WESTBROOK, *Acoustic Analog to the Dynamical Casimir Effect in a Bose-Einstein Condensate*, Phys. Rev. Lett., 109 (2012).
- [83] T. JELTES, J. McNAMARA, V. HOGERVORST, W. VASSEN, V. KRACHMALNI-COFF, M. SCHELLEKENS, A. PERRIN, H. CHANG, D. BOIRON, A. ASPECT, AND C. WESTBROOK, *Comparison of the Hanbury Brown Twiss Effect for Bosons and Fermions*, Nature, 445 (2006).
- [84] T. KARPIUK, T. SOWINSKI, M. GAJDA, K. RZAZWIESKI, AND M. BREWCZYK, *Correspondence Between Dark Solitons and the type II Excitations of the Lieb-Liniger Model*, Phys. Rev. A, 91 (2015).
- [85] A. M. KAUFMAN, E. TAI, A. LUKIN, M. RISPOLI, R. SCHITTKO, P. M. PREISS, AND M. GREINER, *Quantum Thermalization Through Entanglement in an Isolated Many-Body System*, Science, 351 (2016).
- [86] W. KETTERLE, D. DURFEE, AND D. STAMPER-KURN, *Making, Producing and Understanding Bose-Einstein Condensates*, arXiv, 9904034 (1999).
- [87] W. KETTERLE AND N. J. V. VAN DRUTEN, *Advances in Atomic, Molecular and Optical Physics*, 1996.
- [88] K. KHERUNTSYAN, D. GANGARDT, P. DRUMMOND, AND G. SHLYAPNIKOV, *Pair Correlations in a Finite-Temperature 1D Bose Gas*, Phys. Rev. Lett., 91 (2003).
- [89] B. KIBLER, J. FATOME, C. FINOT, G. MILLOT, F. DIAS, G. GENTY, N. AKHMEDIEV, AND J. DUDLEY, *The Peregrine Soliton in Nonlinear Fibre Optics*, Nat. Phys., 6 (2010).
- [90] T. KINOSHITA, T. WENGER, AND D. S. WEISS, *Observation of a One-dimensional Tonks-Girardeau Gas*, Science, 305 (2004).
- [91] ——, *Local Pair Correlations in One-Dimensional Bose Gases*, Phys. Rev. Lett., 19 (2005).
- [92] ——, *A Quantum Newton's Cradle*, Nature, 440 (2006).

- [93] S. KRAFT, A. GÜNTHER, H. OTT, D. WHARAM, C. ZIMMERMANN, AND J. FORTÀGH, *Anomalous Longitudinal Magnetic Field Near the Surface of Copper Conductors*, Journal of Physics B: Atomic, Molecular and Optical Physics, 35 (2002).
- [94] T. D. KÜHNER AND H. MONIEN, *Phases of the One-dimensional Bose-Hubbard Model*, Phys. Rev. B, 58 (1998).
- [95] M. KULKARNI AND A. LAMACRAFT, *Finite-Temperature Dynamical Structure Factor of the One-dimensional Bose Gas: From the gross-pitaevskii Equation to the kardar-parisi-zhang Universality Class of Dynamical Critical Phenomena*, Phys. Rev. A, 88 (2013).
- [96] T. LANGEN, S. ERNE, R. GEIGER, B. RAUER, T. SCHWEIGLER, M. KUHNERT, W. ROHRINGER, I. MAZETS, T. GASENZER, AND J. SCHMIEDMAYER, *Experimental observation of a generalized Gibbs ensemble*, Science, 348 (2015).
- [97] T. LANGEN, R. GEIGER, M. KUHNERT, B. RAUER, AND J. SCHMIEDMAYER, *Local Emergence of Thermal Correlations in an Isolated Quantum Many-body System*, Nat. Phys., 9 (2013).
- [98] S. LELLOUCH, T.-L. DAO, T. KOFFEL, AND L. SANCHEZ-PALENCIA, *Two-component Bose Gases with One-body and Two-body Couplings.*, Phys Rev. A, 88 (2013).
- [99] W. I. LENZ, *Beiträge zum Verständnis der Magnetischen Eigenschaften in Festen Körpern*, Z. Phys., 21 (1920).
- [100] E. LIEB, *Phys. Rev.* 130, 1616 (1963) - *Exact Analysis of an Interacting Bose Gas. II. The Excitation Spectrum*, Phys. Rev., 130 (1963).
- [101] E. LIEB AND W. LINIGER, *Exact Analysis of an Interacting Bose Gas. I. The General Solution and the Ground State*, Phys. Rev., 130 (1963).
- [102] O. J. LUITEN, M. W. REYNOLDS, AND J. T. M. WALRAVEN, *Kinetic Theory of the Evaporative Cooling of a Trapped Gas*, Phys. Rev. A, 53 (1996).
- [103] J. M. LUTTINGER, *An Exactly Soluble Model of a Many-Fermion System*, Journal of Mathematical Physics, 4 (1963).
- [104] S. MANZ, R. BÜCKER, T. BETZ, C. KOLLER, S. HOFFERBERTH, I. MAZETS, A. IMAMBEKOV, E. DEMLER, A. PERRIN, J. SCHMIEDMAYER, AND T. SCHUMM, *Two-point Density Correlations of Quasicondensates in Free Expansion*, Phys. Rev. A, 81 (2010).
- [105] F. MARQUARDT AND A. PÜTTMANN, *Introduction to Dissipation and Decoherence in Quantum Systems*, arXiv, 0809.4403 (2008).
- [106] L. MATHEY, A. VISHWANATH, AND E. ALTMAN, *Noise Correlations in Low-dimensional Systems of Ultracold Atoms*, Phys. Rev. A, 79 (2009).
- [107] H. METCALF AND P. VAN DER STRATEN, *Laser Cooling and Trapping*, Springer-Verlag New York, 1999.

- [108] C. MORA AND Y. CASTIN, *Extension of Bogoliubov Theory to Quasi-condensates*, Phys. Rev. A, 67 (2003).
- [109] N. MOTT, *The Basis of the Electron Theory of Metals, with Special Reference to the Transition Metals*, Proc. Phys. Soc. A, 92 (1968).
- [110] ———, *Metal-Insulator Transition*, Rev. Mod. Phys., 40 (1968).
- [111] E. NICKLAS, M. KARL, M. HÖFER, A. JOHNSON, W. MUSSUL, H. STROBEL, J. TOMKOVIC, T. GASENZER, AND M. OBERTHALER, *Observation of Scaling in the Dynamics of a Strongly Quenched Quantum Gas*, Phys. Rev. Lett., 115 (2015).
- [112] R. OLF, F. F., G. EDWARD MARTI, A. MACRAE, AND D. M. STAMPER-KURN, *Thermometry and Cooling of a Bose Gas to 0.02 Times the Condensation Temperature*, Nat Phys., 11 (2015).
- [113] M. OLSHANII, *Atomic Scattering in the Presence of an External Confinement and a Gas of Impenetrable Bosons*, Phys. Rev. Lett., 81 (1998).
- [114] L. ONSAGER, *Crystal Statistics. I. A Two-dimensional Model with an Order-Disorder Transition*, Phys. Rev., 65 (1944).
- [115] H. OTT, J. FORTAGH, G. SCHLOTTERBECK, A. GROSSMANN, AND C. ZIMMERMANN, *Bose-Einstein Condensation in a Surface Microtrap*, Phys. Rev. Lett., 87 (2001).
- [116] T. OTTENSTEIN, *A New Objective for High Resolution Imaging of Bose-Einstein Condensates*, Master's thesis, University of Heidelberg, 2006.
- [117] B. PAREDES, A. WIDERA, V. MURG, O. MANDEL, S. FÖLLING, I. CIRAC, G. SHLYAPNIKOV, T. W. HÄNSCH, AND I. BLOCH, *Tonks-Girardeau Gas of Ultracold Atoms in an Optical Lattice*, Nature, 113 (2014).
- [118] H. PICHLER, J. SCHACHENMAYER, A. DALEY, AND P. ZOLLER, *Heating Dynamics of Bosons in a Noisy Optical Lattice*, Phys. Rev. A, 87 (2013).
- [119] L. PITAEVSKII, *Vortex Lines in an Imperfect Bose Gas*, Sov. Phys. JETP, 13 (1961).
- [120] V. POKROVSKY AND A. TALAPOW, *Ground State, Spectrum, and Phase Diagram of Two-dimensional Incommensurate Crystals*, Phys. Rev. Lett., 42 (1979).
- [121] A. POLKOVNIKOV, *Universal Adiabatic Dynamics in the Vicinity of a Quantum Critical Point*, Phys Rev. B, 72 (2005).
- [122] A. POLKOVNIKOV, K. SENGUPTA, A. SILVA, AND M. VENGELATORRE, *Nonequilibrium Dynamics of Closed Interacting Quantum Systems*, Rev. Mod. Phys., 83 (2011).
- [123] G. PUPILLO, C. WILLIAMS, AND N. V. PROKOF'EV, *Effects of Finite Temperature on the Mott-Insulator State*, Phys. Rev. A, 73 (2003).
- [124] B. RAUER, P. GRIŠINS, I. E. MAZETS, T. SCHWEIGLER, W. ROHRINGER, R. GEIGER, AND T. LANGEN, *Cooling of a One-dimensional Bose Gas*, Phys. Rev. Lett., 116 (2016).

- [125] J. REICHEL, *Ch.2, Trapping and Manipulating Atoms on Chips*, Wiley-VCH, 2010.
- [126] G. REINAUDI, T. LAHAYE, Z. WANG, AND D. GUÉRY-ODELIN, *Strong Saturation Absorption Imaging of Dense Clouds of Ultracold Atoms*, Optics Letters, 32 (2007).
- [127] S. RICHARD, F. GERBIER, J. H. THYWISSEN, M. HUGBART, P. BOUYER, AND A. ASPECT, *Momentum Spectroscopy of 1D Phase Fluctuations in Bose-Einstein Condensates*, Phys. Rev. Lett., 91 (2003).
- [128] A. RIGOL, M. MARAMATSU, G. BATROUNI, AND R. T. SCALETTAR, *Local Quantum Criticality in Confined Fermions on Optical Lattices*, Phys. Rev. Lett., 91 (2003).
- [129] M. RIGOL, G. BATROUNI, V. ROUSSEAU, AND R. SCALETTAR, *State Diagrams for Harmonically Trapped Bosons in Optical Lattices*, Phys. Rev. A, 79 (2009).
- [130] M. RIGOL, V. DUNJKO, AND M. OLSHANII, *Thermalization and its Mechanisms for Generic Isolated Quantum Systems*, Nature, 452 (2008).
- [131] T. ROM, T. BEST, D. VAN OOSTEN, U. SCHNEIDER, S. FÖLLING, B. PAREDES, AND I. BLOCH, *Free Fermion Antibunching in a Degenerate Atomic Fermi Gas Released from an Optical Lattice*, Nature, 444 (2006).
- [132] A. W. SANDVIK, *Computational Studies of Quantum Spins*, arXiv, 1101.3281 (2011).
- [133] T. SCHUMM, S. HOFFERBERTH, A. L. M., S. WILDERMUTH, S. GROTH, I. BAR-JOSEPH, S. J., AND P. KRÜGER, *Matter-wave Interferometry in a Double Well on an Atom Chip*, Nat. Phys., (2005).
- [134] I. SCHVARCHUCK, C. BUGGLE, D. PETROV, K. DIECKMANN, M. ZIELONKOWSKI, M. KEMMANN, T. TIECKE, W. VON KLITZING, G. SCHLYAPNIKOV, AND J. WALRAVEN, *Bose-Einstein Condensation into Non-equilibrium States Studied by Condensate Focussing*, Phys. Rev. Lett, 89 (2002).
- [135] J. STENGER, S. INOUYE, A. P. CHIKKATUR, D. M. STAMPER-KURN, D. E. PRITCHARD, AND W. KETTERLE, *Bragg Spectroscopy of a Bose-Einstein Condensate*, Phys. Rev. Lett., 82 (1999).
- [136] T. STÖFERLE, H. MORITZ, C. SCHORI, M. KÖHL, AND T. ESSLINGER, *Transition from a Strongly Interacting 1D Superfluid to a Mott Insulator*, Phys. Rev. Lett., 92 (2004).
- [137] E. SURKOV, J. WALRAVEN, AND G. SHLYAPNIKOV, *Collisionless Motion and Evaporative Cooling of Atoms in Magnetic Traps*, Phys. Rev. A, 53 (1996).
- [138] S. TOMONAGA, *Remarks on Bloch's Method of Sound Waves Applied to Many-fermion Problems*, Progress of Theoretical Physics, 5 (1950).
- [139] L. TONKS, *The Complete Equation of State of One, Two and Three-Dimensional Gases of Hard Elastic Spheres*, Phys. Rev., 50 (1936).
- [140] J. M. TRANQUADA, B. J. STERNLIEB, A. J. D., Y. NAKAMURA, AND S. UCHIDA, *Evidence for Stripe Correlations of Spins and Holes in Copper Oxide Superconductors*, Nature, 375 (1995).

- [141] J.-B. TREBBIA, *Etude de gaz quantiques dégénérés quasi-unidimensionnels confinés par une micro-structure*, PhD thesis, Université Paris Sud, 2007.
- [142] J.-B. TREBBIA, C. L. GARRIDO ALZAR, R. CORNELUSSEN, C. I. WESTBROOK, AND I. BOUCHOULE, *Roughness Suppression via Rapid Current Modulation on an Atom Chip*, *Phy. Rev. Lett.*, 98 (2007).
- [143] S. TUNG, G. LAMPORESI, D. LOBSER, L. XIA, AND E. CORNELL, *Observation of the Pre-superfluid Regime in a Two-dimensional Bose Gas.*, *Phys. Rev. Lett.*, 105 (2010).
- [144] A. VAN AMERONGEN, J. VAN ES, P. WICKE, K. KHERUNTSYAN, AND N. VAN DRUTEN, *Yang-Yang Thermodynamics on an Atom Chip.*, *Phys. Rev. Lett.*, 100 (2008).
- [145] E. VAN KEMPEN, S. KOKKELMANS, D. HENZEN, AND B. VERHAAR, *Interisotope Determination of Ultracold Rubidium Interactions from Three High-Precision Experiments*, *Phys. Rev. Lett.*, 88 (2002).
- [146] A. VAN OUDENAARDEN AND J. E. MOOIJ, *One-Dimensional Mott Insulator Formed by Quantum Vortices in Josephson Junction Arrays*, *Phys. Rev. Lett.*, 76 (1996).
- [147] A. VOGLER, R. LABOUVIE, F. STUBENRAUCH, G. BARONTINI, V. GUERRERA, AND H. OTT, *Thermodynamics of Strongly Correlated One-dimensional Bose Gases*, *Phys. Rev. A*, 88 (2013).
- [148] G. C. W. AND P. ZOLLER, *Quantum Noise*, Springer-Verlag, Berlin, 2004.
- [149] S. WHITE, *Density Matrix Formulation for Quantum Renormalization Groups*, *Phys. Rev. Lett.*, 69 (1992).
- [150] J. C. WICK, *The Evaluation of the Collision Matrix*, *Phys. Rev.*, 80 (1950).
- [151] A. YACOBY, H. L. STORMER, N. WINGREEN, AND K. W. PFEIFFER, L. N. ABD WEST, *Nonuniversal Conductance Quantization in Quantum Wires*, *Phys. Rev. Lett.*, 77 (1996).
- [152] C. N. YANG, *Some Exact Results for the Many-Body Problem in one Dimension with Repulsive Delta-Function Interaction*, *Phys. Rev. Lett.*, 19 (1967).
- [153] T. YEFSAH, R. DESBUQUOIS, L. CHOMAZ, K. GÜNTER, AND J. DALIBARD, *Exploring the Thermodynamics of a Two-Dimensional Bose Gas.*, *Phys. Rev. Lett.*, 107 (2011).
- [154] W. ZUREK, U. DORNER, AND P. ZOLLER, *Dynamics of a Quantum Phase Transition*, *Phys Rev. Lett.*, 95 (2005).
- [155] W. ZWERGER, *Mott-Hubbard Transition of Cold Atoms in Optical Lattices*, *J. Opt. B: Quantum Semiclass. Opt.*, 5 (2003).